KINETIC STUDY OF INTRACELLULAR ICE FORMATION IN MICROPATTERNED ENDOTHELIAL CELL CULTURES USING HIGH SPEED VIDEO CRYOMICROSCOPY

A Dissertation
Presented to
The Academic Faculty

By

Shannon Leigh Stott

In Partial Fulfillment
Of the Requirements for the Degree
Doctor of Philosophy in Mechanical Engineering

Georgia Institute of Technology
August 2006

KINETIC STUDY OF INTRACELLULAR ICE FORMATION IN MICROPATTERNED ENDOTHELIAL CELL CULTURES USING HIGH SPEED VIDEO CRYOMICROSCOPY

Approved by:

Dr. Jens O. M. Karlsson, chair
School of Mechanical Engineering
Georgia Institute of Technology

Dr. Andrés J. García
School of Mechanical Engineering
Georgia Institute of Technology

Dr. Hanjoong Jo
Department of Biomedical Engineering
Georgia Institute of Technology

Dr. Athanassios Sambanis
School of Chemical & Biomolecular Engineering
Georgia Institute of Technology

Dr. Cheng Zhu
School of Mechanical Engineering
Georgia Institute of Technology

Date Approved: July 8th, 2006

ACKNOWLEDGEMENTS

First and foremost, I would like to thank my advisor, Dr. Jens Karlsson, for his guidance, patience, and unwavering support. Due to his sharp intellect and exacting standards, I believe I have grown immensely as a scientist over the last four years. I would also like to express my gratitude to my dissertation committee, Dr. Andrés García, Dr. Hanjoong Jo, Dr. Athanassios Sambanis and Dr. Cheng Zhu, for their insights and thoughtful suggestions regarding this work.

I owe many thanks to both past and present members of the Biothermal Sciences Laboratory. Adam Higgins has been by side during my entire tenure in the BSL, with his easy going personality providing much needed balance to my occasional moments of angst. I will greatly miss Adam's creativity, intellect and fabulous Hawaiian shirts. After Megan Dickherber graduated from the lab, her exuberant spirit and brilliance were missed daily. However, I have been fortunate to have Megan transition into one of my best friends and I thank her for her support and faith in me. I would also like to thank Jonathan Barletta, Kevin Carnevale, and Neel Bagchi. While I was never so fortunate to work directly with Dr. Daniel Irimia, I am indebted to his thesis research, for it provided the launching point for much of what is presented in this work.

There are many people who have challenged, supported and guided me during my graduate school career, of which I would like to acknowledge Dr. Bill Wepfer, Dr. Robert Nerem, Dr. Marc Levenston, and Sally Gerrish for their open doors and sage wisdom. I would also like to express my sincerest gratitude to Dr. Clark Bullard, who has been a mentor to me since my first day of graduate school. I would like to thank all of my

fellow colleagues and friends at Georgia Tech for their thoughtful discussions, scientific insights, and most importantly, great moments of hilarity.

My family is and always will be my greatest source of support and strength. To my parents, Donna, Charles and Rosamond Stott, thank you for providing an endless supply of encouragement and love. Thank you Matthew and Wayne for offering much needed comic relief with a dash of serious big-brother protection. Megan, you will always be my little sister, but you will also always be one of my best friends. Thank you to my grandparents, Lucy and Wayne Scull, for the notes of encouragement and constant love. To all of the Vanderploegs, thank you for welcoming me into your family and treating me as such. While technically not family, Marleen Callahan deserves special acknowledgement for being the most amazing best friend.

Graduate school has brought many wonderful things into my life, but the greatest by far was Eric Vanderploeg. Thank you, Eric, for your strength, laughter and willingness to tolerate my many idiosyncrasies. Your enduring love has made this roller coaster called graduate school and incredibly rich and enjoyable ride. As we climb up the next hill, there is no one whose hand I would rather be holding.

This work was funded by NSF Grant BES-0541530. I would like to express my personal gratitude to the following sources of support: the American Association of University Women, the ARCS Foundation, ASME Graduate Teaching Fellowships, the Graves Family Foundation, GTEC, Medtronic Foundation, and the NIH Cellular Engineering Training Grant.

TABLE OF CONTENTS

LIST OF TABLES

LIST OF FIGURES

SUMMARY

Intracellular ice formation (IIF), a major cause of cryoinjury in biological cells, is significantly more pronounced during freezing of tissue than during freezing of suspended cells. While extensive studies of IIF have been conducted for single cells in suspension, few have investigated IIF in tissue. Due to the increased complexity that arises from both cell-substrate and cell-cell interactions in tissue, knowledge of cryobiology of isolated cells cannot simply be extrapolated to tissue. Different theories have been hypothesized for the mechanisms of IIF in tissue, but none have been conclusively proven. Towards the goal of developing mathematical models to accurately predict the probability of IIF in tissues of one or more cell types, we have developed a novel high-speed video cryomicroscopy system capable of image acquisition at sampling rates up to 32,000 Hz. Specifically, the effects of cell adhesion to the substrate and cell-cell interactions were investigated with experimental (micropatterned endothelial cell constructs) and mathematical models (Monte Carlo simulations). We have reported the first direct observations of the IIF process recorded at unprecedented sub-millisecond and sub-micron resolution. For the majority of our experiments, IIF nucleation was determined to occur preferentially at the cell perimeter. This observation was not consistent with the commonly accepted hypotheses of ice nucleation in suspended cells and suggests that an alternative mechanism of IIF initiation is dominant in adherent cells. In addition, the kinetics of ice nucleation were shown to be influenced by time in culture, attached cell perimeter, fibronectin coating density, and degree of cell-cell contact. Moreover, an additional phenomenon, paracellular ice penetration was identified, and the

frequency of formation was correlated with focal adhesion formation. The data and mathematical models presented in this thesis bring closer the goal of elucidating the primary mechanisms contributing to IIF in tissue; providing important contributions to both the fields of cryopreservation (minimizing IIF) and cryosurgery (maximizing IIF).

CHAPTER 1

INTRODUCTION

1.1 Motivation

Successful cryopreservation of living tissue will significantly improve the marketability of tissue engineered products, enabling their mass-production, banking and distribution[1]. However, significant loss of tissue function can result from cell damage caused by intracellular ice formation (IIF) during cooling to cryogenic storage temperatures[2]. While vitrification strategies have shown promise for long term storage of tissues[3]; difficulties with cell toxicity arising from high cryoprotectant concentrations and devitrification upon warming have been shown[4,5]. As such, if the mechanisms of ice formation in tissue can be identified and subsequently controlled, ice-assisted freezing would be a highly desirable strategy for tissue storage. Freezing of biological tissues presents a great challenge, for both cell-substrate and cell-cell interactions are known to significantly impact the kinetics of IIF[6], making the tissue more susceptible to deleterious IIF events. The causes of these effects are unknown, and serve as the primary motivation for the studies presented in this thesis. An increased understanding of the mechanisms that contribute to IIF in attached cells and tissue will aid in the development of mathematical models that would provide great utility in the development of protocols for long term preservation of tissue engineered constructs, and aid in cryosurgery treatment planning.

1.2 Research Objectives

The long-term goal of this research was to develop optimal freezing procedures for tissue containing one or more cell types. The project approach was to develop new tools to investigate the mechanisms of damage associated with the freezing process. From the data obtained from these techniques, new theoretical models of the process of IIF in tissue were developed, towards the rational design and computer-aided optimization of techniques for cryopreservation or cryosurgery. The immediate objectives of the proposed research were to identify the dominant mechanisms of IIF in tissue constructs, to develop theoretical models of these mechanisms, and to test the predictions of the models. The underlying hypothesis of this research was that the probability of IIF is enhanced in tissue as a result of cell-substrate and cell-cell interactions; in particular, cell-substrate interactions are hypothesized to predispose cell membranes to mechanisms of IIF caused by extracellular ice, while cell-cell interactions are hypothesized to enable propagation of intracellular ice. The central hypothesis will be tested by pursuing the following specific aims:

Specific Aim 1. To elucidate the effects of cell-substrate interactions on intracellular ice formation in single micropatterned endothelial cells. The working hypothesis was that injury to adherent cells was caused by interactions between the extracellular ice and the cell, and as such, the kinetics of IIF would vary with cell size as well as alterations of the cell state (e.g., by modulating the substrate adhesive properties). To test this hypothesis, microfabricated substrates were used to provide precise control of cell-surface interactions during cryomicroscopy experiments.

Specific Aim 2. To quantify the kinetics of intercellular ice propagation in primary cells. The working hypothesis was that intercellular ice propagation in interacting primary cells will be modulated by cell-cell interaction. Moreover, we hypothesized that conventional cryomicroscopy systems were limited in their temporal and spatial resolution, preventing accurate measurements of the rate of intercellular ice propagation. A high speed cryomicroscopy system was used with micropatterned bovine and human endothelial cell constructs to determine the rate of intercellular ice propagation, as well as the influence of cell-cell contact on the spontaneous nucleation rate.

Specific Aim 3. To predict the kinetics and distribution of IIF in tissue constructs containing one or more cell types. The working hypothesis was that in tissue, initial IIF events are due to mechanisms associated with cell-substrate interactions, whereas subsequent IIF events are predominantly due to intercellular ice propagation. The interplay between these two rates will determine the overall rate and spatial distribution of IIF in tissue. Moreover, we hypothesized that in heterogeneous tissue (containing multiple cell species), variations in biophysical properties of distinct cell types would result in a large disparity in the freezing kinetics for each cell type. To test these hypotheses, computer simulations of tissue freezing were generated using new Monte Carlo methods.

1.3 Significance and Contribution

The studies performed for this dissertation provided insights into the mechanisms of intracellular ice formation in biological tissue. Additionally, the use of our high speed

cryomicroscopy system provided the first direction observation of the IIF process at unprecedented sub-millisecond and submicron resolution. Quantification of the effect of cell-substrate and cell-cell interactions on the kinetics of IIF enabled the creation of mathematical models that accurately predict the freezing kinetics for both single attached cells and heterogeneous tissues. Moreover, understanding the mechanisms of intracellular ice formation and intercellular ice propagation, as well as the identification of new phenomena associated with IIF, significantly contributed to our understanding of IIF in tissue. The qualitative and quantitative information obtained from this thesis work have brought closer the goal of rational design and computer-aided optimization of techniques for cryopreservation and cryosurgery.

CHAPTER 2

BACKGROUND AND LITERATURE REVIEW

2.1 Cryopreservation and Cryosurgery of Living Tissue

Cryopreservation and cryosurgical procedures both subject living biological tissue to ultra-low temperatures. However, the desired response of the tissue is dramatically different for the two aforementioned applications. In cryopreservation, the goal is to bring living tissue into a state of suspended animation, allowing for long-term storage, sterility control, quality control and tissue banking[7]. Conversely, in cryosurgery, a liquid nitrogen probe is used to create multiple freeze-thaw cycles that selectively destroy tissue[8]. In the past decade, cryosurgery has experienced a renaissance, and is now viewed as an effective treatment for cancerous tissues in the prostate, liver, breast, kidney, and bone[9-14]. Consequently, the ability to predict the response of biological tissue during freezing to cryogenic temperatures is of critical importance to both fields. The fate of the tissue during freezing, whether in cryopreservation or cryosurgery, is in large part determined by the formation of intracellular ice, an event known to be associated with irreversible cell damage[2,15]. Thus, in cryopreservation, to safely bring tissues to cryogenic temperatures, intracellular ice formation (IIF) must be minimized, whereas in cryosurgery, IIF should be maximized to effectively destroy the cancerous tissue. Understanding the biophysical response of tissue to freezing will significantly impact both fields, facilitating treatment planning and protocol optimization.

2.2 Transformation of Water to Ice

Due to the large volume fraction of water in biological cells and tissues, the phase transition of water to ice is of critical importance in the field of cryobiology. Nonetheless, the study of ice nucleation is a complex and difficult problem, with intensive research into nucleation theory spanning the last three centuries. Below the equilibrium melting point water will become thermodynamically unstable and will exist in a metastable or supercooled state[16,17]. In other words, water can remain unfrozen even below the melting temperature of ice. Nucleation of supercooled water can occur through homogeneous or heterogeneous nucleation. In homogeneous nucleation, transformation of supercooled water to ice requires the formation of a thermodynamically stable aggregate of water-molecules with ice-like properties, known as a nucleus or germ[18]. Unstable nuclei will spontaneously form in the supercooled water as a result of the constant motion of molecules in the water, resulting from thermal fluctuations[19]. In order for the ice nucleus to grow and subsequently crystallize the supercooled water, it must first overcome the thermodynamic barrier of surface tension in the interface between the molecules in the crystal structure and those in the surrounding liquid[20]. Once the nucleus grows to reach a critical radius, it will grow irreversibly, transforming the surrounding supercooled water to ice[19].

Ice nuclei do not always grow to reach the critical radius, and often dissolve back into the liquid[19]. As a consequence of the large number of water molecules that must aggregate to form a stable nucleus, homogeneous nucleation is not very efficient, resulting in high degrees of supercooling of the liquid (~40K for pure water). However, heterogeneous nucleation can also initiate ice formation, whereas solid particles act as a

catalytic substrate for crystal nucleation[21]. Through experimental observation, the statistical nature of nucleation is that of a random process, with the random variable being temperature[22,23]. The probability of freezing a volume of aqueous solution can be described by a Poisson process, with the temperature dependence modeled from classical nucleation theory[23]. The kinetics of ice crystal growth in pure water have also been measured experimentally using digital video analysis[24-26], magnetic resonance[27], and cross polarized light[28] techniques. Extensive mathematical models have also been created to predict the velocity of the ice front [29-31].

2.3 Biological Response to Freezing

As mentioned previously, the formation of intracellular ice during freezing of biological cells is a deleterious event, that has been directly correlated with cell death[32]. However, intracellular ice formation is not the only mechanism of damage that can occur during freezing. The cytoplasmic milieu of biological cells is a complex mixture of water, solutes, gases and intracellular organelles, all surrounded by a plasma membrane. The response of cells during freezing will vary based on the rate of change of temperature during cooling[32]. During freezing, ice forms initially in the extracellular liquid, creating a chemical potential difference across the cell membrane. If the cooling rate is sufficiently slow, the cell will attempt to establish a state of equilibrium by expressing water through the cell membrane, creating a state of extensive dehydration[7]. The high levels of dehydration in the cell will result in so-called "solution effects" injury, due to the high concentration of intracellular solutes. Conversely, if cooling rates are high, there is little to no transport of intracellular water out of the cell, increasing the probability of

intracellular ice nucleation. Typically, cryopreservation protocols are optimized by identifying the ideal cooling rate for a specific cell type that minimizes both dehydration and intracellular ice formation (Figure 2.1).

For the studies presented in this thesis, our goal was to explore the mechanisms associated with ice formation in attached cells. As such, experimental conditions during freezing were selected to promote IIF, while reducing secondary effects resulting from cell dehydration. Hence, all experiments were conducted using rapid cooling rates, without the addition of any cryoprotective agents (e.g. glycerol, dimethyl sulfoxide).

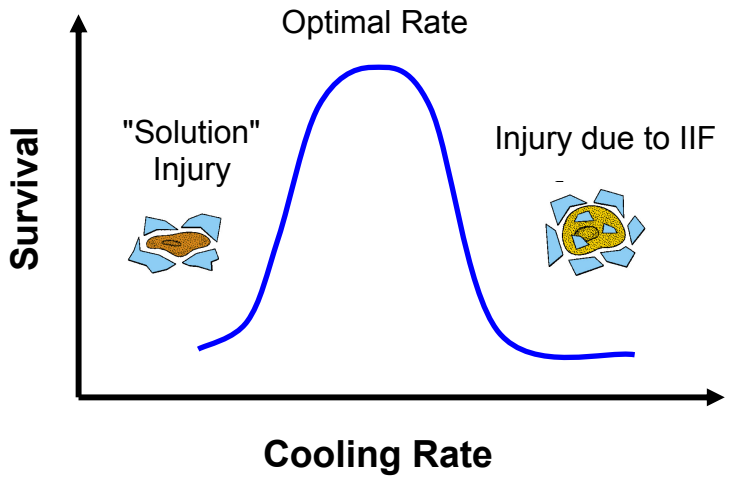

Figure 2.1 Effect of cooling rate on cell survival during freezing. For slow cooling rates, cell damage will result from solution effects, whereas at high cooling rates, injury may result from intracellular ice formation (IIF). Adapted from Karlsson and Toner[7].

2.4 Experimental Observation of Freezing

Cryomicroscopy techniques have previously been used to identify many of the biophysical phenomena that govern the response of biological cells to freezing (*e.g.* IIF, and cell dehydration)[33]. Modern cryomicroscopy systems typically consist of a specimen stage with independent, precise control of stage temperature and cooling rate, fitted onto an optical microscope. Analog video cameras are often attached to the microscope for quantitative image analysis, acquiring images at a rate of 25-30 Hz[34].

During cryomicroscopy experiments, samples are cooled to temperatures below the equilibrium melting point, where extracellular ice will either form spontaneously, or by intentional seeding (*i.e.*, using a cooled needle or seeding block). When a cell freezes, it is typically manifested either by a darkening of the cytoplasm, or by cell 'twitching'. Darkening commonly attributed to the scattering of light by intracellular ice crystals. Cell 'twitching' occurs less frequently, and is evidenced by a sudden motion in the cell, without any associated cell darkening[35,36]. Representative images of a cryomicroscopy experiment are shown in Figure 2.2.

Data obtained from cryomicroscopy experiments are often presented as the cumulative probability of IIF as a function of decreasing temperature. During controlled-rate cooling, the temperature decreases in direct proportion with time, and thus, presenting the data as a function of decreasing temperature is equivalent to plotting the probabilities as a function of increasing time. Thus, plots of the cumulative incidence of IIF as a function of decreasing temperature represent the kinetics of intracellular freezing.

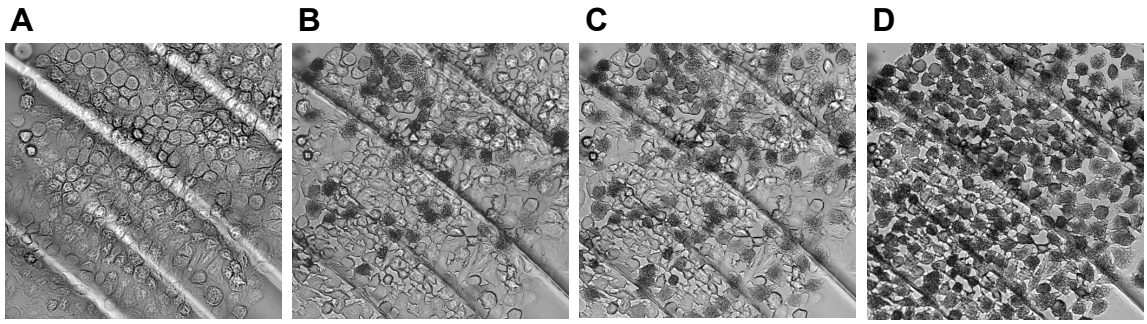

Figure 2.2 Series of micrographs of HeLa cells (grown in monolayer on bare glass coverslips) during a representative cryomicroscopy experiment (cooling at 130°C/min). (A-D). IIF events are indicated by a sudden darkening of the cytoplasm. Temperature points displayed are (A) -1.5°C (B) -18°C, (C) -20.5°C and, (D) -32°C.

2.5 Proposed Mechanisms of IIF in Suspended Cells

Over the last five decades, there have been many postulations regarding the mechanisms of IIF in biological cells. To summarize, three major mechanisms of IIF in biological cells have been hypothesized: (i) membrane failure, (ii) pore theory, and (iii) nucleation.

2.5.1 Membrane Failure Hypothesis

The membrane failure hypothesis assumes a mechanical breakdown of the plasma membrane occurs, allowing extracellular ice to enter the cell, coming in direct contact with the supercooled cytoplasm, and thus initiating IIF[37]. In other words, IIF is hypothesized to be a consequence of cell damage, not the cause[38]. Various mechanisms have been proposed (but not proven) to cause membrane failure, including destabilization of the plasma membrane[39], osmotic contraction, thermal perturbations and electrical transients at the advancing ice front[38], frictional forces on the plasma membrane due to osmotic water efflux[40] and direct mechanical injury of the membrane[41,42].

2.5.2 Pore Theory

Mazur was the first to postulate that extracellular ice played a role in initiating IIF[43]. Mazur's pore theory posits that IIF is caused by the growth of extracellular ice through existing aqueous pores in the plasma membrane[44]. Ice and supercooled water can only coexist if a physical barrier exists between them[44,45]. In pore theory, Mazur[44] hypothesized that for suspended cells, the supercooled intracellular water is protected by the cell membrane. In order for extracellular ice to nucleate the supercooled water, the extracellular ice must assume an organized crystalline structure that matches the dimension of the membrane pore[44]. In other words, the minute size of plasma membrane pores render them impenetrable by ice until a critical temperature is reached, at which time it is thermodynamically favorable for ice crystals of the required dimensions to form. Mazur[44] derived an equation to represent the changes in free energy associated with extracellular ice growing in a pore, effectively using the Kelvin equation to model the change in equilibrium ice crystal radius, a, with temperature:

$$\Delta T = \frac{2\nu_1^L T_{fp}^o \sigma_{SL} \cos\theta}{aL_f} \tag{2.1}$$

where ΔT was defined as the difference between the freezing point of water in the pore and the melting point of planar ice in pure water (T_{fp}^{o}); υ^{L}_{1} as the molar volume of water; σ_{SL} as the interfacial tension between the ice and the liquid water; θ as the contact angle between the ice-water interface and the pore wall; L_f as the molar heat of fusion; and a as the pore radius (Figure 2.3)[44]. Mazur concluded that for a pure ice-water interface, at

temperatures below -10°C, the equilibrium ice crystal radius would be small enough to pass through an 8Å pore (assuming a contact angle, $\theta = 75°$) and thus, initiate IIF[44].

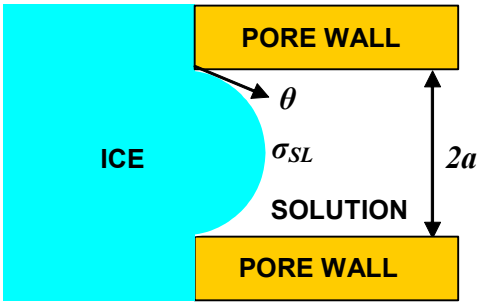

Figure 2.3 Schematic of the extracellular ice growth through a capillary pore of radius a, modified from Mazur[44]. See text for details.

2.5.3 Nucleation Theory

Finally, nucleation theory assumes the existence of intracellular sites that act as catalysts for heterogeneous nucleation of ice. Consequently, the rate of nucleation depends on the nature of these catalytic sites. To predict the occurrence of IIF during freezing of biological cells, Toner *et al.*[23] adapted classical nucleation theory, in which cells are assumed to freeze through three distinct mechanisms: surface-catalyzed nucleation (SCN), volume-catalyzed nucleation (VCN), and homogeneous nucleation.

Briefly, SCN is defined as a heterogeneous nucleation mechanism, in which IIF is catalyzed at the intracellular surface of the plasma membrane as a result of interactions between the extracellular ice and the membrane. Thus, the rate of SCN is predicted to scale with cell surface area[23]. Homogeneous nucleation is a mechanism that results from intracellular water molecules combining together to from a cluster of molecules that

grows spontaneously in into a crystal. Accordingly, the rate of homogeneous nucleation will scale with cell volume. VCN results from the catalysis of ice nucleation by macromolecular structures distributed throughout the cell cytoplasm, and the associated nucleation rate is therefore assumed to scale with cell volume[23]. Toner *et al*. define the contribution of all three mechanisms on the overall rate of IIF, *J(t)*, as:

$$J(t) \equiv I_{SCN} A + I_{VCN} V + I_O V \tag{2.2}$$

where I_{SCN}, I_{VCN} and I_O are the rates of surface-catalyzed, volume-catalyzed, and homogeneous nucleation, and A and V are the cell surface area, and cell volume, respectively. SCN has been shown to be more efficient than VCN, and in the absence of cryoprotectants, is assumed to dominate the other nucleation mechanisms[46]. Thus, if SCN is also the primary mechanism of IIF in attached cells (without cryoprotectants), then *J(t)* will be approximately proportional to the cell surface area:

$$J(t) = A \cdot I_{SCN} \tag{2.3}$$

While SCN is arguably the most commonly accepted theory of IIF for biological cells, conclusive evidence to refute the other hypotheses remains elusive. The challenge in distinguishing between possible IIF mechanisms has in part been due to the inability to image the initiation of IIF directly, and with sufficient temporal and spatial resolution.

2.6 Mathematical Models of IIF in Tissue

Mathematical models of IIF in tissue can be useful in the identification of novel strategies avoiding cell injury (in cryopreservation applications), or for improving the specificity of tissue damage (in cryosurgical applications). The prediction of the cellular response to freezing for single suspended cells has been made possible with ice nucleation models[47], allowing for the design and optimization of cell cryopreservation protocols through computer simulations[48]. Unfortunately, our knowledge of the cryobiology of isolated cells cannot simply be extrapolated to tissue. Due to the dramatic increase in complexity of the problem resulting from additional biophysical phenomena (e.g., cell-substrate and cell-cell interactions, geometric effects, heat and mass transport limitations), innovative approaches are required to predict the response of tissue to freezing.

As a result of the limited knowledge of the mechanisms and kinetics of IIF in tissue, few mathematical models exist for ice formation in tissue[49-55]. The majority of these models represent tissue as a continuous material, with thermal, chemical, or mechanical gradients, with no regard to the cellular structure of tissues[49,52,54]. More recent approaches have considered cellular properties (*e.g.*, water permeability of the membrane and osmotic changes), extrapolating them to finite volumes of tissue[50,51,55]. Although these models provide important insights into tissue freezing, they neglect the effects of cell-substrate and cell-cell interactions, which are known to influence IIF in tissue[56-59]. To address this limitation, Irimia and Karlsson recently developed a mathematical model to predict the effect of cell-cell communication on the kinetics of IIF in tissue[58,59]. In this model, the rate of IIF in each cell was expressed as a sum of contributions from two

distinct mechanisms: the propagation of ice from a frozen neighbor across the corresponding cell-cell interface; and the spontaneous formation of intracellular ice through interaction-independent, non-propagative processes.

2.7 Mechanisms of Ice Formation in Tissue

Before improvements can be made to existing mathematical models, we must first improve our current understanding of the underlying mechanisms of IIF in tissue. Cells adherent to a substrate are known to have a higher probability of IIF during freezing than suspended cells, even in the absence of cell-cell interactions[60]. However, the cause of this effect is unknown. Using microfabrication techniques to control cell shape during freezing, preliminary studies with a transformed cell line (HepG2) suggested that the rate of IIF in attached cells increased with the degree of cell spreading[61]. Since the rate of surface catalyzed nucleation is proportional to the area of the cell membrane[23], cell spreading on a flat substrate may increase the probability of IIF simply by increasing the surface-to-volume ratio of the cell. However, initial data from our laboratory indicate that the rate of IIF is more strongly correlated with cell perimeter than with cell surface area[61]. These results suggest that surface-catalyzed nucleation may not be the dominant mechanism of IIF in adherent cells.

Qualitative observations of freezing differences between suspended cells and monolayers have been long reported[62-64]. In cell suspensions, intracellular ice formation is a stochastic process, randomly occurring in a sample population. During freezing of monolayers, cells have been reported to freeze in a directed, wave-like pattern[57]. Early experimental observations in plant cells led to the hypothesis that intracellular ice could

propagate via cell-cell interfaces[65,66]. From cryomicroscopic observations of onion epidermis, Tsuruta *et al.* hypothesized that ice inside one cell could catalyze IIF in neighboring cells via surface-catalyzed nucleation, thus resulting in intercellular propagation of IIF[67]. Berger and Uhrik were the first to propose an involvement of gap junctions in ice propagation, based on qualitative observations in cell strands from salivary gland tissue, and on the effects of heptanol and dinitrophenol, substances known to decouple GJIC[56]. A subsequent study compared the kinetics of IIF in monolayers for two different cell lines, Madin-Darby canine kidney (MDCK) cells which express gap junctions, and V-79W fibroblasts, which purportedly do not exhibit gap junction expression[68]. Their results indirectly supported gap junction involvement in intercellular ice propagation in monolayers by reporting an increase in IIF kinetics for confluent monolayers of MDCK cells. Acker *et al.*[57] followed up on this study by correlating the temperature dependence of IIF (and subsequent wave-like propagation) with theoretical predictions of ice growth through pores[44]. In this study, low-calcium medium was used to decouple the effects of gap junction intercellular communication (GJIC) in MDCK monolayers. However, reducing medium calcium levels will inhibit all cell-cell activity in MDCK cells, and it has been shown that it will also invoke secondary effects in cell morphology[69] and contractility[70,71], factors that may influence IIF. In addition, the presence or absence of GJIC was not verified (or refuted) in any of their experimental systems.

For the majority of these studies, investigations have been limited to cell monolayers[57], or small aggregates of cells[56,72], introducing many confounding factors (*i.e.*, time in culture, degree of cell spreading, and mass transport limitations) that are

known to affect IIF. Irimia and Karlsson[58,59] addressed these limitations by conducting the first cryomicroscopy experiments using polyethylene glycol micropatterned cell cultures of a human hepatocellular carcinoma cell line (HepG2). They developed a theoretical model of ice propagation for interacting cells, and used cryomicroscopy data to validate the model predictions. Their data indicated that the spontaneous nucleation rate was independent of cell-cell contact, and gave strong support for ice propagation through gap junctions. While their study reported that gap junctions were a primary mediator of ice propagation, their results suggested the presence of a secondary mechanism of ice propagation that was gap junction independent. This secondary mechanism was qualitatively observed as occurring at a rate faster than the gap junction mediated propagation, with the secondary mechanism being so rapid that capturing the events with conventional video acquisition rates (30 frames per second) proved to be difficult. Irimia and Karlsson's study was limited by the use of HepG2 cells, a cell line that is known to have low expression levels and abnormal localization of connexins[73,74]. Recently, it has been shown that under normal culture conditions, HepG2 monolayers do not have detectable levels of functional gap junction intercellular communication (GJIC)[75]. In addition, the geometry of surface bound HepG2 cells is highly dependent on the nature of the cell-surface interface, with minimal cell spreading on most biomaterials[76]. HepG2 cells have been shown to have no adhesion affinity for pure glass substrates[76], the substrate used in Irimia and Karlsson's study. Thus, due to the limited cell spreading of the HepG2 cells after attachment, cell attachment area was more variable in their micropatterned constructs. Further investigation of intercellular ice propagation is needed to confirm Irimia and Karlsson's results using more clinically

relevant, primary cells with better substrate adhesion characteristics and known levels of GJIC.

2.7 Primary Endothelial Cells and Cryopreservation

Endothelial cells were selected for the studies described in this thesis, due to common use in tissue engineered products[77-79] as well as their targeted destruction in cryosurgical procedures[36,80]. Endothelial cells are also desirable due to their ability to readily adapt to their physical environment[81,82], and rapid formation of focal adhesion sites[83]. Many commercially available primary endothelial cells have been shown to adhere and spread in micropatterned surfaces with high efficiency, assuming the shape of the pattern within six hours [81,84]. Expression of numerous integrin subtypes has been shown in endothelial cells[83,85], including $\alpha_5\beta_1$, a receptor for the ligand fibronectin[86]. For investigation of ice propagation via gap junctions, endothelial cells are desirable due to their high levels of gap junction communication[87]. Specifically, aortic endothelial cells have been shown to expression of multiple connexins (Cx37, Cx40, and Cx43) that can form gap junctions which may be homotypic (two identical connexons), heterotypic (two types of connexons), homomeric (a single connexin isoform) and heteromeric (multiple types of connexins)[88,89].

Cryopreservation of attached endothelial cells has proven to be challenging[90,91]. During cryopreservation of human corneas, detachment of endothelial cells from Descemet's membrane has been seen, coinciding with loss of endothelial cell viability[92,93]. In addition, cryopreservation of corneal endothelial cells grown in monolayer (without cryoprotectant) exhibited low recovery of membrane integrity

(<10%) and mild to moderate levels of cell detachment[90]. Using an immortalized human endothelial cell line (ECV304), untreated endothelial cells grown on microcarrier beads, showed ~4% cell survival after cryopreservation[91]. Outside of monolayer freezing, limited studies exist for cryopreservation of suspended endothelial cells[36,91]. Cryomicroscopy studies of human microvascular endothelial cells frozen in suspension, found that IIF occurred at lower temperatures than many cell types[36]. Interestingly, in this same study, 12-19% (depending on the cooling rate) of the suspended endothelial cells did not exhibit any outward indicators of IIF (*i.e.*, darkening or twitching)[36]. Therefore, further information gained regarding the mechanisms of IIF in endothelial cells will provide a significant contribution to the preservation of this cell type.

2.8 Thesis Outline

This thesis serves to contribute to the background literature outlined above by addressing the specific aims presented in Chapter 1. Specifically, in Chapter 3 a novel high speed digital video cryomicroscopy system is detailed and the first experiments quantifying the effects intracellular ice formation in single attached endothelial cells are presented. Chapters 4 and 5 further investigate the role of cell-substrate interactions by varying the cell attachment area, time in culture and ligand coating density. Additionally, changes in focal adhesion formation and cytoskeletal arrangement were investigated. In Chapters 6 and 7, the focus was turned to the effects of cell-cell interactions on IIF. Micropatterns pairs of bovine and human endothelial cells were used to quantify the rate of intercellular ice propagation in primary cells. Chapters 8 and 9 detail our parametric analyses of IIF in heterogeneous tissues, modeled with our new Monte Carlo algorithm.

(based on the methods of Gillespie[94]). Finally, Chapter 10 provides overall conclusions based on the work presented in this thesis, in addition to recommendations for future work.

CHAPTER 3

HIGH SPEED OBSERVATION AND QUANTIFICATION OF INTRACELLULAR ICE CRYSTALLIZATION IN MICROPATTERNED ENDOTHELIAL CELLS

3.1 Introduction

In the field of cryobiology, the most common tool to investigate IIF is quantitative cryomicroscopy. While there are many variants of traditional cryomicroscopy systems[33], video images are typically acquired during experiments at rates of 25-30 Hz. At these sampling rates, the process of IIF manifests either as a sudden darkening, or as "twitching"[35,36,95] of the cell. The exact cause of darkening is unknown, but it is commonly assumed that it is the result of the intracellular ice crystals scattering the transilluminating light. As such, cell darkening is used as the primary indicator of intracellular ice formation in cryomicroscopy experiments. However, when sampling at a rate of 30Hz, it is not possible to temporally resolve the liquid-ice phase transformation process within a given cell. Consequently, the transient dynamics of IIF in biological cells have hitherto remained unobserved.

Based in part on conventional cryomicroscopy studies of suspended cells, three major mechanisms of IIF have been hypothesized: (i) membrane failure, (ii) pore theory, and (iii) nucleation. The membrane failure hypothesis assumes a mechanical breakdown of the plasma membrane occurs, allowing extracellular ice to enter the cell, coming in direct contact with the supercooled cytoplasm, and thus, initiating IIF. Various mechanisms have been proposed as to the cause of membrane rupture, including

destabilization of the plasma membrane[39], osmotic contraction, thermal perturbations and electrical transients at the advancing ice front[38], frictional forces on the plasma membrane due to osmotic water efflux[40] and direct mechanical injury of the membrane by extracellular ice[41,42]. Pore theory posits that IIF is caused by the growth of ice through existing aqueous pores in the plasma membrane[44,45]. Finally, the most widely accepted hypothesis, nucleation theory, assumes the existence of intracellular sites that act as catalysts for heterogeneous nucleation of ice; the rate of nucleation depends on the nature and number of these catalytic sites. For example, one proposed mechanism, surface-catalyzed nucleation (SCN) is assumed to occur as a result of interactions between external ice and the plasma membrane, which create catalytic sites for ice nucleation on the internal surface of the membrane[23]. Another mechanism, volume-catalyzed nucleation (VCN) has been described as catalysis of IIF by macromolecular particles distributed throughout the cell volume[23]. While a considerable volume of cryomicroscopy data has been acquired over the last several decades, none of the above mechanisms of IIF have been definitively proven (or conversely, invalidated).

Despite limited knowledge of the exact mechanism of IIF in suspended cells, cryopreservation of suspended cells has become practical, especially for cell lines that can be propagated in culture to compensate for losses due to cryo-injury. Unfortunately, when the complexity of the system is increased from suspended cells to single attached cells, the post-thaw viability dramatically decreases[90,91]. Cells adherent to a substrate are known to have a higher probability of IIF during freezing than suspended cells, even in the absence of cell-cell interactions[6,59,60,63,64,96]; however, the cause of this effect is unknown. For attached cells, new biophysical phenomena are introduced (*e.g.* cell-

substrate interactions, geometric effects), and thus, novel approaches are required to understand the underlying mechanisms of IIF in attached cells. Successful investigation of the effects of cell adhesion on intracellular ice formation requires precise control of the cell micro-environment during cryomicroscopy experiments. To this end, micropatterning techniques, which allow for strict control of parameters such as cell shape, area, and ligand density on glass substrates, are ideal for cryomicroscopy investigations[58,59].

Towards the goal of elucidating the mechanisms of IIF in single attached cells, we have developed a novel high-speed video cryomicroscopy system using a state-of-the-art CMOS sensor capable of image acquisition at sampling rates up to 32,000 Hz. This system, combined with micropatterned endothelial cells, provided a robust platform to investigate the transient dynamics of IIF in attached cells. In the present study, the IIF process was visualized at sub-millisecond temporal resolution, making possible the identification of the site at which IIF initiated (*e.g.,* by nucleation). Quantification of the kinetics and spatial distribution of IIF initiation events has made possible an increased understanding of the underlying mechanisms of IIF in attached cells, which is of critical importance for rational design of successful cryopreservation protocols for attached cells and tissues.

3.2 Theoretical Background

3.2.1 Probability Analysis

Intracellular ice formation is a stochastic process, in which the cells within a population undergo phase transformations at random time intervals, thus incrementally altering the overall state of the cell population. This process has previously been modeled as a continuous-time Markov chain[58,59,97], in which the probability of observing an intracellular ice formation event in an unfrozen cell is a non-homogeneous Poisson process with a time-dependent rate $J(t)$. Thus, during freezing, the cumulative probability of intracellular ice formation in a population of non-interacting identical cells is given by[23,98]:

$$P_{IIF}(t) = 1 - \exp\left[-\int_0^t J(t')dt'\right] \tag{3.1}$$

Traditionally, experimental quantification of the kinetics of intracellular ice formation has been limited to estimation of $P_{IIF}(t)$ from a running tally of the number of unfrozen cells remaining in the population (N_u):

$$P_{IIF}(t) = \frac{N_u(0) - N_u(t)}{N_u(0)} \tag{3.2}$$

This approach has proven useful for analysis of intracellular ice formation kinetics in suspended cells, allowing parameter estimation and validation for various proposed theoretical models of $J(t)$, by comparing predictions from Equation 3.1 to corresponding empirical values from Equation 3.2. However, because the mechanisms of intracellular

ice formation in adherent cells are largely unknown and uncharacterized, an alternative approach is required for quantifying the kinetics of intracellular ice formation.

In general, intracellular ice formation can occur via multiple independent mechanisms, and the Poisson process rate J is therefore a sum of the individual rates J_μ associated with each active mechanism μ[48]. For purposes of comparing the kinetics of different mechanisms of intracellular ice formation, we now define the cumulative intensity function

$$n_\mu(t) \equiv \int_0^t J_\mu(t')dt' \tag{3.3}$$

which is a quantity representing the cumulative number of events μ in that would be observed an infinite population of initially unfrozen cells. Thus, Equation 3.1 can be rewritten

$$P_{IIF}(t) = 1 - \exp\left[-\sum_\mu n_\mu(t)\right] \tag{3.4}$$

where the summation is taken over all active mechanisms μ. In particular, by including only a single mechanism μ in Equation 3.4, one obtains the cumulative probability function for the hypothetical case of μ being the only active mechanism of intracellular ice formation.

If there is indeed some initial time interval of the freezing process within which a single mechanism μ is dominant, then it follows trivially from Equation 3.2 and Equation 3.4 that

$$n_{\mu}(t) = \ln\left[\frac{N_u(0)}{N_u(t)}\right] \tag{3.5}$$

as long as any non-dominant mechanisms remain negligible. However, during time intervals in which multiple mechanisms of intracellular ice formation are simultaneously active, the kinetics of distinct mechanisms cannot be estimated from N_u data alone without assuming explicit forms of the time-dependence of each of the underlying rates $J_{\mu}(t)$. Because such information is not yet available for intracellular ice formation in adherent cells, a new method for evaluating $n_{\mu}(t)$ was developed.

To estimate n_{μ} from experimental observations of multiple intracellular ice formation mechanisms in a finite population of cells, one can take advantage of the fact that

$$\frac{dN_{\mu}}{dt} = J_{\mu} N_u \tag{3.6}$$

where N_{μ} is the cumulative number of observations of event μ in the population. Thus, combining Equation 3.3 and Equation 3.6, one obtains the result

$$n_{\mu}(t) = \int_0^{N_{\mu}(t)} \frac{dN_{\mu}}{N_u} \tag{3.7}$$

Because intracellular ice formation events of type μ occur at discrete time points t_i, for $i = 1, \ldots, N_{\mu}(t)$, step discontinuities are introduced in $N_{\mu}(t)$ and $N_u(t)$. As a result, the integral in Equation 3.7 can be evaluated using the summation

$$n_{\mu}(t) = \frac{1}{2} \sum_{i=1}^{N_{\mu}(t)} \left(\frac{1}{N_u(t_i^-)} + \frac{1}{N_u(t_i^+)} \right) \tag{3.8}$$

where the superscripts '-' and '+' indicate limiting values approaching from the left and from the right, respectively. If intracellular ice formation events of class μ can be distinguished from the other possible mechanisms, then the time points t_i can be identified, allowing $n_{\mu}(t)$ to be estimated from the experimental data using Equation 3.8. Conversely, if a population of intracellular ice formation events is categorized into two or more subpopulations *a priori*, based on observable characteristics, then Equation 3.8 can be used to quantify the kinetics of formation of each of the defined subpopulations.

3.3 Materials and Methods

3.3.1 Bovine Pulmonary Artery Endothelial Cell Culture

Bovine pulmonary artery endothelial cells (BPAECs) (Cambrex, San Diego, CA) were cultured in MCDB 131 media (Mediatech, Herndon, VA) supplemented with 5% (v/v) fetal bovine serum (Sigma-Aldrich, St. Louis, MO), 2ng/mL basic human fibroblast growth factor (PeproTech, Rocky Hill, NJ), 10ng/mL human epithelial growth factor (Invitrogen Corp., Carlsbad, CA), 1ng/mL vascular endothelial growth factor (Sigma-Aldrich), 2 ng/mL insulin-like growth factor-1 (Invitrogen), 0.001 mg/mL hydrocortisone (Sigma-Aldrich), 2mM L-glutamine (Mediatech), 100U/mL penicillin/100μg/mL streptomycin (Invitrogen), and 50μg/mL ascorbic acid (Sigma-Aldrich). Cells were cultured on tissue culture plastic at 37°C in a humidified 5% CO_2 environment and media were replaced every 48 hours. Flasks where subcultured when they reached 70-85%

confluency and were split at a 1:6 ratio, following the recommendations of the vendor. Total exposure time to trypsin-EDTA (Cambrex, Cat# CC-5012) was 5 min. For all experiments, cells were used at passages 5 through 9.

3.3.2 Fabrication of Micropatterned Substrates

Agarose micropatterned glass coverslips that contained adhesive and non-adhesive domains were fabricated using methods adapted from a technique developed by Nelson and Chen[81] (Figure 3.1A). Briefly, a poly(dimethylsiloxane) (PDMS) (Sylgard 184, Superior Essex, Atlanta, GA) stamp was cast from a silicon template that comprised an array of 20μm diameter circular wells. The use of the silicon master was generously donated by A. García (Georgia Institute of Technology), with fabrication previously described [99]. To prevent adhesion of the PDMS to the silicon template, the wafer was exposed to (tridecafluoro-1,1,2,2-tetrahydrooctyl)-1-tricholorosilane (United Chemical Technologies, Bristol, PA) for 45 minutes under vacuum. The PDMS elastomer and curing agent were mixed at a ratio of 10:1 and cast over the silicon template in a petri dish. The PDMS was subsequently degassed by vacuum to remove all air bubbles, and cured under dry heat for 6 hours at 65°C. The cured PDMS stamp was released from the silicon template and cut using a razor blade to the desired stamp size. The PDMS stamp was placed, patterned side down, against a 12 mm diameter circular glass coverslip (#1.5, Fisher Scientific, Suwanee, GA) such that only the raised 20 μm diameter posts were in contact with the coverslip. A small volume (~5μL) of 100% ethanol (Fisher Scientific) was wicked into the 'mold' created by the PDMS stamp and the coverslip, and allowed to evaporate. An aqueous solution of 0.6% (w/v) agarose (Invitrogen) and 40% (v/v) ethanol was heated to its boiling point while stirring, and then dispensed along the edge

of the stamp/coverslip mold. The agarose was allowed to dry undisturbed at room temperature for approximately two hours. The PDMS stamp was then carefully removed, producing a micropatterned coverslip with bare glass islands surrounded by agarose. Substrates were sterilized in an aqueous solution of 70% ethanol (v/v), rinsed twice with DPBS (Fisher Scientific) and incubated (at 37°C, 5% CO_2) for 1 hour in a 25µg/mL solution of human-plasma fibronectin (FN) (Invitrogen) in DPBS. For experiments with unpatterned substrates, glass coverslips were sterilized and coated with FN using the same protocol described above. After the fibronectin surface treatment, coverslips were rinsed and stored in DPBS at 37°C, 5% CO_2 for up to 6 hours prior to seeding of cells.

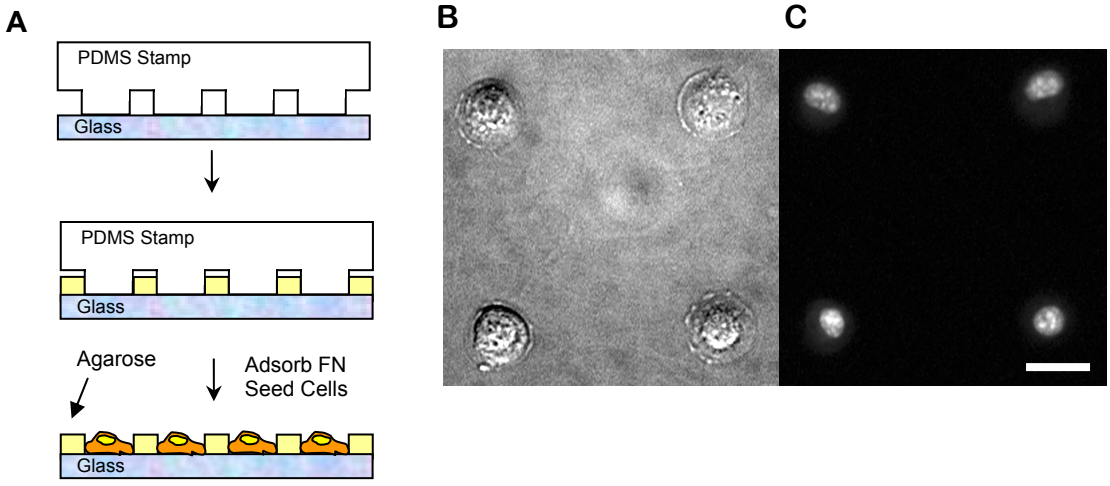

Figure 3.1 BPAEC single cell micropatterns. (A) Schematic of cell micropatterning technique. A PDMS stamp cast from a silicon master was sealed, pattern side down, against a glass coverslip. A solution of agarose was wicked under the stamp and allowed to dry. Removal of the PDMS stamp resulted in a micropatterned coverslip with glass surrounded by non-adhesive agarose. (B) Bright field micrograph of single BPAEC cells cultured in 20 μm diameter micropatterns (C) Epifluorescence micrograph, with nuclear staining using SYTO13 to identify individual cells. Scale bar represents 20 μm.

3.3.3 Sample Preparation

For cryomicroscopy experiments, BPAECs were trypsinized, resuspended in media, centrifuged at 220 x g for 5 min and resuspended in media at a density of ~1E4 cells/mL. Cells were seeded onto patterned or unpatterned coverslips, and subsequently incubated at 37°C for six hours (± 30 min). Prior to freezing experiments, coverslips with adherent cells were incubated for 10 min at 37°C with medium supplemented in 2 μM SYTO13 (Molecular Probes, Eugene, Oregon), a nucleic acid stain, and 10 μM ethidium homodimer (EthD-1) (Molecular Probes), a membrane impermeant stain, to ensure that each micropattern contained a single cell with full membrane integrity. Immediately prior to freezing, coverslips were rinsed with 30 mM HEPES buffer (Cambrex), then removed from the petri dish, inverted, and placed on a 16 mm diameter circular glass coverslip (Linkam Scientific Instruments, Tadworth, Surrey, UK), creating a sandwich. For suspended cell experiments, a 10 μL aliquot of cell suspension (in media, used within 20 minutes of trypsinization) was sandwiched between two 16 mm coverslips.

3.3.4 High Speed Digital Video Cryomicroscopy

A novel high-speed video cryomicroscopy system was created to allow observation of IIF at sub-millisecond temporal resolution. The system consisted of an upright Nikon Eclipse ME600 microscope fitted with a commercially available cooling stage (FDCS 196, Linkam). The sample was cooled by heat conduction to a silver block in contact with a liquid nitrogen vapor stream. The stage temperature was regulated using an electrical resistance heater and a platinum-resistance thermometer imbedded in the silver block, together with a TMS 94 feedback control system (Linkam), LNP liquid

nitrogen pump (Linkam) and Linksys32 software (version 1.1.1; Linkam). The temperature sensor was calibrated by measuring the melting point of ice crystallized from a sample of purified water (ELGA UltraPure). Experiments were recorded using a high speed digital camera equipped with a CMOS sensor (FastCam-X 512PCI, Photron, Tokyo, Japan) and corresponding software (FastCAM Viewer, version 2.2; Photron). Each digital image was synchronized with the Linksys temperature profile through the use of an external switch closure trigger. When the switch was closed by the operator, the resulting signal was detected by both systems and subsequently recorded by both the Photron and Linksys software.

For all attached cell experiments, images were acquired at a rate of 8,000 Hz, with an exposure time of 100 μsec. Single suspended cell experiments were recorded at a rate of 16,000 Hz, with an exposure time of 62 μsec. A lookup table was used to optimize image quality and contrast during acquisition, with image gain and contrast set to constant values for the duration of our experiments. Maximum recording time was limited to approximately eight seconds with the settings used. For all high speed experiments, cells were observed using a 50X objective and 0.45X coupler (Nikon). To meet the light level requirements for the CMOS sensor, all samples were frozen under Köhler illumination, with the microscope halogen lamp set to maximum output.

Control experiments were conducted to validate that IIF was not influenced by the increased light levels required for the high speed system. Light levels typical of conventional video cryomicroscopy were used (~65% of maximum lamp output) as a control. For these experiments, images were acquired at 30 Hz and an exposure of 3 ms, using a high resolution CCD camera (Sensicam, PCO, Kelheim, Germany). Experiments

were then repeated using the high light levels required for high speed video. Due to the slower shutter speeds of the CCD camera, replication of the lighting conditions used for the high speed experiments required additional filters and mirrors to be placed in the light path in order to avoid saturation of the sensor. These filters were placed in the path after the light passed through the sample; thus, the sample was exposed to light levels equivalent to those that would be used during high speed video acquisition.

To promote IIF, cell cultures were frozen at a rapid rate (130°C/min) in the absence of cryoprotectants. Samples were prepared as described above, and placed in the sample holder of the cryomicroscope stage, directly on top of the silver block, which was heated to a temperature of 37°C. After closing the cryostage chamber, the atmosphere was purged using liquid nitrogen vapor to prevent condensation. To seed extracellular ice, the sample temperature was cooled from 37°C to -1.5°C (at 50°C /min), and repositioned such that the edge of the sample was brought into contact with a seeding block (custom-integrated into the cryostage, and cooled to the temperature of the liquid nitrogen). Immediately after seeding the extracellular ice, the sample was repositioned on the silver block and a single cell of normal morphology, fully spread in the circular micropattern was randomly selected for the experiment. For all experiments, the focal plane of camera was set to the basal area of the attached cell. Prior to the rapid cooling step, both brightfield and fluorescent images were taken of the sample. Only cells that stained negative for EthD-1, and which did not share the micropatterned island with other cells (as evidenced by SYTO13 staining), were used in experiments. To minimize dehydration of the sample, the extracellular ice seeding, cell selection and initial imaging were completed within approximately 60 seconds. If this process took longer than three

minutes, the experiment was abandoned. Immediately prior to the freezing process, the halogen lamp was set to maximum output. Then, the stage was cooled at a controlled rate of 130°C/min to -60°C. The high speed camera was set to record images into a circular buffer, and recording was terminated using a manual switch-closure trigger. When conventional indicators of intracellular ice formation (i.e. cell darkening and/or twitching) were observed, the trigger switch was closed, allowing the IIF event to be captured. For experiments with the conventional CCD camera (30Hz), digital video was acquired for the full duration of the cooling process. An additional set of cryomicroscopy experiments was performed for cell darkening analysis, with an increased recording time after each IIF event, capturing the gradual darkening until it reached a steady state level.

3.3.5 Data Analysis

Each experiment was analyzed frame-by-frame to identify the precise time, temperature and initiation site of the IIF event. It should be noted that if extracellular ice obstructed the view of the cell, various analyses were deemed inconclusive and the classification "unknown" was assigned.

3.3.5.1 Cell Volume Changes

The high spatial resolution of our cryomicroscopy system allows for the detection of small scale volume changes during freezing of cell suspensions. As such, we hypothesized that during freezing of single suspended endothelial cells, when the IIF process in a given cell had completed, a noticeable volume change would be evident. To obtain predictions of the expected cell volume change due to IIF, we assumed that the crystallization process was sufficiently fast such that any cell volume changes via

transport across the cell membrane could be ignored. In addition, as an approximation of the system, we assumed that the entire volume of the cell was freezable water. Thus, knowing that the density of water decreases as it undergoes a phase transformation from liquid water to ice, the mass balance can be re-written:

$$V_2 = \frac{V_1 \cdot \rho_1}{\rho_2} \tag{3.9}$$

where V_1 is the volume of the cell prior to ice formation and V_2 is the volume of the frozen cell, and ρ_1 and ρ_2 are the densities of liquid water and ice, respectively. Rewriting Equation 3.9 with respect to the change in cell radius (assuming a spherical cell):

$$\frac{r_2}{r_1} = \left[\frac{\rho_1}{\rho_2}\right]^{\frac{1}{3}} \tag{3.10}$$

where r_1, is the radius of the cell just prior to IIF, and r_2 is the radius immediately following IIF. Substituting the known densities of liquid water and ice, Equation 3.10 can be used to calculate the theoretical change in cell radius for a single suspended cell due to IIF:

$$r_2 = 1.03 \cdot r_1 \tag{3.11}$$

For single suspended cells, the change in cell volume was calculated based on automated measurements of images extracted from the digital video. Two images were selected from each suspended cell experiment; the first image corresponded to the frame

immediately prior to the initiation of the IIF, and the later being the frame immediately after the IIF process had completed in the cell. Both images, in their native, un-altered form, were loaded into Vision Assistant 8.1 (National Instruments, Austin, TX) for analysis. A circle detection algorithm built-in to the software package was used to detect the outer radius of the suspended cell. While the parameters of the search algorithm can be altered to promote detection, they were set to constant limits to prevent any bias. All suspended cell experiments with a circular match score > 900 (out of 1000) measurements of the cell radius were considered for analysis, with ~50% of the data population excluded from analysis.

3.3.5.2 Darkening Analysis

The darkening of the cell was quantified using a custom program developed in LabView 8.0 with IMAQ 8.0 (National Instruments, see Appendix A). Briefly, the program performed a frame-by-frame analysis of the 8-bit grayscale images, dynamically tracking the cell as it drifted during the experiment. Analysis began with the image identified as the first frame of IIF. Using this image, the user defined a bounding box that tightly surrounds the 20 μm diameter micropatterned cell. This initial template was then used to start the particle-tracking algorithm that captures the motion of the cell as it moves throughout the video. An additional 9x9 pixel box was automatically created along the periphery of the cell bounding box. This box served as a control, and recorded intensity changes in the background of the video. After the initial IIF frame was identified, the program proceeded to analyze every subsequent tenth frame, recording the full histogram as well as average grayscale intensity for the cell and the background box. The average grayscale intensity change of the cell was calculated by subtracting the

initial average intensity ($Intensity_{cell1}$) from the measured average intensity for the cell in video frame i (i = 1,2,3,...) frame, and accounting for background intensity changes:

$$\Delta Grayscale = (Intensity_{Cell_i} - Intensity_{Cell_1}) - (Intensity_{Background_i} - Intensity_{Background_1}) \tag{3.12}$$

where $Intensity_{background\ i}$ represents the average intensity of the background box at frame i. For each experiment, the change in grayscale intensity was plotted versus time and fit in Sigma Plot (Systat Software, Inc., Richmond, CA) to a four parameter exponential rise to a maximum:

$$y = y_0 + a\left(1 - \left(\frac{d}{(d-b)}\right)\exp^{(-b\cdot t)} + \left(\frac{b}{(d-b)}\right)\exp^{(-d\cdot t)}\right) \tag{3.13}$$

where y_0 described the initial change in intensity; a, the difference between y_0 and the steady state intensity value; b, d, coefficients related to the time constants of each exponential ($\tau_1 = 1/b$, and $\tau_2 = 1/d$).

Cell darkening was also analyzed in conventional cryomicroscopy videos acquired using the CCD camera. Due to the differences in camera file format, a second program was developed in LabView to analyze these images (see Appendix A). For these experiments (acquired at 30Hz), every image was analyzed, starting one frame prior to the frame identified as the IIF event. Preliminary analysis of 12 conventional cryomicroscopy videos indicated minimal intensity changes in the background signal (the average change in background intensity in the first 30 frames was 0.48 gray levels with a

standard deviation ± 0.78). As such, for the conventional 30Hz videos, the intensity changes in background signal were not considered in our analysis. For each conventional cryomicroscopy experiment (30Hz), the cumulative changes in grayscale intensity were plotted versus time and fit to a 3-parameter exponential model using Sigma Plot:

$$y(t) = y_0 + a \cdot \exp^{-bt} \tag{3.14}$$

where y_0 was the y-intercept; a the steady state intensity value; b, the coefficient related to the time constant of each exponential ($\tau = 1/b$).

3.3.5.3 Paracellular Ice Analysis

Microscale ice dendrites, which we classified as paracellular ice, exhibited slow growth rates that could not be quantified in the same manner as the IIF front (*i.e.* frame-by-frame playback with a distinct starting point). Thus, the start of the paracellular ice initiation was determined by reverse playback of the video at a frame rate of 125Hz (approximately 1.6% of real-time). When the dendrite disappeared from view, the playback would be stopped and the frame number recorded. This method was repeated in triplicate and if the resulting frame varied by more than 100 frames, the process was repeated at 60Hz. Assuming a maximum operator response time of one second, determining the starting point of paracellular ice in this manner introduced a potential error of 125 frames, equivalent to ± 16ms or ± 0.03°C in the estimated temperature of paracellular ice penetration. Paracellular ice dendrites were classified as co-localizing with the subsequent IIF event if the initiation point of the IIF event was within 1.5µm (or 3 pixels) of the paracellular ice dendrite location

3.3.5.4 Statistical Analysis

Unless otherwise noted, data are reported as mean ± standard error of the mean as noted. When reporting the classification of events into categories, standard deviations were estimated by taking the square root of the number of observations in each category. If groups had a normal distribution and homogenous variances, the group means were compared by an independent *t*-test, or by analysis of variance (ANOVA), with post hoc analyses using Tukey's test. Differences were considered significant at the 95% confidence level ($p < 0.05$).

3.4 Results

First, a control study was conducted to investigate if the high light levels required for the high speed system influenced the kinetics of IIF. Two sets of experiments were conducted with BPAEC rectangular micropatterns (30x40μm) using our high resolution CCD camera at 30Hz; one at conventional illumination levels ($n = 79$), and one that replicated the exact light levels used in the high speed system ($n = 115$). Comparison of these two data sets presented in Figure 3.2 reveal that the increasing the light level does not influence the kinetics of IIF ($p = 0.73$).

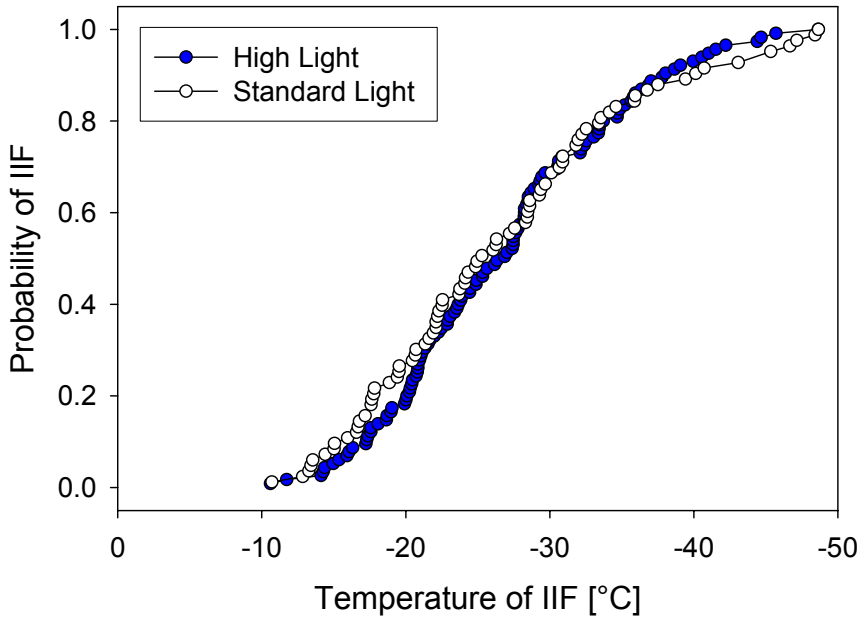

Figure 3.2 Effect of illumination light levels on the kinetics of IIF in traditional cryomicroscopy. BPAECs grown in rectangular micropatterns were frozen using two different light levels to illuminate the sample: cells were illuminated with the maximum light output to mimic the lighting conditions used in high speed experiments (blue circles), and cells illuminated with standard light levels used in traditional cryomicroscopy (open circles).

3.4.1 Characterization of IIF

We report here the first direct observations of the IIF process recorded at sub-millisecond temporal and sub-micron spatial resolution. As such, our first efforts were to characterize the events observed during high speed cryomicroscopy experiments. To this end, micropatterned BPAECs were frozen to a final temperature of -60°C at a rate of 130°C/min. Digital video images of cryomicroscopy experiments were acquired at a sampling rate of 8000 Hz (n = 111). For all experiments, the focal plane of the objective was set to the basal area of the cell. At this focal plane, prior to the initiation of IIF, a novel phenomenon was observed in a small number of cells (22.5% ±4.5%). During cooling, small, dark, finger-like structures appeared at the perimeter of the cell-substrate attachment area, growing slowly (~1μm/s) into the interior of the circle (Figure 3.3). Similar structures were also observed during freezing of unpatterned adherent cells in 20.7% ±5.9% of experiments (n = 58). Often, these protrusions exhibited branching, developing a dendritic morphology during growth. We believe that these structures represent extracellular ice crystals growing into the paracellular space between the glass substrate and the basal cell surface (Figure 3.4). This hypothesis was supported by freezing experiments with suspended cells in which no paracellular ice dendrites were observed (0/15 experiments exhibited paracellular ice dendrites). Thus, we will term the phenomena "paracellular ice penetration"; for convenience, we will refer to the growing paracellular ice structure as "paracellular dendrite", even though these crystallites sometimes assumed non-dendritic morphologies. Interestingly, IIF would often initiate at a location near these paracellular dendrites. This phenomenon, which will be referred

to as "dendrite-mediated initiation" of IIF, will be discussed in more detail later in this chapter.

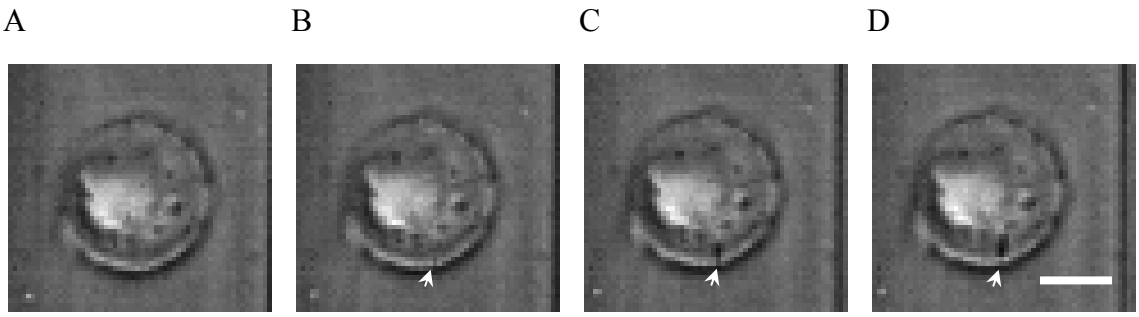

Figure 3.3 Progression of a paracellular ice dendrite. Digital image stills taken from a cryomicroscopy experiment showing paracellular ice formation in a 20μm micropatterned BPAEC cell: (A) Before paracellular ice formation (Temp = -14.5°C, Δt = 0 sec) (B) Small dendrite originating near edge of cell (arrow, highlighted by dashed circle), (Temp = -14.9°C, Δt = 0.28 sec), (C) Paracellular ice dendrite continues to grow (Temp = -15.6°C, Δt = 0.54 sec), (D) Paracellular ice shortly before IIF front initiates (Temp = 16.1°C, Δt = 0.78 sec). Scale bar is 10μm.

Cell darkening, the traditional indicator of IIF, was seen in the majority of our experiments and was used to manually trigger the termination of high-speed video acquisition. In real time, cell darkening appeared to have a sudden onset, with a gradual increase in intensity over time. In 98% of our experiments, cell darkening would be followed by the formation and subsequent release of bubbles from the attached cells. The quantity of bubbles would vary from 1-2 small bubbles per cell, to as many as ~100 forming in a single cell. A small subset of the population (9 ± 2.7%) did not appear to

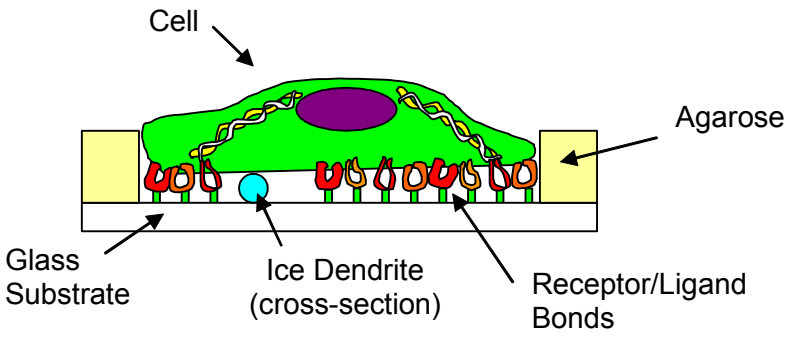

Figure 3.4 Schematic of paracellular ice formation (side view). We have hypothesized that microscale ice dendrites (represented by the blue circle) can penetrate the volume underneath an attached cell. This paracellular space is bounded by a small separation distance between the cell and glass substrate (~10-15nm) and contains supercooled aqueous buffer. Throughout the paracellular region, the adhesion ligand fibronectin will be attached to both the glass substrate and receptors in the cell's plasma membrane, creating localized areas of tight cell attachment. In areas devoid of receptor-ligand bonds, a small aperture may be available for the extracellular ice to penetrate. If conditions are thermodynamically favorable, we postulate that an ice dendrite can grow into the paracellular space via such apertures.

exhibit any darkening or cell 'twitching'. Digital images were still recorded for these experiments, ending data acquisition when the temperature of the cryostage reached -50°C.

All data were initially analyzed through slow motion playback for the full length of the experiments. It was during this stage of analysis that a surprising phenomenon was observed. Just prior to the onset of cell darkening, a single advancing front inside the micropatterned cell was clearly discernible in all experiments. In addition, each front emanated from a point source, the location of which could be pin-pointed by reverse frame-by-frame playback of the video sequence. Both the initiation site and the front can be seen in Figure 3.5. Only one front was observed per cell, with cell darkening initiating shortly after the front passed through the cell. This result was completely unexpected

and to the best of our knowledge, this phenomenon has never before been observed in cryomicroscopy experiments. We have hypothesized that the single advancing front is the advancing interface of a growing intracellular ice crystal, whereas the post-front darkening is a secondary event to IIF.

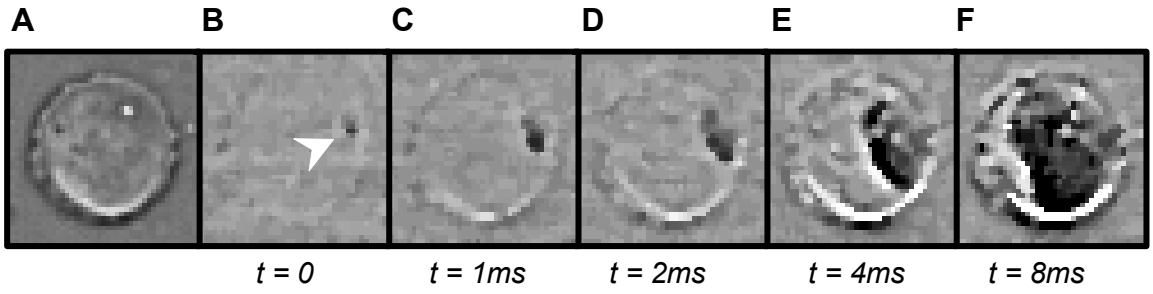

Figure 3.5 High-speed video cryomicroscopy of front initiation in a micropatterned endothelial cell. (A) Adherent cell constrained to a 20μm-diameter circle (processed by averaging the 20 frames prior to front initiation). (B-F) Processed high-speed video images of intracellular ice front growing at a velocity of ~2 μm/ms. The site of IIF initiation (arrowhead) is located at the cell perimeter. To accentuate the front, original images were divided by reference image (A) and filtered using a 3x3 median filter.

To further classify the front, the average temperature of front initiation was T_{avg} = -26.7°C ± 0.8°C. For the small subpopulation of experiments that exhibited no visible signs of IIF (*i.e.*, neither darkening nor twitching), a single front could still be identified during frame-by-frame playback. In other words, cells that would have been classified as 'unfrozen' in traditional cryomicroscopy experiments (due a lack of any visible signs of freezing), actually had a front initiate and pass through the cell. In these experiments, the average temperature of the front initiation was significantly lower (T_{avg} = -44.0°C ± 0.6°C) than the average temperature for the whole population.

All microscopy is based, in part, on observations that are subject to interpretation. In this study, two assumptions were made regarding the cryomicroscopy digital images: (i) that the front observed is inside the micropatterned cell and (ii) that this front is intracellular ice formation (IIF). Experiments and subsequent modeling were conducted to justify both assumptions.

To rule out the possibility that the front may be in the paracellular (rather than intracellular) space, single suspended BPAECs were frozen using the same cryomicroscopy protocol used above (n = 15, data not shown). Since the cells were in suspension and not attached to the substrate, there was no paracellular space in these experiments. Nonetheless, for all cases, a single advancing front was observed, with appearance and growth velocity similar to that observed in attached cells. Further support for an intracellular location of front can be found in our attached cell experiments. In these experiments, the shape and speed of the advancing front has been observed to change as it passes through various intracellular compartments (*e.g.* the nucleus). Such spatial correlation between the front velocity and location of intracellular structure would be highly improbable if the front were not inside the attached cell. Lastly, we acquired fluorescent cryomicroscopy digital video of unpatterned, attached BPAECs loaded with an intracellular cytoplasmic dye, calcein AM. Recording only the fluorescence signal (at 500 Hz) during cooling, a wave-like increase in the intracellular fluorescent signal was observed; these fronts in the fluorescence images advanced at time scales similar to the fronts measured under brightfield illumination. Calcein AM only fluoresces when the fluorescent molecule is cleaved by intracellular enzymes, becoming membrane impermeant. Thus, because the calcein is intracellular, the observed change in

fluorescent intensity during freezing is consistent with an intracellular event; this in turn supports the hypothesis that the front is inside the cell.

Our second assumption, that the front represents intracellular ice crystallization, is supported by our single suspended BPAEC cryomicroscopy experiments. During the temperature plunge, immediately after the front passes through the cell, a small increase in cell volume is evident. The volume expansion was hypothesized to be related to the decrease in the density of water as it transforms from a liquid to solid phase. To test this hypothesis, we quantified the change in cell volume using a shape fitting algorithm in LabView by measuring the projected area prior to and immediately after the IIF front (see Methods). The average measured increase in cell radius was 2.4% ±0.8%, in agreement with the predicted radial increase of 3.0%.

Lastly, we compared the measured velocity of the front growth to predictions of ice crystal growth in pure water solutions. To predict the rate of ice crystal growth in supercooled water, we assumed the crystal velocity to be limited by the rate of conduction of the latent heat of fusion away from the ice crystal interface. This assumption has been used to model the growth of ice in supercooled pure water films on a solid surface[30]. If the rate of crystal growth in our cells is within the heat transfer limit, support is given to the fact that the front is IIF. Using the Neumann solution to the Stefan problem of spherical growth of a crystal nucleating in an infinite supercooled melt[100], the radius of ice crystal was predicted as a function of time. Figure 3.6 displays the prediction of the crystal radius for the average temperature of IIF for the data population (T_{IIFavg} = -26.7 ± 0.8°C). Evaluating the average crystal growth velocity during radial growth from 0 to 20 μm (the distance over which front velocities were estimated in our

micropatterned cells), we calculated an upper limit for the average velocity of ice crystal growth to be 111 μm/ms. From our experimental data, the average velocity of IIF events that initiated at the cell perimeter was determined to be 7.4 ± 0.63 μm/ms. The two results differ by more than an order of magnitude, but this result is not unreasonable. The Neumann solution is the upper bound for the ice crystal velocity in an idealized situation; assuming pure water, a spherical geometry for the ice crystal, and no mass transport resistance (growth rate is limited by heat transfer only). Measurements of crystallization rates in aqueous solutions have shown a decrease in ice crystal velocity as the solution concentration was increased[25], with the decrease in kinetics attributed to, in part, mass transfer limitations. To fully compare our front growth rates with model predictions of both thermal diffusion and mass diffusion, extensive modeling would be required that is beyond the scope of this chapter. For the purposes of the study presented in this chapter, the predictions from our thermal diffusion model (Neumann solution of the Stefan problem) indicate that our growth rates are within the limits of heat transfer limited crystal growth. As such, combining this result with the other supporting evidence presented in this chapter, our assumption that the front observed in high speed video cryomicroscopy experiments is intracellular ice formation is consistent with the data. Thus, from this point forward, the front will be referred to as the IIF event, and it is assumed to occur inside the cell.

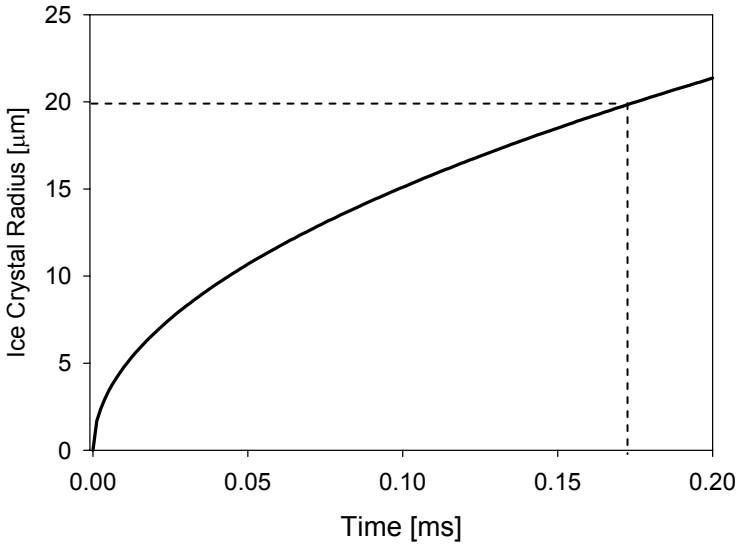

Figure 3.6 Predicted ice crystal radius in a supercooled melt of pure water at T = -26.7°C. The Neumann solution the Stefan problem was used to predict the ice crystal radius as a function of time (black line). The average velocity of an ice crystal 20 μm in radius was estimated from the model prediction. See text for details.

3.4.2 Quantification of Cell Darkening

Conventional cryomicroscopy of suspended and attached cells typically uses cell darkening as an indicator of IIF. As previously mentioned, our high speed cryomicroscopy data indicates that the cell darkening actually occurs *after* the IIF event. The extent of the time lag is illustrated in Figure 3.7 through a series of micrographs extracted from a representative cryomicroscopy video. From these video stills, it is almost impossible to identify the initiation of the IIF front without the assistance of the front motion. During high speed cryomicroscopy (8,000 Hz), the motion of the front (not the gradual change in grayscale intensity), is the primary indicator of the IIF event during slow motion playback. However, for conventional cryomicroscopy, the front is too fast to be captured at a frequency of 30Hz.

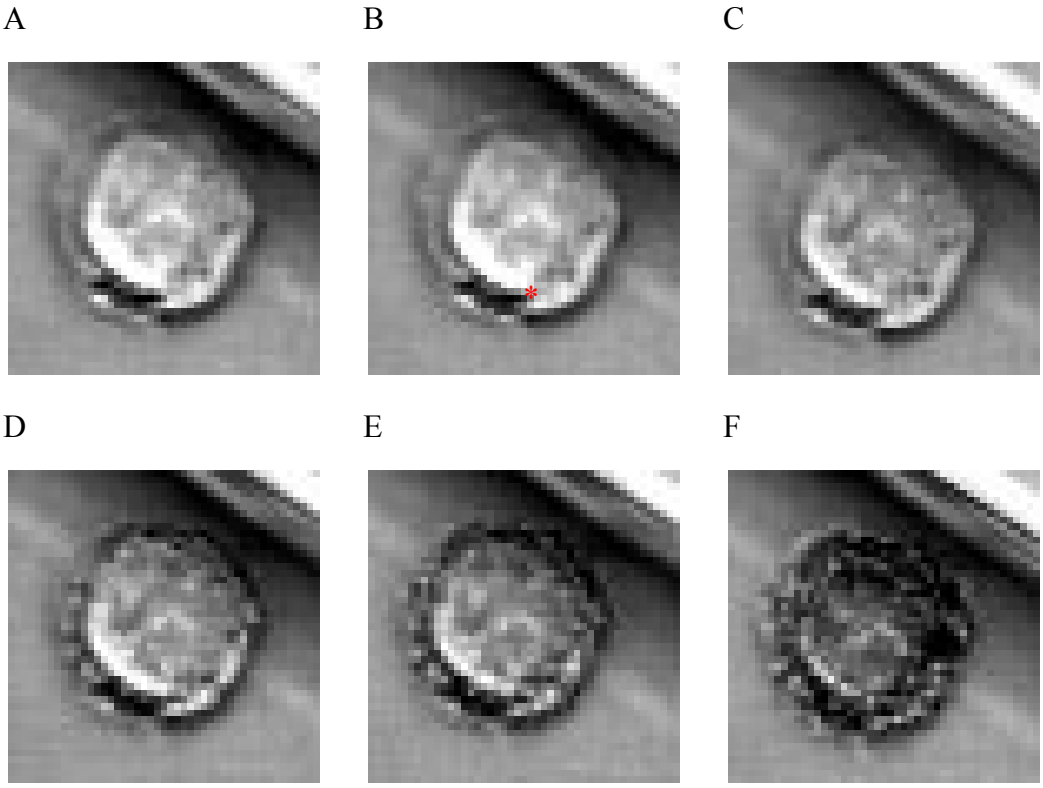

Figure 3.7 High speed cryomicroscopy of cell darkening in a micropatterned endothelial cell. Images were extracted from digital video at the following times: (A) during temperature plunge, 0.1 seconds prior to IIF (Temp = -13.9°C), (B) IIF front initiates in the cell (indicated by red asterisks) (Temp = -14.1°C), (C) Cell 0.1 seconds after IIF front initiated (Temp = -14.3°C), (D) Cell 0.2 seconds after IIF front initiated (Temp = -14.5°C), (E) Cell 0.3 seconds after IIF front initiated (Temp = -14.8°C), and (F) Cell 0.7 seconds after IIF; cell darkening is approaching a steady-state intensity (Temp = -15.7°C).

To quantify the temporal lag that exists between the initiation of the IIF front and the gradual darkening inside the cell, a program was created in LabView to measure the grayscale intensity change in the micropatterned cell during cryomicroscopy experiments. As an example of the program output, Figure 3.8 displays the grayscale intensity changes for a single micropatterned cell during freezing. The video used for Figure 3.8 was the same video presented in Figure 3.7 to assist in interpretation. For this particular example, analysis began 0.1 seconds prior to the initiation of the IIF front, with analysis continuing for every 10th subsequent frame for the duration of the experiment. From the data, it can be seen that the initial IIF event, as indicated by the "B" in Figure 3.8, was captured as a change in average intensity of approximately 3 grayscale levels (out of 255). The subsequent darkening was also captured, rising to an intensity change of 35, a grayscale intensity change roughly ten times greater than the change resulting from the IIF front.

In high speed cryomicroscopy (8,000 Hz), the initiation of the IIF front is readily identified by the moving ice front, not the subsequent cell darkening. However, frame rate limitations in conventional cryomicroscopy force the use of cell darkening as the indicator of IIF. Our results suggest that cell darkening is an indirect measurement of IIF. To gain more information regarding the phenomenon of cell darkening, the kinetics of darkening were analyzed using both conventional and high speed cryomicroscopy experiments.

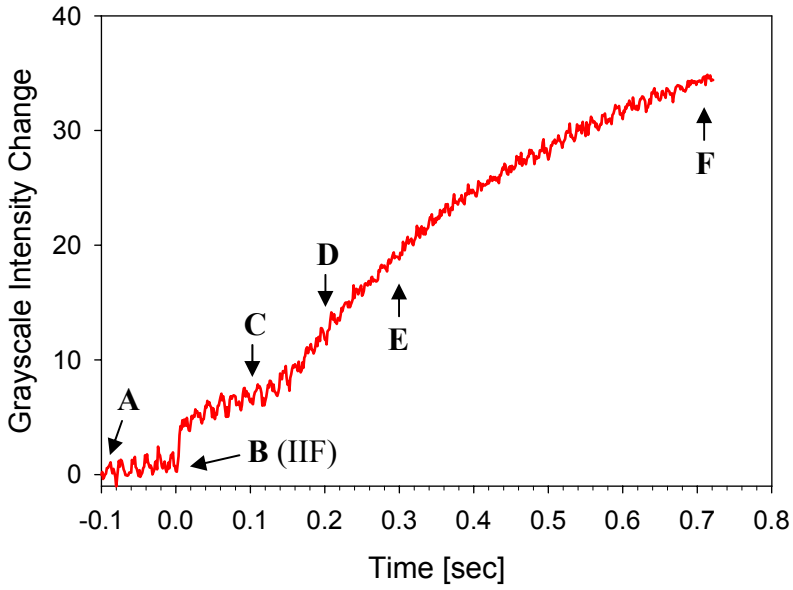

Figure 3.8 Calculated grayscale intensity changes for a single micropatterned cell during the temperature plunge to -60ºC (same data used for Figure 3.7). Analysis began 0.1 seconds prior to IIF initiation, with IIF initiation presented at $t = 0$ s. The grayscale intensity change was calculated using Equation 3.12. The time points for the images presented in Figure 3.7 are indicated by arrows, with notation corresponding to the micrograph letter.

Using the data population acquired at the high light levels (but with the 30Hz camera), videos were analyzed to calculate the first detectable grayscale intensity change associated with IIF in conventional cryomicroscopy. First, videos were analyzed to identify the first frame at which traditional signs of IIF were evident. For the majority of the population, IIF was indicated by a sudden onset of cell darkening. Occasionally, cells would exhibit 'twitching' prior to darkening onset. In these cases, the frame in which the cell twitched was identified as the first frame of IIF. For all experiments, analysis started one frame prior to the operator-defined IIF event, recording the average grayscale intensity change in the cell for every subsequent frame. From our analysis, we determined that for conventional cryomicroscopy, the average grayscale intensity change that corresponded with IIF detection was 0.51 ± 0.08 grayscale levels, with the median value of 0.36 grayscale levels. As demonstrated in Figure 3.9, the initial grayscale intensity change associated with IIF showed a downward trend as the temperature of IIF decreased.

Next we analyzed all high speed videos of 20μm-diameter BPAECs with extended post-IIF recording time (n = 84). For the high speed videos, analysis began at the frame identified as the start of the IIF front, with every 10th subsequent frame analyzed, similar to the data presented in Figure 3.8. To capture both the initial jump in grayscale intensity associated with the IIF front, and the subsequent rise to a maximum intensity change, a five parameter exponential curve fit was applied to all the high speed intensity data (Equation 3.13). Curve fits of the high speed intensity data indicate that the best fit value of the initial change associated with IIF had an average of 0.30 ± 0.10 grayscale levels, and a median value of $y_0 = 7 \times 10^{-10}$ grayscale levels. The curve fit also

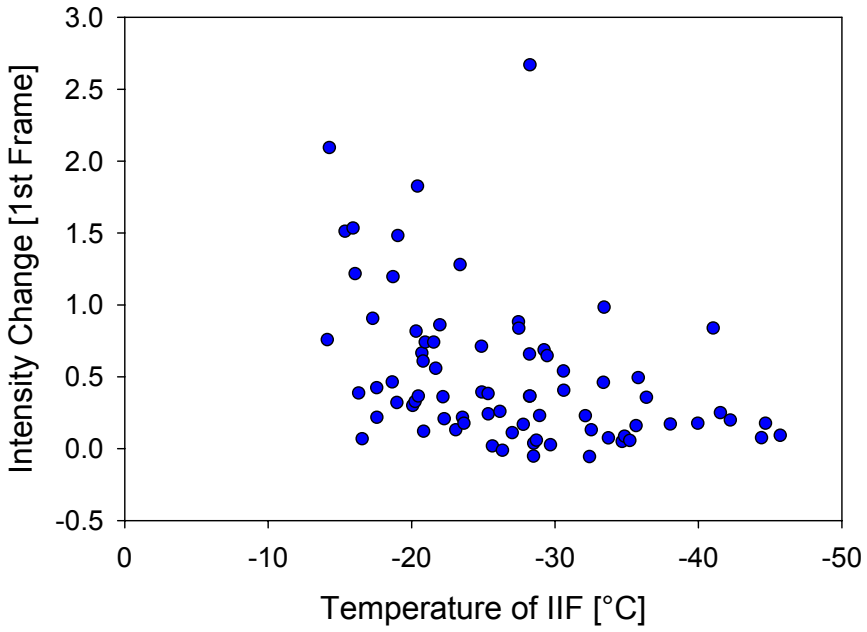

Figure 3.9 Average detectable grayscale intensity change associated with IIF in conventional cryomicroscopy. The average intensity change between the frame identified as the first frame of IIF and the preceding frame was calculated for single micropatterned BPAEC cells. See text for details.

provided the maximum time constant for cell darkening, τ_{max}, for each experiment. The average maximum time constant for all experiments was determined to be 0.24 ± 0.02 s, with the results for all experiments presented in Figure 3.10. The maximum time constant indicates that on average, cells will reach a steady state darkening intensity in 1 to 1.5 seconds after the initial IIF event. In addition, large data scatter is evident in Figure 3.10, indicating that the time scale of darkening is not temperature-dependent.

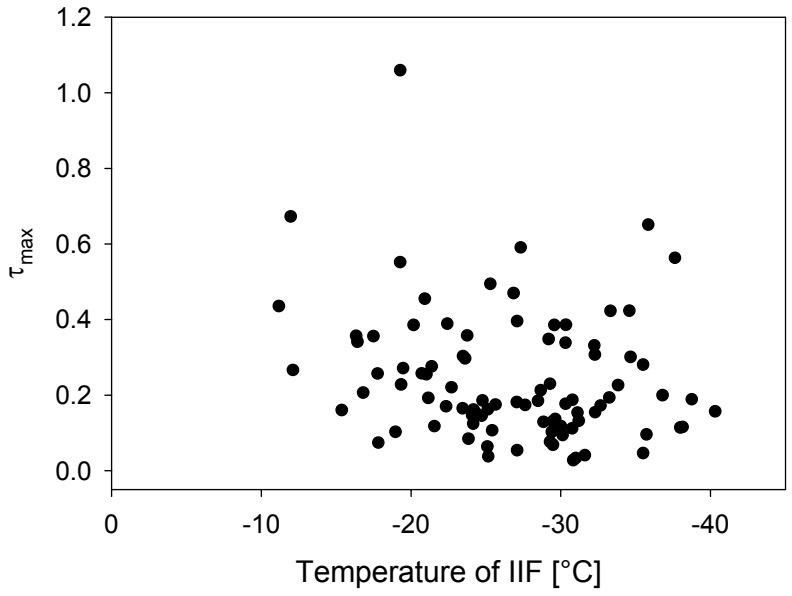

Figure 3.10 Maximum time constant of cell darkening process in high speed cryomicroscopy experiments. Measured changes in grayscale intensity were fit to Equation 3.14 to determine the time scale of cell darkening. See text for details.

3.4.3 Initiation Point of IIF

High speed cryomicroscopy allows for the identification of the time, temperature and spatial location of IIF initiation. On occasion, extracellular ice crystals obscured the IIF initiation site. When this occurred, IIF start location was classified as unknown. For

all other cases, the IIF initiation site was identified and is presented in Figure 3.11. Surprisingly, for the majority of our experiments, the initiation site of IIF was preferentially localized to the perimeter of the adherent cell. Note that although the cell perimeter represents only 10% of the pixels in the projected cell area, over 80% of all observable IIF initiation sites were located there. To ensure that this phenomenon was not an artifact caused by the agarose surrounding each micropatterned cell, control experiments were conducted with single BPAECs cultured on unpatterned glass substrates (n = 58). These samples were frozen under the same conditions and exhibited similar trends, with the majority of IIF events initiating at the cell perimeter (53.5% ± 9.6%).

We next examined how the kinetics of IIF varied with site of initiation. Using Equations 3.4 and 3.8, the probability of IIF was determined for each data subset (peripheral and non-peripheral initiation) and the results can be seen in Figure 3.12. It is evident that for cells in which IIF started at the cell perimeter, the kinetics of IIF were faster and had an earlier onset temperature than cells with non-edge starts. These results suggest that perhaps, two different mechanisms of IIF are occurring in single attached cells.

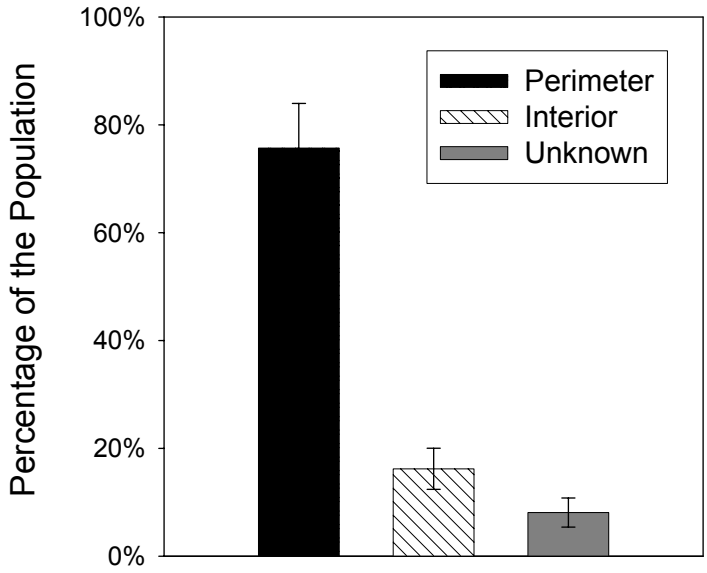

Figure 3.11 Start location of intracellular ice crystals in endothelial cells cultures in 20μm-diameter micropatterns. The black bar represents all data where the initiation site was localized at the cell periphery. A significantly smaller portion of IIF events initiated at an interior location (hatched bar). For cases where extracellular ice crystals were blocking the initiation point, the start location was indeterminable (gray bar). Data are presented as percentage of the population ± SD.

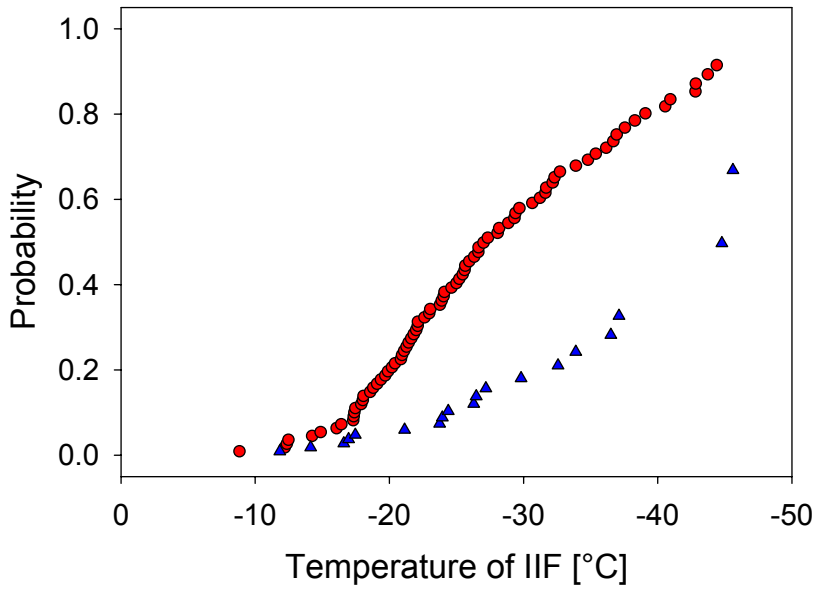

Figure 3.12 Cumulative probability of IIF relative to start location for single micropatterned endothelial cells. The probability for cells in which IIF initiated at the cell perimeter (red circles) indicates that for this subpopulation of nucleation events, IIF kinetics occur at a faster rate than the nucleation events for cells in which IIF initiation at a non-perimeter location (blue triangles).

3.4.4 Front Velocity

For all micropatterned cells with IIF initiating at the cell perimeter, the average velocity for the front was calculated as follows:

$$V_{avg} = \frac{n_{frames} \cdot d_{pattern}}{fps} \tag{3.15}$$

where n_{frames} is the number of frames it took for the ice front to traverse the diameter of the micropattern, $d_{pattern}$ is the diameter of the micropattern (20μm), and fps is the frequency at which the video was taken (in frames per second). The velocity of the ice front should depend on the degree of supercooling. As such, in Figure 3.13, the velocity data were transformed and plotted versus the maximum degree of supercooling, $\Delta T_{\max}$, where $\Delta T_{\max} \equiv T_{fp} - T_{IIF}$, with T_{fp} defined as the equilibrium freezing point of the extracellular buffer solution (T_{fp} = -0.6°C) and T_{IIF} defined as the temperature of IIF initiation. The intracellular supercooling at IIF will take this value if no dehydration occurs in the cell during the seeding of extracellular ice, or during freezing. If some dehydration has occurred, the actual intracellular supercooling will be less than $\Delta T_{\max}$. From our analysis, the velocity of the ice front ranged from 0.6 - 25 μm/ms, with an average velocity of 7.4 ±0.6 μm/ms. In Figure 3.13, large scatter can be seen in the velocity data. A linear regression analysis of the velocity data, indicated an upward trend in the velocity as the degree of supercooling increased (slope = 0.3 μm/mg/K), with a correlation coefficient, R^2 = 0.19, suggesting that the two quantities are correlated ($p < 0.001$). Moreover, there appears to be an upper bound on the velocity, V_{max}, which

increases with the degree of supercooling, $\Delta T_{\max}$. To quantify the upper bound, a line was drawn through the maximum velocity data points in Figure 3.13 by inspection; the equation of this relationship was determined to be $V_{\max} = \left(5.3 \times 10^{-7} \frac{m}{s}\right) \times \left(\frac{\Delta T_{\max}}{1K}\right)^{3.4}$.

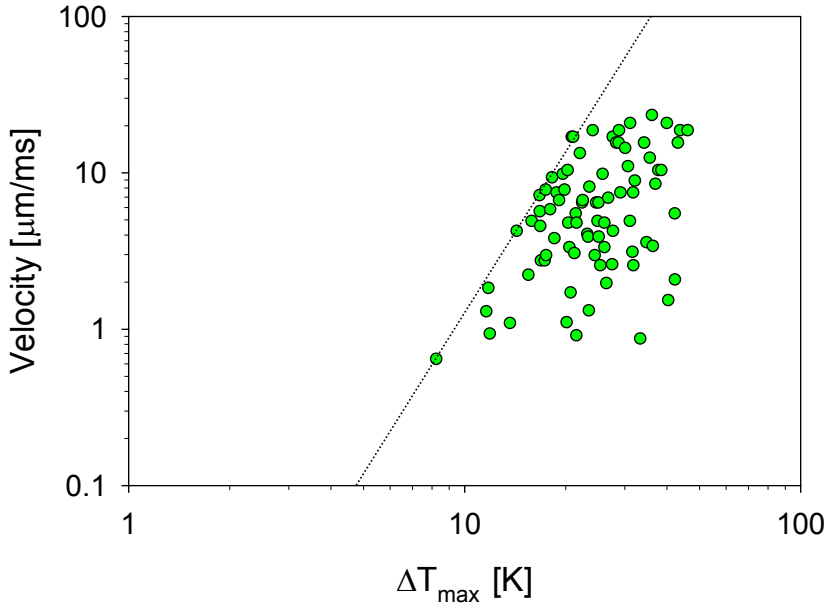

Figure 3.13 Temperature-dependence of the velocity of ice crystal front in 20µm circular patterns. A dashed line was drawn through the velocities at the leading edge of the data set to approximate the dependence of V_{max} on the degree of supercooling, $\Delta T_{\max}$. See text for details.

3.4.5 Paracellular Dendrite-Mediated IIF Initiation

Earlier in this chapter we described a new phenomenon of microscale ice growth that we referred to as paracellular ice penetration. For all of the cells that exhibited paracellular ice penetration (n = 25), 80% ±18.0% of the paracellular ice dendrites co-localized with IIF. To quantify the potential importance of these paracellular ice

events, all data were separated into groups by IIF start location and whether the IIF initiation point co-localized with the paracellular ice dendrite. Table 3.1 displays the results of our analysis, from which several interesting observations can be made. First, ~72% of IIF events that initiated at the interior of the cell were co-localized with paracellular ice dendrites, suggesting a strong correlation between experiments that exhibited paracellular ice dendrite formation and subsequent initiation of IIF at non-peripheral locations. Conversely, ~95% of the IIF events that initiated in the peripheral regions of the attached cells had no association with paracellular ice dendrites.

Table 3.1 Paracellular ice association with IIF. For all high speed cryomicroscopy experiments (n = 111), IIF initiation sites were classified by their spatial location (Periphery, Interior or Unknown) and their co-localization with paracellular ice. Uncertainties represent standard deviations.

IIF Start Location	IIF co-localized with Paracellular Ice	IIF does not co-localize with paracellular ice	Unknown	Total
Periphery	6.3% ± 2.4%	64.9% ± 7.6%	4.5% ± 2.0%	75.7% ± 8.3%
Interior	11.7% ± 3.2%	2.7% ± 1.6%	1.8% ± 1.3%	16.2% ± 3.8%
Unknown	0%	2.7% ± 1.6%	5.4% ± 2.2%	8.1% ± 2.7%
Total	18.0% ± 4.0%	68.5% ± 7.9%	11.7% ± 3.2%	100%

To investigate the kinetics of IIF events associated with paracellular ice dendrites, data were divided into two distinct groups: IIF events associated with paracellular ice, and IIF events with no paracellular ice association. Using Equation 3.4 and 3.8 the cumulative probability for each data population was calculated and is presented in

Figure 3.14. It can be seen that IIF events with no association with paracellular ice froze faster than IIF events co-localized with paracellular ice dendrites. Comparing the kinetics in Figure 3.14 (IIF characterized by paracellular ice association) with those presented in Figure 3.12 (IIF characterized by start location), it can be seen that similar trends exist. The kinetics for IIF events that had no association with paracellular ice are similar to the kinetics of IIF events that initiated at the periphery of the cell, and the corresponding IIF temperature means are statistically similar (p = 0.25). Likewise, the kinetics of IIF events associated with paracellular ice are similar to the kinetics for non-edge IIF starts with no statistically significant difference between the corresponding mean temperatures of IIF (p = 0.45). These results suggest that two appropriate classifications of IIF events are (i) IIF events that initiate at the cell periphery, and (ii) IIF events that co-localize with paracellular ice dendrites.

Further investigating the relationship between paracellular ice dendrites and IIF, the temperature at which the paracellular ice dendrite formed was determined for all occasions in which the acquired video captured the initial phase of paracellular dendrite growth (75% of all paracellular ice penetration events). For all micropatterned endothelial cell experiments presented in this chapter, at most one single paracellular ice dendrite would form prior to IIF. The relationship between the paracellular ice penetration temperature and IIF temperature is shown in Figure 3.15, indicating a temporal correlation between these two phenomena. Strikingly, in ~95% of the data, paracellular ice penetration preceded IIF, suggesting a causal relationship. In particular,

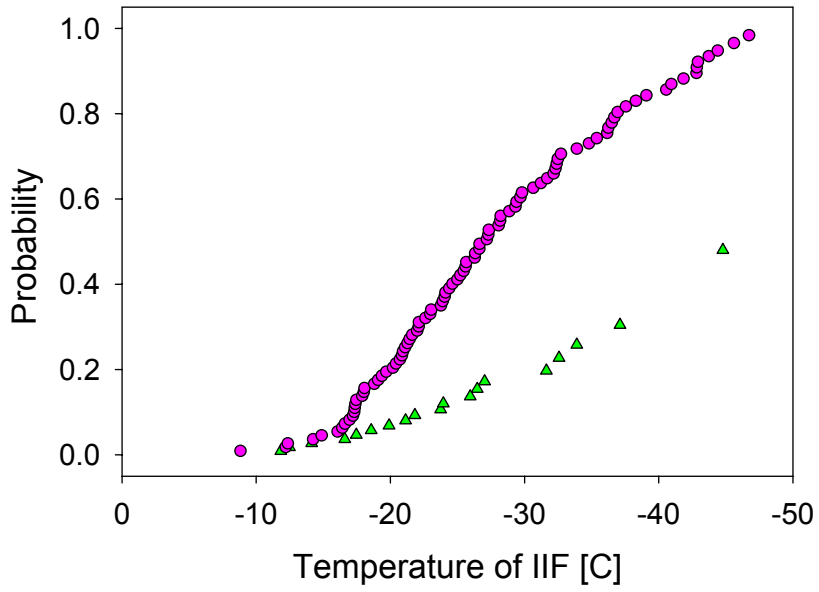

Figure 3.14 Cumulative probability of IIF relative to paracellular ice association. The kinetics for IIF events that co-localized with paracellular ice, (green triangles) were much slower than for cells where IIF was not spatially associated with paracellular ice (pink circles).

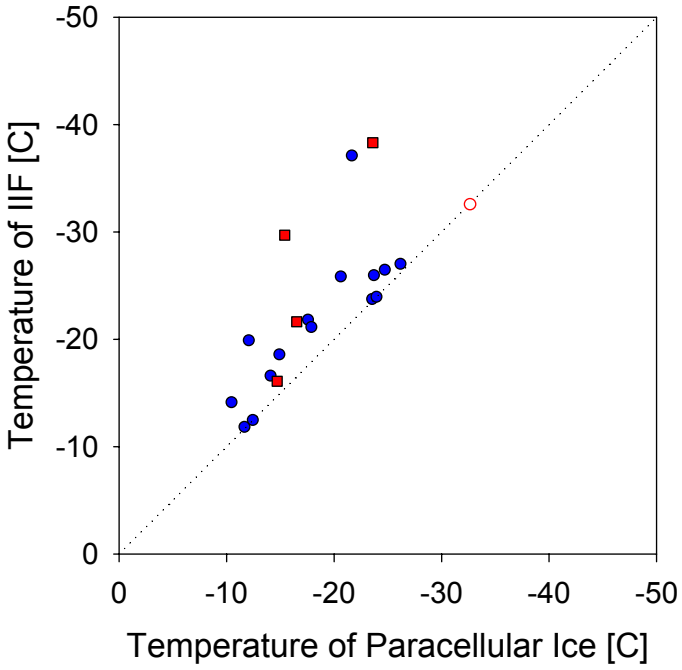

Figure 3.15 Temperature at which paracellular ice initiates growth and the subsequent temperature of IIF for micropatterned endothelial cells. Blue circles represent data where the paracellular ice dendrite was spatially associated with the initiation point of IIF, whereas the red squares represent data in which there was no association between paracellular ice and the start location of IIF. In the data population, there was only one case where a paracellular ice dendrite formed after the IIF event (open red circle). The IIF event that occurred in this cell was associated with a different paracellular ice dendrite (start temperature not recorded due to camera memory limitations). A reference line illustrating a theoretical 1:1 relationship between the temperature of paracellular ice penetration and the temperature of IIF is shown (dotted line).

for all cryomicroscopy videos with at least 0.5 seconds of recording time after IIF (n = 108), there was only one incidence of a paracellular ice dendrite forming after the IIF event. Therefore, we will refer to IIF initiation events that co-localize with paracellular ice dendrites as "dendrite-mediated initiation" (DMI) in what follows.

Next, the time delay between the paracellular ice penetration event and the initiation of IIF was calculated. The cumulative probability distribution of these time delays is shown in Figure 3.16. For all videos in which the initial formation of the paracellular ice dendrite was captured (n = 19), the average time delay between paracellular ice penetration and IIF initiation was 2.20 ± 0.54s. The subset of IIF initiation events co-localized with paracellular ice dendrites had a significantly shorter average time delay (Δt = 1.65 ± 0.54s) than IIF initiation events not associated with paracellular ice dendrites (Δt = 4.30s ± 1.41s, $p < 0.05$).

Our hypothesis that the observed ice dendrites were penetrating the supercooled paracellular space was tested by applying ice crystal pore theory originally developed by Mazur[44] (see Chapter 2 for full theory). Pore theory allows for the prediction of the physical dimensions of pores or channels that ice crystals can penetrate, as a function of temperature. If pore theory predictions are on the same order of magnitude as our experimental results, support will be given not only to the hypothesis that the dendrites are penetrating the paracellular space, but also that these projections are in fact ice dendrites. Recently, Acker *et al*. modified Mazur's pore theory to account for solution effects in their investigation of ice crystal propagation through gap junctions in confluent monolayers[57]. We rearranged the capillary freezing-point depression equation presented

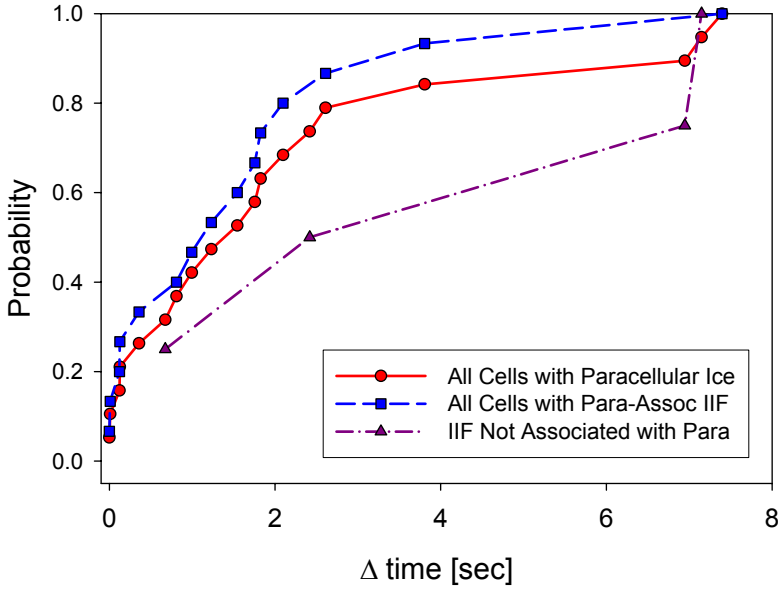

Figure 3.16 Measured time delay between paracellular ice penetration and the subsequent IIF event. Data were classified into three groups: all cells that had paracellular ice dendrites form (solid red line), all cells that had paracellular ice, and co-localized with IIF (dashed blue line), and all cells that had paracellular ice but it was not associated with the subsequent IIF event (dash-dot purple line). See text for details.

in Acker *et al*.[57] to predict the largest pore diameter that an ice crystal could penetrate at our measured temperatures of paracellular ice penetration:

$$d_{pore} = \frac{4\nu_1^s \sigma_{SL} T_{fp}^o \cos\theta}{L_f (T_{fp}^o - T_{penetration}) - \nu_1^L \pi^L T_{fp}^o} \tag{3.16}$$

where d_{pore} is the pore diameter; $T_{penetration}$, the temperature at which extracellular ice penetrates into the pore; T_{fp}^{o}, the freezing point of planar ice-water interface (T_{fp}^{o} = 273.15 K); $\upsilon^{S}_{1,}$ the molar volume of ice; υ^{L}_{1}, the molar volume of water; σ_{SL}, as the interfacial tension between the ice and the liquid water; θ, the contact angle between the ice-water interface and the pore wall; L_f, the molar heat of fusion; and π^{L}, the osmotic pressure of the solution.

To apply pore theory to our data, we first determined the temperatures of at which the paracellular ice dendrites initiated growth. Figure 3.17A presents the distribution of temperatures at which paracellular ice first appeared. It can be seen that these temperatures exhibited an approximately Gaussian distribution around an average dendrite initiation temperature of -18.2 ± 1.1 °C. Next, Equation 3.16 was used to predict the upper limit (θ = 0) for the pore diameter that would allow for ice crystal penetration at our paracellular ice initiation temperatures for various osmotic solution concentrations in the paracellular liquid. Figure 3.16B shows the results of that analysis, displaying the predicted pore diameter as it varies with temperature and paracellular tonicity. Also shown in Figure 3.17B are the lower and upper bound of the distribution of paracellular ice penetration temperatures (from Figure 3.17A). From Figure 3.17B, it can be seen that the predicted pore diameter ranges from 3 – 11 nm if there is no dehydration of the

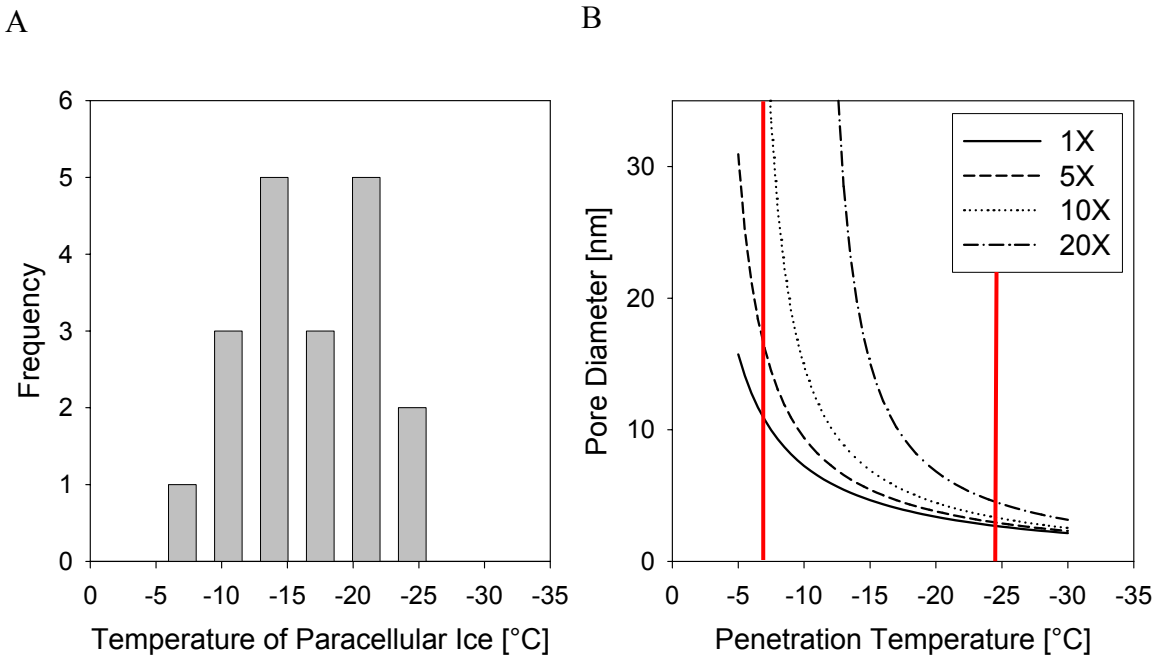

Figure 3.17 Measured paracellular ice penetration temperatures and pore theory predictions. (A) Distribution of the temperatures at which paracellular ice dendrites penetrated into the paracellular space. (B) Prediction of the upper limit (θ = 0º) for the pore diameter that would allow an ice crystal to penetrate the supercooled paracellular space for various tonicities of the paracellular solution (Equation 3.15). The solid vertical lines in (B) represent the upper and lower limit of the measured initiation temperatures of paracellular ice penetration, shown in (A).

paracellular space. If the concentration of the paracellular solution has increased five-fold due to dehydration during cooling, predicted pore diameters consistent with the observed temperatures of paracellular ice penetration are in the range 3-17 nm.

3.5 Discussion

The study presented in this chapter details our first experiments using a novel cryomicroscopy system that is capable of observing intracellular ice formation at sub-millisecond temporal and sub-micron spatial resolution. Using a well defined experimental model, we were able to record the never-before-seen IIF initiation point as well as the phase transformation dynamics and post-freezing intracellular events.

3.5.1 Paracellular Ice Dendrite Penetration

Prior to IIF initiation, a new phenomenon was observed in a small portion of our experiments that we referred to as paracellular ice penetration. These microscale ice dendrites initiated growth at the periphery of the attached cells, and slowly elongated during cooling. Our hypothesis of paracellular ice penetration was based on the assumption that these ice dendrites were penetrating a small opening that existed between the attached cell and the substrate. This opening would give the extracellular ice access to the supercooled water that is trapped underneath the attached cell. We hypothesized that such an aperture would be bounded by the glass substrate, the basal cell membrane, and the focal adhesion clusters that typically form along the periphery of the attached micropatterned cell[99,101]. Pore theory[44,57] supports our hypothesis, predicting that for our paracellular ice dendrite temperatures, the gaps in the paracellular space between the cell

and the substrate must be less than 7nm for ice dendrite growth to initiate. Considering that the separation distance between focal adhesion clusters is on the order of microns, the limiting dimension of these channels was assumed to be the separation distance between the basal membrane of the cell and the substrate. For single bovine aortic endothelial cells attached to glass substrates, Burmeister *et al.*[102] measured the cell-substrate separation distance to be approximately 10 - 15 nm. This separation distance is within an order of magnitude or the pore theory prediction, suggesting that our hypothesis is valid. Our theoretical predictions of pore size could be further enhanced if we modeled the degree of dehydration in the paracellular space during the temperature plunge. It is reasonable to hypothesize that a high degree of water will diffuse out of the paracellular space as the extracellular ice grows. This efflux of water would result in a higher solute concentrate in the supercooled solution underneath the cell, significantly decreasing the degree of supercooling. As a consequence, the predicted pore diameters could significantly increase, resulting in better agreement with our data.

It should be noted that there is a possibility that the paracellular ice dendrite growth initiated at earlier temperature than what was recorded. While our system provides excellent submicron resolution, it cannot pick up events at the nanometer level. Thus, due to the slow growth rate of the paracellular ice dendrites, we are effectively only capturing the ice dendrites when they are physically larger than 0.5μm, not at the exact starting point. If the dendrites were in fact penetrating the paracellular space at a higher temperature, the size of the predicted pore radius would increase, consistent with the 10 -15nm cell-substrate separation distances found in the literature[103,104]

Interestingly, for the majority of paracellular ice dendrites that formed, subsequent IIF events initiated at a spatial location in close proximity to the ice dendrite. In addition, our results show a strong correlation between the temperature of paracellular ice formation and the subsequent temperature of IIF initiation, suggesting that paracellular ice penetration may be a precursor event to IIF in adherent cells, and potentially a causative factor. While more studies need to be conducted to investigate this phenomenon, we can briefly speculate as to a potential mechanism for paracellular dendrite-mediated IIF initiation. Considering that the majority of IIF events initiated at interior (i.e., non-perimeter) locations of the attached cell were associated with paracellular ice, we can hypothesize that perhaps paracellular ice dendrites are the only crystals that can get close enough to the cell membrane to initiate IIF through surface catalyzed nucleation (SCN)[23]. Another possibility is mechanical interactions between the paracellular ice dendrite and the plasma membrane, resulting in mechanical damage[41,105].

3.5.2 IIF Front Velocity

The most surprising result from our data was the appearance of a rapid single, advancing front in our cells during freezing. This front has never been reported before in biological cells. We hypothesized that this front was the interface of a growing intracellular ice crystal, located inside the cell. Subsequent experiments reported in this chapter provided support for this hypothesis. To further characterize the front, the average velocity was calculated and falls within the limits of heat transfer limited crystal growth[100]. The use of video images to determine the kinetics of ice growth is not unusual[24-26]. However, almost all of the previously reported ice crystal growth velocities

are for pure water, growing unrestrained in thin films[30,31] or three-dimensional volumes[24-26], making direct comparison with our results difficult.

To the best of our knowledge, there has only been one previous study of IIF at high temporal resolution (not peer reviewed)[106]. Using a directional solidification stage, Tsuruta *et al*. observed IIF in the epidermis of an onion bulb (*e.g.,* monolayer of high water content plant cells) at a frequency of 1000 Hz[106], with spatial resolution on the order of 10μm. While Tsuruta *et al.* were investigating cell to cell ice propagation, their study reported IIF initiating from the plasma membrane (in contact with a previously frozen cell) and growing directionally to the other side of the cell. While there are many differences between their system our ours, they reported a single measurement of time for the ice front to travel through one onion cell as 221 ms (dimensions of the cell were not given)[106]. From their stated average 'size' of onion cells (50 - 800 μm), we can only speculate that the velocity of this front ranged from 0.23 - 3.6 μm/ms (translating 'size' as the length of rectangular cells)[106]. However, this very rough estimate of velocity is consistent with our measured velocities of the ice front in micropatterned cells.

3.5.3 Post-Front Cell Darkening

For the century, traditional cryomicroscopy has used cell darkening and/or "twitching" as an indicator of IIF, with all kinetic measurements based on this metric[33]. While the cause of darkening is unknown, it is commonly accepted that the darkening is the result of intracellular ice scattering the light used to view the sample. During crystallization, heat is produced at the crystal surface and must be released into the surroundings. Researchers have been able to measure the release of latent heat during freezing through the use of differential scanning calorimetry (DSC)[107]. Support for

darkening as IIF has been given by correlating the temporal scales of DSC measurements with the kinetics of darkening measured during cryomicroscopy observations[105,108,109]. However, for both cryomicroscopy and DSC systems, temporal resolution limitations result in a measurement of crystallization, not the actual nucleation event. The results from our high speed cryomicroscopy system strongly suggest that cell darkening is actually a secondary event to IIF. As such, by measuring cell darkening, traditional cryomicroscopy systems are indirectly measuring the freezing kinetics. In addition, while all cells exhibited an IIF front, ~10% of all cells exhibited no detectable level of subsequent cell darkening. In traditional cryomicroscopy systems it is common for a portion of the population to be reported as 'unfrozen', or 'damaged' due to any lack of cell darkening or twitching[36,105]. Freezing single suspended human endothelial cells, Barrada and Bischof[36] reported that for high cooling rates, 15% of their cell population did not freeze (*e.g.,* exhibited no darkening and/or twitching). During freezing of oocytes, Mazur *et al*.[105] reported that 40% of the population exhibited no outward signs of freezing and hypothesized that the lack of cell darkening was a consequence of prior membrane damage. It is therefore possible that many (or all) of these apparently unfrozen cells have actually experienced IIF with insufficient darkening for detection using conventional video cryomicroscopy. Thus, we believe that by using cell darkening as the primary indicator of IIF, sizable errors may be introduced into kinetic analysis for certain cell types.

Recently, Mazur *et al*.[105] quantified the kinetics of darkening in mouse oocytes, through visual observation of video frames acquired at 30Hz. In Mazur's study, oocytes were evaluated qualitatively for 'ultimate darkness' during freezing, and the mean times to

mid darkening (50% ultimate darkness) and full darkening (100% ultimate darkness) were determined to be dependent on the temperature of darkening initiation. For oocytes darkening above -30 °C, the mean time to full darkening (100% darkening) was 0.34 ± 0.10 s; and for oocytes darkening below -30°C, the mean time to full darkening was 7.6 ± 1.2 s with a high degree of scatter in the data[105]. In other words, the time for oocytes to reach a steady state darkening intensity significantly increased as the temperature of darkening initiation decreased. Our analysis of cell darkening in attached BPAECs indicated a different trend, with the average time to a steady state darkening intensity (~1-1.5 s, evaluated through digital image analysis) relatively insensitive to IIF initiation temperature. In addition, we found that at low temperatures of IIF initiation ($T_{IIF} < -41$°C) no darkening occurred. Comparisons between the two studies are difficult considering that different cooling rates were used, and large differences exist between cell types (*e.g.*, cell volume, and water content). It is possible that for the maximum recording length of our cryomicroscopy system (8 seconds at 8,000Hz), resulted in truncation of the cell darkening.

Determining the exact cause of post-IIF darkening is beyond the scope of this study, but one can make a few speculations from our results. This temperature dependence on darkening in our data is intriguing (i.e., no darkening for $T_{IIF} < -41$°C), and is suggestive of a secondary mechanism that is temperature sensitive. Eutectic crystallization, or the nucleation of high solute concentrations, is manifested by dark crystalline growth and has been shown to be temperature sensitive[110]. Thus, it is reasonable to hypothesize that the IIF event creates a sudden high concentration of solutes in the intracellular space, in turn promoting intracellular eutectic crystallization.

As the solutes crystallize, the cell gradually grows darker. Unfortunately, all studies of eutectic crystallization during freezing focus on eutectic crystallization in the extracellular solution[111-115].

During our experiments, bubbles were released from the intracellular space shortly after darkening initiated. The appearance of bubbles after IIF has been reported previously[116,117], and the common hypothesis is that the bubbles are a consequence of the nucleation of dissolved atmospheric gases during freezing[49,118]. Vascular endothelial cells have also been shown to have high intracellular oxygen levels[119], a gas known to nucleate at low temperatures[49]. The close timing of bubble formation and cell darkening leads one to speculate that the two may be connected. It is possible that initial signs of darkening are the result of small bubbles forming. Similar to our hypothesis of eutectic crystallization, it is just as reasonable to suggest that gaseous solutes are rejected by the advancing ice front, resulting in a rapid concentration increase, and subsequent nucleation[49]. After this initial bubble formation, one can speculate that the subsequent growth may result in cell darkening.

3.5.4 IIF Start Location and Nucleation Theory

A primary goal of the studies presented in this thesis was to test the applicability of commonly accepted nucleation theories to single attached cells. These ice nucleation theories, such as surface-catalyzed nucleation (SCN)[23] and volume-catalyzed nucleation (VCN)[23], were developed for single cell suspensions and were based, in large part on conventional (30Hz) cryomicroscopy observations. The novel temporal resolution of our cryomicroscopy system allowed us to observe for the first time, the exact spatial location of the nucleation site. Specifically, our results demonstrated that for single attached

endothelial cells, the majority of IIF initiation sites were localized to the periphery of the cell. These results are not consistent with either hypothesis of nucleation theory. Since the cell membrane, thought to be the catalyzing mechanism in SCN theory, encompasses the entire cell, and the cytoplasmic volume, important to VCN, is equally distributed throughout the cell (and perhaps slightly more concentrated towards the center of the island), one would expect the IIF nucleation sites to vary randomly throughout the attached cell. Thus, our data suggest an alternative mechanism of IIF initiation may be dominant for adherent cells.

Several alternative hypotheses can be proposed to account for the observed correlation between cell perimeter and rate of IIF. For example, ice nucleation may result from a mechanism analogous to volume catalyzed nucleation, in which IIF is catalyzed by proteins preferentially up-regulated at the periphery of attached cells. In particular, focal adhesion proteins, which are known to localize to the periphery of micropatterned cells[101], are candidates for this putative nucleation catalyst. Alternatively, mechanical forces from the extracellular ice front may damage the cell membrane[41,42], compromising its integrity and allowing ice to enter the cytoplasm. Adherent cells would be expected to be susceptible to such mechanical damage, inasmuch as cell attachment to a substrate results in higher level of tension in the cytoskeleton[120-122] and membrane[123-125]. At this juncture, it is premature to make any conclusions regarding the mechanism of IIF.

In conclusion, data presented in this chapter provides the first direct observation of IIF at unprecedented sub-millisecond resolution. Micropatterned endothelial cells were used to provide precise control over the cell area, shape and time in culture, resulting in a robust system to study the nucleation site in attached cells. A novel phenomenon, paracellular

ice formation, was discovered and quantified for the first time, with data suggesting a possible causative role of these dendrites in IIF initiation. For all experiments, a single advancing ice front initiated from a point source, followed by subsequent cell darkening. In the vast majority of cryomicroscopy experiments, IIF initiated at the cell perimeter. This result suggests that the most commonly accepted theories of nucleation in suspended cells, surface catalyzed nucleation, may not directly translate to attached cells. IIF kinetic data was also presented that suggests two distinct mechanisms of IIF are active in attached cells. Future studies in which parameters such as pattern size, time in culture, and adhesion ligand concentration are varied will be necessary to determine the factors that influence the kinetics of this perimeter-catalyzed nucleation mechanism and the phenomenon of paracellular ice dendrite formation.

CHAPTER 4

EFFECT OF CELL SIZE ON INTRACELLULAR ICE FORMATION AND FREQUENCY OF PARACELLULAR ICE FORMATION

4.1 Introduction

In Chapter 3, a novel cryomicroscopy system developed in our laboratory was presented, capable of recording intracellular ice formation (IIF) events at a rate of 32,000 frames per second. Using this system, we reported the first direct observations of IIF, measuring the exact location of IIF initiation. Surprisingly, the initiation point was located at the cell periphery for the majority of all experiments, suggesting that surface-catalyzed nucleation (SCN) may not be the dominant mechanism of IIF in adherent cells. To further explore the applicability of SCN theory to single attached cells, the study presented in this chapter investigated the effect of cell attachment area on IIF, and compared the resulting kinetics with the predictions of SCN theory. We hypothesized that changes in cell attachment area will influence the kinetics of IIF as a consequence of changes in the total number of available cellular sites able to promote IIF initiation.

Cellular adhesion to extracellular matrix ligands, such as fibronectin, is a highly regulated process that is primarily mediated by the integrin family of receptors[126,127]. For bovine endothelial cells, bound receptors rapidly associate with the cytoskeleton and form focal adhesions, with clusters of vinculin (a focal adhesion protein) detectable within 45-60 minutes of seeding[82]. Focal adhesions are of interest to this study not only because they mediate strong adhesion to the substrate[128], but because they are typically

located near the perimeter of attached cells[101,129]. In addition, it has been shown that as the available cell attachment area increases, focal adhesion proteins will change their spatial location[99].

Surface modification techniques can be used to obtain precise control over cell-substrate interactions while eliminating confounding factors[99,101,130,131]. Cell micropatterns provide reproducible geometric configurations, independent control of experimental variables (*e.g.*, time in culture, cell spreading, and cell shape) all while being simple enough to be rigorously analyzed with theoretical models[58]. For example, it has been shown using micropatterning techniques, that cell shape provides global control of focal adhesion assembly[101,132]. Thus, simple micropatterning techniques[81,133] were modified for this study, such that the kinetics of IIF could be analyzed while the cell perimeter and attachment area were varied in a controlled manner.

This study attempts to remove some of the uncertainty surrounding the mechanisms of IIF in attached cells for the purpose of developing a better understanding of the effects of cell-substrate interactions on freezing. To this end, high speed cryomicroscopy was combined with micropatterning techniques, allowing for investigation of IIF in adherent cells with different contact areas, while maintaining a constant cell shape. Through systematic variations of cell attachment area and perimeter, the resulting kinetics were compared to the predictions of SCN theory, the most commonly accepted nucleation theory for attached cells. The results of this study provide further support to our hypothesis that SCN is not the dominant mechanism of IIF in attached cells.

4.2 Theoretical Background

Testing of nucleation theory requires the ability to measure the nucleation frequency in biological cells. However, in conventional cryomicroscopy systems, only the overall crystallization rates can be measured experimentally. Thus, all previous validation of nucleation theory has been done by making the assumption that the crystallization time is negligible in comparison with the nucleation time. Our high speed cryomicroscopy system allows for unique opportunity to measure the nucleation rate of IIF as it varies with cell attachment area. SCN theory predicts that the overall rate of nucleation should scale with cell surface area. Thus, if SCN holds true for single attached cells, as available contact area increases, the rate of IIF should increase proportionally to the increase in attached cell area. To determine the size dependence of IIF initiation from experimental measurements of the probability of IIF, we substitute Equation 2.3 into Equation 3.1:

$$\frac{A_1 \int_0^t I_{SCN}\, dt}{A_2 \int_0^t I_{SCN}\, dt} = \frac{\ln(1 - P_{IIF_1})}{\ln(1 - P_{IIF_2})} \tag{4.1}$$

where A_1 and A_2 are the size of attached cell areas, and P_{IIF1} and P_{IIF2} are the respective probabilities of IIF for each cell size. Re-arranging Equation 4.1:

$$\ln(1 - P_{IIF_2}) = \frac{A_2}{A_1}\left[\ln(1 - P_{IIF_1})\right]. \tag{4.2}$$

Thus, if SCN is the dominant mechanism of IIF, a plot of -ln(1-P_{IIF1}) vs. -ln(1-P_{IIF2}) should be approximately linear with a slope A_2 / A_1.

In Chapter 3, previous results in 20 μm diameter endothelial cell patterns revealed that the majority of IIF nucleation events initiated at the cell perimeter. These results suggested that SCN was not the dominant mechanism of IIF for attached cells, and that an IIF initiation mechanism that correlates with the cell perimeter drove the kinetics of IIF. We will refer to this mechanism as peripheral initiation (PI), and postulate that the corresponding kinetics can be described by an average IIF initiation rate per unit length perimeter, I_{PI}, such that the rate of IIF initiation per cell is approximately:

$$J(t) = P \cdot I_{PI} \tag{4.3}$$

where P is the cell perimeter. Substituting Equation 4.3 into Equation 3.1, and rearranging, we have:

$$\ln(1 - P_{IIF_2}) = \frac{P_2}{P_1}\left[\ln(1 - P_{IIF_1})\right] \tag{4.4}$$

By increasing cell attachment area (through the use of micropatterning techniques), and measuring the initiation frequency of IIF events (with high speed cryomicroscopy), we tested whether IIF kinetics align with SCN theory (Equation 4.2) or with our proposed peripheral initiation mechanism (Equation 4.4).

4.3 Materials and Methods

4.3.1 Bovine Pulmonary Artery Endothelial Cell Culture

Bovine pulmonary artery endothelial cells (BPAECs) (Cambrex, San Diego, CA) were cultured in MCDB 131 media (Mediatech, Herndon, VA) supplemented with 5% (v/v) fetal bovine serum (Sigma-Aldrich, St. Louis, MO), 2ng/mL basic human fibroblast growth factor (PeproTech, Rocky Hill, NJ), 10ng/mL human epithelial growth factor (Invitrogen Corp., Carlsbad, CA), 1ng/mL vascular endothelial growth factor (Sigma-Aldrich), 2 ng/mL insulin-like growth factor-1 (Invitrogen), 0.001 mg/mL hydrocortisone (Sigma-Aldrich), 2mM L-glutamine (Mediatech), 100U/mL penicillin/100μg/mL streptomycin (Invitrogen), and 50μg/mL ascorbic acid (Sigma-Aldrich). Cells were cultured on tissue culture plastic at 37°C in a humidified 5% CO_2 environment and media were replaced every 48 hours. Flasks where subcultured when they reached 70-85% confluency and were split at a 1:6 ratio, following the recommendations of the vendor. Total exposure time to trypsin-EDTA (Cambrex, Cat# CC-5012) was 5 minutes. For all experiments, cells were used at passages 5 through 9.

4.3.2 Fabrication of Microfiche Photomasks

Low cost microfabrication masks containing 15μm-level feature sizes were generated by converting printed masks onto microfiche[133,134]. Masks were designed in AutoCAD 2006 (Autodesk, Inc, San Rafael, CA), and were printed onto premium photo paper (Hewlett Packard, Palo Alto, CA) at a resolution of 1200 dpi. The printed masks were optically reduced by a factor of 25 onto microfiche (Fuji Super HR, ~70μm thick)

by New England Document Systems (Manchester, NH). The resulting microfiche films were used as photolithography masks.

4.3.3 Fabrication of Micropatterned Substrates

Photolithography techniques were used to create silicon masters that contained arrays of cylindrical wells of varying diameter (30μm and 40μm). Briefly, in a class 10 cleanroom, silicon wafers were spin-coated with SU-8 photoresist (Microchem Co., Newton, MA) to a thickness of 7μm. Substrates were baked on a hotplate at 65°C for 2 min, ramped to 95°C for 5 min, and then returned to 65°C. Microfiche films were used as photomasks by placing the microfiche directly onto the photoresist-coated wafer. A blank photolithography mask (Photronics, Brookfield, CT) was used to gently sandwich the microfiche against the wafer. The photoresist-coated substrates were exposed under UV (9.65 $mJ \cdot cm^{-2} \cdot s$ at 405nm) for 16.5 seconds, using an OAI mask aligner (Optical Associates, Inc, San Jose, CA) in contact mode. Post-exposure, the microfiche was removed and the substrate was baked on a hotplate (65°C for 1min, 95°C for 1min, and 65°C for 1min). After baking, the photoresist was developed in SU-8 Developer (Microchem) for 1 minute, under gentle agitation. The developed wafer was rinsed in 100% isopropyl alcohol for 1min, blown dry with a nitrogen gun and baked for 10 minutes at 95°C on a hotplate. The use of 20 μm silicon master was generously donated by A. García (Georgia Institute of Technology), with fabrication previously described[99].

Agarose micropatterned glass coverslips that contained adhesive and non-adhesive domains were fabricated using methods adapted from Nelson and Chen[81]. Full

details of the technique can be found in Chapter 3. Briefly, poly(dimethylsiloxane) (PDMS) (Sylgard 184, Superior Essex, Atlanta, GA) stamps were cast from the silicon templates described above. The PDMS stamp was placed, patterned side down, against a 12mm diameter circular glass coverslip (#1.5, Fisher Scientific, Suwanee, GA). A small volume (~5μL) of 100% ethanol (Fisher Scientific) was wicked into the 'mold' created by the PDMS stamp and the coverslip, and allowed to evaporate. An aqueous solution of 0.6% (w/v) agarose (Invitrogen) and 40% (v/v) ethanol was heated to its boiling point while stirring, and then dispensed along the edge of the stamp/coverslip mold. The agarose was allowed to dry undisturbed at room temperature for approximately two hours. The PDMS stamp was then carefully removed, producing a micropatterned coverslip with bare glass islands surrounded by non-adhesive agarose. Substrates were sterilized in an aqueous solution of 70% ethanol (v/v), rinsed twice with DPBS (VWR) and incubated (at 37°C, 5% CO_2) for 1 hour in a 25μg/mL solution of human-plasma fibronectin (FN) (Invitrogen) in DPBS. After the fibronectin surface treatment, coverslips were rinsed and stored in DPBS at 37°C, 5% CO_2 for up to 6 hours prior to seeding of cells.

4.3.4 Sample Preparation

For cryomicroscopy experiments, BPAECs were trypsinized, resuspended in media, centrifuged at 220 x g for 5 min and resuspended in media at a density of ~1E4 cells/mL. Cells were seeded onto patterned or unpatterned coverslips, and subsequently incubated at 37°C for six hours (± 30 min). Prior to freezing experiments, coverslips with adherent cells were incubated for 10 min at 37°C with medium supplemented in 2 μM SYTO13 (Molecular Probes, Eugene, Oregon), a nucleic acid stain, and 10 μM

ethidium homodimer (EthD-1) (Molecular Probes), a membrane impermeant stain, to ensure that each micropattern contained a single cell with full membrane integrity. Immediately prior to freezing, coverslips were rinsed with 30 mM HEPES buffer (Cambrex), then removed from the petri dish, inverted, and placed on a 16 mm diameter circular glass coverslip (Linkam Scientific Instruments, Tadworth, Surrey, UK), creating a sandwich.

4.3.5 High Speed Digital Video Cryomicroscopy

A high-speed video cryomicroscopy system was created to allow observation of IIF at sub-millisecond time scales in single attached cells. Full details of the system can be found in Chapter 3. Briefly, the system consisted of an upright Eclipse ME600 microscope (Nikon, Tokyo, Japan) fitted with a commercially available cooling stage (FDCS 196, Linkam). System calibration was conducted by measuring the melting point of ice crystallized from a sample of purified water. Experiments were recorded using a high speed digital camera (FastCam-X 512PCI, Photron, Tokyo, Japan) and corresponding software (FastCAM Viewer, version 2.2; Photron).

For all experiments, images were acquired at a rate of 8,000 Hz, with an exposure time of 100 μsec. Maximum recording time was limited to approximately eight seconds with the settings used. For all high speed experiments, cells were observed using a 50X objective and 0.45X coupler (Nikon). To meet the light level requirements for high-speed imaging, all samples were frozen under Köhler illumination, with the microscope halogen lamp set to maximum output.

To promote IIF, cell cultures were frozen at a rapid rate (130°C/min) in the absence of cryoprotectants. Samples were prepared as described above, and placed in the

sample holder of the cryomicroscope stage, directly on top of the silver block, which was heated to a temperature of 37°C. After closing the cryostage chamber, the atmosphere was purged using liquid nitrogen vapor to prevent condensation. To seed extracellular ice, the sample temperature was cooled from 37°C to -1.5°C (at 50°C /min), and repositioned such that the edge of the sample was brought into contact with a seeding block (custom-integrated into the cryostage, and cooled to the temperature of the liquid nitrogen). Immediately after seeding the extracellular ice, the sample was repositioned on the silver block and a single cell of normal morphology, fully spread in the circular micropattern was randomly selected for the experiment. For all experiments, the focal plane of camera was set to the basal area of the attached cell. Prior to the rapid cooling step, both brightfield and fluorescent images were taken of the sample. Only cells that stained negative for EthD-1, and which did not share the micropatterned island with other cells (as evidenced by SYTO13 staining), were used in experiments. To minimize dehydration of the sample, the extracellular ice seeding, cell selection and initial imaging were completed within approximately 60 seconds. If this process took longer than three minutes, the experiment was abandoned. Immediately prior to the freezing process, the halogen lamp was set to maximum output. Then, the stage was cooled at a controlled rate of 130°C/min to -60°C. The high speed camera was set to record images into a circular buffer, and recording was terminated using a manual switch-closure trigger. When conventional indicators of intracellular ice formation (i.e. cell darkening and/or twitching) were observed, the trigger switch was closed, allowing the IIF event to be captured. Each experiment was analyzed frame-by-frame to identify the precise time, temperature and location of the IIF event.

4.3.6 Paracellular Ice Analysis

Microscale ice dendrites, which we classified as paracellular ice, exhibited slow growth rates that could not be quantified in the same manner as the IIF front (*i.e.* frame-by-frame playback with a distinct starting point). Thus, the start of the paracellular ice initiation was determined by reverse playback of the video at a frame rate of 125Hz (approximately 1.6% of real-time). When the dendrite disappeared from view, the playback would be stopped and the frame number recorded. This method was repeated in triplicate and if the resulting frame varied by more than 100 frames, the process was repeated at 60Hz. Assuming a maximum operator response time of one second, determining the starting point of paracellular ice in this manner introduced a potential error of 125 frames, equivalent to ± 16ms or ± 0.03°C in the estimated temperature of paracellular ice penetration. Paracellular ice dendrites were classified as co-localizing with the subsequent IIF event if the initiation point of the IIF event was within 1.5μm (or 3 pixels) of the paracellular ice dendrite location.

4.3.7 Immunostaining for Focal Adhesions and Stress Fibers

Cells in micropatterns were fixed in 4% (v/v) paraformaldehyde in PBS (Sigma-Aldrich) six hours after seeding. Following fixation, cells were rinsed three times in wash buffer (1X DPBS with 0.05% (v/v) Tween20 (Sigma-Adlrich)), permeabilized in 0.1% (v/v) TritonX-100 (Sigma-Aldrich), and rinsed twice in wash buffer. For visualization of the focal adhesion protein vinculin, samples were blocked with 2% goat serum (Sigma-Aldrich) in DPBS and incubated with murine anti-vinculin monoclonal antibody, purified clone 7F9 (Chemicon, Temecula, CA) in 2% goat serum, and visualized with FITC-conjugated anti-mouse IgG secondary antibody (Chemicon). The

cell nucleus and F-actin were stained with 0.1% DAPI and 0.25 μg/mL TRITC-conjugated phalloidin (Chemicon) in PBS, respectively. Negative controls were included by replacing the anti-vinculin antibody incubation solution with 2% goat serum in DPBS. To reduce variability between experimental groups (*i.e.* 20, 30, and 40μm circles), coverslips were seeded from the same passage, and staining would immediately follow (using the same solution preparations). After staining, coverslips were mounted on glass slides (Superfrost, Fisher Scientific) with anti-fade mounting solution (Molecular Probes). Coverslips were imaged on an Eclipse ME600 microscope with a Plan Apochromat VC 100X oil immersion objective, NA 1.4 (Nikon), under UV illumination (X-Cite 120 Lamp, Nikon). All images were recorded under the same camera settings, using a high resolution CCD camera (Sensicam, PCO, Kelheim, Germany) and IP Lab vs. 3.6 (Scanalytics, Rockville, MD). For each data population, a minimum of four coverslips were analyzed, with an average of 25 cells imaged from each coverslip.

4.3.8 Live Cell Imaging of Focal Adhesions

Interference reflection microscopy (IRM) was used to visualize focal adhesion spatial arrangement in living cells[129]. Briefly, micropatterned coverslips were rinsed twice in 30mM HEPES buffer (Cambrex), and mounted on microscope slides. IRM imaging was performed on an Eclipse ME600 upright microscope with an oil immersion (oil type DF, n_D = 1.5150, Cat# 16242, Cargille Laboratories, Cedar Grove, NJ) 100X Objective, NA 1.4 (Nikon), IRM filter cube (Nikon, generously provided by A. García, Georgia Institute of Technology) under epi-illumination (halogen lamp source with an aperture stop). Images were recorded using a high resolution CCD camera (Sensicam, PCO, Kelheim, Germany) and IP Lab vs. 3.6 (Scanalytics, Rockville, MD).

4.3.9 Cell Dimensions and Focal Adhesion Analysis

Micropatterned cell dimensions and focal adhesion location were quantified using a custom program developed in LabView 8.0 with IMAQ 8.0 (National Instruments, Austin, TX). All fluorescent images were input into the program in their native, 12-bit grayscale format, unprocessed. The program opens the image file indicated by the user and automatically detects the position of the cell using a multi-algorithm search sequence. The detection algorithm determines the dimensions of the cell by fitting a circle to points detected at the cell periphery (goodness of fit set to 95%, see Figure 4.1). For focal adhesion quantification, we were only interested in the focal adhesions at the cell periphery. Thus, a region of interest was defined by two concentric circles, with dimensions ±10% of the measured cell radius. This annular region of interest was then extracted from the overall image and 'unwrapped' to convert the annulus to a rectangular image for processing. To isolate vinculin proteins for subsequent morphometry, the grayscale images was segmented using LabView's local background thresholding algorithm (the first and only image processing step used in this program). Segment area and position were recorded for each image. Additionally, the positions and dimensions of bounding boxes (completely encompassing each segment) were obtained for each segment. These dimensions were then used to calculate the linear distance, or gap, that exists between each segment (see Figure 4.2). A gap was defined as a totally unobscured path in the y-direction that was five pixels or greater (0.5 μm or greater).

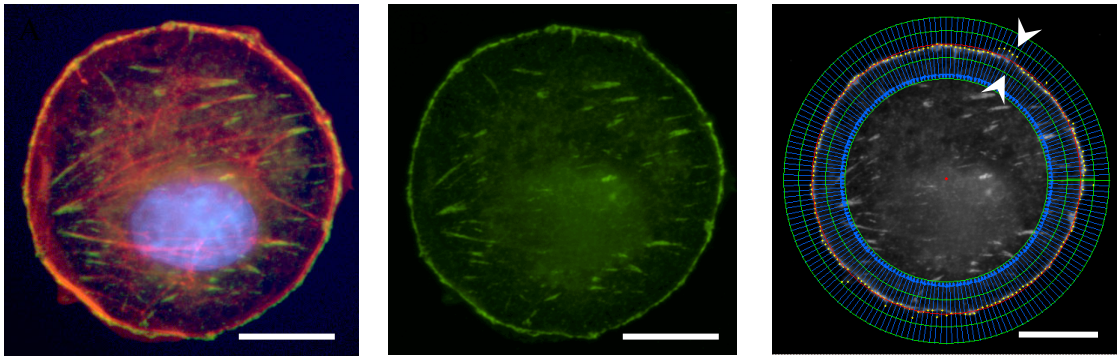

Figure 4.1 Cell size quantification. Fluorescent micrographs of individual BPAECs were analyzed in a custom LabView program that measured overall cell dimensions, and isolated the cell periphery. (A) Pseudo-colored fluorescent micrograph of a 30μm diameter BPAEC cell (red = F-actin, green = vinculin, blue = nucleus). (B) The green fluorescent signal (vinculin) was isolated and used for analysis. (C) Screen capture from the program output, displaying the result of the circle-detection algorithm. The best-fit circle (red overlay) is displayed over the vinculin image. The concentric circles (green, as indicated by arrows) display the region of the micrograph that was classified as the cell periphery (± 10% radius). Scale bar represents 10 μm. See text for details.

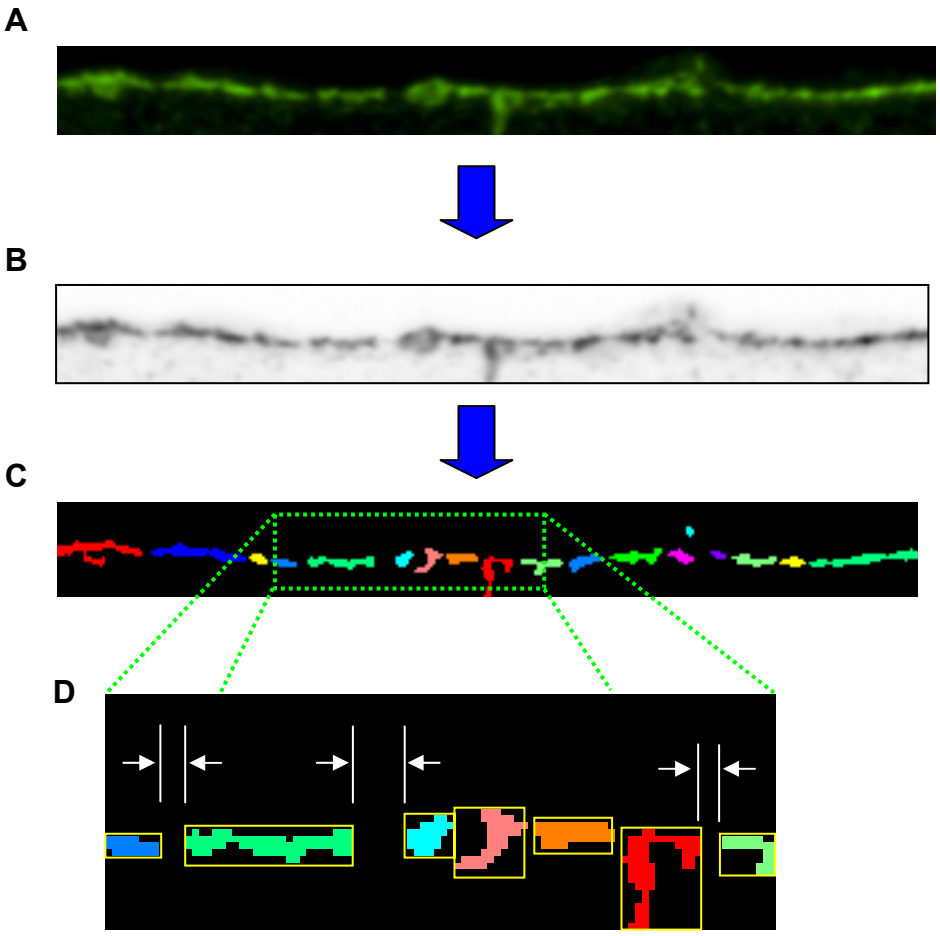

Figure 4.2 Flow chart demonstrating focal adhesion gap size quantification. (A) The region that was defined as the cell periphery was isolated from Figure 1B and 'unwrapped'; a portion of the unwrapped image is displayed here. (B) The inverse of this image is shown (not in the program, but provide here to assist in the visualization of the vinculin stain). (C) The unwrapped fluorescence image was converted to a binary image and segmented; each segment represents a focal adhesion cluster. (D) Bounding boxes (shown in yellow) were created around all segments in the unwrapped image. An algorithm then calculated the longitudinal distance that separates the edges of the bounding boxes (illustrated by the white arrows). See text for further details.

4.3.10 Statistical Analysis

Unless otherwise noted, data are reported as mean ± standard error of the mean as noted. When reporting the classification of events into categories, standard deviations were estimated by taking the square root of the number of observations in each category. If groups had a normal distribution and homogenous variances, the group means were compared by an independent *t*-test, or by analysis of variance (ANOVA), with post hoc analyses using Tukey's test. Differences were considered significant at the 95% confidence level ($p < 0.05$).

4.4 Results

To test the hypothesis that the underlying mechanism of IIF in attached cells correlates with perimeter, agarose micropatterns were created to provide precise control of cell perimeter while maintaining a constant cell shape. Three different cell sizes were investigated by varying the diameter of the micropatterns: 20, 30, and 40μm. Using the 20μm island diameter as the baseline, we effectively varied the perimeter by a factor of 1.5 (30μm /20μm) and 2.0 (40μm /20μm), while varying the cell attachment area by a factor of 2.25 (30μm /20μm) and 3.5 (40μm /20μm). The actual dimensions of the cells when seeded on the micropatterned islands were quantified using immunofluorescent staining and an automated image analysis program developed in LabView (Appendix B). The attached cell diameters were determined to be slightly larger than the predicted values: 23.4 ± 0.04 μm ($n = 97$), 36.3 ± 0.08 μm ($n = 109$), and 44.4 ± 0.10 μm ($n = 102$), for the 20 μm, 30 μm, and 40 μm patterns, respectively. These measured cell dimensions

were used for all analysis, but for ease of reference, we will refer to their nominal values in the text.

All cells were frozen at a rapid cooling rate (130 ºC/min) to -60 ºC, while acquiring high speed video at 8,000Hz. The phenomena observed during freezing were similar to those described in Chapter 3. In particular, IIF manifested as a moving front, radiating outward from a single point source. Following IIF, a slower process manifesting as cell darkening, commenced. For the majority of IIF events, the release of bubbles from the cell would also be observed following the IIF event. Prior to IIF, slight to moderate deformation of the cell membrane was often observed, especially in cells with larger cell attachment area. As Figure 4.3 demonstrates, localized areas of the cell membrane would appear to be deformed (presumably by the extracellular ice).

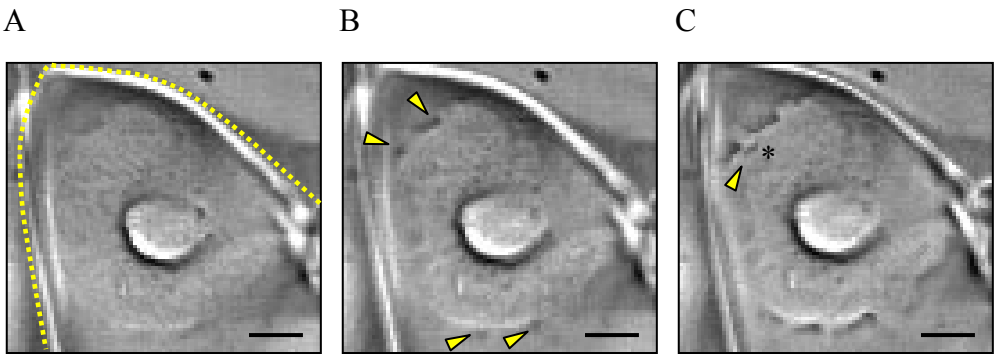

Figure 4.3 Deformation of an attached endothelial cell during freezing. A series of micrographs extracted from a cryomicroscopy experiment of a 40 μm diameter BPAEC cell are presented (Köhler illumination). (A) Micrograph of cell during the temperature plunge; T = -9.6°C, Δtime = 0 sec. The edge of the extracellular ice crystal is indicated by the yellow dashed line, which touches the outer perimeter of the cell. (B) Micrograph of the cell as the extracellular ice continues to grow; arrows indicate where the cell edges are starting to deflect; T = -10.1°C, Δtime = 0.175 sec. (C) Micrograph of the cell immediately prior to IIF, T = -11.9°C, Δtime = 1.163 sec. Deflection along the cells edges is more prominent, with a paracellular ice dendrite initiating from one of the deflection points, as indicated by the arrow. The subsequent IIF event initiation location is indicated by the red asterisks. Scale bars represent 10 μm.

The cumulative frequency of IIF was measured as a function of temperature in single BPAEC cells adherent in circular islands of 20 μm (n = 111), 30 μm (n = 121) and 40 μm (n = 111) diameter. As pattern size increased, the mean temperature of IIF also increased (20 μm: -26.7 ± 0.8°C, 30 μm: -22.3 ± 0.8°C, 40 μm: -19.7 ± 0.5°C). The effect of cell attachment area on the mean temperature of IIF was found to be statistically significant ($p < 0.05$). In agreement with our previous results (Chapter 3), the majority of IIF initiation sites occurred at the cell periphery. As shown in Figure 4.4, as the cell diameter increased, the number of IIF events that initiated at the cell perimeter decreased. A linear regression was fit to the data in Figure 4.4, yielding a slope of -0.33 ± 0.6 %perimeter/μm, and a y intercept of 99 ± 6.2 % ($R^2 = 0.97$). Thus, the data suggests that as the cell perimeter is decreased, the percentage of IIF events that initiate at the cell periphery will approach 100%.

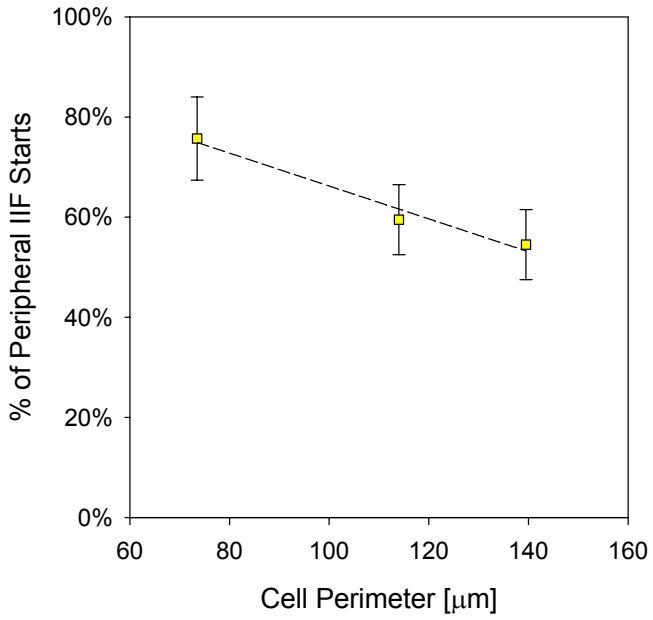

Figure 4.4 Percentage of IIF events that initiated at the cell periphery. Data are presented as percentage of the population ± SD. A linear regression (dashed line) was fit to the data. See text for details.

The primary objective of this study was to quantify the effects of cell size on the kinetics of IIF. Specifically, we were interested in testing the validity of surface-catalyzed nucleation (SCN) theory for attached cells. For the first time, we were able to measure the nucleation frequency of IIF events in attached cells, and quantify how that frequency varied with available contact area. As such, all IIF kinetic data were transformed to determine the overall kinetics of IIF for each cell attachment area. To make comparisons between data populations, the 20 μm diameter data population was selected as the reference case for this and all subsequent analyses in this chapter. The data transforms for all nucleation events are presented in Figure 4.5, with $P_{IIF}{}'_1{}'$ (*x-axis*) representing the 20 μm kinetics and $P_{IIF}{}'_2{}'$ (*y-axis*) representing the 30 μm kinetics (red symbols) and 40 μm kinetics (blue symbols). As discussed in the theoretical background,

if SCN was the dominant mechanism of IIF, as cell attachment area increased, the nucleation kinetics should increase proportionally to the ratio of attached cell areas (Equation 4.2). Conversely, if our hypothesized mechanism, peripheral initiation (PI), was the primary mechanism of IIF in attached cells, the nucleation kinetics should increase proportionally to the ratio of cell perimeters (Equation 4.4). Thus, to determine which model was a better fit with the data, a linear regression was applied to the data transforms in Figure 4.5. For all of our regression analyses, the linear portions of the transforms (the first 80% of the data) were used for the fits (closed symbols). The results of our regression analyses reveal that as cell diameter was increased from 20 μm to 30 μm, the slope of the kinetic transforms was 1.44 ± 0.04 (R^2 = 0.93). Additionally, when the cell diameter was increased from 20 μm to 40 μm, the slope of the kinetic transforms was 2.74 ± 0.03 (R^2 = 0.99). It can be seen in Figure 4.5 that the data transformed provided inconclusive results. If SCN were the dominant mechanism, the slopes of the regression lines should scale with the ratios of the attached cell areas (A_{30}/A_{20} = 2.4, A_{40}/A_{20} = 3.6). Likewise, if PI were the dominant mechanism, the slopes of the regression lines should equal the ratios of the cell perimeter (P_{30}/P_{20} = 1.55, P_{40}/P_{20} = 1.9). Furthermore, the results for the experimental conditions (30 μm and 40 μm) are not in agreement with one another. The 30μm transformed data (slope = 1.44), scales well with the measured ratio of perimeters (P_{30}/P_{20} = 1.55), and not with the ratio of areas (A_{30}/A_{20} = 2.4). In contrast, the 40μm transformed data (slope = 2.74) scales more closely with the ratio of areas (A_{40}/A_{20} = 3.6), than with perimeter (P_{40}/P_{20} = 1.9), but neither is a good fit.

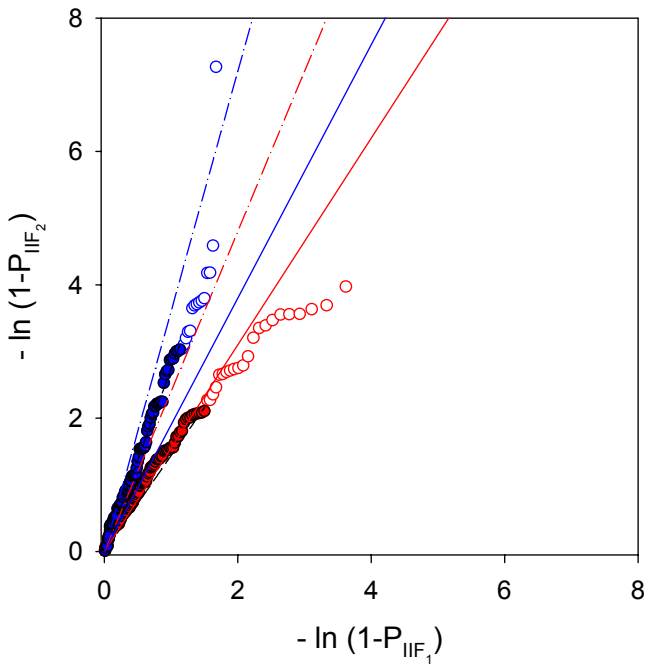

Figure 4.5 Data transform for all nucleation events, as cell size is increased. All IIF kinetic data were transformed with *PIIF '1'* (*x-axis*) representing the 20 µm kinetics and *PIIF '2'* (*y-axis*) representing the 30 µm kinetics (red symbols) and 40 µm kinetics (blue symbols). The first 80% of each data population was fit with a linear regression (dashed lines); data excluded from the fit (last 20%) is indicated by open circles. Reference lines are shown for the measured ratio of perimeters (P_{30}/P_{20} = 1.55, solid red line, P_{40}/P_{20} = 1.9, solid blue line) and for the measured ratio of areas (A_{30}/A_{20} = 2.4, dash-dot red line, A_{40}/A_{20} = 3.6, dash-dot blue line).

Previous results with the 20 μm data presented in Chapter 3 suggested that the IIF kinetics could be classified by two distinct data populations: cells in which IIF initiated at the cell periphery, and cells with dendrite-mediated initiation of IIF. Thus, to account for the discrepancies noted above, for each cell attachment area the data populations were divided into two populations: (i) IIF that initiated at the cell periphery, and (ii) IIF events that initiated at internal locations inside the cell. For all IIF events that initiated at the cell periphery, data were transformed using Equation 3.8. The results of the data transforms are presented in Figure 4.6, where the kinetics of periphery-initiated IIF events in the 20 μm diameter patterns are represented by $N_{periphery\ '1'}$ *(x-axis)*, and the 30 μm kinetics (red symbols) and 40 μm kinetics (blue symbols) are represented by $N_{periphery\ '2'}$ (*y-axis*). Looking at Figure 4.6, it can be seen that as available contact area increased, the kinetics of IIF events that initiated at the cell periphery increased. To quantify the increase in kinetics, linear regression analyses were conducted. For peripheral initiated IIF events, increasing the cell diameter from 20 μm to 30 μm resulted in a ~30% increase in nucleation kinetics (slope of regression was 1.31 ± 0.02 (R^2 = 0.99)); whereas increasing the cell diameter from 20 μm to 40 μm resulted in a two-fold increase in nucleation kinetics (slope of regression was 2.07 ± 0.04 (R^2 = 0.98)). Comparison of the regression line slopes indicates that for both data populations (30 μm and 40μm), the increase in nucleation kinetics correlates well with the ratio of cell perimeters (30μm/20μm: slope = 1.31 (P_{30}/P_{20} = 1.55); 40μm/20μm: slope = 2.07 (P_{40}/P_{20} = 1.9)).

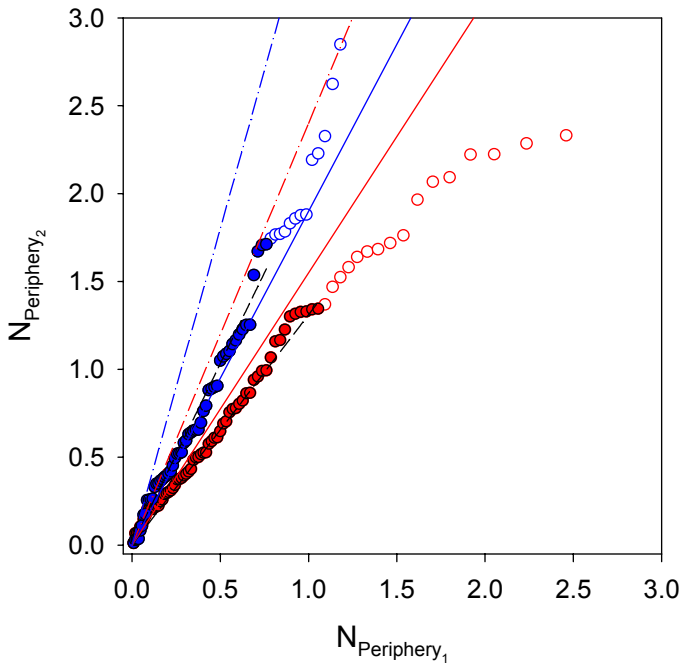

Figure 4.6 Nucleation kinetics for all IIF events that initiated at the cell periphery, as cell size is varied. For all IIF events that initiated all the cell perimeter, data were transformed using Equation 3.8. $N_{Periphery\ 1}$ (*x-axis*) represents the 20 µm kinetics and $N_{Periphery\ 2}$ (*y-axis*) represents the 30 µm kinetics (red symbols) and 40 µm kinetics (blue symbols). The first 80% of each data population was fit with a linear regression (dashed lines); data excluded from the fit (last 20%) is indicated by open circles. Reference lines are shown for the measured ratio of perimeters (P_{30}/P_{20} = 1.55, solid red line, P_{40}/P_{20} = 1.9, solid blue line) and for the measured ratio of areas (A_{30}/A_{20} = 2.4, dash-dot red line, A_{40}/A_{20} = 3.6, dash-dot blue line).

The phenomenon of paracellular ice dendrite formation was first presented in Chapter 3, where data were shown suggesting that these ice dendrites are a precursor to IIF in a subpopulation of cells. However, for the data presented in Chapter 3, only a small population exhibited paracellular ice. For the present study, as the contact area of the micropatterned cell increased, the percentage of paracellular ice dendrites that formed also increased. Figure 4.7 presents the percentage of the population (± SD) that exhibited paracellular ice dendrite growth as it varied with cell perimeter. As seen in Figure 4.7, the increase in paracellular ice events scales almost directly with the increase in cell perimeter. A linear regression applied to the data yields a slope of 0.29% para/cell perimeter (R^2 = 0.95). This results suggests that the frequency of paracellular ice formation exhibits a growth rate opposite of the percentage of IIF events that initiate at the cell periphery (Figure 4.4, slope of regression = -0.33 %perimeter starts/cell perimeter).

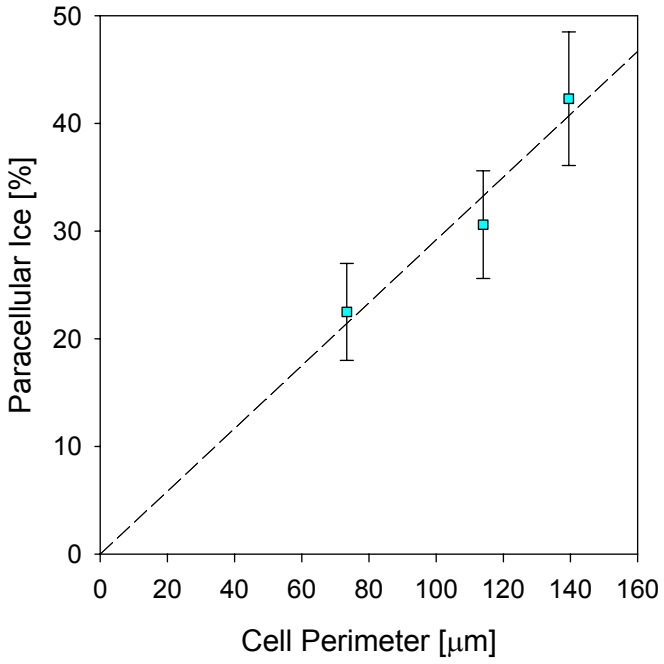

Figure 4.7 Frequency of paracellular ice dendrite formation as it relates to cell perimeter. For all cell patterns investigated (*ca*. 20, 30 and 40μm in diameter), the percentage of the cell population (±SD) that exhibited paracellular ice dendrites formation are presented.

Similar to our analysis in Chapter 3 (Figure 3.14), we investigated the temporal correlation between paracellular ice penetration and IIF. The 40 μm cell diameter data population had a significantly higher number of experiments that exhibited the paracellular ice phenomenon (42%, or 48 of 111 experiments had paracellular ice dendrite formation), and thus, was selected for this analysis. Unlike the 20 μm diameter cells, there were experiments in which multiple paracellular ice dendrites would form, each appearing at different locations around the cell. Figure 4.8 presents the relationship between the IIF initiation temperature and each paracellular ice penetration temperature for the 40μm cell diameter data. Horizontal bars were added to all data points that represent the span of recording time for each video; the left error bar represents the temperature at which the recording started, and the right error bar represents the temperature at the end of the video. These error bars were added so that the potential error due to post-IIF data truncation could be visualized. On average, 2.9 ± 0.3 s of video were acquired prior to IIF, whereas 0.7 ± 0.2 s of video were acquired after IIF. If paracellular ice dendrite formation were a random event, we would expect ~22% of the ice dendrites to appear after IIF. However, as shown in Figure 4.8, no paracellular ice dendrites were observed after IIF. In addition, comparable to our results in Figure 3.14, a correlation between the temperature at which the paracellular ice dendrites form and the subsequent temperature of IIF can be seen.

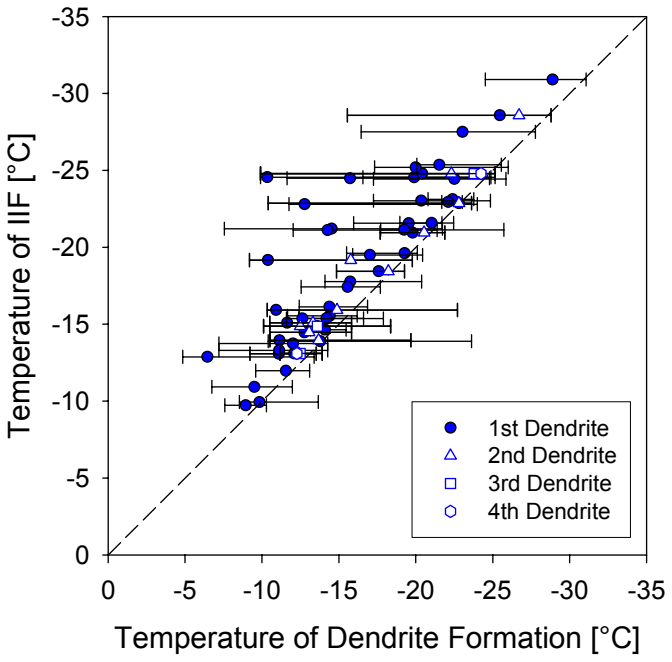

Figure 4.8 Paracellular ice penetration temperature as it relates to the temperature of IIF. Shown are the temperatures for the first (closed circles), second paracellular (open triangles), and third (open squares), and fourth (open hexagons) paracellular ice dendrites that formed for each experiment. Error bars represent data recording span.

Considering the evident correlation between the temperature of paracellular ice penetration and the subsequent temperature of IIF, we next analyzed the kinetics for all IIF initiation events that co-localized with paracellular ice dendrites. Co-localization was defined as all IIF events that initiated within 1.5 μm of the paracellular ice dendrite. For this data subpopulation, we transformed the nucleation events for the 20, 30 and 40μm diameter cells using Equation 3.8, and the results are presented in Figure 4.9. Again, the 20 μm cell kinetics were used as the reference data and are represented as $N_{para\ 1}$ (*x-axis*), whereas $N_{para\ 2}$ (*y-axis*) represents the transformed 30 μm (red symbols) and 40 μm (blue symbols) kinetics for IIF events that co-localized with IIF. It can be seen in Figure 4.9 that as the cell diameter increased the kinetics of IIF events that co-localized with paracellular ice dendrites also increased. Regression analysis indicates that as the cell diameter is increased from 20μm to 30μm, the kinetics increased by a factor of ~2.2 (slope of regression was 2.16 ± 0.24 (R^2 = 0.89)). Likewise, as the diameter of the cells was increased from 20μm to 40μm, regression analysis indicates the kinetics increased by a factor of ~3.5 (slope of regression was 3.50 ± 0.20 (R^2 = 0.97)). These results indicate that the size dependence of the slope is stronger than a simple direct proportionality with cell perimeter (as previously seen in Figure 4.6). The underlying rate between the data populations appears to scale approximately with attached cell area (A_{30}/A_{20} = 2.4, and A_{40}/A_{20} = 3.6).

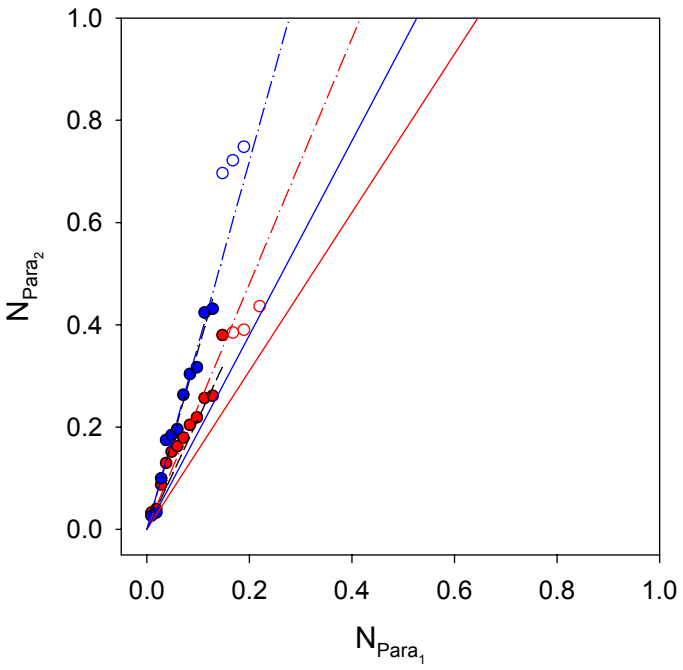

Figure 4.9 Nucleation transform for all IIF events that co-localized with paracellular ice dendrites. For all IIF events that initiated within 1.5um of the paracellular ice dendrite, data were transformed using Equation 3.8. $N_{Para\ 1}$ (*x-axis*) represents the 20 µm kinetics and $N_{Para\ 2}$ (*y-axis*) represents the 30 µm kinetics (red symbols) and 40 µm kinetics (blue symbols). The first 80% of each data population was fit with a linear regression (dashed lines); data excluded from the fit (last 20%) is indicated by open circles. Reference lines are shown for the measured ratio of perimeters (P_{30}/P_{20} = 1.55, solid red line, P_{40}/P_{20} = 1.9, solid blue line) and for the measured ratio of areas (A_{30}/A_{20} = 2.4, dash-dot red line, A_{40}/A_{20} = 3.6, dash-dot blue line).

In Chapter 3, we had hypothesized that paracellular ice dendrites were penetrating the paracellular space that existed between the basal cell membrane and the substrate. The ability of ice to grow into the paracellular space requires the presence of gaps between the focal adhesion clusters that typical exist along the periphery of adherent cells. In the present study, a two-fold increase in paracellular ice dendrite formation was seen as cell diameter was increased from 20μm to 40μm. Thus, we next investigated the spatial location of focal adhesion proteins in our micropatterns to determine if any differences existed between the cell patterns. Live cell imaging of focal adhesions was conducted using interference reflection microscopy (IRM). As Figure 4.10 shows, focal adhesions appear as dark clusters in IRM images, resulting from their close proximity to the substrate[129]. As expected, focal adhesions were predominantly located at the cell perimeter, with some punctuated dark regions in the central locations of the cell. In approximately 25% of the cells imaged with IRM, distinct gaps were seen in the focal adhesions along the cell periphery. Having confirmed that clear breaks existed between focal adhesion clusters in living micropatterned cells, (and that they were not an artifact of cell fixation) the remainder of our focal adhesion analysis was done using immunohistochemistry techniques on fixed micropatterned cells.

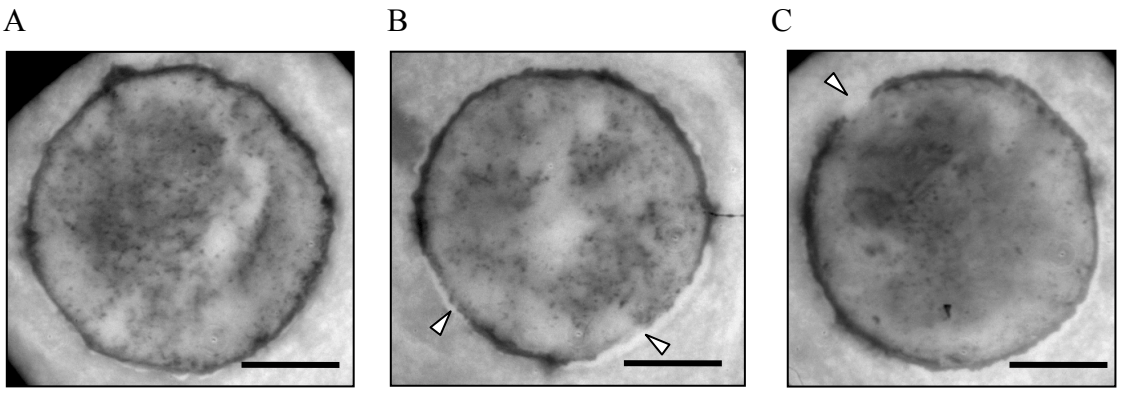

Figure 4.10 IRM images of BPAECs in agarose micropatterns. Micrographs of three representative living cells in 30μm agarose patterns. Focal adhesions were visible at the peripheral edges of the pattern (areas of dark intensity), with the majority of the cells exhibiting a fairly solid band around the entire perimeter (A). However, in some cells (B) small gaps could seen, as indicated by the arrows. In approximately 25% of the population, sizable gaps were evident (C). All scale bars represent 10 μm.

Immunofluorescence staining for the focal adhesion protein vinculin was conducted for all attached cell diameters (20, 30 and 40μm), and analyzed in quantities similar to our cryomicroscopy experiments (20 μm, n = 97; 30 μm, n = 109, and 40 μm, n = 102). The protein vinculin[135] has been shown to be one of the first intercellular molecules recruited to focal adhesions[136], and as such, was selected as a marker for focal adhesion formation[135] in our micropatterned cells. The samples were also stained for actin stress fibers (F-actin), as well as the cell nucleus. Representative micrographs from the 30μm patterns can be seen in Figure 4.11. All images were analyzed using a custom LabView program, quantifying the dimensions of the gaps between focal adhesion clusters, as well as the focal adhesions themselves. A conservative measurement threshold was applied to all data, considering only measurements that were greater than or equal to five pixels, or 0.5 μm. This measurement limit was selected to be roughly

twice the optical resolution of our system. The Rayleigh criterion for a self-luminous body (fluorescent signals) predicts that using a 1.4 NA 100X objective at a wavelength of 530nm (green fluorescence) the optical resolution of our system is 0.22 μm. This resolution does not consider any additional benefits gained from signal deconvolution through image processing. As such, applying our measurement threshold, the average number of gaps (≥ 0.5μm) per cell was quantified for all cell sizes, with the results presented in Figure 4.12. It can be seen that as the cell perimeter increased, the average number of gaps of this size class per cell significantly increased ($p < 0.05$). The results of the linear regression for the data were: slope = 0.123 ± 0.04 #gaps/cell perimeter and $y_0 = -1.13 \pm 1.76$ ($R^2 = 0.98$).

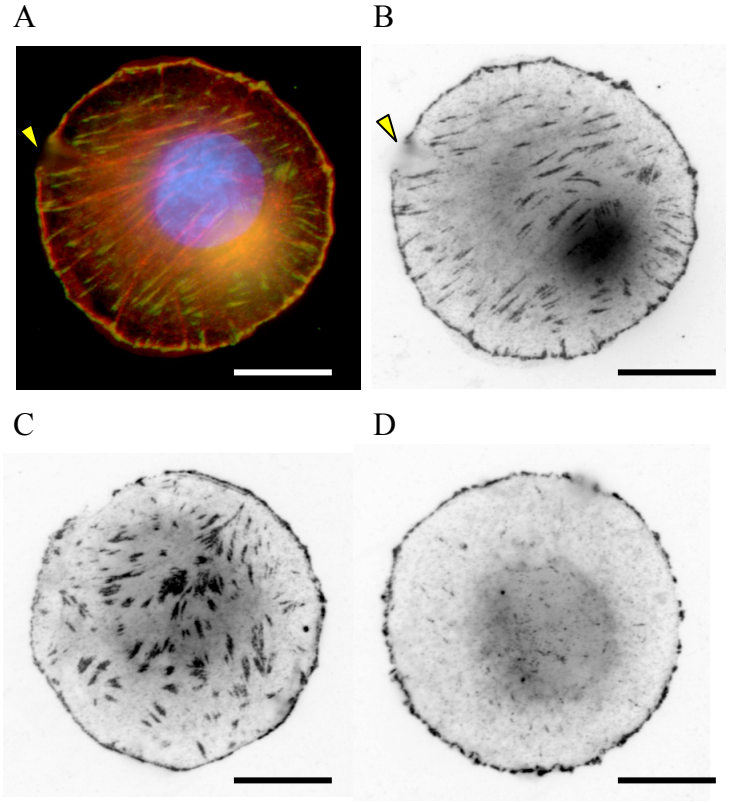

Figure 4.11 Immunofluorescent staining of BPAECs in micropatterns. (A) Pseudo-colored micrograph of an endothelial cell in a 30μm micropattern, displaying all three fluorescent signals captured: red (F-actin), green (focal adhesion protein, vinculin) and blue (nucleus). (B) Inverted image of the green fluorescence signal isolated from image (A). A large gap in vinculin staining is visible in (A) and (B) (indicated by arrows), which is approximately the same size as the gap seen in the living cell image (Figure 4.10C). Additional micrographs of vinculin staining are shown (C) and (D) to demonstrate the variability in focal adhesion formation as well as the frequency of breaks in staining patterns. All scale bars represent 10μm.

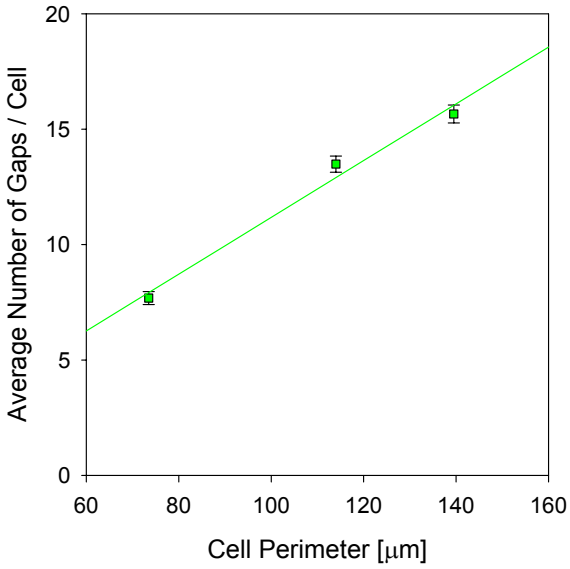

Figure 4.12 Frequency of gaps between peripheral focal adhesion proteins in micropatterned cells. The average number of gaps of length ≥0.5 μm between focal adhesion clusters was calculated from immunofluorescent images; data are presented as the mean ± SEM. As the cell perimeter increased, the average number of gaps per cell increased. A regression line was fit to the data (solid green line).

Having determined that that the average number of gaps between focal adhesion clusters increased as cell perimeter increased, we next quantified the size of these gaps for the 20, 30 and 40μm data populations. Figure 4.13A displays the average gap length as a function of cell size, showing that average lengths were approximately 1 μm for each size. Analyzing the data with a 1-way ANOVA, there was no statistically significant effect of cell attachment area ($p > 0.05$). We also measured the average area of the focal adhesion clusters ≥ 0.25 μm^2 (5 pixel x 5 pixels) and the results can be seen in Figure 4.13B. The focal adhesion clusters in the 20μm diameter cells were significantly larger ($p < 0.05$) than the clusters in the 30 and 40 μm diameter cells. However, there was no

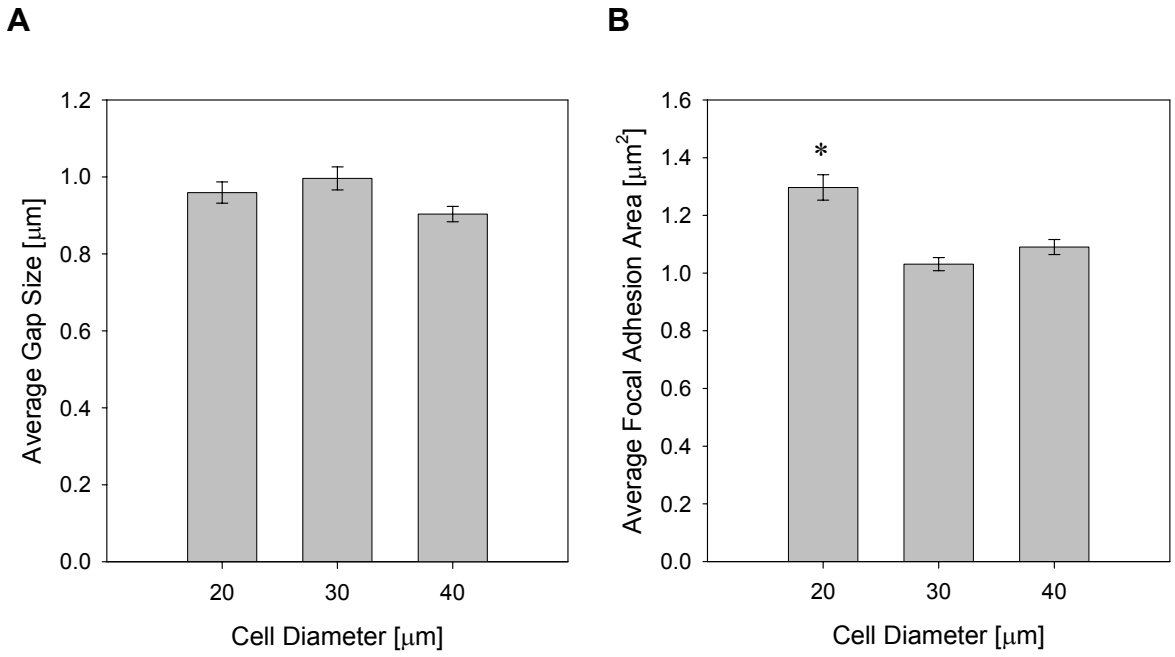

Figure 4.13 Differences in gaps size and focal adhesion area as cell diameter increases. (A) The average gap size between focal adhesion clusters is statisically similar for all three cell sizes ($p > 0.05$). (B) The average segment area (representing positive staining for vinculin) along the perimeter of the cell was significantly larger for the 20μm data population in comparison to the 30μm and 40μm data groups ($p < 0.05$). However, there are no statisical differences between the 30μm and 40μm data groups ($p = 0.389$). Statistical significance ($p < 0.05$) is indicated by (*).

statistical difference in the average adhesion cluster area between the 30 and 40μm ($p = 0.389$). Thus, data indicates that while the average number of gaps between focal adhesion clusters increases as cell perimeter increases, the size of both the gaps and the area of the focal adhesion clusters stays approximately the same.

To conlude our analysis, we wanted to test our theory that the nucleation rate in single attached cells could be described by two independent mechanisms of IIF. We believe that both mechanisms resulted from extracellular ice interacting with the attached cell, but in separate, distinct ways. For all IIF events that initated at the cell periphery (refered to as 'PI'), as the available cell attachment area was increased, the initiation frequency of IIF scaled with the ratio of cell perimeters (Figure 4.6). A second mechanism of IIF was also evidenced in our data, in which an ice dendrite would form from the extracellular ice, penetrating the supercooled space between the cell and the substrate. For the majority of cases, this ice dendrite would co-localize with the IIF initiation point. We classified this mechanism of IIF as dendrite-mediated initiation (DMI), and the kinetics of IIF were shown to scale approximately with attached cell area (Figure 4.9). Thus, we can predict the rate of IIF initiation for both mechanisms as cell size is increased:

$$n_{PI\,2} = \frac{P_2}{P_1} n_{PI\,1} \tag{4.5}$$

and

$$n_{DMI_2} = \frac{A_2}{A_1} n_{DMI\,1} \tag{4.6}$$

where n_{PI1} and n_{DMI1} are calculated from experimental data for the 20 μm cells using Equation 3.8, P_1 and P_2 are the cell perimeters, and A_1 and A_2 are the cell attachment areas, where the subscript '*2*' refers to the larger cell sizes (*i.e.*, the 30 μm and 40 μm diamter cells). Using Equation 3.1, assuming that the two mechanism of IIF are independent, the probability of IIF can be written as:

$$P_{IIF\ 2} = 1 - \exp^{-(n_{PI\,2} + n_{DMI_2})} \tag{4.7}$$

Substituting Equations 4.5 and 4.6 into Equation 4.7, we can predict the probability of IIF as the cell attachment area increases:

$$P_{IIF\ 2} = 1 - \exp^{-(\frac{P_2}{P_1} n_{PI\,1} + \frac{A_2}{A_1} n_{DMI_1})} \tag{4.8}$$

Using only the 20μm diameter IIF data, the probability of IIF was predicted for the 30 μm and 40 μm population using Equation 4.8. The results of that prediction, along with the actual experimental results, are shown in Figure 4.14. As an intitial test of our model, we predicted the probability of IIF for the 20 μm data population (green line). In comparison with the corresponding 20 μm experimental data (green circles), Chi-squared analysis indicates that the data and model predictions are statistically similar ($p > 0.1$). In Figure 4.14, a slight discrepancy can be detected between the predicted and experimental 20 μm data. This can be explained by the fact that for a small portion of our data population (~8%), extracellular ice obscured the view of the cell during the experiment. Because these events were neither classified as "PI" nor "DMI", they were excluded from

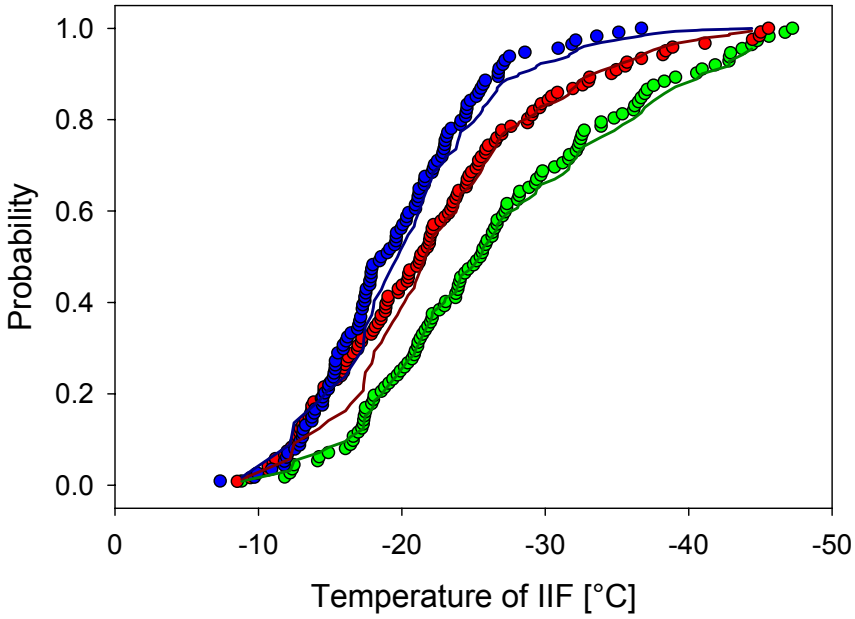

Figure 4.14 Prediction of IIF kinetics in micropatterned endothelial cells. Using only the data from the 20µm cell diameter population (solid green circles), the probability of IIF was predicted for 20µm (dark green line), 30µm (dark red line) and 40µm (dark blue line) cell diameters. The corresponding experimental data (obtained using high speed cryomicroscopy) is also presented (30µm, solid red circles, and 40µm, solid blue circles) for comparison. See text for details.

the caclulated values of n_{PII}, and n_{DMII} in Equation 4.8. Looking at the predictions for the 30 μm and 40 μm diameter cells, it can be seen that our model predictions closely match the corresponding experimental results, with the predictions determined to be statistically similar to the corresponding data ($p > 0.1$). Thus, the agreement between our model predictions and our experimental results (Figure 4.14) supports our hypothesis that the kinetics of IIF in single attached cells can be modeled as two independent mechanisms of IIF initiation, namely peripheral initation and dendrite-mediated initiation.

4.5 Discussion

This study investigated the effect of cell attachment area on the kinetics of IIF in single attached cells, and was motivated in part by data in Chapter 3, which demonstrated that for one cell size (20μm diameter), the majority of IIF events initiated at the cell perimeter. This result was inconsistent with the most commonly accepted theory of ice nucleation in biological cells, surface-catalyzed nucleation (SCN)[23]. SCN posits that IIF results from interactions between the extracellular ice and the plasma membrane of the cell and that the corresponding nucleation rate therefore scales with available surface area[23]. Thus, since the extracellular ice crystals have access to the entire apical surface of an attached cell, if SCN were the dominant mechanism of IIF in this system, we would expect the IIF initiation sites to be uniformly and randomly distributed over the entire cell area. This was not the case for the 20μm data presented in Chapter 3. The studies presented in the present chapter investigated if this result was specific a particular cell diameter (20 μm), or if it consistently scaled with increasing cell dimensions. For the

first time, the effect of cell attachment area on IIF kinetics was directly measured, providing data that could be compared with the predictions of SCN theory.

Our data indicate that as cell diameter increased, the probability of IIF increased, suggesting that the larger the cell attachment area, the more susceptible the cell will be to freezing injury. Previous results in Chapter 3 suggested that the IIF kinetics could be classified by two distinct populations: IIF events that initiated at the cell edge, and IIF events that co-localized with paracellular ice dendrites. Categorizing the data as such, our data indicated that for IIF events that initiated at the cell periphery, the kinetics of IIF could be described by an underlying rate that was directly proportional to cell perimeter. This result is significant because it strongly suggests that SCN theory[23] does not accurately describe the kinetics of IIF in attached cells.

Studying micropatterned NIH3T3 fibroblast, Gallant *et al*.[99] recently derived a quantitative relationship between cell adhesive area and the recruitment of focal adhesion components. In their study, a saturation level was evident for both cell adhesion strength and focal adhesion recruitment as cell size was increased. Spatial organization of focal adhesion clusters was shown to be strongly regulated by cell attachment area, and above a critical value (10μm-diameter circles for NIH3T3 cells) cell adhesive area was no longer limiting, allowing integrins to arrange in discrete clusters surrounded by regions with low integrin packing[99]. Our immunofluorescent staining results for the focal adhesion protein vinculin indicate similar trends. Analysis of the spatial location of focal adhesions in our micropatterns demonstrated that the average number of gaps between focal adhesions per cell increased proportionally to the increase in perimeter. We can hypothesize that for our BPAEC micropatterns, as the available attachment area

increases, the focal adhesions redistribute along the cell periphery to maintain a constant adhesion state. Our analysis also indicates that the average area of the focal adhesion clusters along the cell periphery was statistically similar between the 30μm and 40μm data populations. Thus, it is reasonable to hypothesize that as a consequence of this focal adhesion re-distribution, a higher number of gaps or breaks will result between the focal adhesion clusters, due to having reached the saturation level of available cell receptors.

Interestingly, this redistribution of focal adhesion proteins (and subsequent gap formation) correlated with the increase in kinetics for IIF events that initiated at the cell periphery. Thus, we hypothesize that the peripheral IIF initiation mechanism is associated with gaps in the perimeter. While it is beyond the scope of this study to investigate establish the complete mechanisms of peripheral initiation of IIF, qualitative evidence is seen during freezing that suggests the involvement of mechanical interactions between the extracellular ice and the membrane spanning the gaps between focal adhesion clusters. During freezing, localized points along the edges of the cell were observed to deflect during cooling (Figure 4.3). It is possible that IIF is initiated as a result of local rupture of the membrane, caused by such deflection.

Extracellular ice has been known to have a role in IIF, for between the temperature range of -5°C and -15°C, IIF will only occur in the presence of extracellular ice[23,44]. Compared to single suspended cells, adherent cells would be more susceptible to the forces from the advancing extracellular ice, considering that motion and deformation of suspended cells are not constrained by attachment to a fixed substrate and that tension in the membrane and cytoskeleton is increased in attached cells[120-122]. Evidence of extracellular ice interacting with the cell membrane during freezing has also been

previously reported[41,72,105]. During freezing of suspended red blood cells, Ishiguro and Rubinsky[41] reported that cells were pushed into channels that form between the dendritic extracellular ice crystals, and were eventually deformed by the advancing extracellular ice. They further reported a correlation between cell survival and the nature of mechanical interactions between the cell and extracellular ice[41]. Recently, Mazur *et al.*[105] reported that oocytes were physically distorted by extracellular ice during freezing, and when frozen without cryoprotectant additives, this deformation was thought to result in membrane damage. Mazur *et al.* further hypothesized that IIF may be related to the deformation of the cell surface by extracellular ice[105]. Considering the data from this study and the supporting literature, we postulate that as the extracellular ice grows, it pushes against the attached cell membrane, that there is a maximum force that the membrane can withstand before rupture results. When this limit is breached, the barrier between extracellular ice and the supercooled cytoplasm is removed and IIF is initiated.

The spacing of focal adhesion proteins was also shown to correlate with the frequency of paracellular ice dendrite formation. As cell perimeter increased, the percentage of cells that exhibited paracellular dendrite formation increased proportionately. Similar to our results in Chapter 3, a strong correlation was shown between the paracellular ice penetration temperature and the temperature of IIF. Pore theory was previously applied to our data (see Chapter 3), demonstrating that the observed temperature range of paracellular ice penetration was consistent with the predicted rang in which it is thermodynamically favorable for extracellular ice to initiate ice growth into the paracellular space. In the present study, the increase in paracellular ice formation can be readily explained by the increase in the number of gaps between

focal adhesion proteins. In other words, the more available gaps along the cell perimeter, the higher the probability for ice dendrite growth to initiate.

While the frequency of paracellular ice penetration correlated with cell perimeter (or number of available gaps), the kinetics of IIF for events co-localized with paracellular ice did not scale with perimeter as cell attachment area increased. Rather, the data indicated that as the micropatterned cell diameter increased, the rate of IIF initiation increased proportionally to the cell attachment area. We can hypothesize that the paracellular ice dendrite may physically interact with the basal membrane causing rupture, or a mechanism similar to SCN could be occurring where the ice produces a change in the membrane, creating a catalytic site for ice nucleation. It is important to note that as cell diameter increased, a significant increase in paracellular ice dendrite formation occurred. For the 40 μm diameter patterns, multiple paracellular dendrites were shown to form prior to IIF, with 42% of all experiments exhibiting paracellular ice formation. For large attached cells, this potential precursor to IIF is no longer a small portion of the population. Further investigation is required to fully understand the mechanisms and events that drive this phenomenon.

Ultimately, studies such as these provide the greatest utility if the results can be used to accurately predict the kinetics of IIF in attached cells. Our data suggest that two distinct mechanisms of IIF are active in attached endothelial cells. One of these mechanisms, peripheral initiation, scales directly with cell perimeter. The second mechanism, dendrite-mediated initiation, scales roughly with cell attachment area and is preceded by the growth of an extracellular ice dendrite into the paracellular space of the attached cell. From the results obtained in this study, we developed a semi-

phenomenological model to predict the probability of IIF due to the two proposed mechanisms of IIF. Using only the data from the 20μm-diameter experiments, we predicted the kinetics of IIF as the attached cell diameter increased. Comparison of our prediction with the actual measured data shows good agreement, lending support to our two-mechanism hypothesis.

In conclusion, this study has provided evidence to suggest that SCN is not the dominant mechanism of IIF in single attached cells. A semi-phenomenological model was created to predict the kinetics of IIF as cell attachment area increased and when compared to experimental data it was shown to accurately predict the kinetics. Findings such as these are critical to increasing our understanding of the underlying mechanisms and events that lead to IIF in cells and tissues. These results will also assist in the development of theoretical models of nucleation in attached cells, thus facilitating rational cryopreservation protocol design for adherent cells and tissues.

CHAPTER 5

EFFECT OF LIGAND DENSITY AND TIME IN CULTURE ON IIF IN MICROPATTERNED ENDOTHELIAL CELLS

5.1 Introduction

Cell adhesion is a time sensitive process that is driven by receptor mediated interactions with the extracellular matrix (ECM). During the early stages of adhesion, cells will actively shape the matrix around them, with the process controlled both globally and locally by specific regulatory pathways[128]. The development of focal adhesions begins with the binding of activated membrane-bound integrin receptors to ECM ligands (such as fibronectin)[127,137]. Once bound, these receptors will interact with a diverse set of cytoplasmic proteins, resulting in the polymerization of actin. As a consequence, focal adhesion proteins, such as vinculin and talin, are activated and rapidly associate with the cell membrane to form focal complexes. In turn, this response increases intracellular tension, driving focal adhesion development[128]. Previous work, presented in Chapter 4, investigated the effect of cell attachment area on the kinetics of IIF. It was found that as cell size increased, cells were more susceptible to intracellular ice formation, and that the rate of the dominant mechanism of IIF appeared to be proportional to the number of gaps between focal adhesions at the cell perimeter. Thus, we are now interested in maintaining a constant cell size, but varying one of the many parameters that can influence the size and spacing of focal adhesions. Specifically, the parameters investigated were time in culture and ligand coating density.

Formation of focal adhesions is a complex process that has very specific temporal steps. For endothelial cells, these steps occur in rapid succession, with focal adhesion proteins such as vinculin, detectable within 60 minutes post-seeding[82,83]. The relationship between focal adhesion formation and adhesion strengthening has been shown[99,138]. Recently, Reinhart-King *et al.*[82] investigated the time course of actin polymerization and the appearance of stress fibers in bovine endothelial cells cultured on fibronectin-coated substrates. Their results indicated that total filamentous actin (F-actin) levels increased during spreading and peaked after 3 hours in culture, with stress fibers not appearing until 2-3 hours post-plating. This peak was followed by a decrease to steady state F-actin values at 24 hours[82]. In the field of cryobiology, time in culture has also been shown to influence post-thaw viability[139,140]. Thus, to investigate the effect of culture time on IIF in attached cells, two time points were selected: 3 hours ± 30min (peak F-actin levels, low levels of focal adhesion clustering), and 6 hours ± 30min (decreased F-actin levels, more advanced focal adhesion clustering). Due to the short doubling time of our cells (~15 hours), longer time frames were not feasible, for we could no longer guarantee the cell evaluated was not a recently divided cell, and as such, would have a significantly lower time in the attached state.

Several studies have investigated the effects of ligand coating density on cell attachment and spreading[141,142]. Reinhart-King *et al*.[82] reported that at low ligand coating densities (1 μg/mL), very little vinculin clustering was evident at 24 hours post-seeding. Variations in ligand coating density have also been shown to increase cell adhesion properties. García *et al*. [143] reported increased adhesion strength in K562 cells as fibronectin coating density on bare glass was increased. While the effect of fibronectin

coating density has been investigated in standard culture, few studies have investigated the effects of ligand coating density in micropatterned substrates[99]. Often, to promote full spreading of the cell in the pattern, saturation levels of the adhesion ligand are be used[101]. Whereas ligand coating density is often varied in cell attachment and adhesion assays, we are not aware of any reports of the effects of ligand density during cryopreservation of attached cells or tissues.

In this study, the effects of culture time and fibronectin coating density of IIF were quantified using high speed cryomicroscopy. Previously we have shown that the probability of IIF in attached cells can be decreased by reducing cell attachment area. However, reducing cell attachment area is not always a feasible strategy in tissue design. For example, human endothelial cells have been shown to enter an apoptotic pathway as a consequence of culture on micropatterned islands less than 10μm in diameter[144]. Thus, by investigating additional parameters that can be varied in tissue engineered products, such as ligand coating density and culture time, potentially novel strategies can be identified to reduce IIF during cryopreservation. Additionally, the knowledge of how these two parameters influence ice formation will further elucidate the primary mechanisms of IIF in attached cells.

5.2 Theoretical Background

5.2.1 Paracellular Ice Penetration and Dendrite-Mediated Initiation of IIF

In Chapter 4, the frequency of paracellular ice penetration was shown to correlate with the number of gaps between focal adhesion clusters at the cell periphery. However,

the rate of initiation of IIF events that co-localized with the paracellular ice dendrites was shown to scale by a factor larger than the ratio of cell perimeters. Thus, to further investigate the kinetics of IIF events that co-localized with paracellular ice dendrites, we modeled the process of dendrite-mediated IIF initiation as a two-step process: (i) the initial penetration of the paracellular dendrite, and (ii) the subsequent initiation of IIF near the dendrite.

The first step of the process, the penetration of an ice dendrite into the paracellular space, was assumed to follow a Poisson process, with a time-dependent rate, *J(t)*. Thus, during freezing, the cumulative probability of paracellular ice penetration, P_{PIP}, is given by[23]:

$$P_{PIP}(t) = 1 - \exp\left[-\int_0^t J_{PIP}(t)dt\right] \tag{5.1}$$

Thus, we can define the cumulative intensity function of the Poisson process as follows:

$$n_{PIP(t)} = \int_0^t J_{PIP}(t)dt = -\ln\left(1 - P_{PIP}(t)\right) \tag{5.2}$$

The experimentally obtained kinetics of paracellular ice penetration can be used to estimate $P_{PIP}(t)$ by keeping a running tally of the cumulative number of cells in which paracellular ice was observed (N_{PIP}), relative to the entire population of cells (N) :

$$P_{PIP}(t) = \frac{N_{PIP}(t)}{N} \tag{5.3}$$

Thus, knowing the probability of paracellular ice penetration, Equation 5.2 can be written to express the cumulative intensity function, $n_{PIP:}$

$$n_{PIP}(t) = -\ln\left(1 - \frac{N_{PIP}(t)}{N}\right) \tag{5.4}$$

Once the paracellular ice dendrite has formed, the second step of the process, dendrite-mediated initiation (DMI) of IIF, was assumed to at its own independent rate. To model the kinetics of DMI, a similar approach was taken to the theory presented in Chapter 3. Thus, to predict the nucleation rate of dendrite-mediated IIF events, n_{DMI}, at a time t, Equation 3.8 can be re-written as:

$$n_{DMI}(t) = \frac{1}{2}\sum_{i=1}^{N_{DMI}(t)}\left(\frac{1}{N_u(t_i^-)} + \frac{1}{N_u(t_i^+)}\right) \tag{5.5}$$

where N_{DMI} is the number of IIF initiation for events that co-localized with the paracellular ice dendrite, $N_u(t)$ is the number of unfrozen cells at time t, and the superscripts '-' and '+' indicate limiting values approaching from the left and from the right, respectively.

5.3 Materials and Methods

5.3.1 Bovine Pulmonary Artery Endothelial Cell Culture

Bovine pulmonary artery endothelial cells (BPAECs) (Cambrex, San Diego, CA) were cultured in MCDB 131 media (Mediatech, Herndon, VA) supplemented with 5%

(v/v) fetal bovine serum (Sigma-Aldrich, St. Louis, MO), 2ng/mL basic human fibroblast growth factor (PeproTech, Rocky Hill, NJ), 10ng/mL human epithelial growth factor (Invitrogen Corp., Carlsbad, CA), 1ng/mL vascular endothelial growth factor (Sigma-Aldrich), 2 ng/mL insulin-like growth factor-1 (Invitrogen), 0.001 mg/mL hydrocortisone (Sigma-Aldrich), 2mM L-glutamine (Mediatech), 100U/mL penicillin/100µg/mL streptomycin (Invitrogen), and 50µg/mL ascorbic acid (Sigma-Aldrich). Cells were cultured on tissue culture plastic at 37°C in a humidified 5% CO_2 environment and media were replaced every 48 hours. Flasks where subcultured when they reached 70-85% confluency and were split at a 1:6 ratio, following the recommendations of the vendor (total exposure time to trypsin-EDTA (Cambrex, Cat# CC-5012) was 5 minutes). For all experiments cells were used at passages 5 through 9.

5.3.2 Fabrication of Micropatterned Substrates

Agarose micropatterned glass coverslips that contained adhesive and non-adhesive domains were fabricated using methods adapted from a technique developed by Nelson and Chen[81]. Full details of the technique can be found in Chapter 3. Briefly, a poly(dimethylsiloxane) (PDMS) (Sylgard 184, Superior Essex, Atlanta, GA) stamp was generated from a silicon master that contained an array of 20µm diameter circular wells. The use of the silicon master was generously donated by A. García (Georgia Institute of Technology), with fabrication previously described [99]. The PDMS stamp was placed, patterned side down, against a 12 mm diameter glass coverslip (#1.5, Fisher Scientific, Suwanee, GA) such that only the raised 20 µm diameter posts were in contact with the coverslip. A small volume of 100% ethanol (~5µL) was pre-wicked into the 'mold' created by the PDMS stamp and the coverslip. After the ethanol dried, a solution of 0.6%

agarose (Invitrogen)/40% ethanol in water was heated while stirring to the boiling point, and dispensed along the edge of the stamp/coverslip mold. The agarose was allowed to dry undisturbed at room temperature for approximately two hours. The PDMS stamp was then carefully removed, resulting in a coverslip with bare glass islands surrounded by agarose. Substrates were sterilized in 70% ethanol/30% diH_20, rinsed twice with DPBS and incubated (37°C, 5% CO_2) for 30 minutes to 12 hours until coated with adhesion ligand.

For fibronectin concentration studies, micropatterned coverslips were incubated (37°C, 5% CO_2) for one hour in a solution of either 25µg/mL ('high' concentration), or 0.2µg/mL ('low' concentration) human-plasma fibronectin (FN, Invitrogen) in DPBS. After incubation, the fibronectin solution was aspirated off and the coverslips were rinsed twice in DPBS, 5 min each wash. Coverslips were then incubated for one hour in a 1% solution of heat denatured bovine serum albumin (BSA, Sigma-Aldrich) in DPBS. Following this, coverslips were rinsed twice in DPBS and stored in the incubator in DPBS until use. For the time-course studies (3 and 6 hours), all coverslips were coated with the high density of FN (25µg/mL), with no BSA blocking. For all conditions evaluated, an early apoptosis detection kit (Yo-Pro1, Molecular Probes) was used in conjunction with a live/dead assay (Molecular Probes) utilizing calcein AM and ethidium homodimer.

5.3.3 Sample Preparation

For cryomicroscopy experiments, BPAECs were subcultured and seeded onto patterned coverslips, and incubated (37°C, 5% CO_2) for 3hours ± 30min or 6 hours ± 30min post-seeding. Coverslips were incubated for 10 min at 37°C with

medium supplemented in 2 μM SYTO13 (Molecular Probes, Eugene, Oregon), a nucleic acid stain, and 10 μM ethidium homodimer (EthD-1) (Molecular Probes), a membrane impermeant stain, to ensure that each micropattern contained a single cell with full membrane integrity. Immediately prior to freezing, coverslips were rinsed with in 30 mM HEPES (Cambrex). For all experiments, the cell culture coverslip was removed from the petri dish, inverted, and placed on a 16 mm diameter glass coverslip (Linkam Scientific Instruments, Tadworth, Surrey, UK), creating a sandwich.

5.3.4 High Speed Digital Video Cryomicroscopy

A novel high-speed video cryomicroscopy system was created to observe IIF at sub-millisecond time scales in single attached cells. Full details of the system can be found in Chapter 3. Briefly, the system consisted of an upright Eclipse ME600 microscope (Nikon, Tokyo, Japan) fitted with a commercially available cooling stage (FDCS 196, Linkam). System calibration was conducted by measuring the melting point of ice crystallized from a sample of purified water. Experiments were recorded using a high speed digital camera (FastCam-X 512PCI, Photron, Tokyo, Japan) and corresponding software (FastCAM Viewer, version 2.2; Photron).

For all experiments, images were acquired at a rate of 8,000 Hz, with an exposure time of 100 μsec. Maximum recording time was limited to approximately eight seconds with the settings used. For all high speed experiments, cells were observed using a 50X objective and 0.45X coupler (Nikon). To meet the light level requirements for high-speed imaging, all samples were frozen under Köhler illumination, with the microscope halogen lamp set to maximum output.

To promote IIF, cell cultures were frozen at a rapid rate (130°C/min) in the absence of cryoprotectants. Samples were prepared as described above, and placed in the sample holder located directly on top of the silver block, set to 37°C. After closing the cryostage chamber, the atmosphere was purged using liquid nitrogen vapor to prevent condensation. To seed extracellular ice, the sample temperature was cooled from 37°C to -1.5°C (at 50°C /min), and repositioned such that the edge of the sample was brought into contact with a seeding block (a silver block integrated into the cryostage stage and cooled to the temperature of the liquid nitrogen). Immediately after seeding the extracellular ice, the sample was repositioned on the silver block and a cell was randomly selected for the experiment. Prior to the temperature plunge, both brightfield and fluorescent images were taken of the sample, to ensure that each pattern contained exactly one cell (nucleic acids stained by SYTO 13) with full membrane integrity (negative for Eth-Homo1 uptake). For all experiments, the focal plane of camera was set to the basal area of the attached cell. Prior to the temperature plunge, both brightfield and fluorescent images were taken of the sample. To minimize dehydration of the sample, the extracellular ice seeding, cell selection and imaging were performed in approximately 60 seconds. If this process took longer than three minutes, the experiment was abandoned. Immediately prior to the temperature plunge, the halogen lamp was set to maximum output, and the stage was cooled to -60°C at a controlled rate of 130°C/min. The high speed camera was set to record images into a circular buffer, and recording was terminated using a manual switch-closure trigger. When conventional indicators of intracellular ice formation (i.e. cell darkening and/or twitching) were observed, the trigger switch was closed, allowing

the IIF event to be captured. Each experiment was analyzed frame-by-frame to identify the precise time, temperature and initiation site of the IIF event.

5.3.5 Paracellular Ice Analysis

Microscale ice dendrites, which we classified as paracellular ice, exhibited slow growth rates that could not be quantified in the same manner as the IIF front (*i.e.* frame-by-frame playback with a distinct starting point). Thus, the start of the paracellular ice initiation was determined by reverse playback of the video at a frame rate of 125Hz (approximately 1.6% of real-time). When the dendrite disappeared from view, the playback would be stopped and the frame number recorded. This method was repeated in triplicate and if the resulting frame varied by more than 100 frames, the process was repeated at 60Hz. Assuming a maximum operator response time of one second, determining the starting point of paracellular ice in this manner introduced a potential error of 125 frames, or ± 0.03°C.

5.3.6 Immunostaining for Focal Adhesions and Stress Fibers

Cells in micropatterns were fixed in 4% (v/v) paraformaldehyde in PBS (Sigma-Aldrich) six hours after seeding. Following fixation, cells were rinsed three times in wash buffer (1X DPBS with 0.05% (v/v) Tween20 (Sigma-Adlrich)), permeabilized in 0.1% (v/v) TritonX-100 (Sigma-Aldrich), and rinsed twice in wash buffer. For visualization of the focal adhesion protein vinculin, samples were blocked with 2% goat serum (Sigma-Aldrich) in DPBS and incubated with murine anti-vinculin monoclonal antibody, purified clone 7F9 (Chemicon, Temecula, CA) in 2% goat serum, and visualized with FITC-conjugated anti-mouse IgG secondary antibody (Chemicon). The

cell nucleus and F-actin were stained with 0.1% DAPI and 0.25 μg/mL TRITC-conjugated phalloidin (Chemicon) in PBS, respectively. Negative controls were included by replacing the anti-vinculin antibody incubation solution with 2% goat serum in DPBS. To reduce variability between experimental groups, all coverslips were seeded from the same passage, and staining would immediately follow (using the same solution preparations). After staining, coverslips were mounted on glass slides (Superfrost, Fisher Scientific) with anti-fade mounting solution (Molecular Probes). Coverslips were imaged on an Eclipse ME600 microscope with a Plan Apochromat VC 100X oil immersion objective, NA 1.4 (Nikon), under UV illumination (X-Cite 120 Lamp, Nikon). All images were recorded under the same camera settings, using a high resolution CCD camera (Sensicam, PCO, Kelheim, Germany) and IP Lab vs. 3.6 (Scanalytics, Rockville, MD). For each data population, a minimum of four coverslips were evaluated, analyzing at least 10 randomly selected cells per coverslip.

5.3.7 Quantitative Analysis of F-Actin and Focal Adhesions

All fluorescent images were analyzed using two different programs developed in LabView8.0 with IMAQ 8.0 (National Instruments, Austin, TX). The first program analyzed the fluorescent signals for the entire cell region to quantify total F-actin and vinculin levels in each cell (see Appendix C). In this program, prior to image processing the average intensity of each cell was calculated by measuring the average intensity for a bounding box that contained the micropatterned cell. After the intensity was measured, LabView's local thresholding algorithm was applied to the images, reducing background noise and in turn, isolating peaks in intensity. The results of this algorithm were then used to convert the image type from 12-bit to binary, with each continuous binary

'segment' displayed in a different color. The areas of individual clusters (representative of actin or vinculin staining) were calculated for each cell imaged. In addition, the total area of all clusters in each cell was calculated. The second program analyzed staining localized to cell perimeter, quantifying the negative space or 'gaps' that existed between clusters of vinculin staining (details of the second program were previously described in Chapter 4).

5.3.8 Statistical Analysis

Unless otherwise noted, data are reported as mean ± standard error of the mean as noted. When reporting the classification of events into categories, standard deviations were estimated by taking the square root of the number of observations in each category. If groups had a normal distribution and homogenous variances, the group means were compared by an independent *t*-test, or by analysis of variance (ANOVA), with post hoc analyses using Tukey's test. Differences were considered significant at the 95% confidence level ($p < 0.05$).

5.4 Results

5.4.1 Effect of Time in Culture

BPAECs were cultured in 20μm-diameter cell islands for 3 hours ± 30min, or 6 hours ± 30 min, post-seeding. Micropatterned cells were visually inspected prior to freezing, to ensure that all cells were fully spread in the patterns. To quantify the degree of cell spreading, fluorescent images (vinculin stain) of fixed cells were analyzed to determine the average cell diameter for each culture condition. After 3 hours in culture,

the average diameter for the cells was measured to be 22.9μm ± 0.1μm (n = 43), whereas for 6 hours in culture, the measured diameter was 23.4μm ± 0.04μm (n = 97). Additionally, in separate analysis of live cells, substrates exhibited no markers of apoptosis, and had high viability (> 95%).

All micropatterned cells were frozen at a rapid rate (130°C/min) to -60°C, using our cryomicroscopy system with high speed video acquisition (8,000 Hz). As with previous studies, the time, temperature and initiation site of intracellular ice formation events were determined for each cell frozen. The cumulative probability of IIF for each time condition studied was calculated and is presented in Figure 5.1. It can be seen that cells cultured for six hours post-seeding (green circles) had a faster rate of IIF than cells cultured for three hours (red circles). For the six hour culture time, the average temperature of IIF (T_{IIFavg}) was determined to be -26.6°C ±0.8°C (n = 111), whereas for the three hour data, the temperature decreased to T_{IIFavg} = -29.9°C ±0. 8°C (n = 121). This decrease in average temperature of IIF (as a result of decreased culture time) was determined to be statistically significant ($p < 0.05$).

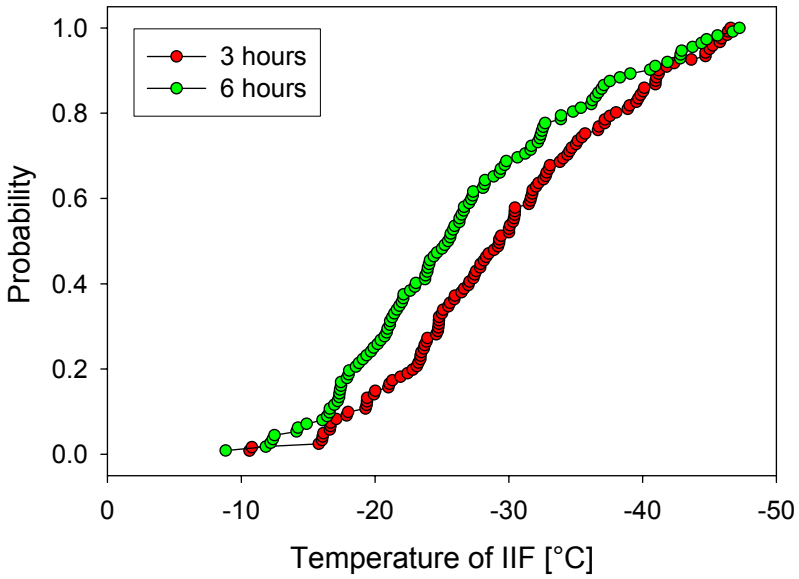

Figure 5.1 Cumulative probability of IIF for 20um-diameter BPAECs cultured for 3 hours and 6 hours. BPAEC cells culture 6 hours ± 30min (green circles, n = 111) post-seeding demonstrated an increased cumulative probability of IIF in comparison with cells cultured for 3 hours ± 30min (red circles, n = 121).

The location of IIF initiation inside the micropatterned cells was determined for each experiment, with the results presented in Table 4.1. It can be seen that for both culture conditions (3 and 6 hours), the majority of IIF events initiated at the cell periphery. In addition, as culture time increased, no significant differences were seen for the location of IIF initiation.

Table 5.1 Location of IIF initiation in BPAECs cultured for 3 and 6 hours.

	Periphery	**Interior**	**Unknown**
3 Hours (n = 121)	69.4% ± 7.6%	16.5% ± 3.7%	14.0% ± 3.4%
6 Hours (n = 111)	75.7% ± 8.3%	16.2% ± 3.8%	8.1% ± 2.7%

While no significant differences were seen in the percentage of IIF events that initiated at the cell periphery, we investigated how the kinetics for IIF events that initiated at the cell periphery varied between the two data populations. Using the transform presented in Chapter 3, Equation 3.8 was used to calculate the nucleation frequency for all IIF events that initiated at the cell periphery, n_{PI}:

$$n_{PI}(t) = \frac{1}{2}\sum_{i=1}^{N_{PI}(t)}\left(\frac{1}{N_u(t_i^-)} + \frac{1}{N_u(t_i^+)}\right) \tag{5.6}$$

where N_{PI} is the cumulative number of observations of peripheral-initiated IIF events in the population, and $N_u(t)$ is the number of unfrozen cells in the population at time t. By transforming the data using Equation 5.6, the relative magnitudes of the rate of peripheral initiation of IIF can be estimated by comparing the quantity n_{PI}, for the two populations. By fitting the data with a regression line, the resulting slope indicates the rate at which the kinetics increase (or decreased) between populations. In Figure 5.2, the transforms of the kinetic data for the 3 and 6 hour data populations are presented, with the 3 hour data ($n_{PI\,3hrs}$) used as the reference (*x-axis*). Thus, it can be seen by looking at Figure 5.2, that as culture time increased, the rate of peripheral initiated IIF events increased. To

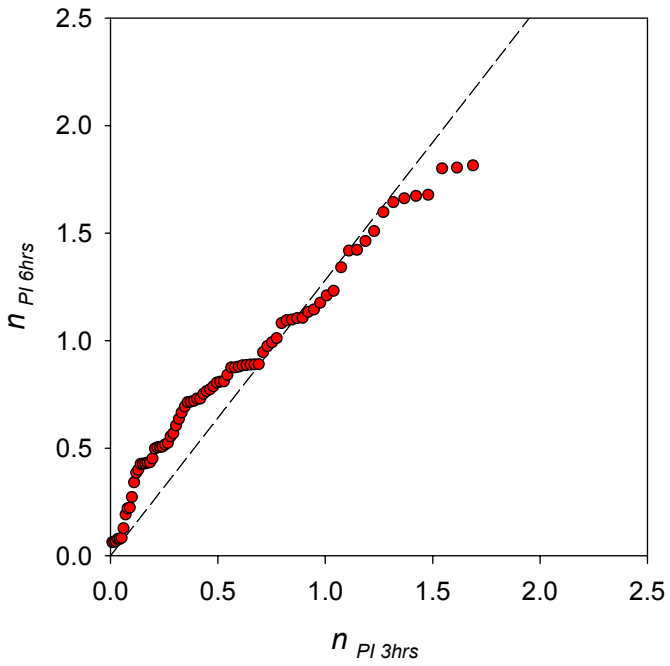

Figure 5.2 Transform of kinetics for all IIF events that initiated at the cell periphery, as culture time was increased. Using the 3 hour transformed data ($n_{PI\ 3hrs}$) as the baseline, all data were transformed using Equation 5.6. A regression line (dashed line) was fit to all of the transformed data. See text for details.

quantify the rate of increase, a linear regression was applied, yielding a slope of 1.29 ± 0.16 ($R^2 = .89$). Thus, while the number of peripheral-initiated IIF events was similar between the two groups, as culture time was increased (from 3 to 6 hours), the rate for peripheral-initiated IIF events increased by ~30%.

In Chapters 3 and 4 the phenomenon of paracellular ice dendrite formation was introduced and quantified for the experimental conditions studied. In the present study, the frequency of formation for these microscale ice dendrites was affected by experimental conditions, as shown in Figure 5.3. As post-seeding culture time increased from 3 hours to 6 hours, the percentage of paracellular ice dendrites formed increased by ~40%. However, it should be noted that this increase may be an artifact of the low number of paracellular ice dendrites formed in the 3 hour data population. The difference in paracellular ice penetration events between the 3 and 6 hour population is no larger than the estimated standard deviation, and as a consequence may not be real.

Next, data were transformed to investigate how the kinetics associated with paracellular ice formation and subsequent IIF initiation events. First, for each culture condition, the frequency of paracellular ice penetration was analyzed by transforming the kinetics of dendrite penetration using Equation 5.4. Second, the effect of these dendrites on subsequent IIF formation was analyzed by transforming the kinetics of IIF events that co-localized with the paracellular ice dendrites, using Equation 5.5. (where co-localization was defined as IIF initiation within 1.5 μm of dendrite formation, see Chapter 3). Figure 5.4 presents the results of this analysis, where the rate of paracellular ice penetration (n_{PIP}, red circles), and the rate of subsequent dendrite-mediated initiation of IIF (n_{DMI}, gray circles) are shown relative to the 3 hour culture time. Applying a linear

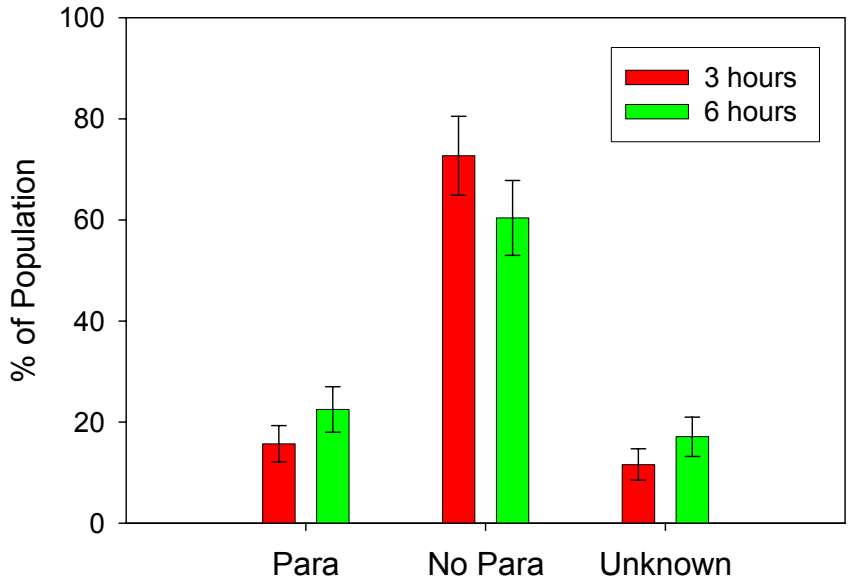

Figure 5.3 Effect of culture time on the frequency of paracellular ice dendrite formation. BPAEC cells cultured in 20μm diameter patterns for 3 hours (red bars) and 6 hours (green bars) were analyzed for paracellular ice dendrite formation. Cells that were visually obscured by extracellular ice were deemed 'unknown'; bars represent ± SD. As culture time increased from 3 to 6 hours, the percentage of paracellular ice dendrites increased.

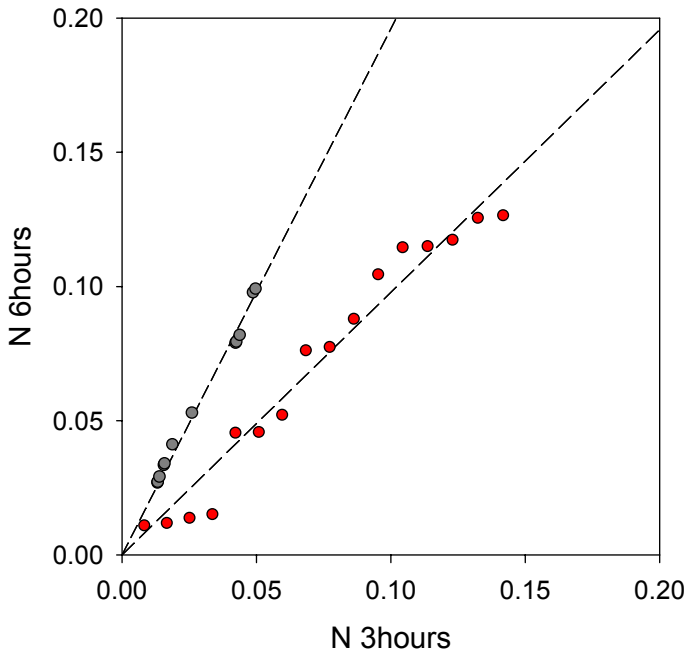

Figure 5.4 Effect of culture time on kinetics of paracellular ice dendrite formation and subsequent IIF initiation. As culture time was increased, data were transformed to investigate the rate of paracellular ice penetration, n_{PIP} (red circles, transformed using Equation 5.4) and the rate of dendrite-mediated initiation of IIF, n_{DMI} (gray circles, transformed using Equation 5.6). All data is presented relative to the 3 hours culture time (*x-axis*). Linear regression analyses are also shown (dashed lines).

regression to the data for the rate of paracellular ice penetration (n_{PIP}) the resulting slope was 0.98 ± 0.01 (R^2 = 0.96), suggesting no effect of culture time on the rate of dendrite formation. Analyzing the subsequent rate of IIF initiation events that co-localized with the dendrite, n_{DMI}, the slope of the regression yields 1.96 ±0.003 (R^2 = 0.99), indicating a two-fold increase in the rate of dendrite-mediated IIF. Thus, our results suggest that as culture time was increased, the overall rate of dendrite formation remained constant; however, cells cultured for 6 hours were much more susceptible to IIF mediated by the paracellular ice dendrites.

To quantify some of the differences that exist between the experimental groups at the cell-substrate level, immunofluorescent techniques were combined with a custom image-processing program to analyze the quantity and spatial location of the focal adhesion protein vinculin, as well as F-actin fibers. Micropatterned BPAEC cells were fixed 3 hours, and 6 hours post-seeding, and subsequently stained. Since fluorescent image intensity was one of the factors analyzed, all coverslips were stained simultaneously, using the same dye preparations (see Methods for further details). The overall fluorescent intensity of TRITC-conjugated phalloidin was measured for each cell after 3 and 6 hours of culture. The results of our analysis can first be seen qualitatively in Figure 5.5. Unprocessed fluorescence micrographs of the F-actin signal are shown for 3 hours (Figures 5.5A-C) and 6 hours (Figures 5.5G-I) post-seeding, with the corresponding segmented image below (Figures 5.5D-F and J-L). The binary segments represent localized peaks of F-actin fluorescence detected by the algorithm.

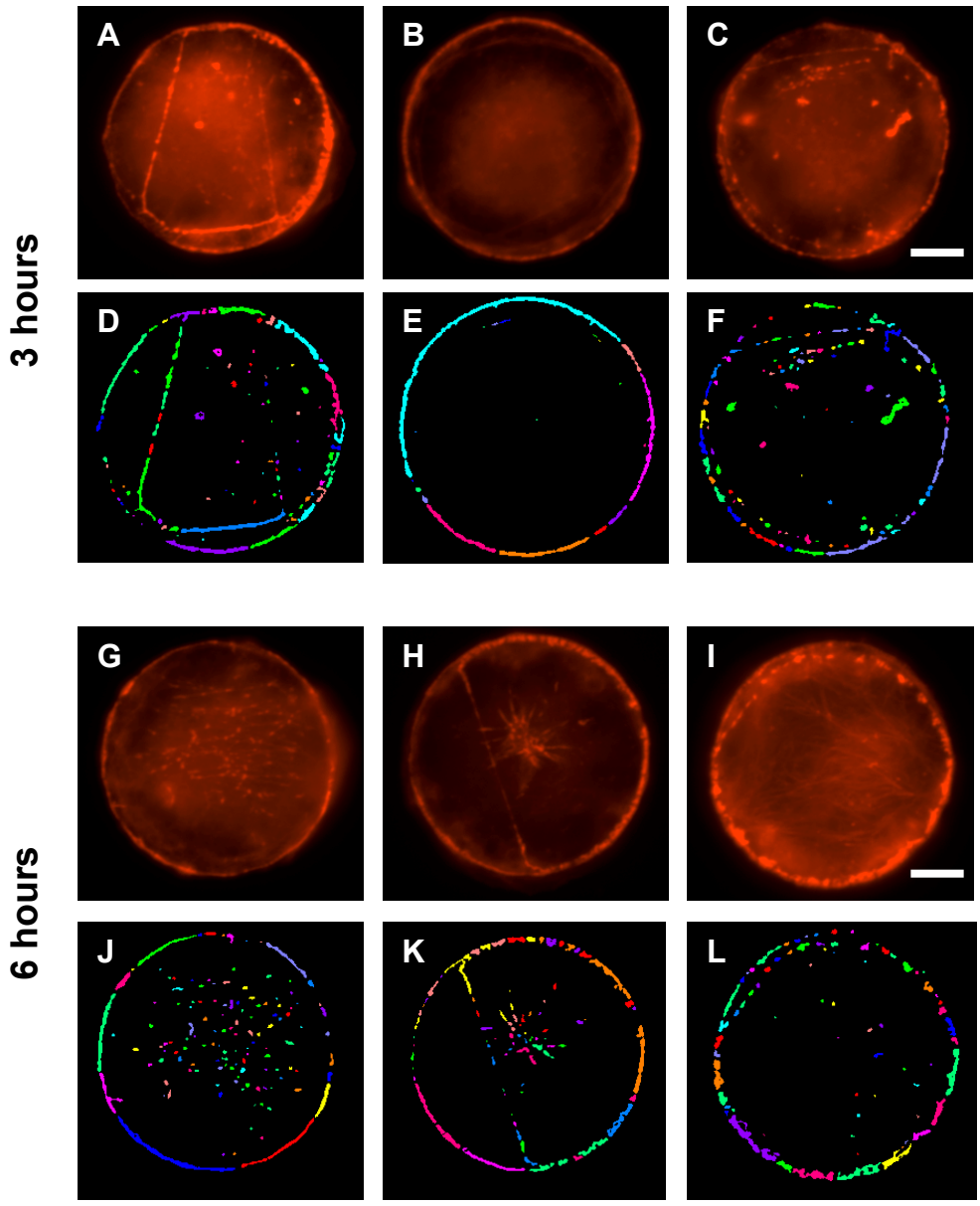

Figure 5.5 Effect of time in culture on F-actin levels for BPAECs in 20μm micropatterns. Representative fluorescent micrographs of TRITC-phalloidin were selected from the 3 hour (A-C) and 6 hour (G-I) data populations. The corresponding segmented images are shown below (D-F) and (J-L). Scale bars represent 5 μm. See text for details.

Looking at the images presented in Figure 5.5, qualitative differences can be seen in the intensity of the F-actin signal between the three and six hour groups. Overall, the signal intensity appears to be higher in the 3 hour images than in the 6 hour images. In addition, the actin appears more globular and less defined in the 3 hour group, with a high level of background 'haze'. In Figure 5.5B, faint traces of actin filaments can be seen along the cell periphery, whereas in the 6 hour figures, well-defined actin filaments are evident throughout the cells. Since these observations are subjective, we will now turn to the quantitative results from our image analysis.

Fluorescent images were acquired under UV-excitation using red (TRITC, F-actin) and green (FITC, vinculin) filter sets for the 3 hour (n = 43) and 6 hour (n = 97) data populations. All 'red' fluorescence images were analyzed to determine the average intensity of the F-actin fluorescence signal (units are arbitrary), the average area of individual F-actin clusters, and the average total area of F-actin per cell. All 'green' fluorescence images were analyzed in a similar fashion, but measuring the focal adhesion protein, vinculin. Due to the theoretical optical resolution of our system (0.22 μm, see Chapter 4) a conservative measurement threshold was applied, excluding all measurements < 5 pixels in length, or < 5 x 5 pixels in area (0.5 μm, and 0.25 μm^2, respectively). The results of our analysis can be found in Table 5.2. Comparisons between populations were done using Students t-test, with significance defined as $p < 0.05$. Our data indicates a significant decrease in F-actin intensity as culture time was increased from 3 to 6 hours. However, despite this decrease in fluorescence intensity, measurements of individual actin fiber clusters as well as the total area of F-actin in each

cell were not significantly different between the groups. Likewise, no significant differences were found in the vinculin measurements.

Table 5.2 Binary segment analysis for changes in F-actin and vinculin staining as culture time was increased. Data are presented as mean ± SEM; significance between populations was defined as $p < 0.05$, and is indicated by (*).

	3 hours	**6 hours**
F-actin intensity (per cell)	975 ± 30	844 ± 22.3 *
Area of individual F-actin clusters	4.7 ± 0.6 μm^2	5.7 ± 0.5μm^2
Total F-actin area (per cell)	93.3 ± 6.2 μm^2	99.1 ± 4.3μm^2
Vinculin intensity (per cell)	281 ± 8	264 ± 7
Area of individual vinculin clusters	3.5 ± 0.6 μm^2	3.1 ± 0.3 μm^2
Total vinculin area (per cell)	69.9 ± 9.7μm^2	56.4 ± 3.9μm^2

Despite finding no significant differences in the overall vinculin measurements (based on analyzing the entire cell area), qualitative observation of the vinculin fluorescent images (see Figure 5.6) suggested that distinct differences existed between the two populations at the cell periphery. Looking at the vinculin micrographs (and corresponding segmented images) for cells cultured for 3 hours (Figure 5.6A-F), it was evident that the majority of vinculin was located at the cell perimeter. Continuous, large segments of vinculin can be seen at the cell periphery, while the center of the cell is almost devoid of any vinculin protein. In contrast, after 6 hours in culture, the staining patterns changed. Overall, while the average size and total area of vinculin clusters may be statistically similar between data populations, the organization and spatial location

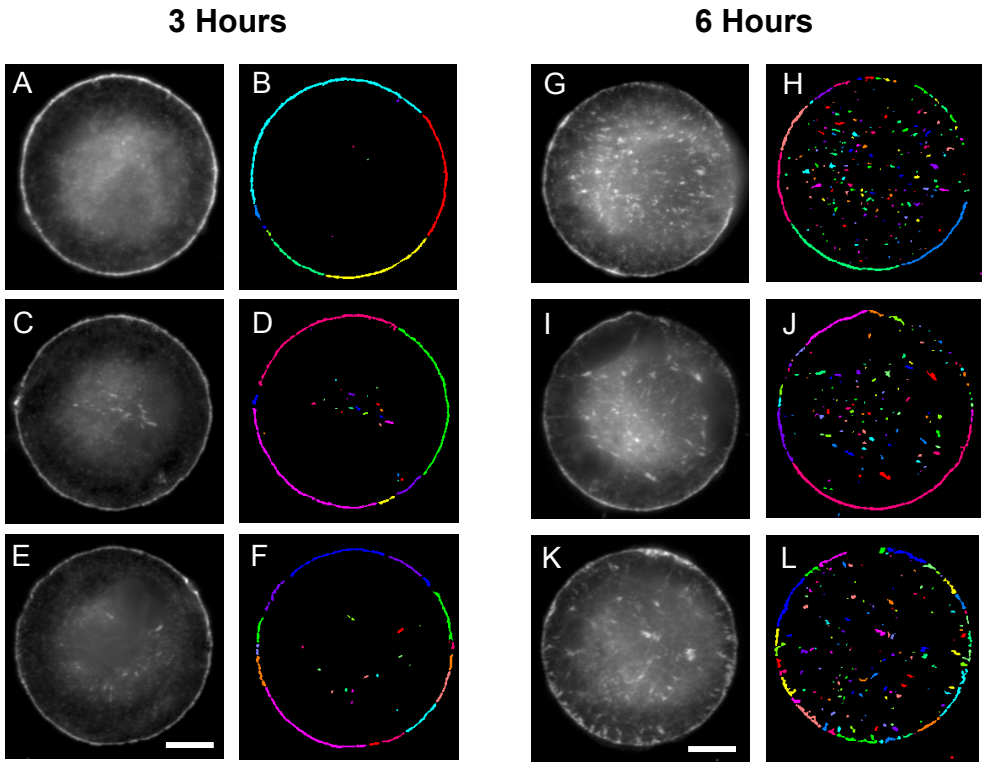

Figure 5.6 Micrographs of vinculin staining as time in culture is varied. Representative fluorescent micrographs of the focal adhesion protein vinculin were selected from the 3 hour (A,C,E) and 6 hour (G,I,K) data populations. The corresponding binary images are shown to the right (B,D,F) and (H,J,L). Scale bars = 5 μm.

varied. For cells stained after 6 hours in culture (Figures 5.6G-L), a high quantity of small vinculin clusters were seen in the central regions of the cell. Additionally, the vinculin staining at the perimeter of the cell appeared to be more punctuated, with fewer continuous vinculin segments. Since the perimeter of the cell is the primary location for interaction between the attached cell and extracellular ice during freezing, we next performed a quantitative analysis of vinculin staining along the cell perimeter.

Similar to our analysis in Chapter 4, all vinculin images were analyzed to calculate the gap distance between focal adhesion clusters, along the cell periphery. As shown in Figure 5.7, the peripheral region of each cell (± 10% cell radius) was extracted, unwrapped and segmented to quantify the distance between vinculin clusters for each data population.

Figure 5.8 shows the average distance between vinculin clusters at the cell periphery, and the average number of such gaps per cell. Because limitations in the spatial resolution of optical microscopy may introduce artifacts in measurement of the smallest gaps sizes, gaps smaller than 0.5 μm were analyzed separately from larger gaps. Data indicate that as culture time increased from 3 to 6 hours, the average number of gaps per cell increased (see Figure 5.8A). Significant differences between 3 and 6 hours of culture time were found to exist in the number of small gaps (< 5pixels) as well as in the total number of gaps detected. For the 'All Gaps' data group, as the culture time was increased from 3 to 6 hours, the average number of gaps per cell increased by ~20%. While the number of gaps increased for all data subsets, the overall gap size was statistically similar for all groups (see Figure 5.8B). These results were in agreement with our qualitative assessment of the fluorescent cell images.

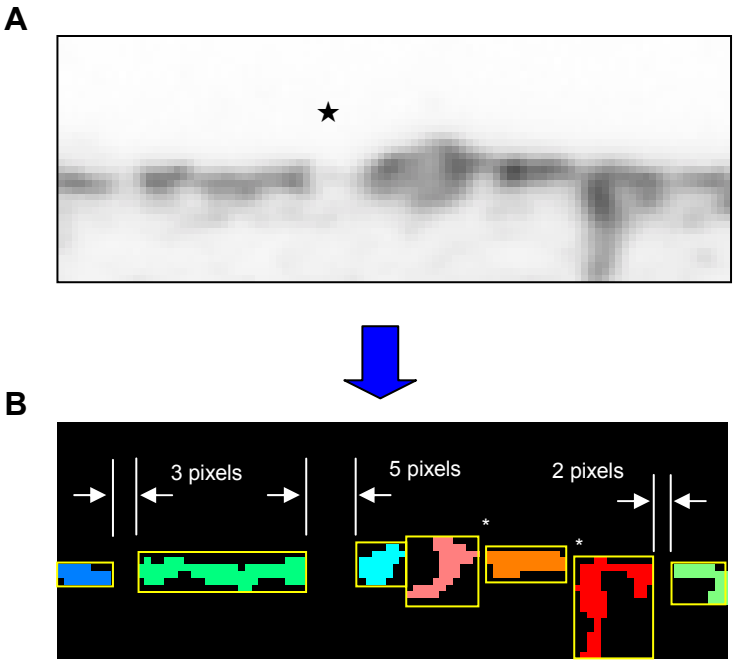

Figure 5.7 Illustration of binary gap measurements in comparison with native fluorescent image. (A) Fluorescent image of vinculin (inverted for clarity), taken from a micrograph of a single BPAEC cell cultured in a 20μm diameter island. The image was segmented, with different segments representing areas of vinculin staining (B). The linear distance, or gap between each segment was calculated, with all detectable gaps indicated in (B); 1 pixel gaps are indicated by (*). In (A), the gap indicated by (★) is the smallest gap that will pass the minimum limit (≥ 5 pixels or 0.5μm) used in Figure 5.8.

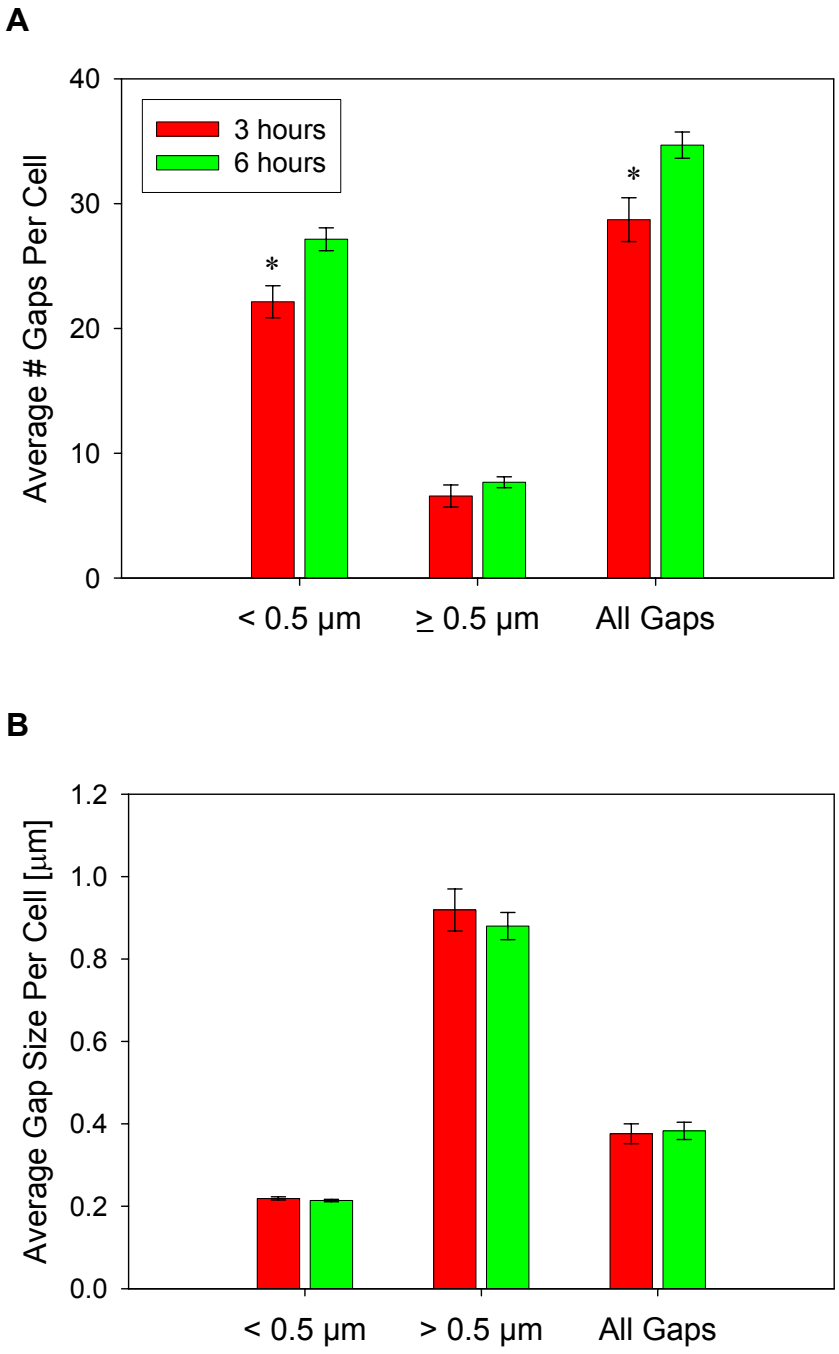

Figure 5.8 Effect of culture time on focal adhesion organization at the cell perimeter. Analyzing the vinculin staining only at the cell perimeter the (A) average number of gaps per cell, and the (B) average gap size per cell were calculated as culture time was increased from 3 hours (red bars) to 6 hours (green bars); data presented as mean ± SE. Data are presented using three different limits on the detected gap segments: all segments less than 5 pixels '< 0.5µm', all gap segments that were 5 pixels or more '≥ 0.5µm', and all gap segments measured 'All Gaps'. Significant differences ($p < 0.05$) are indicated by (*).

5.4.2 Effect of Ligand Coating Density.

The effect of ligand density was analyzed by coating our micropatterned substrates with two different fibronectin (FN) densities, varying the concentration of fibronectin by two orders of magnitude. The 'high' FN density (25µg/mL) was selected to fully saturate the cell attachment area, while the 'low' FN density (0.2µg/mL) was chosen to provide only enough adhesion ligand so that the cells were fully spread in the patterns. To reduce additional adsorption of adhesion ligands from the medium, the substrates used in this portion of the chapter were blocked with 1% bovine serum albumin after FN coating. The degree of cell spreading for each ligand density was quantified through image analysis of fixed cells. For the low FN density, the average diameter for the cells was measured to be 23.2µm ±0.5µm (n = 81), whereas for the high FN data, the measured diameter was 23.1µm ±0.4µm (n = 74). Thus, for each culture condition, cells were fully spread with statistically similar dimensions (p = 0.37).

All cells were frozen at a rapid rate (130°C/min) to -60°C, using our high speed cryomicroscopy system (8,000 Hz). The time, temperature and initiation site of intracellular ice formation were measured for each cell frozen. Figure 5.9 presents the cumulative probability of IIF as it varied with fibronectin coating density. As shown in Figure 5.9, as the fibronectin density was increased, the rate of IIF decreased. Substrates coated with a low density of fibronectin froze earlier, with a median temperature of IIF, T_{IIF50} = -25.1 °C (n = 109), whereas for high fibronectin density, the median temperature decreased to T_{IIFavg} = -29.0 °C (n = 104). Analyzing the data for the location at which IIF initiation, a slight decrease in the percentage of cells that IIF initiated at the cell periphery was seen as fibronectin concentration was decreased. (Table 5.3).

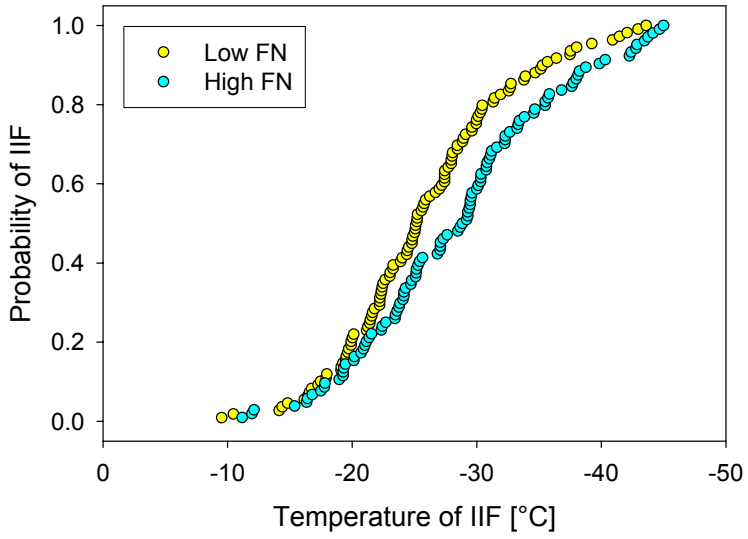

Figure 5.9 Cumulative probability of IIF for 20um-diameter BPAECs cultured in micropatterns coated with different fibronectin densities. BPAECs cultured for 6 hours ± 30min on substrates coated with a low density of FN (yellow circles), and with a high density of FN (cyan circles), were frozen at 130°C/min to -60°C.

Table 5.3 Location of IIF Initiation as it varied with fibronectin coating density. Data presented are percentage of population ± SD.

	Periphery	**Interior**	**Unknown**
Low FN	64.2 ± 7.7%	33.0 ± 5.5%	2.8 ± 1.6%
High FN	74.0 ± 8.4%	21.2 ± 4.5%	4.8 ± 2.2%

Next, our cryomicroscopy data was separated by IIF initiation location to investigate effect of fibronectin density on the nucleation rate for IIF events that initiated at the cell periphery. Data were transformed using Equation 3.8, and the results are presented in Figure 5.10. The slope of the regression line fit to the data was 1.29 ± 0.02

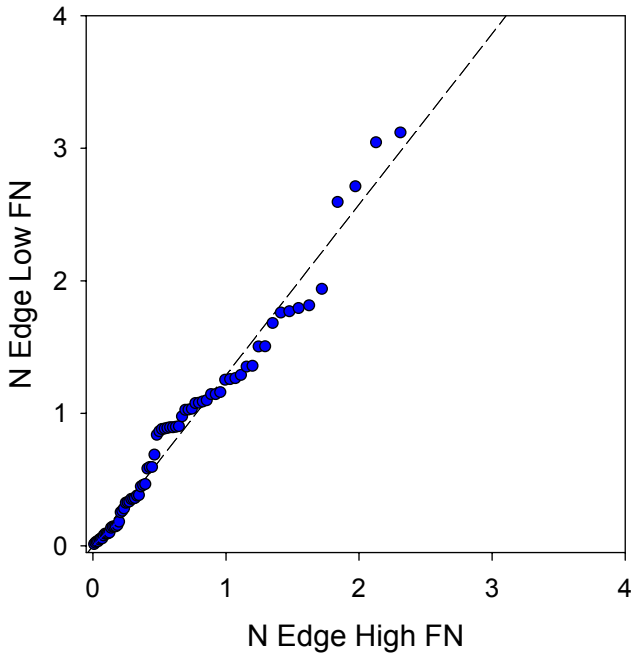

Figure 5.10 Transform of IIF kinetics for all events that initiated at the cell edge, varying FN coating density. All data were transformed using Equation 3.8, with the high FN data selected as the reference case. A regression line was fit to the data (dashed line).

(R^2 = 0.98); indicating that as fibronectin density was decreased, the nucleation rate for IIF events that started at the edge increased by 29%.

The effect of FN density on the incidence of paracellular ice penetration is shown in Figure 5.11. increased for the low FN coating group. As the fibronectin coating density decreased from 25 to 0.2μg/mL, the percentage of the population that exhibited paracellular ice growth approximately doubled.

The influence of fibronectin coating density on the rate of paracellular ice penetration and on the rate of dendrite-mediated initiation of IIF is shown in Figure 5.12. Considering only experiments that exhibited paracellular ice formation, we first computed the rate of paracellular ice penetration using Equation 5.4. We then used Equation 5.5 to quantify the rate of dendrite-mediated initiation. Plotting the data against the high FN density data, linear regression (with intercept forced through the origin) yielded best fit lines with slopes 1.60 ± 0.03 (R^2 = 0.85) and 2.03 ± 0.03 (R^2 = 0.93) for the paracellular ice penetration kinetics and the dendrite-mediated initiation kinetics, respectively. These results indicate that, as fibronectin density was decreased from 25μg/mL to 0.2μg/mL, the average rate of paracellular ice penetration increased by 60%. However, the average rate of dendrite-mediated initiation of IIF increased by 100% when the density of FN was decreased. This is interesting, because if paracellular ice dendrites caused IIF at similar rates in the two experimental groups, then the rate of dendrite-mediated initiation should increased by an amount similar to the observed 60% increase in the paracellular penetration rate.

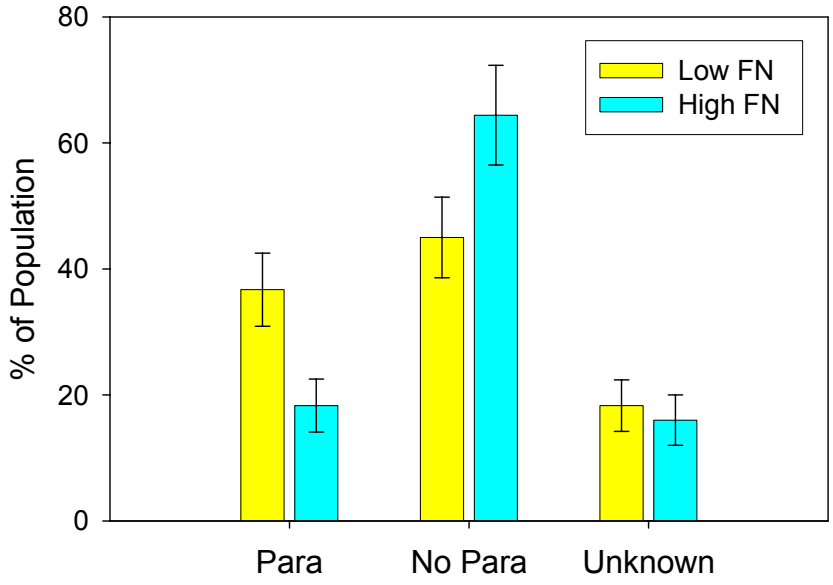

Figure 5.11 Effect of FN coating density on the frequency of paracellular ice dendrite formation. Percentage of the data population that exhibited paracellular ice grown is shown for the low FN data group (yellow bars) and the high FN group (cyan bars); bars represent ± SD. As fibronectin coating density is increased, the percentage of paracellular ice that forms during freezing decreases.

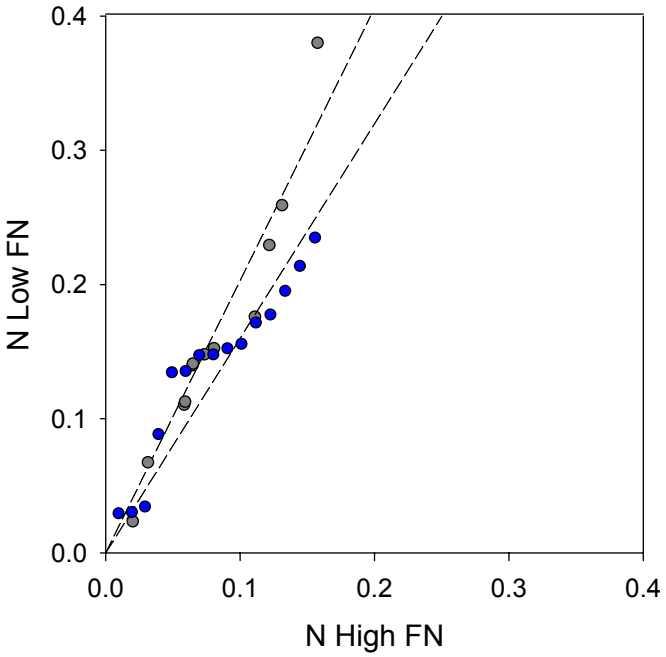

Figure 5.12 Effect of FN coating density on paracellular ice kinetics. Data were transformed to investigate the kinetics of paracellular ice dendrite formation (blue circles) as it varied with fibronectin coating density. Comparing the high FN (*x-axis*) and low FN (*y-axis*) data transforms, the rate of dendrite formation increased by approximately 60% (slope of regression line = 1.60 ±0.03, $R^2 = 0.85$). The rate of IIF events that co-localized with paracellular ice dendrite formation is also shown (gray circles, slope of regression line = 2.03 ±0.03, $R^2 = 0.93$).

To investigate the effect of FN density on the overall size and distribution of focal adhesions in attached cells, immunofluorescent images of vinculin were quantified using the same image processing program detailed in the previous section. BPAECs cultured on 20μm islands coated with high FN (n = 74) and low FN densities (n = 81) were fixed after six hours in culture and fluorescently labeled for vinculin. Representative micrographs used for this analysis can be seen in Figure 5.13. Images from the low fibronectin density group demonstrate a high degree of discontinuity in focal adhesion staining at the cell periphery. In addition, many small clusters of vinculin staining were dispersed throughout the attachment area. Conversely, for the high FN coating density, large continuous clusters of vinculin outline the cell perimeter, with only a small quantity of vinculin clusters in the central region of the cells.

All images were analyzed to determine the average intensity of the vinculin fluorescence signal (units are arbitrary). Then, after image segmentation and exclusion of clusters smaller than 0.25 μm^2, the average area of individual vinculin clusters and the average total area of vinculin clusters per cell were quantified. The results of our analysis can be found in Table 5.4. Comparisons between populations were done using Students t-test, with significance defined as $p < 0.05$. Varying fibronectin coating density resulted in significant changes in both the average area of focal adhesion clusters and the total area of focal adhesions. As fibronectin density was increased from 0.2μg/mL to 25μg/mL, the average area of vinculin segments increased two-fold. Additionally, the increase in FN density also resulted in an overall 43 % increase in the total area for all vinculin clusters in a cell.

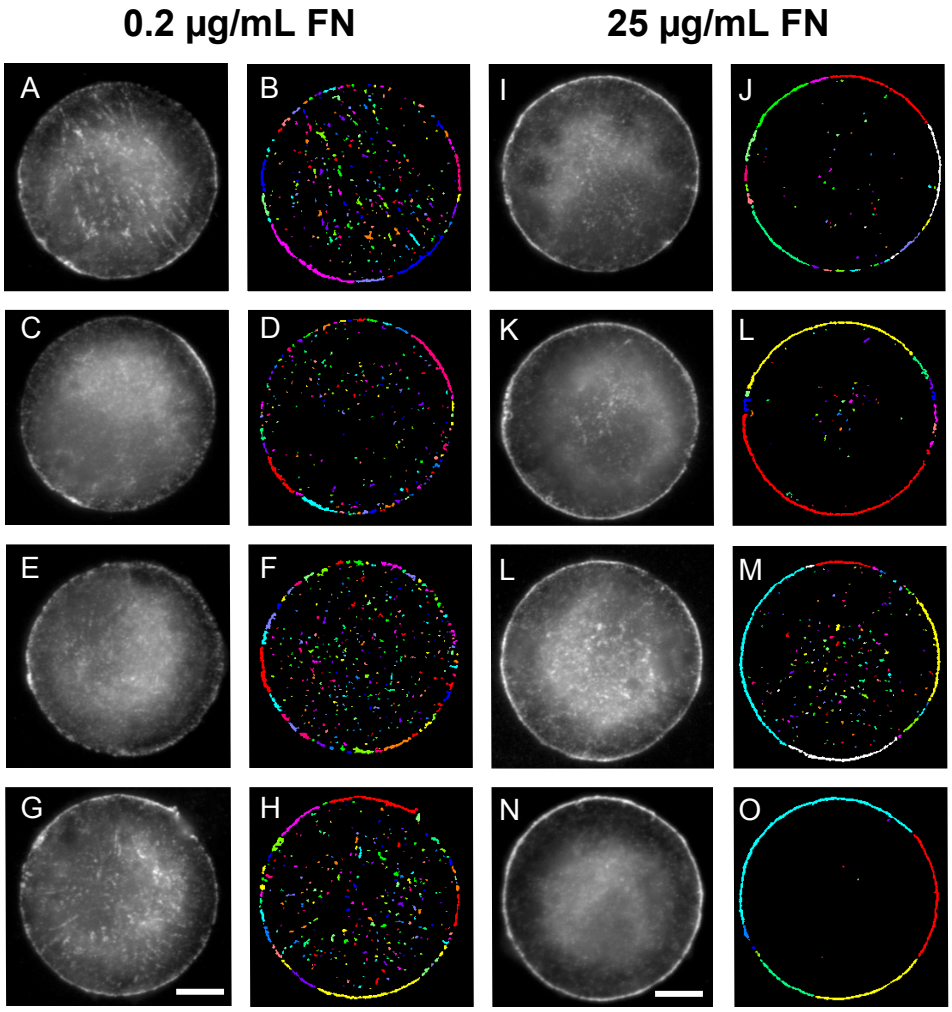

Figure 5.13 Micrographs of vinculin staining, as fibronectin coating density was varied. Representative fluorescent micrographs of the focal adhesion protein vinculin were selected from the low FN (A, C, E, G), and high FN data populations (I, K, L, N) data populations. The corresponding binary images are also shown (B, D, F, H) and (J, L, N, O). Scale bars = 5 µm.

Table 5.4 Segment analysis for changes in vinculin staining as fibronectin coating density was varied. Data are presented as mean ± SEM, applying minimum detection limit of 0.25μm^2; significance was defined as $p < 0.05$, and is indicated by (*).

	Low FN (0.2μg/mL)	**High FN (25μg/mL)**
Vinculin intensity (per cell)	222 ± 5	232 ± 6
Area of individual vinculin clusters	2.0 ± 0.2μm^2	3.9 ± 0.5 μm^2 *
Total vinculin area (per cell)	53.8 ± 4.2μm^2	76.7 ± 8.6μm^2 *

Lastly, the focal adhesion spacing along the cell perimeter was analyzed using the algorithms described above. Briefly, the peripheral region of the micropatterned cell was extracted from the fluorescent image based on the measurement of the cell radius. The size and quantity of gaps between focal adhesion clusters was quantified for each micrograph, with the results are presented in Figure 5.14. As discussed previously, gaps smaller than 0.5 μm were analyzed separately from larger gaps, because the former measurements are more susceptible to artifacts. In Figure 5.14A, it can be seen that the average number of gaps statistically increased for the low fibronectin group (yellow bars), whereas no statistical difference was found for the average number of gaps ≥ 0.5 μm in size. For all gap measurements, the average increase in gap number per cell was ~20%. In addition, we measured a decrease in average gap size between the two data populations. As FN coating density decreased, the average gap size decreased by 26% for gaps ≥ 0.5 μm in size; considering all detected gaps, a 17% decrease was measured.

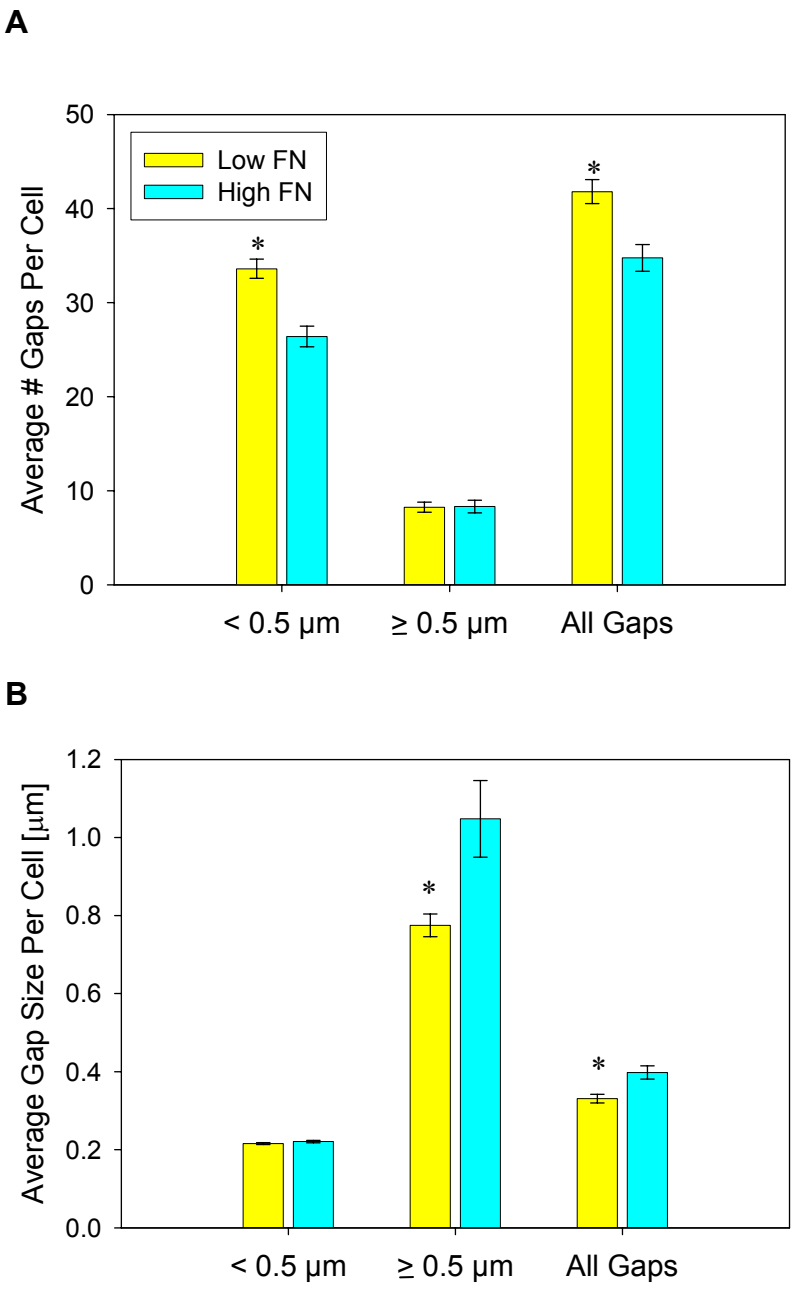

Figure 5.14 Effect of fibronectin density on focal adhesion organization at the cell perimeter. Analyzing the vinculin staining only at the cell perimeter the (A) average number of gaps per cell, and the (B) average gap distance were calculated as FN density was increased from 0.2µg/mL (yellow bars) to 25µg/mL (cyan bars). Data are presented as mean ± SEM, with significance ($p<0.05$) indicated by (*).

5.5 Discussion

Previously, cell size was systematically increased and the kinetics of IIF were shown to increase proportionally with cell perimeter. In this chapter, cell size was held constant while the effects of different culture conditions on the kinetics of IIF were investigated. Two parameters were specifically selected with the intent of varying the adhesion state of the attached cell: culture time and ligand coating density. First, the influence of time in culture was investigated by freezing BPAECs cultured in 20μm-diameter micropatterns 3 and 6 hours post-seeding. These two time points were selected based on data in the literature that indicated a peak in F-actin intensity three hours post-seeding for bovine endothelial cells followed by a subsequent decline[82]. Data from the same study also indicated that focal adhesion clusters started to appear 2-3 hours post-seeding[82]. Cell adhesion is a complex, time sensitive, process with a specific hierarchical order[128]. Therefore, by freezing cells three and six hours post seeding, we attempted to capture two different snapshots of the cell during the adhesion process. The second parameter varied, fibronectin (FN) coating density (0.2 μg/mL and 25μg/mL), was also chosen with the intent of changing the adhesion state between the two culture conditions. Changes in FN density have been shown to influence both the spatial organization of focal adhesion proteins as well as the overall adhesion strength of the cell[99,128,143].

Our data indicated that as culture time was increased from 3 hours to 6 hours post-seeding, attached cells were more susceptible to IIF. Similarly, as fibronectin coating density was decreased, attached cells had a higher probability of IIF. Interestingly, the vinculin staining at the cell periphery in our low fibronectin group had spatial patterns similar to those seen in the 6 hour culture group. Likewise, the 3 hour

staining (large clusters of vinculin at the periphery) was similar to the high fibronectin data. Quantitative analysis of vinculin proteins demonstrated that both increasing time in culture and decreasing FN coating density resulted in an increase in the average number of gaps between vinculin clusters along the cell periphery. These results were consistent with the data presented in Chapter 4, in that both the rate of peripheral-initiated IIF events and the rate of paracellular ice penetration increased proportionally with the number of gaps along the cell periphery.

In agreement with our previous studies, the majority of IIF events initiated at the cell periphery for all conditions investigated. As noted above, the correlation between the increase in the rate of peripheral-initiated IIF events and the increase in the number of gaps in focal adhesion clusters was seen in all of our studies. This suggests that the presence of continuous clusters of focal adhesions at the cell perimeter may have a protective effect against IIF. In Chapter 4, it was qualitatively observed that during freezing, the attached cells appeared to deform in response to extracellular ice growth, and the amount of deformation appeared to increase as the number of gaps increased (see Figure 4.3). Others have also observed cell deformation in response to advancing extracellular ice crystals[41,105]. Considering the rate of peripheral initiation of IIF appeared to correlate with the number of gaps, one could speculate that IIF may result from membrane damage caused by deformation by extracellular ice. Potentially, large continuous clusters of focal adhesion proteins (i.e., cells with fewer gaps) could act as a reinforcing wall, protecting the cell membrane from deformation caused by the extracellular ice.

We hypothesized that paracellular ice dendrites could penetrate the supercooled space beneath the attached cell, entering through gaps between focal adhesion clusters. In this chapter, both time in culture and fibronectin coating density influenced the frequency of paracellular ice formation. From our data, it was shown that increasing culture time increased the probability of paracellular ice penetration. However, it was determined that the rate at which these paracellular ice dendrites formed was not influenced by culture time. Decreasing fibronectin coating density also resulted in an increase in the proportion of cells that experienced paracellular ice penetration. In addition, as fibronectin density was decreased, the rate of paracellular ice penetration increased by 60%. It is interesting to note that quantitative analysis of vinculin staining for the low FN group indicated a significant reduction in total area of vinculin clusters, relative to the high FN group. Thus, this reduction in focal adhesion protein cluster area may be indicative of a reduction in cell adhesion properties, and consequently this reduced adhesion state may result in a larger cell-substrate distance (smaller and fewer anchoring points), increasing the temperature at which paracellular ice penetration is possible. Thus, we postulate that the probability of paracellular ice penetration will depend on both on the probability of finding a gap (proportional to the number of gaps) and the probability of being able to penetrate that gap (proportional to gap height).

The overall rate of dendrite-mediated IIF initiation was assumed to be governed by two processes: the initial rate of paracellular ice penetration, and following this, the susceptibility of the cell to IIF resulting from the presence of the paracellular ice dendrite. As culture time was increased, our data suggested that the increase in the rate of dendrite-mediated IIF initiation was solely due to the increased susceptibility to damage by ice

dendrites in cells cultured for 6 hours. When fibronectin coating density was decreased, the increase in the rate of paracellular ice penetration was not large enough to account for the overall increase in dendrite-mediated initiation. As such, our results indicate that cells cultured on the low fibronectin coated substrates were also more susceptible to dendrite-mediated IIF initiation. Knowing that both the 6 hour culture time and low fibronectin groups both have an increased susceptibility to IIF that co-localized with paracellular ice, it is interesting to again note the similarities in vinculin staining patterns between the two groups. Keeping in mind that this increase in susceptibility to IIF is separate from the number or rate of paracellular ice dendrites formed, one can speculate that the increased focal adhesion clustering in central locations of the cells might make the cells more susceptible to IIF initiation by the paracellular ice dendrites. One interpretation is that strain is imposed on the cell membrane by the paracellular ice dendrite as it grows underneath the cell. The larger the separation between anchoring points (*e.g.* fewer focal adhesions in the central area of the cell), less stress results in the membrane as the paracellular ice applies strain. Therefore, in the 6 hour and low fibronectin groups, the increased number of focal adhesion clusters in the central area of the cell may make these data populations more susceptible to IIF resulting from paracellular ice dendrites.

The studies presented in this chapter support our previous results that suggested a major role for cell-substrate interactions in probability of IIF. Variations in cell culture time and fibronectin coating density resulted in significant changes in the kinetics of intracellular ice formation. Consistent with our previous results, a strong correlation existed between the spatial arrangement of focal adhesion proteins at the cell periphery

and the frequency of paracellular ice formation. A similar correlation has also been seen between the kinetics of IIF that initiate at the cell periphery and the number of gaps between focal adhesion clusters. The importance of this work extends beyond our primary goal of elucidating the dominant mechanisms of IIF in attached cells and tissue. Understanding the effect of different culture parameters (such as culture time and adhesion ligand density) on the probability of IIF greatly assists the development of alternative strategies to reduce freezing related injury in attached cells.

CHAPTER 6

INTERCELLULAR ICE PROPAGATION IN MICROPATTERNED BOVINE ENDOTHELIAL CELLS

6.1 Introduction

Cryopreservation of living tissues is a challenging problem, in part due to the many biophysical phenomena that must be considered. Thus far, this thesis has focused on the effects of cell-substrate interactions on the initiation of intracellular ice formation (IIF) during freezing of adherent cells. However, the probability of IIF is known to be significantly enhanced in monolayer cultures in comparison to single adherent cells, a phenomenon that is largely attributed to the intercellular propagation of ice via cell-cell contacts[6,58,60,63,64].

Qualitative observations of freezing differences between suspended cells and monolayers have been long reported[62-64]. In cell suspensions, intracellular ice formation occurs independently in each cell, and thus the incidence of IIF in a sample population can be described by a Poisson process. In cell monolayers, the probability of IIF is known to be enhanced, a phenomenon largely attributed to the propagation of ice via cell-cell contacts[56,58,60]. From cryomicroscopic observations of onion epidermis, Tsuruta *et al.* hypothesized ice inside one cell could catalyze IIF in neighboring cells via surface-catalyzed nucleation, thus resulting in intercellular propagation of IIF[106]. In 1996, Berger and Uhrik were the first to propose an involvement of gap junctions in ice propagation, based on qualitative observations in cell strands from salivary gland tissue[56].

A subsequent study in confluent monolayers indirectly supported gap junction involvement in intercellular ice propagation in monolayers[96]. Recently, using micropatterned constructs of a transformed human hepatocellular carcinoma cell line human (HepG2), Irimia and Karlsson performed experiments that provided direct evidence for gap junction involvement in intercellular ice propagation[58]. While their study affirmed intercellular ice propagation occurred in a two-cell system, their results suggested the presence of a secondary mechanism of ice propagation that was gap junction independent. This secondary mechanism was qualitatively observed to be so rapid that capturing the events with conventional video acquisition rates (30 frames per second) proved to be difficult[58].

For all previous studies of the effects of cell-cell interactions on IIF, the largest limitation in obtaining an accurate description of the kinetics of ice propagation resulted from the conventional techniques used to measure IIF. In all of these studies, the average temporal resolution used to observe intercellular ice propagation was 30Hz, often preventing discernment of the majority of propagation events. It should also be noted that the primary indicator used to identify IIF in these experiments was cell darkening. Previous results in Chapter 3 demonstrated that cell darkening is actually an indirect measurement of IIF, with darkening commencing with variable time delays after IIF. Darkening has also been shown to be temperature sensitive, with a small fraction of the population (~10%) exhibiting no signs of darkening post-IIF. Thus, using this gradual, temperature-sensitive event as a means to quantify rapid kinetic changes may introduce large errors in the measurement of ice propagation.

Our high speed cryomicroscopy system was combined with cell micropatterning techniques to provide precise control of the cell attachment area, degree of cell-cell contact, and time in culture. Additionally, the use of a micropatterned cell pair provides a simple system that can be rigorously analyzed with mathematical models. Irimia and Karlsson previously developed the first theoretical model of tissue freezing that explicitly describes the kinetics of ice propagation from cell to cell[58]. In the current study, we have incorporated a new micropatterning technique[81], but have maintained the same two-cell pattern design. By keeping the system design constant, we can apply the same theoretical model to data from primary endothelial cells.

Our study of intracellular ice propagation in two-cell constructs allowed us to address many of the key questions remaining regarding the effect of cell-cell interaction on IIF. First, the use of primary endothelial cells will be the first such study of intercellular ice propagation in primary cells. Second, the temporal resolution limitations that were present in all previous studies have been overcome by the use of our high speed cryomicroscopy system. For each cell in the micropattern, each distinct IIF event can be recorded, allowing for direct measurement of the propagation rate kinetics. Lastly, the hypothesis that ice propagates across the cell-cell interface can be tested, by quantification of the initiation point of IIF in each cell. The theoretical results derived from the data can easily be scaled up to model ice propagation in two-dimensional tissue[145]. Mathematical models based on these results, such as the models presented in Chapters 8 and 9, will have great utility in the design of cryopreservation strategies and cryosurgical treatment planning.

6.2 Theoretical Background

Irimia and Karlsson recently developed a continuous-time Markov-chain model to predict the effect of cell-cell communication on the kinetics of IIF in a two-cell pair[58]. In their model, it was assumed that as soon as an IIF initiation event occurred in one cell, intercellular ice propagation to neighboring cells was possible. For a two-cell system (Figure 6.1), only one of three IIF states can occur: an unfrozen state (*i.e.* neither cell is frozen), a partially frozen, singlet state (*i.e.* ice present in only one of the cells) or a fully frozen, doublet state (*i.e.* both cells are frozen).

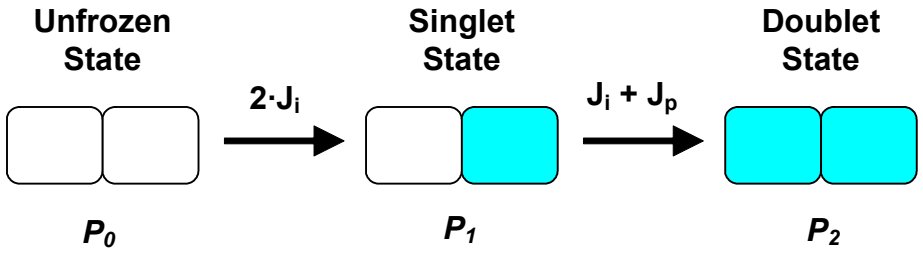

Figure 6.1 Schematic demonstrating the possible IIF states for pair of cells, and the possible state transitions. Unfrozen cells are represented by open rectangles, while cells frozen by IIF are illustrated as blue rectangles. State transitions were modeled as sequential reactions, with rate constants shown. The state of an ensemble of cell pairs was described by the probabilities P_0, P_1, and P_2 of the unfrozen, singlet, and doublet state, respectively. Adapted from Irimia and Karlsson[58].

At any point in time, for N cell pairs (*i.e.* $2N$ cells), there will be N_0 unfrozen pairs, N_1 partially frozen pairs, and N_2 fully frozen pairs, where $N_0 + N_1 + N_2 = N$. As a result of this interdependence of state variables, the state on the system can be described by two state variables: the probability of the unfrozen state,

$$P_0 \equiv \frac{N_0}{N} \tag{6.1}$$

and the probability of the single state

$$P_1 \equiv \frac{N_1}{N}. \tag{6.2}$$

The probability of the double state is not an independent state variable and thus, can be defined as

$$P_2 = 1 - P_0 - P_1. \tag{6.3}$$

Irimia and Karlsson assumed that the rate of IIF in each cell, J, was expressed as a sum of contributions from two distinct mechanisms: the propagation of ice from a frozen neighbor across the corresponding cell-cell interface, J_p; and the spontaneous formation of intracellular ice, J_i, that is independent of the state of the neighboring cell. It was assumed that the transition between states could be described by a sequential reaction (Figure 6.1) because the probability of two IIF events initiating at the exact same time is infinitesimally small. For either cell in the micropattern to initiate the first transition from the unfrozen state, P_0, to the partially frozen state, P_1, a cell must freeze via spontaneous nucleation, at a rate, J_i. Thus, the rate of depletion of unfrozen pairs is given by

$$\frac{dN_0}{dt} = -2J_i N_0, \tag{6.4}$$

where t is time. The next transition from the singlet state to doublet state (Figure 1), can occur by either the interaction-independent mechanism (*i.e.* spontaneous initiation of IIF), or by intercellular ice propagation (*i.e.* ice traveling from the frozen cell to the unfrozen cell). The rate of doublet formation is given by

$$\frac{dN_2}{dt} = (J_i + J_p) \cdot N_1, \tag{6.5}$$

where J_p is the average rate of intercellular ice propagation from a frozen cell to an unfrozen cell.

For convenience, a dimensionless time was defined as:

$$\tau \equiv \int_0^t J_i dt, \tag{6.6}$$

as well as a dimensionless ice propagation rate

$$\alpha \equiv \frac{J_p}{J_i}. \tag{6.7}$$

Combining equations 1-7, the kinetics of IIF in an ensemble of cell pairs can be described by the state equation,

$$\frac{d}{d\tau}\begin{bmatrix} P_0 \\ P_1 \end{bmatrix} = \begin{bmatrix} -2 & 0 \\ 2 & -(1+\alpha) \end{bmatrix} \cdot \begin{bmatrix} P_0 \\ P_1 \end{bmatrix}, \tag{6.8}$$

and the overall probability of IIF is given by,

$$P_{IIF} = 1 - P_0 - \frac{1}{2} P_1 . \tag{6.9}$$

Irimia and Karlsson[58] showed that for the limiting case of effects of cell-cell interaction (α=0), the solution of Equation 6.8 gives:

$$P_{IIF} = 1 - P_0^{\frac{1}{2}} . \tag{6.10}$$

and

$$\tau = -\frac{1}{2} \ln P_0 \tag{6.11}$$

Thus, even if intercellular ice propagation occurs in the system ($\alpha > 0$), Equation 6.10 can be used in conjunction with the observed kinetics of the unfrozen state to determine the hypothetical probability of intracellular ice formation due only to the spontaneous IIF initiation rate, J_i.

Irimia and Karlsson[58] demonstrated that Equation 6.8 can be solved analytically if the interaction parameter α is constant, obtaining

$$P_1(\tau) = \frac{2}{1-\alpha} \cdot (e^{-(1+\alpha)\cdot\tau} - e^{-2\tau}) \text{ for } \alpha \neq 1. \tag{6.12}$$

6.3 Materials and Methods

6.3.1 Bovine Pulmonary Artery Endothelial Cell Culture

Bovine pulmonary artery endothelial cells (BPAECs) (Cambrex, San Diego, CA) were cultured in MCDB 131 media (Mediatech, Herndon, VA) supplemented with 5% (v/v) fetal bovine serum (Sigma-Aldrich, St. Louis, MO), 2ng/mL basic human fibroblast growth factor (PeproTech, Rocky Hill, NJ), 10ng/mL human epithelial growth factor (Invitrogen Corp., Carlsbad, CA), 1ng/mL vascular endothelial growth factor (Sigma-Aldrich), 2 ng/mL insulin-like growth factor-1 (Invitrogen), 0.001 mg/mL hydrocortisone (Sigma-Aldrich), 2mM L-glutamine (Mediatech), 100U/mL penicillin/100μg/mL streptomycin (Invitrogen), and 50μg/mL ascorbic acid (Sigma-Aldrich). Cells were cultured on tissue culture plastic at 37°C in a humidified 5% CO_2 environment and media were replaced every 48 hours. Flasks where subcultured when they reached 70-85% confluency and were split at a 1:6 ratio, following the recommendations of the vendor (total exposure time to trypsin-EDTA (Cambrex, Cat# CC-5012) was 5 minutes). For all experiments, prior to seeding, cells were G_0 synchronized by holding at confluence for 24 hours. Cells were seeded onto fibronectin coated micropatterned coverslips at passages 4 through 6.

6.3.2 Fabrication of Micropatterned Substrates

Standard photolithography techniques were used to create silicon masters that contained rectangular features of dimensions 30x40μm and 30x80μm, with an 80μm distance between each feature (see Figure 6.2). Briefly, in a class 10 cleanroom, silicon wafers were spin-coated with SU-8 photoresist (Microchem Co., Newton, MA) to a

thickness of 5μm. Photoresist-coated substrates were exposed under UV through a chromium-glass mask, using a Karl Suss MA-6 mask aligner (Karl Suss, Waterbury Center, VT). Post-exposure, the substrate was baked on a hotplate (65°C for 5min, 90°C for 5min, and 65°C for 5min). After baking, the photoresist was developed in SU-8 Developer (Microchem) for 1 minute, using constant agitation. The developed wafer was rinsed in isopropyl alcohol for 1min, blown dry with a nitrogen gun and baked for 10 minutes at 95°C on a hotplate.

Agarose micropatterned glass coverslips that contained adhesive and non-adhesive domains were fabricated using methods adapted from a technique developed by Nelson and Chen[81]. Full details of the technique can be found in Chapter 3. Briefly, a poly(dimethylsiloxane) (PDMS) (Sylgard 184, Superior Essex, Atlanta, GA) stamp was generated from a silicon master described above. The PDMS stamp was placed, patterned side down, against a 12 mm diameter glass coverslip (#1.5, Fisher Scientific, Suwanee, GA) such that only the raised posts were in contact with the coverslip. A small volume of 100% ethanol (~5μL) was pre-wicked into the 'mold' created by the PDMS stamp and the coverslip. After the ethanol dried, a solution of 0.6% agarose (Invitrogen)/40% ethanol in water was heated while stirring to the boiling point, and dispensed along the edge of the stamp/coverslip mold. The agarose was allowed to dry undisturbed on the benchtop for approximately four hours. The PDMS stamp was then carefully removed, resulting in a coverslip with bare glass islands surrounded by agarose. Substrates were sterilized in 70% ethanol/30% diH_20, rinsed twice with DPBS and incubated (37°C, 5% CO_2) for 30 minutes to 12 hours until coated with adhesion ligand.

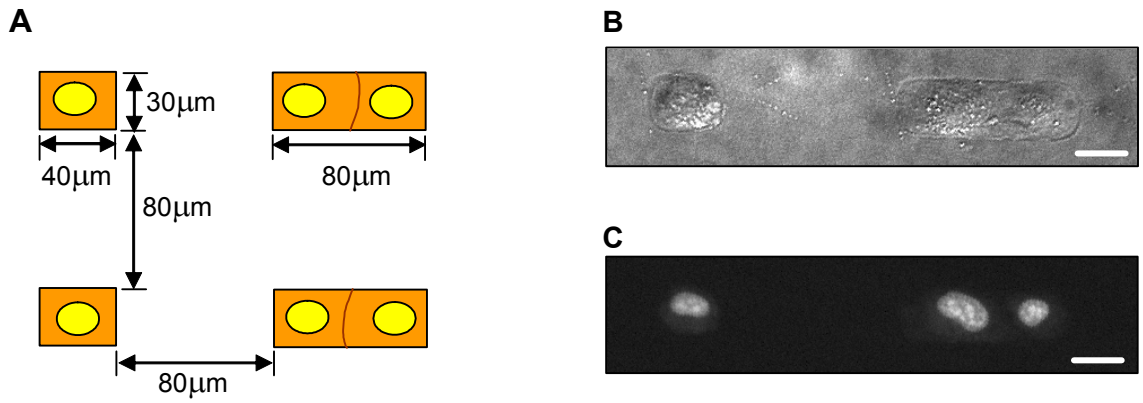

Figure 6.2 BPAEC one- and two-cell micropatterns. (A) Schematic of cell micropattern dimensions and array spacing. (B) Bright field micrograph of BPAEC cells cultured in one-cell (*left*) and two-cell (*right*) patterns. (C) Epifluorescence micrograph, with nuclear staining using SYTO13 to identify individual cells in patterns. Scale bars represent 30µm.

6.3.3 Sample Preparation

For cryomicroscopy experiments, BPAECs were subcultured and seeded onto patterned coverslips, and incubated (37°C, 5% CO_2) for 6 hours ± 30min post-seeding. Coverslips were incubated for 10 min at 37°C with medium supplemented in 2 µM SYTO13 (Molecular Probes, Eugene, Oregon), a nucleic acid stain, and 10 µM ethidium homodimer (EthD-1) (Molecular Probes), a membrane impermeant stain, to ensure that each micropattern contained a single cell with full membrane integrity. Immediately prior to freezing, coverslips were rinsed with in 30 mM HEPES (Cambrex). For all experiments, the cell culture coverslip was removed from the petri dish, inverted, and placed on a 16 mm diameter glass coverslip (Linkam Scientific Instruments, Tadworth, Surrey, UK), creating a sandwich.

6.3.4 High Speed Digital Video Cryomicroscopy

A novel high-speed video cryomicroscopy system was created to observe IIF at sub-millisecond time scales in single attached cells. Full details of the system can be found in Chapter 3. Briefly, the system consisted of an upright Eclipse ME600 microscope (Nikon, Tokyo, Japan) fitted with a commercially available cooling stage (FDCS 196, Linkam). System calibration was conducted by measuring the melting point of ice crystallized from a sample of purified water. Experiments were recorded using a high speed digital camera (FastCam-X 512PCI, Photron, Tokyo, Japan) and corresponding software (FastCAM Viewer, version 2.2; Photron).

For all experiments, images were acquired at a rate of 4,000 Hz, with an exposure time of 130 μsec. Maximum recording time was limited to approximately eight seconds with the settings used. For all high speed experiments, cells were observed using a 50X objective and 0.45X coupler (Nikon). To meet the light level requirements for high-speed imaging, all samples were frozen under Köhler illumination, with the microscope halogen lamp set to maximum output.

To promote IIF, cell cultures were frozen at a rapid rate (130°C/min) in the absence of cryoprotectants. Samples were prepared as described above, and placed in the sample holder located directly on top of the silver block, set to 37°C. After closing the cryostage chamber, the atmosphere was purged using liquid nitrogen vapor to prevent condensation. To seed extracellular ice, the sample temperature was cooled from 37°C to -1.5°C (at 50°C /min), and repositioned such that the edge of the sample was brought into contact with a seeding block (a silver block integrated into the cryostage stage and cooled to the temperature of the liquid nitrogen). Immediately after seeding the extracellular ice,

the sample was repositioned on the silver block and a cell was randomly selected for the experiment. Prior to the temperature plunge, both brightfield and fluorescent images were taken of the sample, to ensure that each pattern contained exactly one cell (nucleic acids stained by SYTO 13) with full membrane integrity (negative for Eth-Homo1 uptake). For all experiments, the focal plane of camera was set to the basal area of the attached cell. Prior to the temperature plunge, both brightfield and fluorescent images were taken of the sample. To minimize dehydration of the sample, the extracellular ice seeding, cell selection and imaging were performed in approximately 60 seconds. If this process took longer than three minutes, the experiment was abandoned. Immediately prior to the temperature plunge, the halogen lamp was set to maximum output, and the stage was cooled to -60°C at a controlled rate of 130°C/min. The high speed camera was set to record images into a circular buffer, and recording was terminated using a manual switch-closure trigger. When conventional indicators of intracellular ice formation (i.e. cell darkening and/or twitching) were observed, the trigger switch was closed, allowing the IIF event to be captured. Each experiment was analyzed frame-by-frame to identify the precise time, temperature and initiation site of the IIF event.

6.3.4 Cell-Cell Communication Assays

Two different dye transfer techniques were used to validate that intercellular communication was possible at our experimental conditions. First, scrape loading techniques[146,147] were used with confluent monolayers to verify that cell-cell communication had been established at six hours post-seeding. BPAECs were seeded at a high density onto fibronectin coated glass coverslips (unpatterned). At 6 hrs ±30 min, the coverslips were rinsed twice with 1X DPBS, with the final rinse aspirated off, using

care to not dry out the coverslips. Working in the dark, a small quantity (75μL) of dye solution, 1% lucifer yellow (Molecular Probes) and 10μM ethidium homodimer (EthD-1, Molecular Probes) in DPBS, was dispensed on top of the coverslip. A diamond cutter pen (Fisher Scientific) was then used to 'scrape' the monolayer, introducing the dye solution into the cells along the incision line. The coverslip (with dye solution) was returned to the incubator for two minutes. Following incubation, the dye solution was removed, and the coverslip was rinsed 4X in 1X DPBS. Standard culture medium was added to the dish and the coverslip was incubated for an additional 10 min at 37°C, 5% CO_2. Coverslips were fixed in 4% (v/v) paraformaldehyde (VWR) for 30 minutes and mounted on glass slides for quantification. Scrape loading was performed on six different coverslips, at approximately uniform intervals during the full 6 hr ± 30min time period after cell seeding. Coverslips were examined under epifluorescence microscopy (Nikon Eclipse ME600 microscope), using a 10X objective with 1X Coupler. Gap junction intercellular communication (GJIC) was considered to be active in cells that exhibited uptake of lucifer yellow but negative staining for EthD-1.

An ester dye-loading technique[148,149] was used to confirm cell-cell communication in our two-cell micropatterns. Briefly, a tissue culture flask containing a confluent monolayer of cells was loaded with a fluorescent dye solution (2μM calcein AM, 10μM DiI in serum-free medium) for 20 minutes at 37°C, 5% CO_2. After aspirating off the dye solution, the monolayer was washed four times in standard medium (with serum), with an incubation period of five minutes at 37°C between each wash. The culture in this flask, along with that in a second flask (not exposed to dye solution) was both trypsinized, and the two cell suspensions were seeded onto our micropatterned coverslips at a 1:1 ratio

(unloaded:loaded cells) and incubated for up to 24 hours at 37°C. Micropatterns that contained two BPAEC cells were observed under fluorescence microscopy at 15 minute intervals following seeding to qualify the extent of cell-cell coupling as a function of time. If an unloaded cell (negative for DiI) stained positive for calcein (cell permeable only through gap junctions), GJIC communication was determined to have been established.

6.3.5 Statistical Analysis

Unless otherwise noted, data are reported as mean ± standard error of the mean as noted. When reporting the classification of events into categories, standard deviations were estimated by taking the square root of the number of observations in each category. If groups had a normal distribution and homogenous variances, the group means were compared by an independent *t*-test, or by analysis of variance (ANOVA), with post hoc analyses using Tukey's test. Differences were considered significant at the 95% confidence level ($p < 0.05$).

6.4 Results

The effect of cell-cell interactions on IIF was investigated using BPAECs cultured in one and two-cell micropatterns (shown in Figure 6.2). For both the single cell (30x40μm) and two-cell (30x80μm) patterns, the available attachment area for each cell was limited on average to a 30x40μm area. By designing the patterns in this manner, the single cell pattern served as a control, to assess if the rate of spontaneous ice formation, J_i, was affected by cell-cell contact[61]. Prior to freezing, cells were cultured for six hours,

a time point selected based on the doubling rate for our cell population (~15 hours). Time in culture has been shown previously to influence IIF[61,139,140,150]. Thus, to ensure that each cell analyzed had the same post-seeding culture time (*i.e*. to reduce the probability of analyzing a recently divided cell) frozen at a time that was less than half of the population doubling time.

The existence of gap junction intercellular communication (GJIC) was verified in our micropatterned cells using two different assays. To confirm that GJIC was active six hour post-seeding, confluent monolayers were scrape loaded to introduce the polar tracer lucifer yellow (only permeable through gap junctions; MW 457.24 g/mol) and ethidium homodimer (EthD-1, not permeable through intact membranes or gap junctions) into the cells. Cells that had been injured through the physical scrape would uptake both lucifer yellow and EthD-1. Neighboring cells in the monolayer that had established GJIC would contain lucifer yellow (only permeable through gap junctions), but not EthD-1. Figure 6.3 shows a representative result from a scrape-loading, illustrating dye transfer up to five cells deep. Dye transfer was evident in all coverslips analyzed, indicating that GJIC had been established in the BPAEC monolayers after six hours in culture.

Since scrape loading of two-cell micropatterns was physically impossible, an ester-loading technique was used to verify GJIC in our two-cell micropatterns. Briefly, a monolayer of BPAECs was loaded with the fluorescent dyes calcein-AM and DiI. The lipophilic dye DiI acts as a cell tracer, staining the plasma membrane with a red fluorescence, whereas calcein fluoresces green intracellularly, and is only cell permeable through gap junctions. These donor cells were seeded onto our two-cell micropatterns alongside unstained BPAECs serving as recipients. Analysis of the ester-loading

communication assay began with the identification of all two-cell patterns that contained a single donor cell (red and green fluorescence) in contact with a single unloaded cell (negative for red fluorescence). For all cell pairs staining with this pattern, cell-cell coupling was determined by the presence of calcein in the recipient cell. All two-cell patterns were analyzed in real-time, observing the coverslips under epifluorescence every 15 minutes. Dye transfer was confirmed within 45 minutes of seeding time. Within 1.5 hours, all eligible cells in two-cell patterns had established GJIC. Thus, our ester-loading data confirms successful cell-cell communication was established in our two-cell micropatterns within 1.5 hours post-seeding (see Figure 6.4). Additionally, our scrape loading results verify that GJIC was active specifically at six hours post seeding.

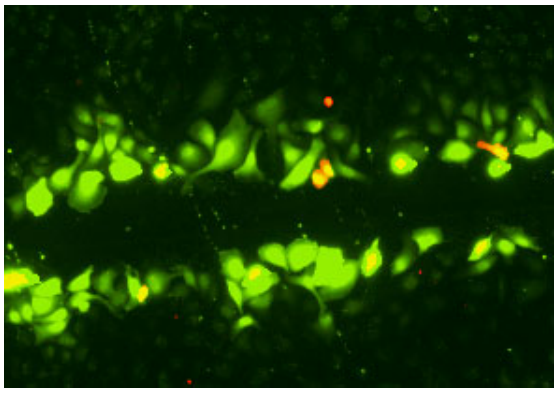

Figure 6.3 Scrape loading of BPAEC monolayer at 6 hours. Micrograph of a representative epifluorescent image taken during scrape loading experiments. Fluorescent dye was introduced into monolayers of BPAEC cells six hours post seeding through scrape loading, to determine if GJIC had been established. Red cells indicate uptake of EthD-1, denoting the cells that were initially loaded with fluorescent dye. Green cells indicate the presence of lucifer yellow (cell permeable only through gap junctions). Any cell that stains green (but not red) was determined to have established GJIC.

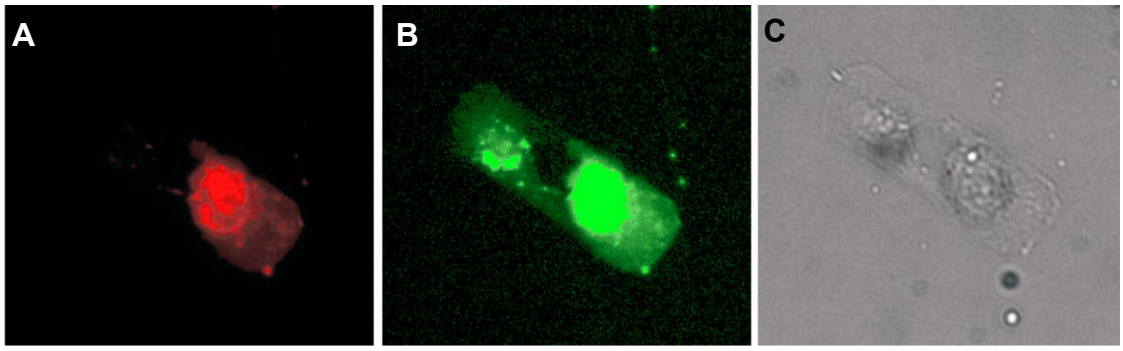

Figure 6.4 Evidence of gap junction communication in BPAECs cultured for two hours in micropatterns. Two cells, one loaded with calcein and DiI, and one cell containing no fluorescent dye, were seeded onto our two-cell micropatterns. After two hours of culture time, images were obtained of the (A) red fluorescent signal to identify cells originally loaded with the ester-dye solution, and (B) green fluorescent signal to identify cells that contained calcein. For reference, a brightfield image of the cell pair was also obtained (C). Cells that stain positive for green fluorescence (calcein) but negative for red fluorescence (DiI) indicate that GJIC communication has been established with a neighboring 'loaded' cell, providing entry of calcein.

Having verified that cell-cell communication was established in our two-cell micropatterns, single (n = 148) patterns were frozen at a rapid rate (130°C/min) to -60°C after six hours in culture. All single cell cryomicroscopy experiments (30x40μm patterns), exhibited similar behavior to that reported in Chapters 3, 4, and 5. Briefly, a single IIF event manifesting as an advancing front, occurred in each cell, with the majority of phase transformation events initiating at the cell periphery (85.1% ±7.6%). After the ice front traveled through the micropatterned cell, a gradual darkening of the cell would commence. Additionally, the phenomenon of paracellular ice dendrite formation was observed in 25 ± 4.1% of the single adherent cells.

For our two-cell experiments (30x80μm patterns, n = 102 pairs), the first cell in the pair to freeze behaved similarly to the single-cell patterns. However, for the second

cell in the pattern, IIF would initiate shortly after the first cell froze, with 84.3 ± 0.1% of IIF events initiating at the cell-cell interface. A series of micrographs from a representative two-cell cryomicroscopy experiment is presented in Figure 6.5.

Next, we compared the distribution of IIF initiation sites in single and two-cell constructs. As shown in Figure 6.6, for the majority of our single cell micropatterns (no cell-cell contact), IIF events initiated at the cell periphery. In two-cell constructs, we distinguished between initiation sites at the cell-cell interface and those at the remainder of the cell periphery. In two-cell constructs, the probability that the first IIF initiation event occurred at the cell periphery was ~30%, less than the corresponding probability of IIF in single-cell constructs. This decrease corresponds approximately to the ~20% loss of the cell perimeter resulting from cell-cell contact. As shown in Figure 6, for the second cell in the pair to freeze, the probability of IIF initiation at the cell-cell interface is almost three times the corresponding probability in the first cell to freeze.

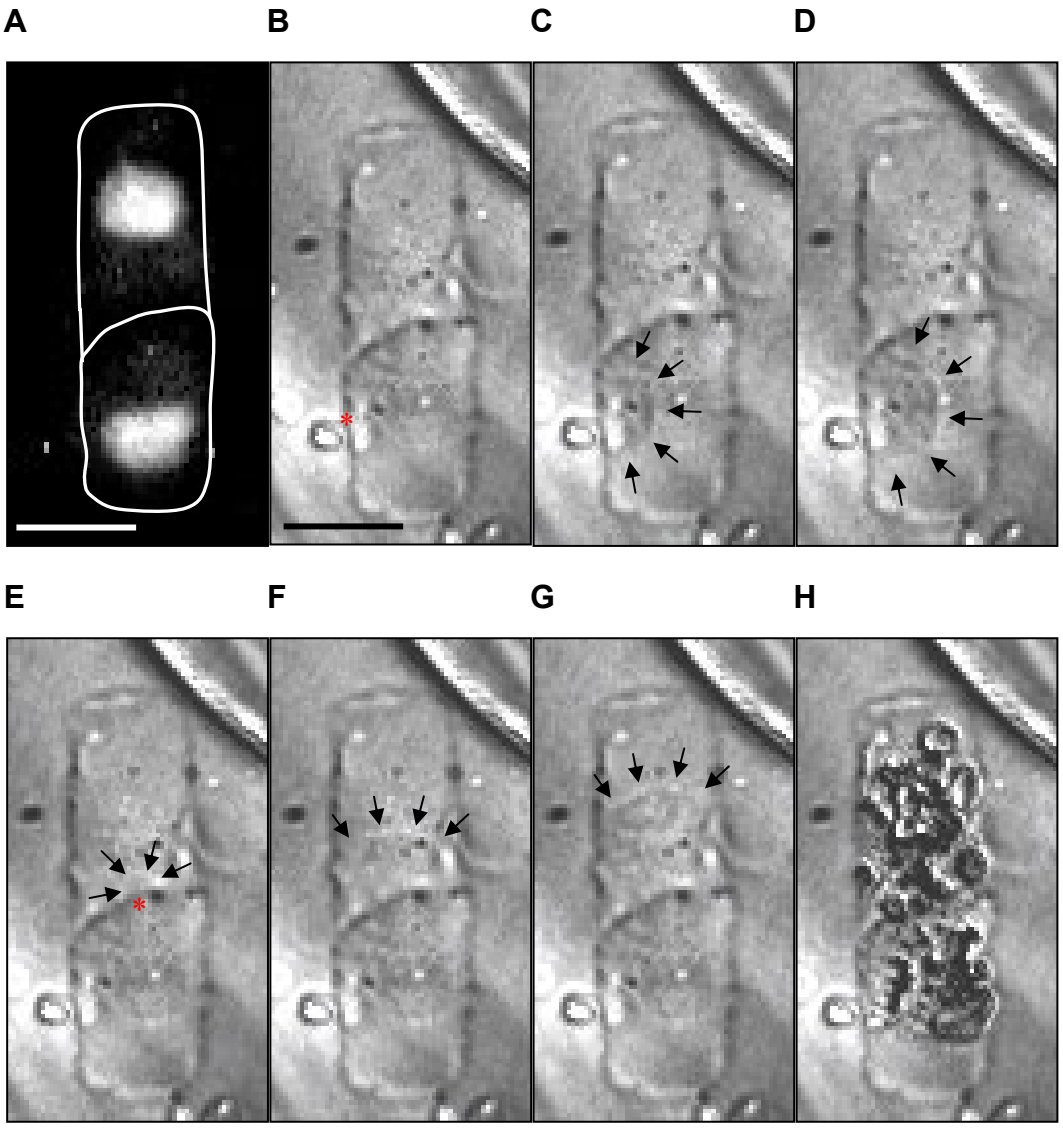

Figure 6.5 Micrographs from a 2-cell BPAEC high speed cryomicroscopy experiment. (A) Fluorescent image of SYTO13, indicating that there are exactly two cells in the pattern. Cells were outlined (white lines) to indicate their positions. (B) Micrograph of cell pair at the frame of IIF initiation, with red asterisks indicating IIF initiation site (Δt = 0 *msec*, Temp = -26.44°C). (C) Micrograph of two-cell pair shortly after IIF initiation in the first cell, with the leading edge of the IIF front indicated by black arrows (Δt = 1.5 *msec*) (D) IIF front continues to travel through the first cell, approaching the cell-cell interface (Δt = 2.0 *msec*) (E) Micrograph of cell pair shortly after IIF initiated in second cell, with the second initiation point indicated by red asterisks (Δt = 3.5 *msec*) (F) IIF front from second IIF event travels upward in the cell (Δt = 4.5 *msec*). (G) The front from the second IIF event continues to travel through the cell (Δt = 5.5 *msec*). (H) Micrograph of the fully frozen cell pair, with darkening and bubble formation evident (Δt = 634 *msec*). Scale bars represent 30μm.

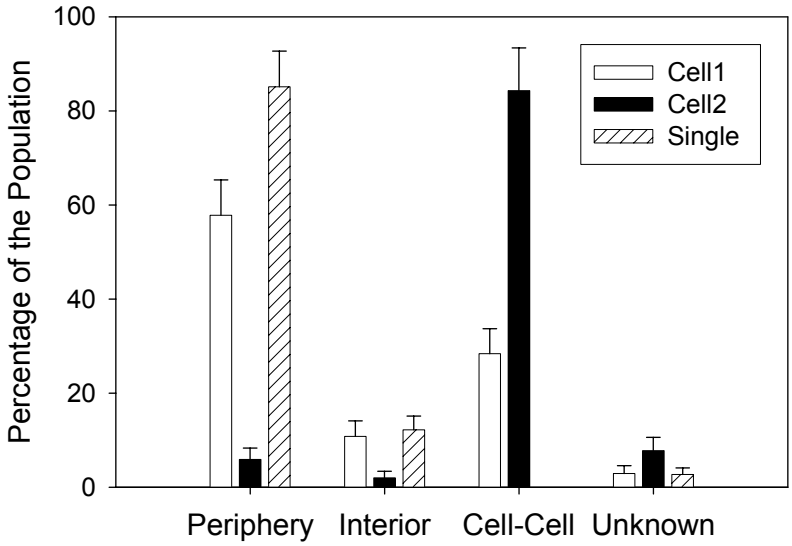

Figure 6.6 Initiation point of IIF in one- and two-cell patterns. The IIF initiation point was determined for the first cell ('cell 1', open bars), and the second cell ('cell 2', black bars) to freeze in a 2-cell pair, as well as for single BPAECs in 30x40μm patterns ('single', hatched bars). Bars represent the standard deviation.

The kinetic data obtained from our experiments was used to calculate the cumulative probability of IIF as a function of temperature for the single and two-cell patterns. As shown in Figure 6.7, the cumulative probability for the two-cell data (blue squares) is similar to the single cell data (green circles). This result suggests that for primary endothelial cells, the kinetics of IIF in one and two-cell patterns are approximately the same. Figure 6.7 also shows the kinetics associated with spontaneous IIF initiation in the cell pair (open squares), calculated using Equation 6.10. If the rate of spontaneous IIF initiation, J_i, was independent of cell-cell contact, the probability of spontaneous IIF in the two-cell constructs should equal the cumulative probability of IIF in the single cell patterns. However, it is evident from the data that the introduction of cell-cell contact significantly decreased the spontaneous nucleation rate, J_i.

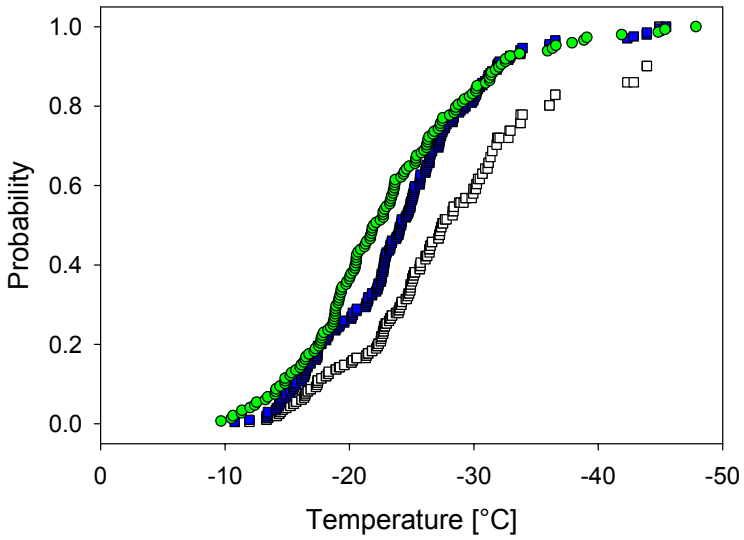

Figure 6.7 Cumulative probability of IIF in one- and two-cell micropatterns. Cells were cultured in one-cell patterns (green circles) or two-cell patterns (blue squares) before freezing. The probability for spontaneous ice formation in the two-cell constructs was calculated using Equation 6.10 (open squares). See text for details.

From our high speed cryomicroscopy data, we were able to quantify the time delay between the initiation of IIF in the first cell and the initiation of IIF in the second cell each two-cell pair. This time delay represents the persistence time, Δt, for the singlet state and can be used as an indicator of the kinetics of intercellular ice propagation. The cumulative probability distribution of Δt for the two-cell data is presented in Figure 6.8. For all two-cell experiments, the median persistence time was determined to be 14.75 ms. Our data indicate that for the majority of the population, ice propagation occurs at a fast rate, whereas a small portion of the population exhibited long lag times between subsequent IIF events, sometimes on the order of seconds. The data were transformed to investigate the early rise in persistence time (Figure 6.8B), allowing for analysis of the fastest events. As shown in Figure 6.8B, the kinetics of the fastest propagation events exhibited an initial linear rise. Linear regression for this initial rise (with intercept forced through the origin) yielded a best fit line with a slope of 48.6 ± 1.6 nucleation events/s (R^2 = 0.95). Thus, the kinetics of the fastest propagation events are consistent with a Poisson process, with a characteristic rate, J_p, of ~50 events per second.

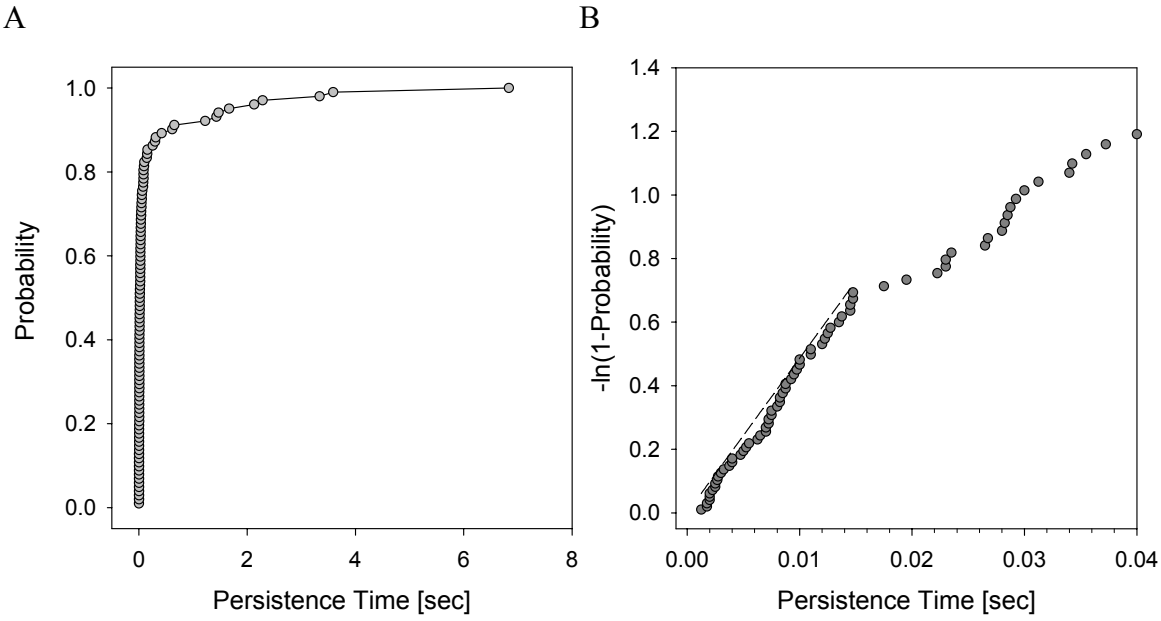

Figure 6.8 Cumulative probability of the singlet state persistence time. (A) The persistence time, Δt, represents the time delay between the partially frozen (singlet) state and fully frozen (doublet) state. After a rapid initial rise, a small portion of the data possesses a significantly large lag time between successive IIF events. (B) Transform of cumulative probability to investigate the early kinetics of propagation in the two-cell patterns; linear regression is also shown (dashed line).

Our two-cell cryomicroscopy data were used to determine the probabilities of the unfrozen (P_0), singlet (P_1), and doublet (P_2) states as a function of temperature (Figure 6.9). The results are consistent with previous theoretical predictions[58], with a monotonic decrease of the number of unfrozen pairs, P_0, and a corresponding increase in the number of fully frozen pairs, P_2. The probability of the singlet state exhibited a slight transient increase, but is relatively close to zero. Using Equation 6.10, a prediction was made for the hypothetical case of no intercellular ice propagation between cells, or $\alpha = 0$ (*i.e.* only the mechanism of spontaneous IIF initiation, with rate J_i, is active). Comparing this hypothetical case (dashed line) with the measured singlet state (red diamonds), it can be seen that the actual singlet state probabilities were significantly lower, indicating that intercellular ice propagation did in fact occur.

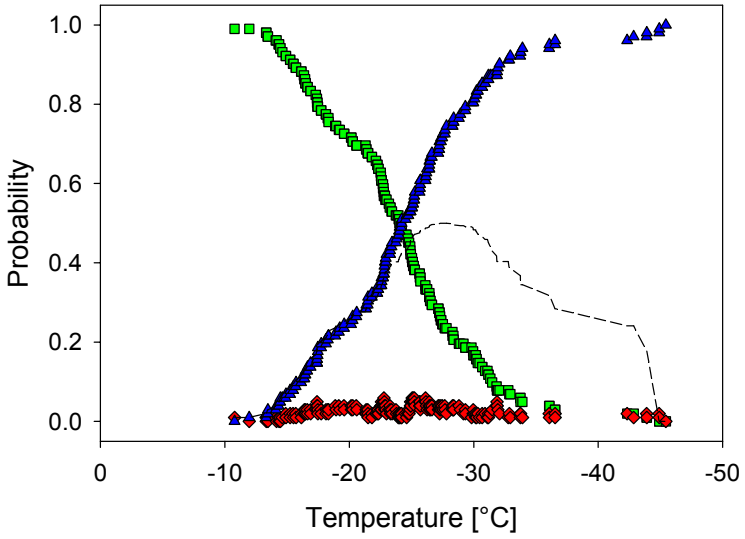

Figure 6.9 Probability of IIF states during freezing of two-cell BPAEC patterns. The probabilities of the unfrozen state, (P_0, green squares), singlet state (P_1, red diamonds), and doublet state (P_2, blue triangles) are shown for BPAECs frozen to -60°C at a rate of 130°C/min. Also shown is the hypothetical probability of the singlet state (dashed line), assuming no intercellular ice propagation ($\alpha = 0$), determined using Equation 6.10.

From the theoretical model developed by Irimia and Karlsson[58], the probability of the singlet state, P_1, was found to be sensitive to the value of the non-dimensional intercellular ice propagation rate, α. Thus, assuming that the non-dimensional intercellular ice propagation rate is approximately constant for our experimental conditions, α can be determined from our measured probabilities of the singlet state, P_1, by fitting the theoretical solution (Equation 6.12) to the data. Prior to applying the nonlinear regression, the temperatures were converted to non-dimensional time, τ, using Equation 6.11. The results of this analysis are presented in Figure 6.10, with nonlinear regression yielding a best fit $\alpha = 42.0 \pm 2.3$.

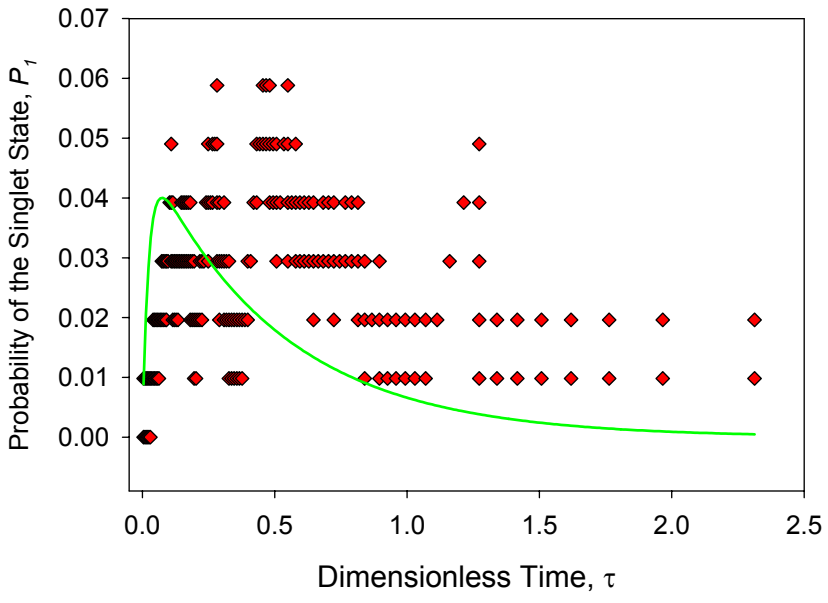

Figure 6.10 Propagation rate determination in BPAECs. Probability of the singlet state, P_1, measured during cryomicroscopy of BPAECs cultured in micropatterned pairs (red diamonds) and predicted using the best fit of Equation 6.12 (solid green line).

An alternative explanation for the apparent intercellular ice propagation of ice is the possibility that the IIF events in the two cells micropatterned in close vicinity to one another are not independent (for example, as a result of interactions with extracellular ice). Thus, to investigate any potential role that the extracellular ice crystals may have in correlating IIF events in the neighboring cells, two single BPAEC cells were frozen in the same cryomicroscopy experiment (n = 72 'pairs' or 144 cells). Effectively, this was the same as freezing a two-cell pair, but forcing an 80μm separation distance between each cell in the pair (eliminating cell-cell contact and communication). Assuming a random and independent distribution of IIF events along the perimeters of each 30x40μm pattern, the probability of IIF initiating at the same location for a two cell pair would be 25% (four different sides). Analyzing the initiation site in each cell 'pair', 24.7% ±5.8% of all IIF events initiated on the same edge of the pattern; which indicates that initiation sites in the two cells are not correlated.

The freezing kinetics in these disconnected cell 'pairs' were investigated in the same manner as the tradition two-cell micropatterns. Namely, the probability of the unfrozen, singlet and doublet states were calculated as a function of temperature (Figure 6.12). Again, the hypothetical case of no intercellular ice propagation between cells, or $\alpha = 0$ (*i.e.* only the spontaneous nucleation rate, J_i, is active) was predicted using Equation 6.10. This time, comparison of the hypothetical case (dashed line) with the measured singlet state (red diamonds), indicated that the two curves were statistically similar ($p = 0.48$). Thus, it was concluded that no intercellular ice propagation occurred

in BPAECs separated by 80µm, suggesting that extracellular ice interacting with the cells does not lead to correlation between the two IIF events.

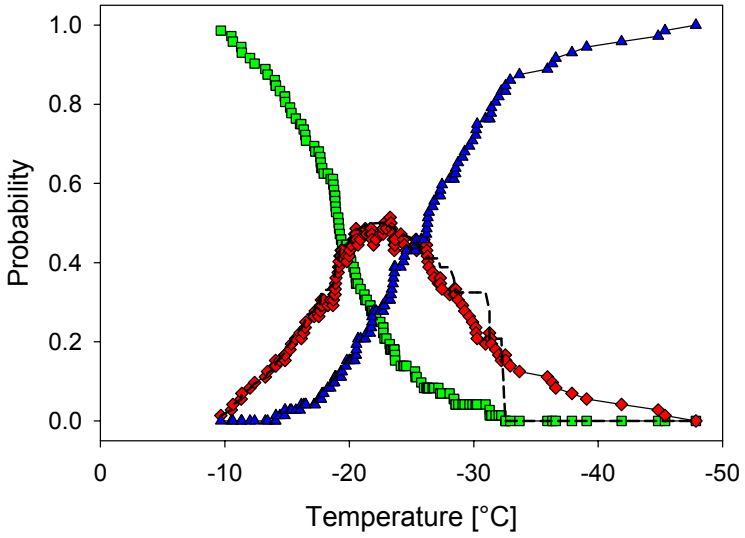

Figure 6.11 Probability of IIF states during freezing of single BPAEC patterns, separated by 80µm distance. The probabilities of the unfrozen state, (P_0, green squares), singlet state (P_1, red diamonds), and doublet state (P_2, blue triangles) are shown for pairs of single BPAECs (physically separated by 80µm) frozen to -60°C at a rate of 130°C/min. Also shown is the hypothetical probability of the singlet state (dashed line), assuming no intercellular ice propagation ($\alpha = 0$), determined using Equation 6.10.

6.5 Discussion

Monolayers and tissues have long been known to have an increased susceptibility to ice formation in comparison with single suspended or attached cells[6,58,60,63,64]. One of the major factors hypothesized to contribute to this increased rate of ice formation is the introduction of cell-cell contacts[60]. In the last decade the first major studies to specifically investigate the effects of cell-cell interactions on IIF, and have primarily focused on the role of gap junctions in ice propagation[56,57]. However, for the majority of

these studies, investigations have been limited to cell monolayers[57], or small aggregates of cells[56,72], introducing many confounding factors (*i.e.*, time in culture, degree of cell spreading, and mass transport limitations) that are known to affect IIF. Many of these limitations were addressed by Irimia and Karlsson[58,59], who conducted the first cryomicroscopy experiments using PEG micropatterned cell cultures. In their two studies, HepG2 cells were micropatterned in one-, two-, and four-cell arrays, and were subsequently frozen with and without the addition of a known gap junction blocker, 18β-glycyrrhetinic acid. Using conventional cryomicroscopy techniques, their data indicated that the spontaneous nucleation rate, J_i, was independent of cell-cell contact, and gave strong support for ice propagation through gap junctions. Irimia and Karlsson's study was limited by the use of HepG2 cells, a transformed hepatoma cell line that is known to have low expression levels of connexins[74], and has been shown to have limited GJIC under standard culture conditions[75]. Yet for all of these studies, the largest impedance against obtaining an accurate description of the kinetics of ice propagation results from the conventional techniques used to measure IIF.

This study provides the first direct measurement of the kinetics of intercellular ice propagation in two-cell micropatterned pairs, at sub-millisecond resolution. Intercellular ice propagation is a rapid event that occurs within a few milliseconds of the initial IIF event. Conventional cryomicroscopy systems are limited to a temporal resolution of 33ms, which results in an inability to describe the kinetics for the fastest propagation events. Recording at 30Hz, Irimia and Karlsson[59] reported that 123 cell pairs, or 50% of the total population, had IIF in both cells of the pair in the same video frame. For the two-cell experiments presented in this chapter, 65% of all cell pairs were completely

frozen within 30ms (or the span of a single frame in conventional video). It should also be noted that in all conventional cryomicroscopy, cell darkening is used as the primary indicator of IIF. As reported in Chapter 3, cell darkening is an indirect indicator of IIF and the kinetics of darkening vary based on IIF temperature.

The use of cell micropatterns allowed for the unique opportunity to rigorously analyze the kinetics of IIF and propagation with theoretical models. Using the propagation model developed by Irimia and Karlsson[58], our results indicated that the rate of IIF in two-cell constructs was not increased by the presence of cell-cell contact. This result can be explained, in part, by the decrease in the spontaneous nucleation rate, J_i, as cell-cell contact was introduced. The spontaneous IIF initiation rate has been hypothesized to be independent of cell-cell contact, a claim that was supported by Irimia and Karlsson[58] in their study of HepG2 cells. However, in their study, verification of cell-cell communication was never established, especially important considering the decreased expression of gap junction proteins in HepG2 cells[74]. Primary bovine endothelial cells were selected for this study, in part due to their high expression levels of connexin proteins[88,89]. Verification of cell-cell communication was obtained, with data indicating that gap junction intercellular communication was established within 1.5 hours for all micropatterned cell pairs, in agreement with data in the literature[148,149]. Thus, it is possible that extensive cell-cell contact may decrease the kinetics of the spontaneous nucleation rate for our experimental system. This possibility is supported by data in the literature, in which controlled cell-cell contact in micropatterned BPAECs resulted in a decrease in cell adhesion and cytoskeletal tension[84,151]. Additionally, as reported in Chapters 3 and 4, changes in the cell focal adhesion arrangement (a consequence of

altered adhesion state and cell-cell contact) can influence the kinetics of IIF. Further investigation would be required to determine the exact cause of the decrease in J_i in our data.

The temporal resolution of our cryomicroscopy system allowed for the identification of the IIF initiation site for each cell in the micropatterned pair. As expected, the majority if IIF events for the second cell (transitioning from the partially frozen to fully frozen state) initiated at the cell-cell interface. Intercellular ice propagation was confirmed to be present in our micropatterned endothelial cell pairs through the analysis of the probability of states. The non-dimensional rate of propagation, α, was determined to be ~42 for our endothelial cell patterns, by fitting our data to model predictions. However, it should be noted that the fit was not ideal. The theoretical prediction of the singlet state is successful within a certain range (*i.e.,*variations in α over three orders of magnitude). For BPAECs in two-cell pairs, the propagation rate was so high; we were no longer in the ideal range for the model. It is also possible that more than one non-dimensional propagation rate is required to accurately describe the kinetics of ice propagation for endothelial cells. However, the results of the fit still provide a reasonable estimate of α, indicating that the non-dimensional propagation rate is large; specifically, four times larger than the propagation rate measured in HepG2 cells (α = 10.4 for HepG2)[59]. If intercellular ice were propagating through gap junctions[56], an increase in propagation rate would be expected for endothelial cells, due to their high level of connexin expression[88]. In turn, this study lends additional support to the theory of ice propagating through intercellular pores. The spatial location of each IIF event in cell 2 (at the cell-cell interface) and the increase in

propagation rate for a connexin-rich cell source, all are consistent with the hypothesis that ice is propagating through gap junctions. However, classifying propagation as solely due to propagation through gap junctions is premature at this juncture.

Analysis of the persistence time, or the time delay between each IIF event in the two-cell pair, indicated that the majority of the two-cell population exhibited rapid propagation kinetics, characteristic of a Poisson process. The data also suggests that there may be two different kinetic rates for propagation in our primary cell patterns. After the initial rapid rise in kinetics (the majority of cell pairs transitioned from the singlet to doublet state within 15ms), the subsequent time delay increased to larger lag times, on the order of seconds. This observation is similar to the fast and slow mechanisms of ice propagation reported by Irimia and Karlsson[58].

The results of this study have shown that cell-cell contact does not increase the probability of IIF for BPAECs cultured in micropatterned cell pairs. Rather, cell-cell contact decreased the rate of spontaneous initiation of IIF for the cell-pair, effectively negating the increase in kinetics due to ice propagation. Intercellular ice propagation was determined to occur with a non-dimensional rate of propagation equal to 42, a four-fold increase from the measured rate of propagation in a transformed cell line (HepG2). The study also reports the first measurement of the kinetics of the fastest propagation events for interacting cells. The results of this work provide significant insights into mechanisms of ice propagation between two interacting cells. Similar to the successes with modeling IIF in single suspended cells, understanding the complex processes that initiate IIF and ice propagation will be critical to developing model-based protocols for cryopreservation and cryosurgery.

CHAPTER 7

EFFECT OF CELL-CELL CONTACT AREA ON INTERCELLULAR ICE PROPAGATION IN HUMAN ENDOTHELIAL CELLS

7.1 Introduction

As described in Chapter 6, primary bovine endothelial cells were shown to exhibit intercellular ice propagation at a significantly higher rate than previously measured for a human heptocellular carcinoma cell line[58]. In addition, when an unfrozen cell was in direct contact with a frozen cell it was shown that IIF initiation preferentially occurred at the cell-cell interface, consistent with the previously proposed hypothesis that ice can propagate through gap junctions[56,96]. Since gap junctions are located at the cell-cell interface, we hypothesized that increasing the degree of cell-cell contact would increase the rate of intercellular ice propagation. Thus, the primary goal of the study presented in this chapter was to investigate the effects of cell-cell interactions on the rate of intercellular ice propagation by carefully controlling the degree of cell-cell contact.

The rectangular patterns used to investigate the effects of cell-cell interactions in studies described in Chapter 6 successfully limited the number of cells in the patterns (2 cells), as well as maintained a relatively reproducible degree of cell-cell contact. However, the bovine endothelial cells did not always occupy exactly 50% of the rectangular pattern, resulting in sample-to-sample variations in cell-substrate contact area. In addition, the bovine cells would often grow with a degree of angularity at the cell-cell interface. Thus, to provide precise control over the degree of cell-cell contact,

we designed a new two-cell system based on a bowtie pattern configuration previously shown to be successful in investigating cell-cell communication between endothelial cells[81,151].

In addition to changes in the two cell micropattern design, a new endothelial cell source, human aortic endothelial cells (HAECs), was used for this study. The change in cell type was motivated in part by future research plans to incorporate short-interfering RNA (siRNA) techniques to alter expression of connexin proteins (the components of gap junctions)[152,153]. Additionally, human endothelial cells would be a more relevant cell source for tissue engineering applications, as well as a likely target for destruction in cryosurgery.

Motivated by the high rate of intercellular ice propagation measured in bovine endothelial cells (Chapter 6), the present study investigated changes in the rate of ice propagation as a function of cell-cell contact. For this investigation, micropatterning techniques were used to provide precise control of the degree of cell-cell contact in human endothelial cells during freezing. The results of this work will further elucidate the dominant factors that govern the rate of ice propagation in attached cells, providing potential strategies to control intercellular ice propagation.

7.2 Materials and Methods

7.2.1 Human Aortic Endothelial Cell Culture

Human aortic endothelial cells (HAECs) (Cambrex, San Diego, CA) were cultured in MCDB 131 media (Mediatech, Herndon, VA) supplemented with 5% (v/v)

fetal bovine serum (Sigma-Aldrich, St. Louis, MO), 2ng/mL basic human fibroblast growth factor (PeproTech, Rocky Hill, NJ), 10ng/mL human epithelial growth factor (Invitrogen Corp., Carlsbad, CA), 1ng/mL vascular endothelial growth factor (Sigma-Aldrich), 2 ng/mL insulin-like growth factor-1 (Invitrogen), 0.001 mg/mL hydrocortisone (Sigma-Aldrich), 2mM L-glutamine (Mediatech), 100U/mL penicillin/100µg/mL streptomycin (Invitrogen), and 50 µg/mL ascorbic acid (Sigma-Aldrich). Cells were cultured on tissue culture plastic at 37°C in a humidified 5% CO_2 environment and media was replaced every 48 hours. Flasks where subcultured when they reached 70-85% confluency and were split at a 1:4 ratio, following the recommendations of the vendor (total exposure time to trypsin-EDTA (Cambrex, Cat# CC-5012) was 5 minutes). Cells were seeded onto fibronectin coated micropatterned coverslips at passages 7 through 10.

7.2.2 Fabrication of Micropatterned Substrates

Standard photolithography techniques were used to create silicon masters that contained bowtie patterns with variable cell-cell contact area (see Figure 7.1). Briefly, in a class 10 cleanroom, silicon wafers were spin-coated with SU-8 photoresist (Microchem Co., Newton, MA) to a thickness of 7µm. Substrates were baked on a hotplate at 65°C for 2 min, ramped to 95°C for 5 min, and then returned to 65°C. Microfiche films were used as photomasks (see Chapter 4) by placing the microfiche directly onto the photoresist-coated wafer. A blank photolithography mask (Photronics, Brookfield, CT) was used to gently sandwich the microfiche against the wafer. The photoresist-coated substrates were exposed under UV (9.65 $mJ \cdot cm^{-2} \cdot s$ at 405nm) for 16.5 seconds, using an OAI mask aligner (Optical Associates, Inc, San Jose, CA) in contact mode. Post-exposure, the microfiche was removed and the substrate was baked on a hotplate (65°C for 1min, 95°C

for 1min, and 65°C for 1min). After baking, the photoresist was developed in SU-8 Developer (Microchem) for 1 minute, under gentle agitation. The developed wafer was rinsed in 100% isopropyl alcohol for 1min, blown dry with a nitrogen gun and baked for 10 minutes at 95°C on a hotplate.

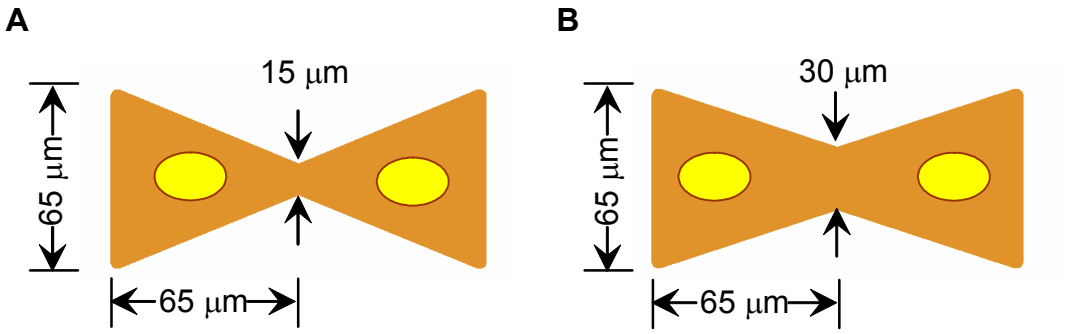

Figure 7.1 Schematic of HAEC bowtie micropatterns with (A) 15 μm and (B) 30 μm cell-cell contact distance.

Agarose micropatterned glass coverslips that contained adhesive and non-adhesive domains were fabricated using methods adapted from a technique developed by Nelson and Chen[81]. Full details of the technique can be found in Chapter 3. Briefly, a poly(dimethylsiloxane) (PDMS) (Sylgard 184, Superior Essex, Atlanta, GA) stamp was generated from a silicon master described above. The PDMS stamp was placed, patterned side down, against a 12 mm diameter glass coverslip (#1.5, Fisher Scientific, Suwanee, GA) such that only the raised posts were in contact with the coverslip. A small volume of 100% ethanol (~10μL) was pre-wicked into the 'mold' created by the PDMS stamp and the coverslip. After the ethanol dried, a solution of 0.6% agarose (Invitrogen)

and 40% ethanol (Fisher Scientific) was heated while stirring to the boiling point, and dispensed along the edge of the stamp/coverslip mold. The agarose was allowed to dry undisturbed on the benchtop for approximately 2 hours. The PDMS stamp was then carefully removed, resulting in a coverslip with bare glass islands surrounded by agarose. Substrates were sterilized in 70% ethanol/30% diH_20, rinsed twice with DPBS and incubated (37°C, 5% CO_2) up to 12 hours before coating with adhesion ligand.

7.2.3 Sample Preparation

For cryomicroscopy experiments, HAECs were trypsinized and seeded onto patterned coverslips, and incubated (37°C, 5% CO_2) for 18 hours ± 5% post-seeding (see Figure 7.2). Coverslips were incubated for 10 min at 37°C in medium supplemented with 2 μM SYTO13 (Molecular Probes, Eugene, Oregon), a nucleic acid stain, and 10 μM ethidium homodimer (EthD-1) (Molecular Probes), a membrane impermeant stain, to ensure that each micropattern contained a two cells cell with full membrane integrity. Immediately prior to freezing, coverslips were rinsed with in 30 mM HEPES (Cambrex). For all experiments, the cell culture coverslip was removed from the petri dish, inverted, and placed on a 16 mm diameter glass coverslip (Linkam Scientific Instruments, Tadworth, Surrey, UK), creating a sandwich.

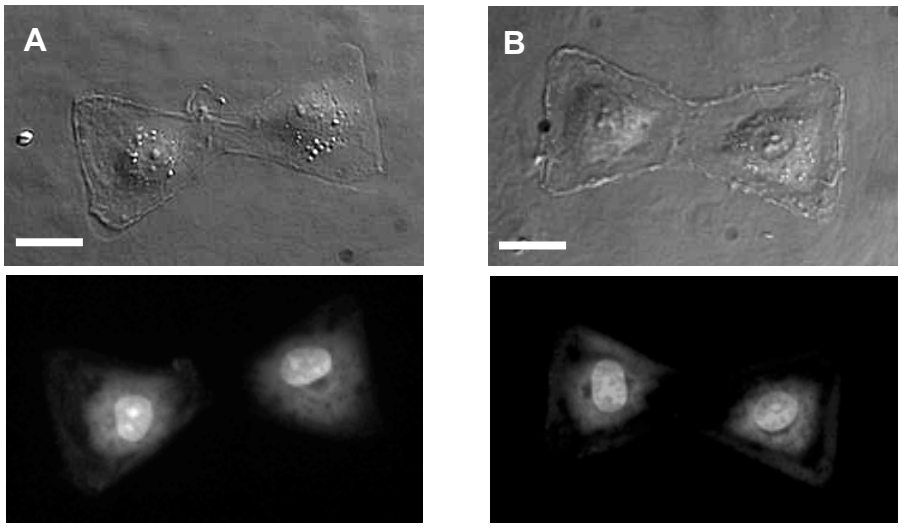

Figure 7.2 HAECs cultured in bow-tie micropatterns for 18 hours. Micrographs of HAEC cells cultured in two-cell bowtie patterns with (A) 15 μm and (B) 30 μm cell-cell contact distance. Top images were obtained in DIC; bottom images are nuclear staining using SYTO13, used to identify individual cells in patterns during freezing. Scale bars represent 30μm.

7.2.4 High Speed Digital Video Cryomicroscopy

A novel high-speed video cryomicroscopy system was created to observe IIF at sub-millisecond time scales in attached cells. Full details of the system can be found in Chapter 3. Briefly, the system consisted of an upright Eclipse ME600 microscope (Nikon, Tokyo, Japan) fitted with a commercially available cooling stage (FDCS 196, Linkam). System calibration was conducted by measuring the melting point of ice crystallized from a sample of purified water. Experiments were recorded using a high speed digital camera (FastCam-X 512PCI, Photron, Tokyo, Japan) and corresponding software (FastCAM Viewer, version 2.2; Photron).

For all experiments, images were acquired at a rate of 4,000 Hz, with an exposure time of 140 μsec. Maximum recording time was limited to approximately eight seconds

with the settings used. For all high speed experiments, cells were observed using a 50X objective and 0.45X coupler (Nikon). To meet the light level requirements for high-speed imaging, all samples were frozen under Köhler illumination, with the microscope halogen lamp set to maximum output.

To promote IIF, cell cultures were frozen at a rapid rate (130°C/min) in the absence of cryoprotectants. Samples were prepared as described above, and placed in the sample holder located directly on top of the silver block, set to 37°C. After closing the cryostage chamber, the atmosphere was purged using liquid nitrogen vapor to prevent condensation. To seed extracellular ice, the sample temperature was cooled from 37°C to -1.5°C (at 50°C /min), and repositioned such that the edge of the sample was brought into contact with a seeding block (a silver block integrated into the cryostage stage and cooled to the temperature of the liquid nitrogen). Immediately after seeding the extracellular ice, the sample was repositioned on the silver block and a cell was randomly selected for the experiment. Prior to the temperature plunge, both brightfield and fluorescent images were taken of the sample, to ensure that each pattern contained exactly one cell (nucleic acids stained by SYTO 13) with full membrane integrity (negative for Eth-Homo1 uptake). For all experiments, the focal plane of camera was set to the basal area of the attached cell. Prior to the temperature plunge, both brightfield and fluorescent images were taken of the sample. To minimize dehydration of the sample, the extracellular ice seeding, cell selection and imaging were performed in approximately 60 seconds. If this process took longer than three minutes, the experiment was abandoned. Immediately prior to the temperature plunge, the halogen lamp was set to maximum output, and the stage was cooled to -60°C at a controlled rate of 130°C/min. The high speed camera was

set to record images into a circular buffer, and recording was terminated using a manual switch-closure trigger. When conventional indicators of intracellular ice formation (i.e. cell darkening and/or twitching) were observed, the trigger switch was closed, allowing the IIF event to be captured. Each experiment was analyzed frame-by-frame to identify the precise time, temperature and initiation site of the IIF event.

7.2.5 Cell-Cell Communication Assays

Two different dye transfer techniques were used to validate that intercellular communication was possible for our experimental conditions. First, a scrape loading dye transfer technique[154] was used with confluent monolayers to verify that cell-cell communication had been established at 18 hours post-seeding. HAECs were seeded at a high density onto fibronectin coated glass coverslips (unpatterned). At 18 hours ± 5%, the coverslips were rinsed twice with 1X DPBS, with the final rinse aspirated off, using care to not dry out the coverslips. Working in the dark, a small quantity (60µL) of dye solution, 4mg/ml biocytin (Molecular Probes) and 5mg/ml rhodamine dextran (Molecular Probes) in DPBS, was dispensed on top of the coverslip. A diamond cutter pen (Fisher Scientific) was then used to 'scrape' the monolayer, introducing the dye solution into the cells along the incision line. The coverslip (with dye solution) was returned to the incubator for two minutes. Following incubation, the dye solution was removed, and the coverslip was quickly rinsed 3X with 1X DPBS. Coverslips were fixed in 4% (v/v) paraformaldehyde (VWR) for 20 minutes and stored in DPBS until secondary staining. Since biocytin is not a fluorescent molecule, an avidin-conjugated dye must be used to visualize the probe in the monolayers. Briefly, coverslips were rinsed 1X with wash buffer (0.05% Tween in DPBS) and then incubated in 0.1% Triton-X, rinsed 2X with

wash buffer, and blocked for 20 minutes with 50µl of 2% goat serum in DBPS. Coverslips were incubated for 30 minutes in a 1:100 dilution of the avidin-conjugated fluorescent dye (Alexa 488, Molecular Probes) in 1X DPBS, rinsed once with wash buffer and once in DPBS prior to mounting on slides. Scrape loading was performed on six different coverslips, at approximately uniform intervals during the full 18 hr ± 5% time period after cell seeding. Coverslips were examined under epifluorescence microscopy (Nikon Eclipse ME600 microscope), using a 10X objective with 1X Coupler. Gap junction intercellular communication (GJIC) was considered to be active in cells that exhibited uptake of biocytin (MW 372.48) but were negative for rhodamine dextran.

An ester dye-transfer technique[148,149] was used to confirm cell-cell communication in our two-cell micropatterns. Briefly, a tissue culture flask containing a confluent monolayer of cells was loaded with a dual fluorescent dye solution (2µM calcein AM, 10µM DiI in serum-free medium) for 20 minutes at 37°C, 5% CO_2. After aspirating off the dye solution, the monolayer was washed four times in standard medium (with serum), with an incubation period of five minutes at 37°C between each wash. The culture in this flask, along with that in a second flask (not exposed to dye solution) were both trypsinized, and the two cell suspensions were seeded onto our micropatterned coverslips at a 1:1 ratio (unloaded:loaded cells) and incubated for up to 24 hours at 37°C. Micropatterns that contained two HAEC cells were observed under fluorescence microscopy at 30 minute intervals following seeding to quantify the extent of cell-cell coupling as a function of time. If an unloaded cell (negative for DiI) stained positive for calcein (cell permeable only through gap junctions), GJIC communication was determined to have been established.

7.2.6 Statistical Analysis

Unless otherwise noted, data are reported as mean ± standard error of the mean. When reporting the classification of events into categories, standard deviations were estimated by taking the square root of the number of observations in each category. If groups had a normal distribution and homogenous variances, the group means were compared by an independent *t*-test, or by analysis of variance (ANOVA), with post hoc analyses using Tukey's test. Differences were considered significant at the 95% confidence level ($p < 0.05$).

7.3 Results

Prior to investigating the effects of cell-cell contact on intercellular ice propagation, experiments were conducted to validate the human endothelial two-cell system. For the study presented in this chapter, three experimental parameters were changed from the system presented in Chapter 6. First, the cell source was changed from bovine endothelial cells to human aortic endothelial cells (HAECs), with the media formulation remaining the same. Second, the cell micropatterns were changed from 30x80μm rectangles (Figure 6.2) to a bowtie configuration (Figure 7.1) with variable cell-cell contact distance (15μm and 30μm). Finally, the post-seeding culture time was increased from 6 hours ± 30 min to 18 hours ± 54 min due to longer population doubling times in HAEC cells.

7.3.1 Pilot study: HAECs in 30x80μm Rectangular Patterns, 6 hours ± 30minutes

First, we tested for any species-specific differences in ice propagation kinetics between the human and bovine cells. The stochastic nature of IIF events requires a high number of experimental repetitions for accuracy (typically $n \geq 50$); however, an approximate evaluation of the kinetics of IIF can be performed using a smaller number of replicate experiments. Thus, a pilot study was conducted, effectively repeating the experiments in Chapter 6 using HAEC cells. HAEC cells were seeded in 30x80μm rectangular patterns and were frozen 6 hours ± 30 min post-seeding. The time, temperature, and location of IIF initiation in each cell in the two-cell pattern were determined. The first cell of the pair to freeze will be referred to in the text as 'cell 1', whereas the second cell of the pair to freeze will be referred to as 'cell 2'. Table 7.1 compares the resulting IIF initiation location determined for bovine cells (n = 102 pairs) and human cells (n = 10 pairs) frozen under identical experimental conditions. Similar trends between the two species can be seen, with the majority of IIF events in cell 2 initiating at the cell-cell interface for both cell types. For the HAEC cells, a slight increase was seen in the number of IIF events that initiated at the cell-cell interface in cell 1, but this observed difference was within the experimental uncertainty.

Table 7.1 Location of IIF initiation in BPAEC and HAEC cultured for 6 hours in 2-cell rectangular patterns (pilot study). Uncertainties represent estimated standard deviations.

	BPAEC		**HAEC**	
	Cell 1	**Cell 2**	**Cell 1**	**Cell 2**
Periphery	58 ± 8%	6 ± 2%	50 ± 22%	10 ± 10%
Cell-Cell	28 ± 5%	84 ± 9%	50 ± 22%	90 ± 30%
Interior	11 ± 3%	2 ± 1%	0 %	0%
Unknown	3 ± 2%	8 ± 3%	0 %	0%

The persistence time of the singlet state (see Chapter 6), *i.e.*, the time delay between the initiation of IIF in the first cell and subsequent initiation of IIF in the second cell of the two-cell pair, can be used as an indicator of the rate of intercellular ice propagation. Thus, to compare the propagation kinetics between the bovine (n = 102) and human (n = 10) cells, the singlet state persistence time was calculated for each cell pair, with the results presented in Figure 7.3. As reported in Chapter 6, the median persistence time for the bovine cells was 14.75 ms. For the human cells, the median persistence time was determined to be 11.4 ms, signifying that both cell types have similar time delays between successive IIF events. Thus, our pilot study suggests that the bovine and human cells cultured in 30x80μm rectangular patterns exhibited similar kinetics of ice propagation.

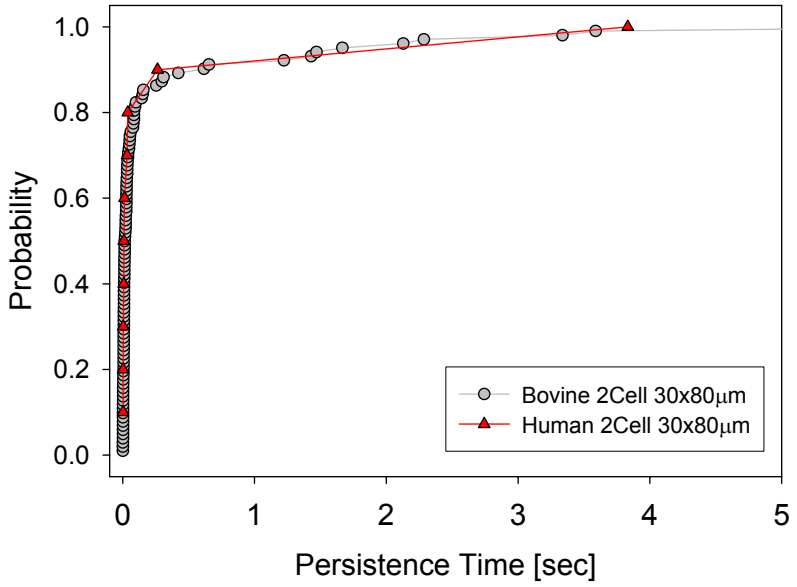

Figure 7.3 Cumulative probability of the singlet state persistence time in bovine and human endothelial cells cultured for 6 hours in 2-cell rectangular patterns (pilot study). The persistence time represents the time delay between the partially frozen (singlet) state and fully frozen (doublet) state. Data are presented for bovine (gray circles) and human (red triangles) cells frozen in 2-cell patterns.

7.3.2 Validation of Cell-Cell Communication at 18 hours

Similar to the gap junction intercellular communication (GJIC) assays conducted in Chapter 6, two different techniques were used to validate that GJIC was active in HAEC constructs at 18 hours post-seeding. First, HAEC monolayers cultured for 18 hours were scrape loaded to introduce biocytin (a non-fluorescent small molecule that is permeable through gap junctions) and rhodamine dextran (not permeable through intact membranes or gap junctions) into the cells. After two minutes of dye loading, monolayers were fixed and stained with an avidin-conjugated fluorescent dye to visualize the biocytin tracer molecule. A representative result from our scrape loading experiment is shown in Figure 7.4. Cells that stained both green (biocytin) and red (dextran) indicated the location of the initial scrape. Cells that stained positive for green only, indicated dye transfer through gap junction channels. As shown in Figure 7.4, our results indicated that GJIC was active in HAEC monolayers 18 hours post seeding. All coverslips analyzed ($n = 6$) demonstrated sizeable levels of dye transfer, with dye transfer typically present 5-6 cells deep.

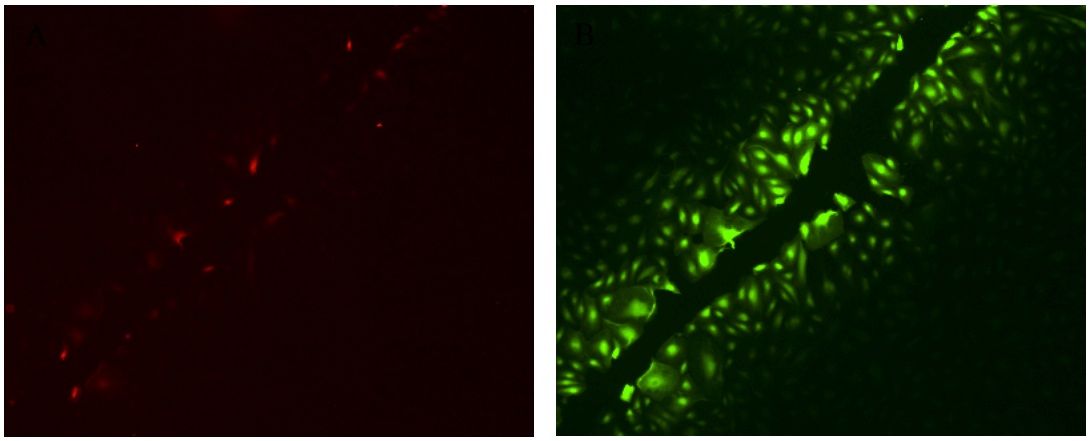

Figure 7.4 Scrape loading of HAEC monolayers at 18 hours post-seeding. Micrographs of a representative epifluorescent image taken during scrape loading experiments: (A) red fluorescent signal (rhodamine dextran) to identify cells originally loaded with fluorescent dye and (B) green fluorescent signal to identify cells with positive transfer of biocytin through gap junctions. Any cell that stains green (but not red) was determined to have established GJIC.

Next, we verified that GJIC had been established in our two-cell bowtie micropatterns using an ester-dye transfer technique. Briefly, GJIC was verified through dye transfer from a donor cell (loaded with calcein AM, and DiI), to an unstained recipient cell. Donor cells are identified by positive staining for both calcein (green fluorescence) and DiI (red fluorescence). Recipient cells either have no detectable fluorescence (*i.e.*, no GJIC has been established), or stain positive for calcein (verifying GJIC). Figure 7.5 presents a representative series of micrographs from our ester-dye transfer experiments. It can be seen in Figure 7.5A that 2 hours post seeding HAEC cells are fully spread in the bowtie micropattern. In Figure 7.5B, it is evident that the top cell is the donor cell, through positive staining for DiI (red fluorescence). Finally, in Figure 7.5C, transfer of calcein (only permeable through gap junctions) from the donor cell to the recipient cell is evident, verifying GJIC had been established. From our experiments,

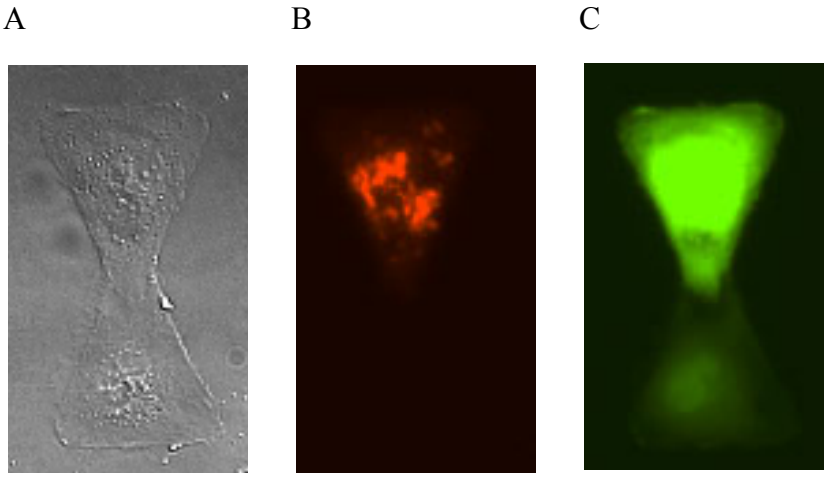

Figure 7.5 Ester dye transfer at 2 hours in HAECs in bowtie patterns. Two cell populations, donor cells (stained with calcein and DiI), and recipient cells (not stained) were seeded onto our two-cell bowtie micropatterns. After two hours of culture time (A) brightfield image of HAEC cells in bowtie pattern (B) red fluorescent image of cells signifying a donor cell in the top bowtie position, and (C) green fluorescent image indicating dye transfer from the donor cell to the recipient cell located in the bottom bowtie position.

after 2 hours, 100% of donor-recipient pairs exhibited detectable levels of dye transfer (n = 11 cell pairs). After 18 hours in culture, dye transfer appeared to reach a steady state value, for gradients in dye transfer between donor/recipient cells (such as those shown in Figure 7.5C) were no longer evident. Thus, based on the results of both GJIC assays, it was concluded that cell-cell communication had been established in our HAEC bowtie patterns 18 hours post-seeding.

7.3.3 Effect of Donor-Specific Differences on IIF Kinetics

Changing endothelial cells systems from bovine to human increased the potential for donor-specific differences that may result from environmental factors, disease or life style choices. Therefore, to investigate for donor-specific differences in IIF kinetics, experiments were conducted with two different lots of HAECs, referred to as lot A and lot B. Lot A was obtained from a Caucasian female, aged 40 years, smoker, positive for alcohol consumption, negative for hypertension and diabetic state unknown (Cambrex, Lot# 4F1523) . For lot B, cells were harvested from a Hispanic woman, aged 52 years, non-smoker, non-drinker, negative for hypertension and negative for diabetes (Cambrex Lot# 5F0001).

Using the 2-cell bowtie patterns with 15 μm cell-cell contact (Figure 7.1A), both lots were cultured, seeded and frozen under near-identical conditions. The cumulative probability of IIF for each cell in the pair was calculated, with the results for lot A (n = 108 pairs) and lot B (n = 73 pairs) presented in Figure 7.6. It can be seen in Figure 7.6 that both lots exhibit similar kinetics. The average temperatures of IIF for both populations were determined to be statistically similar (Cell 1:

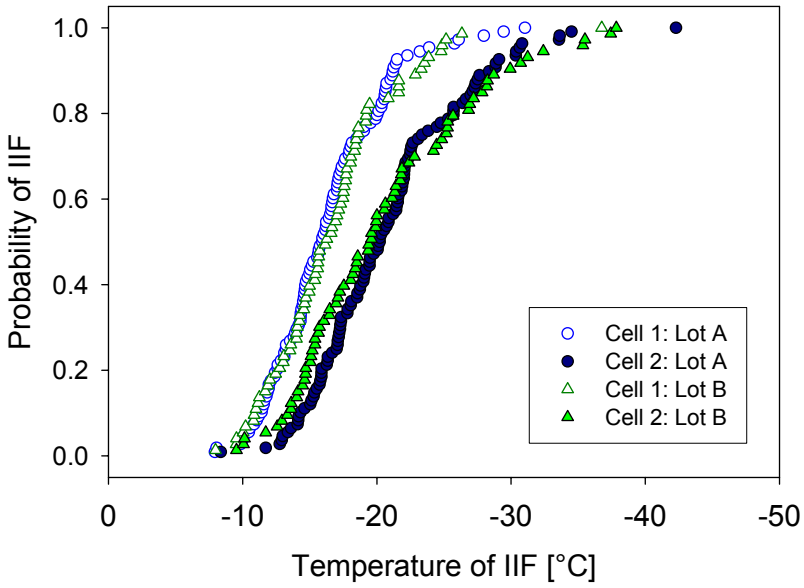

Figure 7.6 Effect of HAEC donor lot on the probability of IIF in two-cell bowtie patterns. HAEC cells cultured in 2-cell bowtie patterns (Figure 7.1A) were frozen 18 hours post-seeding. Two different lots were used for experiments: Lot A (blue circles) and Lot B (green triangles). The probability of IIF for the first cell in the pair to freeze (cell 1) is indicated by open symbols; whereas the probability for the second cell in the pair to freeze (cell 2) is indicated by closed symbols.

$T_{IIFavg\ A}$ = -16.3 ± 0.4°C, $T_{IIFavg\ \ B}$ = -16.7 ± 0.6°C, p = 0.63; Cell 2: $T_{IIFavg\ A}$ = -20.9 ± 0.5°C, $T_{IIFavg\ \ B}$ = -20.6 ± 0.8°C p = 0.76). Therefore, for the experimental conditions investigated in this study we assumed no lot-specific effects were influencing our data. From this point forward, all data presented for the 15 μm bowties will reference the data obtained from lot A (n = 102 pairs).

7.3.4 Kinetics of IIF in HAEC Bowtie Micropatterns with 15 μm Cell-Cell Contact Distance

Control experiments were conducted with single cell patterns to determine the rate of spontaneous IIF initiation (*i.e.*, independent of cell-cell contact). In Chapter 6, separate 30x40μm micropatterns had to be used for the single cell controls in order to constrain the cell attachment area to half of the two-cell pattern area. For this study, a separate pattern geometry for the single cell control was unnecessary, because single attached HAEC cells were found to spread in one half of the two-cell bowtie pattern (Figure 7.7). Thus, single HAEC cells occupying half of the two-cell bowtie pattern were frozen at a rapid rate (130°C/min) to -60°C at 18 hours ± 5% post-seeding. The time, temperature and initiation site of IIF were determined. All single cell cryomicroscopy experiments exhibited similar behavior to that reported in Chapters 3-6. A single advancing IIF front was observed in all cells (n = 103 cells), with the average temperature of IIF, $T_{IIF\ avg}$ = -19.7 ± 0.5 °C. For the single cell controls, half of all IIF events initiated at an interior location of the cell (50 ± 7 %). Moreover, all of these interior IIF initiation events were co-localized with paracellular ice dendrites.

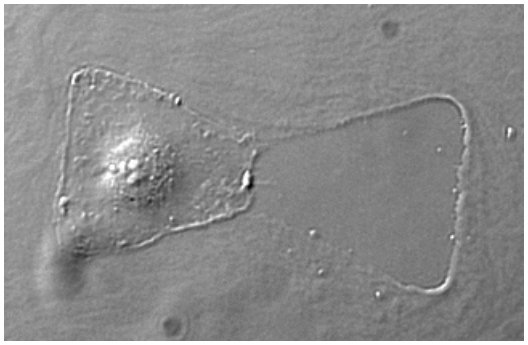

Figure 7.7 Single HAEC cells in bowtie patterns. For control experiments, single HAEC cells were cultured in two-cell patterns and subsequently frozen at a rapid rate, 18 hours post-seeding. Image is a representative micrograph of a single HAEC cell in a two-cell bowtie pattern (30μm cell-cell contact area, DIC).

Next, pairs of HAEC cells were frozen in the bowtie patterns (15μm cell-cell contact distance, n = 108 pairs), with one cell occupying each half of the bowtie (Figure 7.2A). Unlike our BPAEC data presented in Chapter 6, the first cell in the bowtie pattern did not exhibit similar trends in IIF initiation site in comparison to the single cell controls. Figure 7.8 presents the IIF initiation site for the single cell control, the first cell in the pair to freeze (cell 1), and the second cell in the pair to freeze (cell 2). It can be seen in Figure 7.8, that for cells grown in pairs (cell 1 and cell 2), the percentage of the population in which IIF initiated at the cell periphery was appreciably less than the corresponding percentage for the single cell control. Instead, by introducing cell-cell contact, the majority of IIF events in the two-cell pairs initiated at a non-peripheral location (~66% of IIF events in cell 1 and cell 2 initiated at the cell interior). However, the most unexpected finding is the complete lack of IIF events initiating at the cell-cell interface. Out of 108 cell pairs frozen, none had IIF initiate at the cell-cell interface.

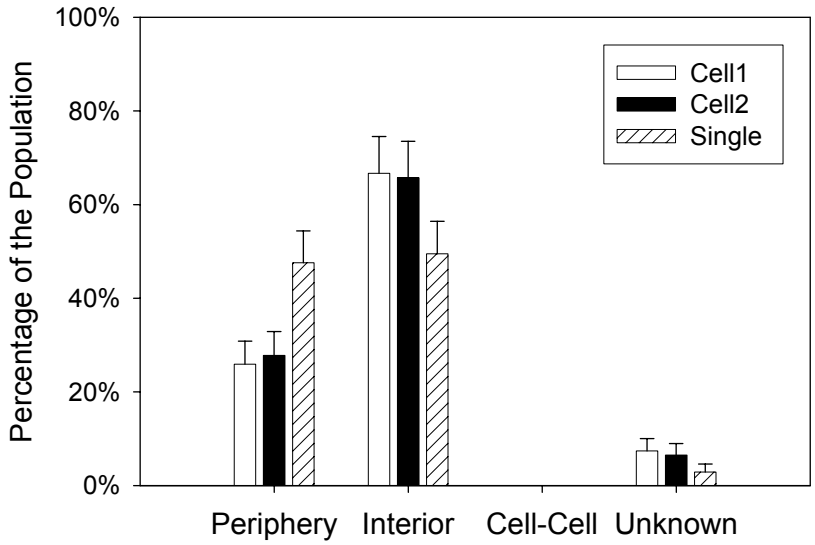

Figure 7.8 Initiation point of IIF in one- and two-cell HAEC 15μm cell-cell contact area bowtie patterns. The IIF initiation point was determined for the first cell ('cell 1', open bars), and the second cell ('cell 2', black bars) to freeze in the 2-cell pair, 15 μm cell-cell contact distance. Data is also shown for the single cell controls ('single', hatched bars). Data are presented as percentage of the population ± SD.

During analysis of video sequences, a high frequency of paracellular ice penetration (PIP) was evident in all cell populations. Multiple paracellular ice dendrites would form prior to IIF, often with pronounced secondary branching. The percentage of the population that exhibited PIP was quantified, with the results presented in Figure 7.9. It can be seen that for all conditions (cell 1, cell 2, and single cell control), ~80% of the experiments exhibited PIP.

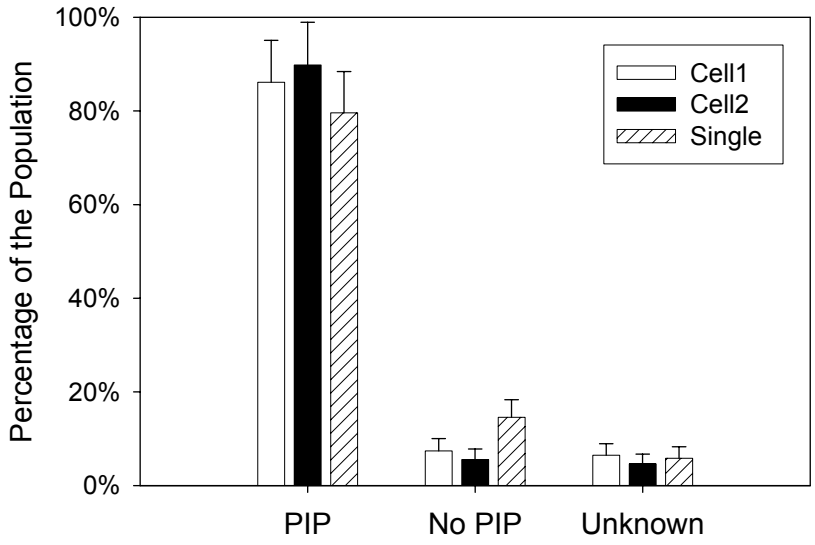

Figure 7.9 Frequency of paracellular ice penetration (PIP) during freezing of HAEC bowties. Data are presented as percentage of the population ± SD.

Due to the high frequency of paracellular ice penetration, we explored this phenomenon further by quantifying the start location of the first paracellular ice dendrite for each cell. For all experiments, paracellular dendrites initiated growth at the perimeter of the cell, which was classified as having four different spatial locations (Figure 7.10). The two longest edges of the triangle were counted as one side and were classified as the 'long' end (~184 μm total length), whereas the short base of the triangle was classified as the 'short' end (~65 μm). The top of the triangle was the interface between the two cells, and as such, it was classified as 'cell-cell' (~15 μm). The two corners of the triangle were considered to be one classification.

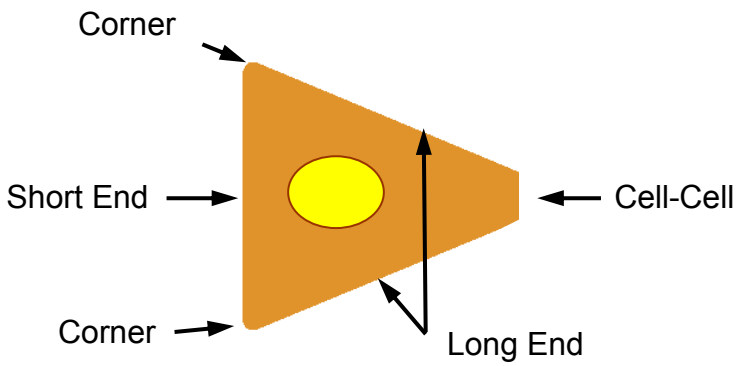

Figure 7.10 Schematic of cell perimeter classification. To identify the location of paracellular ice penetration, the outer perimeter of half the bowtie pattern (one cell) was classified as shown above. See text for details.

The resulting frequency of paracellular ice penetration for each location is presented in Figure 7.11. It can be seen that for all conditions, the majority of paracellular ice dendrites initiated at the long end of the cell. It can be seen in Figure 7.11 that frequency correlates with the physical lengths of the edges. For example, the short end of the bowtie half accounts for ~21% of the cell perimeter and roughly 20% of all paracellular ice dendrites initiation points. These results suggest that the location of paracellular ice penetration was not sensitive to any angularity in the cell shape, because the frequency of PIP initiation site correlated with available the length of each pattern edge.

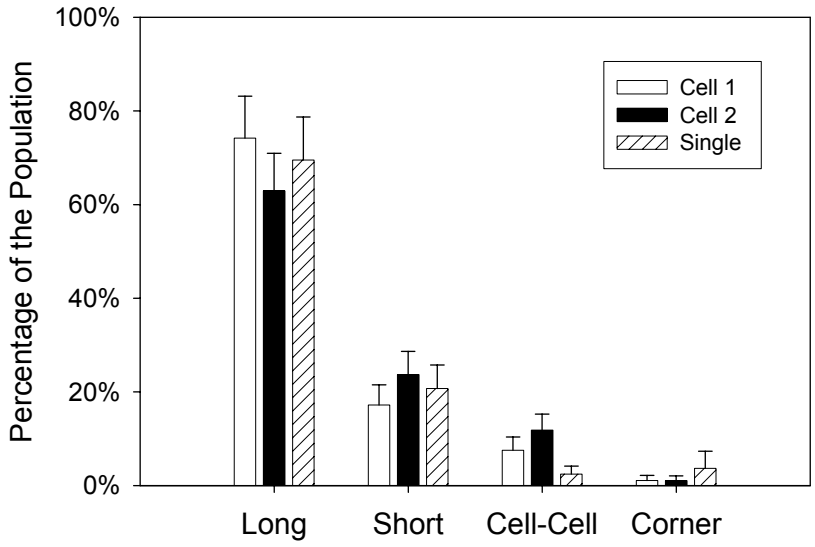

Figure 7.11 Location of paracellular ice penetration in HAEC bowties patterns. The peripheral location (see Figure 7.10) at which the first paracellular ice dendrite formed was determined for the first cell ('cell 1', open bars), and the second cell ('cell 2', black bars) to freeze in the 2-cell pair, as well as for the single cell control ('single', hatched bars). Data are presented as percentage of the population ± SD.

Similar to our analysis in Chapter 6, the kinetic data obtained from our experiments was used to calculate the cumulative probability of IIF as a function of temperature for the single and two-cell HAEC bowtie patterns. As shown in Figure 7.12, the cumulative probability for the two-cell data is almost identical to the single cell data. Similar to our results with the bovine cells, our data suggests that the overall kinetics of IIF in cell pairs are not influenced by the introduction of cell-cell contact. However, in contrast to the bovine data, the rate of spontaneous initiation of IIF (calculated using Equation 6.10) does not appear to be influenced by cell-cell contact. Figure 7.12 shows that the rate of spontaneous initiation of IIF in the two-cell patterns is similar to the cumulative probability of IIF in the single cell control.

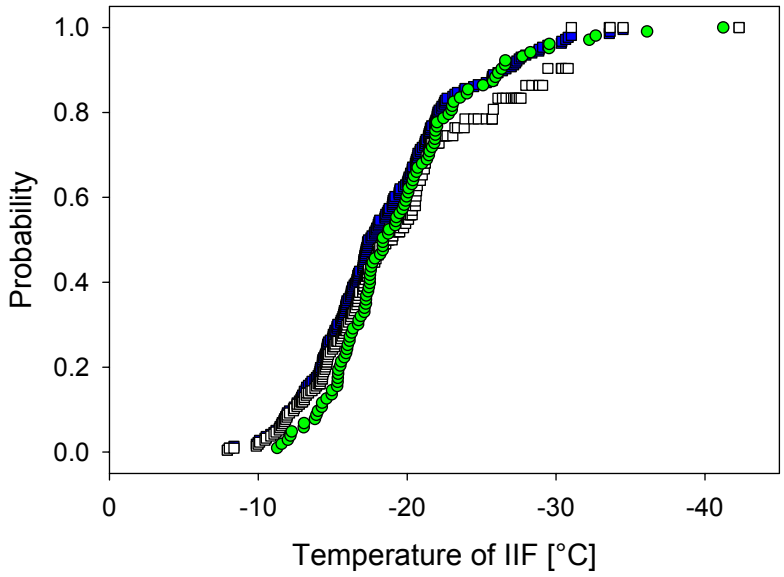

Figure 7.12 Cumulative probability of IIF in one- and two-cell HAEC bowtie micropatterns. Cells were cultured in one-cell patterns (green circles) or two-cell patterns (blue squares) for 18 hours prior to freezing. The probability of spontaneous ice formation in the two-cell constructs was calculated using Equation 6.10 (open squares).

For HAEC cells frozen in the 15μm bowtie patterns, we quantified the singlet state persistence time, or the time delay between the initiation of IIF in the first cell and the subsequent initiation of IIF in the second cell of each two-cell pair. The cumulative probability distribution of the persistence time is presented in Figure 7.13, where a slow steady increase can be seen in the data, in sharp contrast to the persistence time presented in Figure 7.5. For our HAEC 2-cell bowtie patterns, the median persistence time was 1.62 seconds, which is about two orders of magnitude longer than the median persistence time for the BPAEC pairs (Chapter 6, 14.75 ms), and the median persistence time for the HAEC pairs cultured in the rectangular patterns (pilot study, 11.4ms).

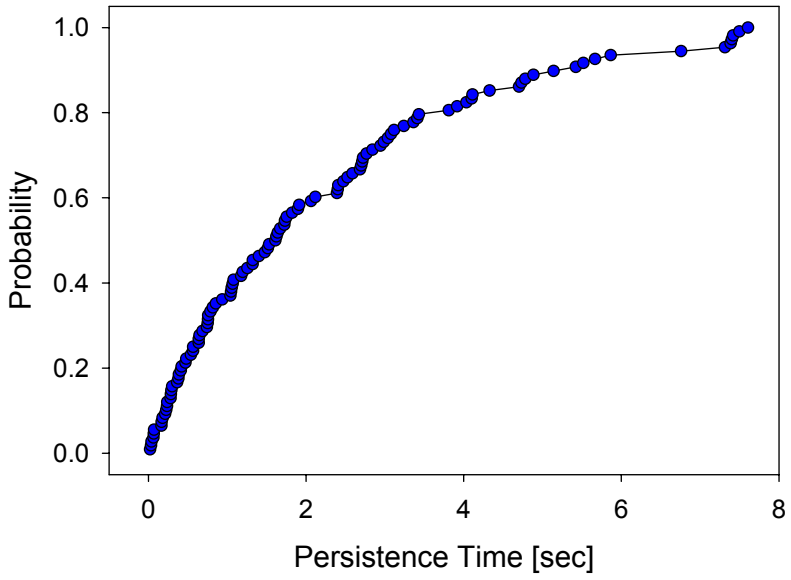

Figure 7.13 Cumulative probability of the singlet state persistence time in HAEC two-cell pairs cultured for 18 hours in bowtie patterns.

Next, our two-cell cryomicroscopy data were used to determine the probabilities of the unfrozen (P_0), singlet (P_1), and double (P_2) states as a function of temperature. Similar to our analysis in Chapter 6, the assumption was made that the non-dimensional intercellular ice propagation rate, α, is approximately constant for our experimental conditions. Thus, α was determined by fitting the theoretical solution, Equation 6.12, to our measured probabilities of the singlet state, P_1. Prior to fitting the data, the experimentally measured temperatures were converted to non-dimensional time, τ, using Equation 6.11. The results of this analysis are presented in Figure 7.14, with non-linear regression yielding a best fit $\alpha = 0.81 \pm 0.03$ ($R^2 = 0.89$). The resulting non-dimensional rate of propagation, α, was close to unity, indicating that propagation rate, J_p, and the rate of spontaneous initiation of IIF, J_i, were of the same order of magnitude ($\alpha = J_p / J_i$).

Thus, our data suggest that despite confirmation of GJIC in our HAEC 2-cell, 15μm cell-cell contact area patterns, the mechanism of intercellular ice is propagation is ineffective during freezing.

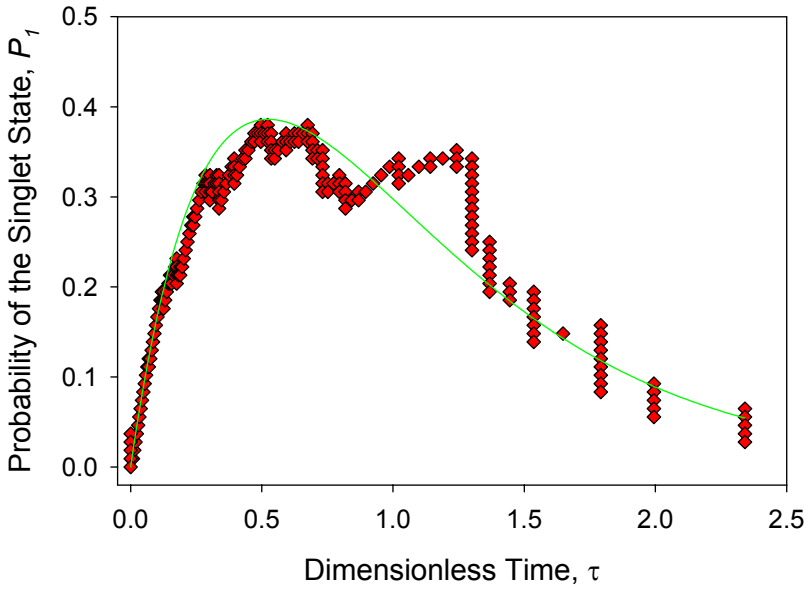

Figure 7.14 Propagation rate determination in HAECs cultured in two-cell pairs with a 15μm cell-cell contact area. Probability of the singlet state, P_1, measured during cryomicroscopy of HAECs cultured in bowtie micropatterns (red diamonds) and predicted using the best fit of Equation 6.12 (green line).

7.3.5 Effect of Cell-Cell Contact Distance on the Rate of Intercellular Ice Propagation

Next, the cell-cell contact distance was increased from 15μm to 30μm (Figure 7.1B), effectively increasing the degree of cell-cell contact by a factor of 2. Similar to our previous experiments, cells were frozen at a rapid rate (130°C/min) to -60°C, 18 h ± 5% post-seeding. The initiation location for each cell in the pair (n = 90 pairs)

was determined, with the results presented in Figure 7.15. It can be seen that the results are similar to those presented for the HAECs cultured with 15 μm cell-cell contact area (Figure 7.7). However, a small percentage of cells (~ 5%) had IIF initiate at the cell-cell interface. The frequency of paracellular ice penetration was also determined (cell 1 = 87.8 ± 9.9%, cell 2 = 93.3 ± 10.1% of cells exhibited PIP), with results similar to those measured in the HAEC cells with 15μm cell-cell contact area (Figure 7.8).

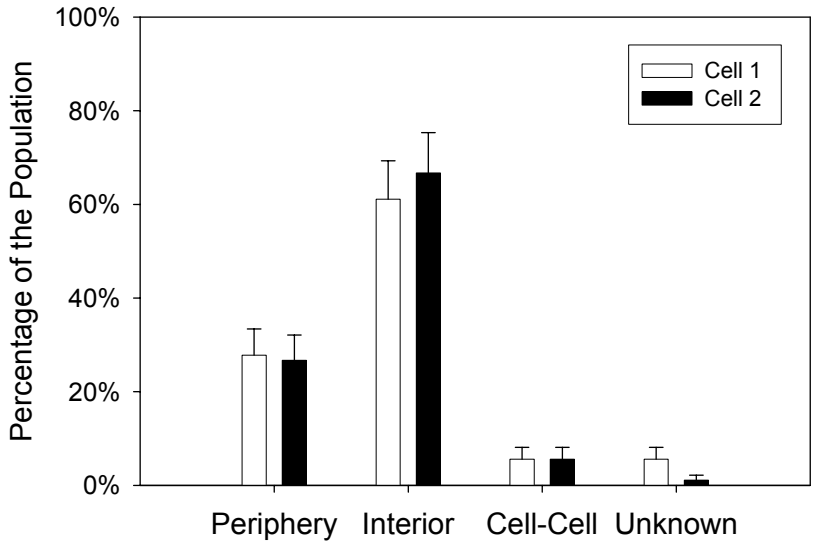

Figure 7.15 Initiation point of IIF in HAECs frozen in 2-cell pairs with 30μm cell-cell contact area. The IIF initiation point was determined for the first cell ('cell 1', open bars), and the second cell ('cell 2', black bars) to freeze in the 2-cell pair. Data are presented as percentage of the population ± SD.

From our experimental data, the probability of IIF was determined for each cell, with the results presented in Figure 7.16. For HAECs cultured in the 30μm bowties, the probability of IIF is presented alongside the previously measured probability of IIF in the

15μm bowties. Looking at Figure 7.16, it can be seen that increasing the degree of cell-cell contact by a factor of 2 had a small effect on the kinetics of IIF. However, the mean temperatures of IIF for each cell in the pair were determined to be statistically different (Cell 1: $T_{IIFavg\ 15um}$ = -16.3 ± 0.4°C, $T_{IIFavg\ 30um}$ = -15.1 ± 0.4°C, $p < 0.05$; Cell 2: $T_{IIFavg\ 15um}$ = -20.9 ± 0.5°C, $T_{IIFavg\ 30um}$ = -19.1 ± 0.6°C, $p < 0.05$).

The persistence time, or the time delay between successive IIF events in the two-cell pair, can be used as an indicator of the kinetics of intercellular ice propagation. Thus, we compared the persistence time for the 15μm HAEC bowties (Figure 7.13) to the measured persistence time in the 30μm HAEC bowties. The results, shown in Figure 7.17, suggest that the persistence time for the 30μm HAEC cell pairs is slightly shorter than the persistence time for the 15μm pairs. However, for both the 15μm and 30μm cell pairs, considerable lag times exist between IIF initiation in the first cell and subsequent IIF initiation in the second cell, suggesting a very low propagation rate for both cell populations.

Lastly, we determined the non-dimensional propagation rate, α, for the HAECs cultured in 30μm bowties. The theoretical solution of the probability of the singlet state (Equation 6.12) was fit to the experimentally measured probabilities of the singlet state, with the results presented in Figure 7.18. Prior to applying the non-linear regression, the temperatures were converted to non-dimensional time, τ, using Equation 6.11. The regression yields a best fit α = 1.03 ± 0.04 (R^2 = 0.81). Despite increasing the cell-cell contact area by a factor of two, the resulting propagation rate, α = 1.03, indicates there are only slight levels of intercellular ice propagation in the HAEC two-cell bowties patterns.

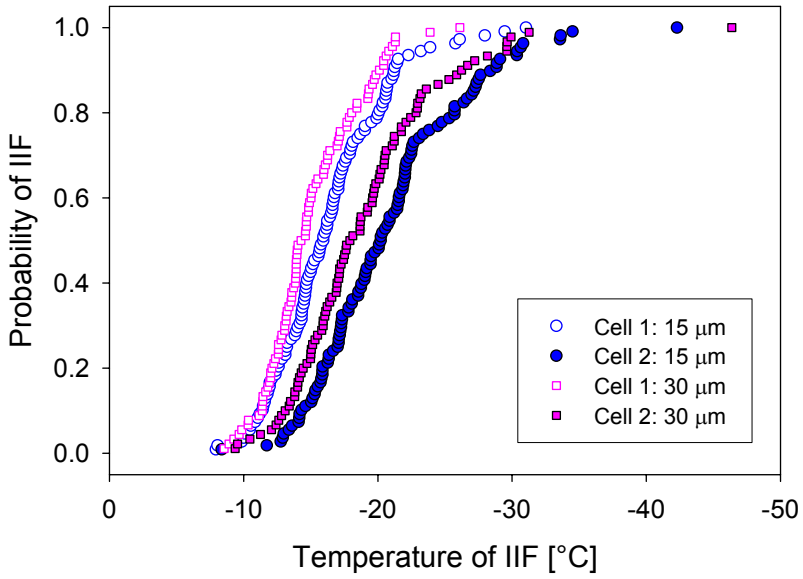

Figure 7.16 Effect of cell-cell contact area on kinetics of IIF in HAEC two-cell bowties. HAECs cultured in bowtie patterns with 15μm (blue symbols) and 30μm (pink symbols) cell-cell contact areas were frozen after 18 hours in culture. The probability of IIF for the first cell in the pair to freeze (cell 1) is indicated by open symbols; whereas the probability for the second cell in the pair to freeze (cell 2) is indicated by closed symbols.

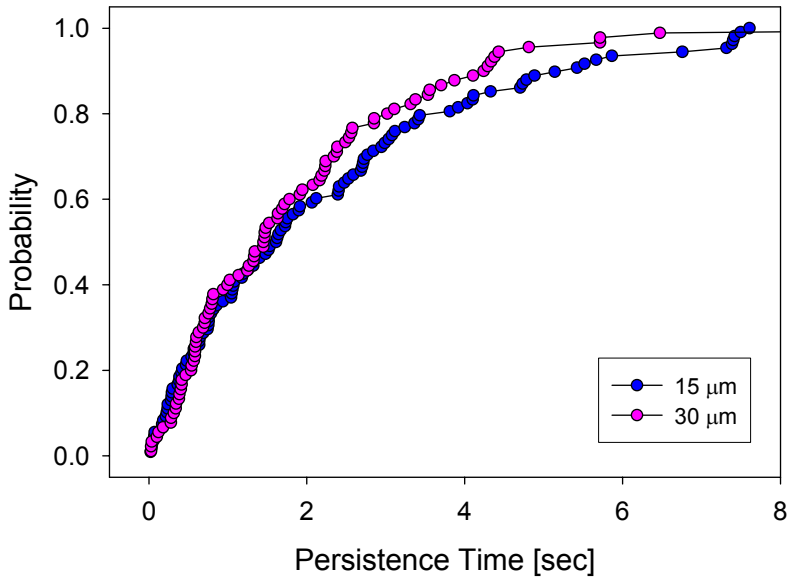

Figure 7.17 Effect of cell-cell contact area on persistence time in HAEC cell pairs. The persistence time, or time delay between the partially frozen and fully frozen state, is shown for HAECs cultured in pairs with a 15μm (blue circles) and 30μm (pink circles). See text for details.

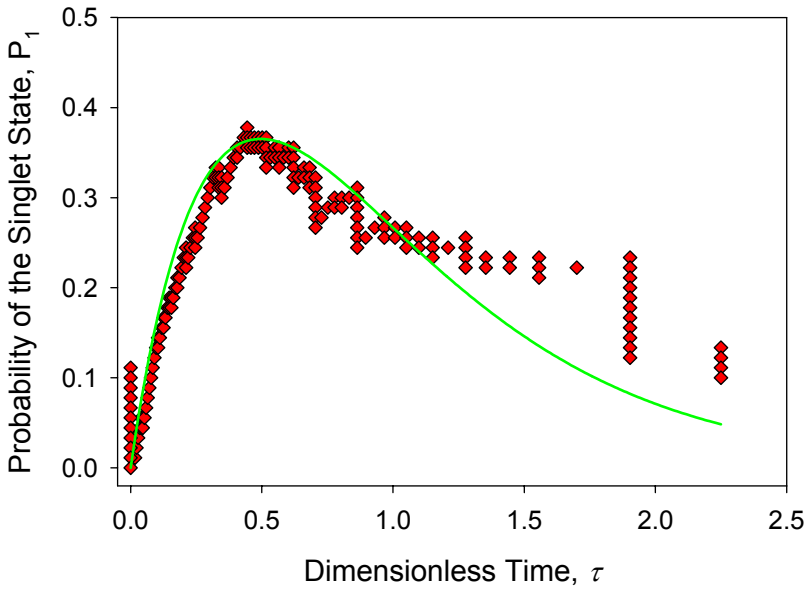

Figure 7.18 Propagation rate determination for HAECs frozen in 2-cell pairs with 30um cell-cell contact area. Fitting the theoretical solution (Equation 6.11) to our experimentally measured probabilities, non-linear regression yield a best fit $\alpha = 1.03$. See text for details.

7.4 Discussion

Anecdotal evidence of cell-cell interactions increasing the probability of IIF has been long reported[65,66]. In 1996, Berger and Uhrik[56] were the first to hypothesize that intercellular ice crystals could propagate across the cell-cell interface via gap junctions. Since Berger and Uhrik's initial hypothesis[56], cryomicroscopy studies have been conducted using cell monolayers[57,96,155] as well as micropatterned cell pairs[58,59] to investigate the role of gap junctions in intercellular ice propagation. While all of these studies have significantly contributed to our understanding of intercellular ice propagation, they also all assumed that manipulation of culture conditions[57], pharmacological additives[56,58,61] and cell sources[6,57] altered levels of gap junction communication, without independent verification. Considering the sensitive gating mechanisms of gap junction channels[156], it is not unreasonable to question the presence of gap junction intercellular communication (GJIC). As such, for the studies of intercellular ice propagation presented in Chapter 6, careful effort was made to verify GJIC prior to freezing. Data obtained from the studies presented in Chapter 6 confirmed ice propagation in primary bovine endothelial cells and demonstrated that IIF preferentially initiated at the cell-cell interface for cells in contact with a frozen cell. However, the cryomicroscopy data presented in the present chapter indicates the absence of intercellular ice propagation in human endothelial cells cultured in bowtie patterns even with confirmed GJIC. Given our previous findings as well as the literature evidence implicating gap junctions in intercellular ice propagation, this result is striking.

Pilot studies of HAECs frozen in rectangular patterns cultured for 6 hours, revealed similar kinetics to the bovine studies presented in Chapter 6, suggesting that

HAECs were capable of exhibiting high rates of intercellular ice propagation. Endothelial cells were specifically chosen for our propagation studies due to their expected high rate of ice propagation. We had hypothesized that their high levels of connexin expression[88], and reported low viability in monolayer cryopreservation[90,91] would result in an excellent cell system for ice propagation studies. However, as evidenced in the data, dramatic changes were seen in the propagation rate as the two-cell micropatterns were changed from a rectangular to a bowtie shape.

The effect of donor-source variability was investigated, and our data indicate that for two different human donors with variability in age, race and medical history, the kinetics of IIF were statistically similar. The importance of these results extends beyond the validation of this current study. Determining that the response of the cells to freezing was not specific to donor source is critical for demonstrating the potential of cryopreservation strategies for long-term storage of living tissue. Tissue engineered products may contain autologous cells, resulting in a different donor source for each tissue generated. Even in the mass production of allograft tissues, often more than one donor source is used[157]. Thus, our data suggests the feasibility of developing a successful cryopreservation protocol for living tissues that is not sensitive to donor variability.

The data presented in this chapter also suggest that the mechanisms that control intercellular ice propagation may not depend solely on active gap junction communication. HAECs cultured in two-cell bowtie micropatterns were frozen after 18 hours in culture and demonstrated no signs of intercellular ice propagation. Increasing the degree of cell-cell contact by a factor of two had a minimal effect on the overall kinetics of IIF ($\alpha \approx 1$ for both 15 μm and 30 μm cell-cell contact area). Although

cryomicroscopy data yielded no evidence of intercellular ice propagation, visual inspection of all the micropatterns revealed tight, well-defined cell-cell contact, with GJIC verified via dye transfer assays. Preliminary data from our laboratory (not shown) indicate HAEC bowties frozen at 6 hours post-seeding, exhibit similar kinetics to those presented for bowtie patterns in the present chapter, suggesting that culture time did not influence the ice propagation mechanism. One could speculate that cell-cell interactions mediate intercellular ice propagation, but through some mechanism other than gap junctions. A previous study of intercellular ice propagation in HepG2 cells demonstrated that the addition of a known gap junction blocker significantly reduced the rate of ice propagation[58]. Considering that HepG2 cells have recently been shown to have no detectable gap junction communication when cultured in monolayers under standard conditions[75], the question arises as to why the gap junction blocker influenced the kinetics of ice propagation. One can speculate that non-specific effects of the gap junction blocker may have altered cell-cell adhesion properties, in turn effecting the ice propagation rate.

In contrast to the absence of intercellular ice propagation, a high frequency of paracellular ice penetration (PIP) was found in the HAEC bowties. In Chapter 4, data suggested that the frequency of paracellular ice penetration was directly proportional to the length of the cell perimeter for single bovine endothelial cells cultured in circular micropatterns. Data from the current study for human endothelial cells further supports this correlation. For the bowtie patterns used in this study, the perimeter of each cell is ~315 μm, approximately 2.25 times larger than the measured perimeter of the 40 μm diameter bovine cells investigated in Chapter 4. Comparing the frequency of paracellular

ice penetration between the 40μm circular data (~40% PIP, Figure 4.7) and the single cell control bowtie experiments (~80% PIP), as the perimeter increases by a factor of 2.25, the frequency of paracellular ice penetration increases by a factor of 2. Considering that two different species of cells were used, as well as different cell geometries, these results not only support our previous results but also suggest that our findings may extend beyond a particular species and/or culture condition.

In conclusion, from our cryomicroscopy data it was determined that for human endothelial cells in bowtie patterns, no intercellular ice propagation occurred across the cell-cell interface during freezing after 18 hours in culture. Moreover, the rate of ice propagation was shown to be relatively insensitive to the degree of cell-cell contact. A high frequency of paracellular ice penetration and subsequent dendrite-mediated initiation of IIF was also evidenced in our data. Further studies are required before we can fully understand the mechanisms influencing ice propagation; however, the absence of intercellular ice propagation was an unexpected result. Our data suggests that gap junction communication alone is not sufficient to result in high levels of intercellular ice propagation. Our pilot studies further suggest that cell shape (controlled through micropattern geometry), may have a role in modulating the rate of intercellular ice propagation. Elucidating the mechanism that resulted in the reduction in intercellular ice propagation would have major implications in the fields of cryobiology and cryosurgery. The capacity to 'turn off' a major damage mechanism associated with tissue freezing would greatly assist in the development of successful freezing protocols.

CHAPTER 8

EFFECT OF MICROPATTERN GEOMETRY ON THE KINETICS OF INTRACELLULAR ICE FORMATION IN CO-CULTURED TISSUE

8.1 Introduction

Engineered tissues containing more than one cell type are desirable due to the enhancements that cell-cell interactions bring to maintaining the normal physiology of many tissues[158]. The interest in co-cultured tissues is broad with promising applications in mimicking the natural *in vivo* state of cardiovascular[159-161], orthopaedic[162], hepatic[163] and urological[164,165] tissues. In addition, various fabrication techniques can be used to create patterned, 2D co-cultures, providing precise control over the degree heterotypic and homotypic interactions. Lithography[166-168], microfluidics[160,169], step wise changes in surface chemistry[170,171] and laser direct writing[172] have all been used to enhance tissue function via direct spatial control of each cell population in co-cultured tissues. Whereas these applications show great potential for replicating the complexity of native tissue, the feasibility of marketing an engineered co-cultured tissue directly depends on the ability to store these products for extended periods of time.

Cryopreservation is a promising strategy for long-term storage of co-cultured tissues, enabling their mass-production, banking and distribution. However, significant loss of tissue function can result from cell damage caused by intracellular ice formation (IIF) during cooling to cryogenic storage temperatures[1,2]. The design and optimization of cryopreservation protocols that minimize IIF is required to maximize post-thaw tissue

viability. One challenge to optimizing tissue freezing procedures is the effect of cell-cell interactions that can enhance IIF[60,64], an effect thought to be due to intercellular propagation of deleterious ice crystals via gap junctions[56,58]. Given that optimal freezing conditions vary by cell type (due to differences in biophysical properties)[2], the optimization of cryopreservation procedures for co-cultured tissue constructs is challenging. The greater the discrepancy in IIF kinetics between two cell types, the more difficult it will be to find a freezing protocol that maximizes overall tissue survival.

Mathematical models of ice nucleation have made the prediction of the cellular response to freezing possible[47,173], allowing the design and optimization of cell cryopreservation protocols through computer simulations[48]. Unfortunately, the knowledge of the cryobiology of isolated cell suspensions cannot simply be extrapolated to tissue. Due to the dramatic increase in complexity of the problem resulting from additional biophysical phenomena (e.g., cell-substrate and cell-cell interactions, geometric effects, heat and mass transport limitations in macroscopic systems), novel approaches are required to predict the response of tissue to freezing. As a result of the limited knowledge of the mechanisms and kinetics of IIF in tissue, few mathematical models exist for ice formation in tissue[49-51,53-55,174]. The majority of these models represent tissue as a continuous material, with thermal, chemical, or mechanical gradients, with no regard to the cellular structure of tissues[49,54,174]. More recent approaches have considered cellular properties (*e.g.*, water permeability of the membrane and osmotic changes), extrapolating them to finite volumes of tissue[50,51,55]. Although these models provide important insights into tissue freezing, they neglect the effects of cell-substrate and cell-cell interactions. To address this limitation, we have previously

developed a mathematical model to predict the effect of cell-cell communication on the kinetics of IIF in tissue[58,175]. In this model, the rate of IIF in each cell was expressed as a sum of contributions from two distinct mechanisms: the spontaneous initiation of intracellular ice; and the propagation of ice from a frozen neighbor across the corresponding cell-cell interface. The mechanisms of IIF that result in the spontaneous initiation of intracellular ice are independent of the state of neighboring cells and may include surface and volume catalyzed nucleation[23], osmotic rupture[40], or mechanical rupture[41]. However, this model has only been applied to cryosurgical applications[175]. Hence, the question of how co-culture, specifically, variable biophysical tissue properties, may influence the freezing of such tissues has yet to be explored.

The goal of the studies described in this chapter was to develop a theoretical model to predict the dynamics of tissue freezing, taking into account heterogeneity in the tissue biophysical properties resulting from co-culture of distinct cell types. Specifically, we have undertaken a parametric analysis to investigate the influence of micropatterned tissue geometry as well as the effects of the rates of ice nucleation and propagation in the two species of cells. Predictive models such as the one presented here can provide great utility in gaining insight into the influence of two different cell types on the kinetics of ice formation. In addition, such models can be used to develop novel strategies for improving uniformity of freezing kinetics for co-cultured tissues.

8.2 Theoretical Background

8.2.1 Modeling Assumptions

Previous observations in micropatterned cell constructs have demonstrated that the kinetics of IIF in tissue can be described by two distinct mechanisms: ice can form by spontaneous nucleation inside cells, and ice can also propagate between cells that are in contact[58]. As such, in our model of IIF in heterogeneous tissue, a cell in a tissue can freeze via (1) IIF initiation events, *i.e.* spontaneous IIF that does not depend on the presence of ice in neighboring cells or (2) intercellular ice propagation, i.e. IIF induced by the presence of ice in an adjacent cell. Thus, if an unfrozen cell k interacts with n neighboring cells $j = 1,\ldots,n$, then the probability of IIF in the unfrozen cell will be a nonstationary stochastic process described by a characteristic rate J_k^{IIF}:

$$J_k^{IIF}(t) = J_k^i(t) + \sum_{j=1}^{n} f_j(t) J_{j,k}^p(t) \tag{8.1}$$

where t is time; J_k^i, the characteristic rate of spontaneous IIF initiation in cell k; $J_{j,k}^p$, the characteristic rate of IIF in cell k caused by intercellular ice propagation from cell j (if the latter is frozen); f_j, the state of cell j ($f_j = 0$ if cell j is unfrozen; $f_j = 1$ if cell j contains intracellular ice).

The coupled processes of ice formation and ice propagation were simulated in a two-dimensional composite tissue comprising two distinct cell types. As illustrated in Figure 8.1, five different geometric patterns were considered, each configuration consisting of self-contained islands of one cell type (denoted as the "inner" cell type),

surrounded by cells of a different type (denoted as the "outer" cell type). These geometrical configurations were designed to be similar to micropatterned co-cultured tissue constructs evaluated in the literature[168]. For all geometric configurations evaluated, each cell type occupied 50% of the total tissue volume. By designing the control volumes as such, we effectively varied the percentage of heterotypic interactions while maintaining constant cell volumes.

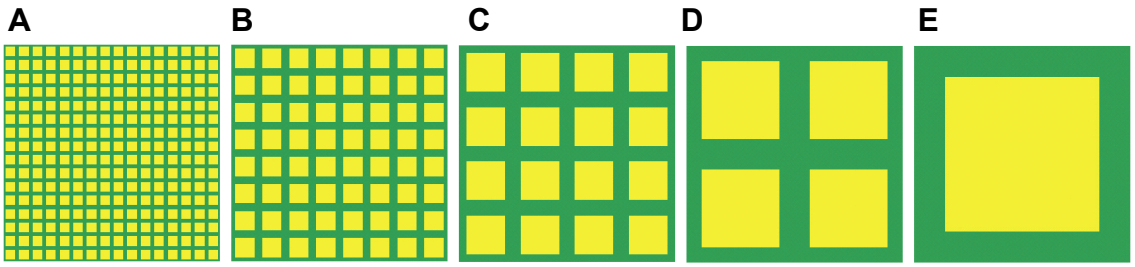

Figure 8.1 Schematic of co-cultured tissue geometries evaluated, with islands of one cell type surrounded by a second cell type. Different geometries were evaluated by changing the size of the inner cell islands, effectively varying the ratio of heterotypic interactions: (A) 5x5 cell islands, 20% heterotypic interactions, (B) 10x10 cell islands, 10% heterotypic interactions, (C) 20x20 cell islands, 5% heterotypic interactions, (D) 40x40 cell islands, 3% heterotypic interactions, and (E) 80x80 cell island, 1% heterotypic interactions.

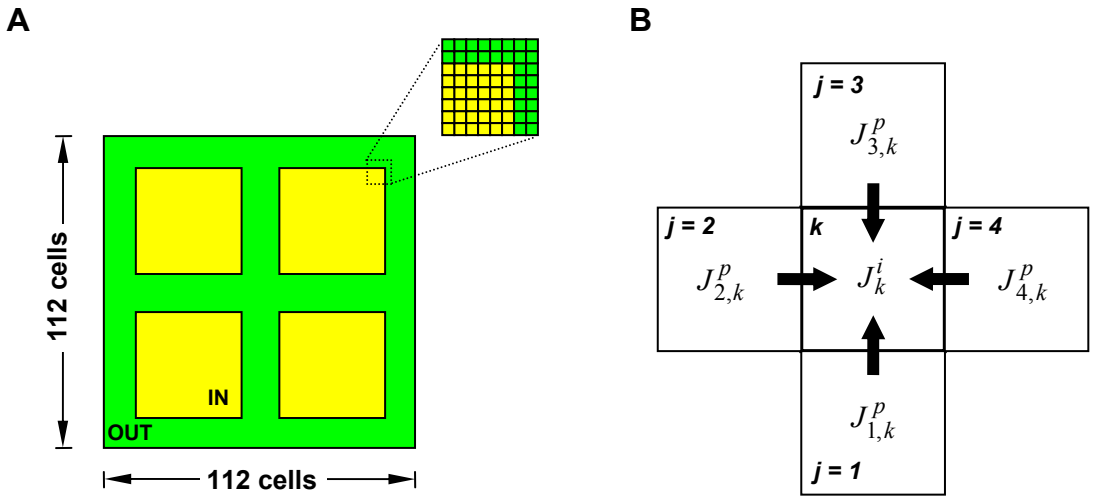

Figure 8.2 Illustration of tissue geometry and possible mechanisms of IIF. (A) Schematic of the co-culture tissue geometry, with islands of one cell type ("in") surrounded by cells of a different type ("out"), centered on a 112×112 lattice. (B) Schematic illustrating possible mechanisms of IIF for a single cell, k, in the lattice, which interacts with four neighboring cells (j = 1,…,4). The rate of intercellular ice propagation from cell j to cell k is $f_j \cdot J^{p}_{j,k}$ and the rate of interaction-independent IIF in cell k is J^{i}_{k}. See text for definition of symbols.

The magnitudes of the rates of IIF initiation and intercellular ice propagation are expected to depend on tissue type. In the present study, the distribution of IIF between the two tissue types was investigated for sections of tissue represented as a lattice of 112 x 112 cells, each interior cell being in communication with four neighbors (Figure 8.2). Thus, if cell k is located inside the micropatterned islands, we define $J_k^i = J_{in}^i$, whereas if cell k is located outside the islands, we define $J_k^i = J_{out}^i$. Similarly, for homotypic interfaces (cells k and j are of the same tissue type), we define $J_{j,k}^p = J_{in}^p$ and $J_{j,k}^p = J_{out}^p$ to describe the rate of intercellular ice propagation inside and outside the islands, respectively. For the sake of simplicity, the present parametric analysis is restricted to regimes in which the characteristic IIF rates in the two tissue types differ only by a multiplicative factor; specifically,

$$\frac{J_{out}^i(t)}{J_{in}^i(t)} = \gamma \tag{8.2}$$

$$\frac{J_{out}^p(t)}{J_{in}^p(t)} = \beta \tag{8.3}$$

where γ and β are constants.

At heterotypic interfaces (cells k and j are of different tissue types), we define $J_{j,k}^p = J_{het}^p$, and consider regimes in which the rates of intercellular ice propagation at heterotypic and homotypic interfaces differ only by a constant multiplicative factor. Thus, we define a nondimensional constant ε to describe the relative magnitudes of the rates of heterotypic and homotypic propagation, as follows:

$$\varepsilon \equiv \frac{J^{p}_{het}(t)}{\min\left\{J^{p}_{out}(t), J^{p}_{in}(t)\right\}}. \tag{8.4}$$

In a previous study of intercellular ice propagation in heterogeneous tissue[175], we have assumed that heterotypic propagation is rate-limited by the cell type with lower connexin expression, i.e., $\varepsilon = 1$; here, we relax that assumption, and consider also values of ε less than or greater than unity in Equation 8.4.

A nondimensional time scale (τ) was defined such that the model becomes invariant to the rates of spontaneous intracellular ice formation, *i.e.*, the model predications can be made without making any *a priori* assumptions regarding the mechanisms or kinetics of this process:

$$\tau \equiv \int_0^t J_{io} \cdot dt \tag{8.5}$$

where $J_{io} = \sqrt{J^{i}_{out} \cdot J^{i}_{in}}$.

Given that the average rate of ice propagation across a cell-cell junction for each cell type ($J_{in}{}^{p}$ and $J_{out}{}^{p}$), is approximately proportional to the nucleation rate[58], we defined an average nondimensional propagation rate, α, for the entire tissue

$$\alpha = \sqrt{\frac{J^{p}_{out} \cdot J^{p}_{in}}{J^{i}_{out} \cdot J^{i}_{in}}}. \tag{8.6}$$

We have recently developed a Monte Carlo algorithm to simulate the effects of cell-cell interaction on IIF in a 2D tissue[175], using methods initially developed by Gillespie[94] for simulation of the stochastic time evolution of coupled chemical reactions.

This new algorithm is a more accurate and efficient Monte Carlo algorithm than those previously used in our past models[58,59]. Using the computer values of the rates of interaction-independent IIF (J_k^i) and intercellular ice propagation ($J_{j,k}^p$) for each cell in the tissue, Gillespie's algorithm is able to predict the site, mechanism, and timing of each random IIF event.

Towards the goal of minimizing the preferential destruction of one cell type, we defined a disparity ratio as:

$$DisparityRatio = \frac{\tau_{50}^{slow}}{\tau_{50}^{fast}} \tag{8.7}$$

where τ_{50}^{fast} is the nondimensional time point corresponding to 50% IIF in the population with the fastest kinetics (*i.e.,* freezes first), and τ_{50}^{slow} corresponding to 50% IIF in the slower populations (Figure 8.3). Thus, if the disparity ratio is zero, both cell types are freezing at the same rate, the optimal situation for construct preservation. This disparity metric was used to provide a useful benchmark to compare across all simulations.

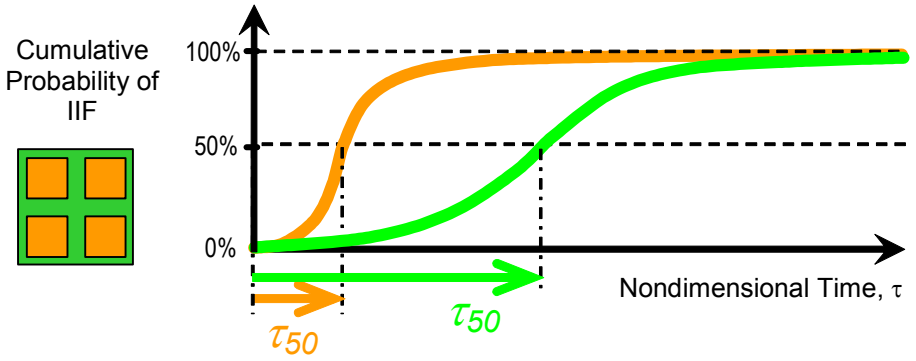

Figure 8.3 Illustration of the disparity ratio metric. During freezing of a tissue comprised of two cell types, the distinct biophysical properties of each cell type may result in different freezing kinetics. In this example, the cells in the inner islands (orange) froze at a faster rate than the cells in the surrounding area (green). Thus, to quantify the differences in freezing kinetics between the two cell populations in the tissue, we defined a disparity ratio (Equation 8.7) where τ_{50}^{fast} is set by the inner island population ($\tau_{50}^{in} < \tau_{50}^{out}$), and $\tau_{50}^{slow} = \tau_{50}^{out}$.

8.3 Results and Discussion

A parametric analysis was conducted to investigate the effects of various tissue properties, including the ratio of rates of spontaneous IIF (γ), and the ratio of propagation rates (β) on the kinetics of IIF in a co-cultured tissue. Different tissue geometries were also investigated (shown in Figure 8.1), effectively varying the ratio of heterotypic interactions. Our adaptation of Gillespie's Monte Carlo algorithm[94] was used to predict the kinetics of IIF for all parameters investigated. To account for statistical fluctuations due to the stochastic nature of the IIF process, results from an ensemble of 35 simulations were pooled for each set of tissue parameters investigated. We confirmed that our results converged within 35 simulations by comparison with ensembles comprising of 100 simulations (data not shown). We also assumed that within a given cell type, the biophysical properties were spatially uniform; a reasonable assumption if gradients in

temperature and cell water concentration are negligible on the length scale of the tissue control volume.

Representative results from our Monte Carlo simulations of the IIF process in tissue are shown in Figure 4. Figures 8.4A-D illustrate the sequence of IIF events during freezing of a homogeneous tissue, *i.e.*, cells in the islands and surrounding areas have identical biophysical properties ($\gamma = 1$; $\beta = 1$). It can be seen that IIF initiates randomly throughout the tissue via spontaneous nucleation events (cells frozen by spontaneous nucleation are colored red), followed by growth of domains of frozen cells via intercellular ice propagation (cells frozen by propagation are colored blue). A sequence of images from a representative simulation of IIF in a heterogeneous tissue is shown in Figures 8.4E-H, where intracellular ice can be observed to form preferentially in the cells surrounding the islands, due to a higher rate of intercellular ice propagation (*i.e.,* $\beta = 100$). As a result, the probability of IIF is reduced for cells within the islands; at a time when less than 10% of the island cells exhibit IIF, almost the entire surrounding cell population is frozen (Figure 8.4G). This situation could result if the cell population inside the islands has reduced levels of connexin expression, and hence a lower intercellular propagation rate, in comparison with the cells in the surrounding tissue. Developing a cryopreservation protocol for a tissue with such properties would be quite challenging, due to the large disparity in IIF kinetics between the two cell populations. Thus, the goal of the parametric study presented in this chapter was to evaluate the effectiveness of all potential strategies that may be utilized to minimize this difference in IIF kinetics between the two cell types.

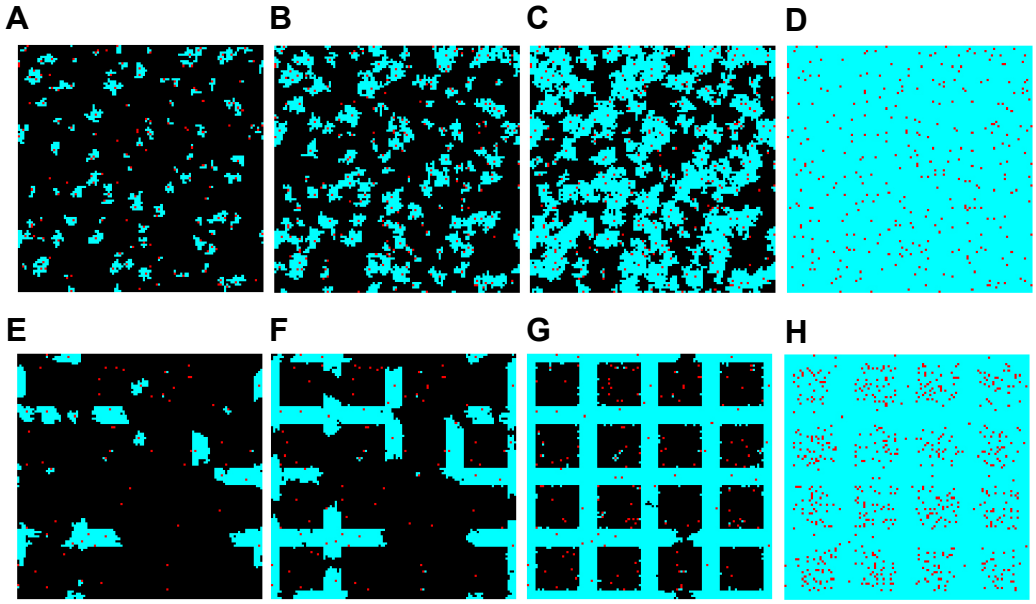

Figure 8.4 Progression of IIF during representative simulations of freezing of homogeneous tissue (A-D), or micropatterned co-culture, with $J_{out}^{p} = 100^{*} J_{in}^{p}$ (E-H). The tissues are shown at 10% (A,E), 25% (B,F), 50% (C,G) and 100% (D,H) frozen volume; black regions represent unfrozen tissue, whereas red sites indicate cells frozen via interaction-independent IIF, and blue sites indicate cells frozen via intercellular ice propagation.

For all tissue geometries presented in Figure 1, IIF was simulated using various combinations of values for the spontaneous nucleation rates, J_{in}^{i} and J_{out}^{i}, and the intercellular ice propagation rates, J_{in}^{p} and J_{out}^{p}. In addition to the nucleation and propagation rates, we also varied the degree of interaction at a heterotypic cell-cell interface, represented by our parameter, ε. The results of our simulations were used to calculate the disparity ratio, or the discrepancy in freezing kinetics between the two cell types, and the results are presented in Figure 8.5. As a reminder, the ideal situation for co-cultured tissue preservation occurs when the disparity ratio equals zero. Thus, looking at the contour plots presented in Figure 8.5, an optimal valley of compatibility for cryopreservation (minimal disparity) is evidenced by the dark purple shaded region. As the color spectrum increases, disparity increases, creating a greater challenge to achieving uniform freezing kinetics between the two cell types. Our results reveal that if the average rate of ice propagation and/or spontaneous ice nucleation differs in two co-cultured cell types, the probability of IIF (and hence, cell damage) can dramatically differ between the two cell types. The predictions of the disparity metric in Figure 8.5 demonstrate different trends in the data. For a given set of tissue nucleation and propagation properties, the valley of compatibility (purple zone) becomes broader as the percentage of heterotypic interactions increases (*i.e.*, smaller cell islands). This orientation of this valley of compatibility is shown to be sensitive to the degree of interaction at a heterotypic cell-cell interface, ε, and relatively insensitive to any changes in tissue geometry (*i.e.*, percentage of heterotypic interactions). It is also evident that the worst case scenario for all tissue parameters occurs along the diagonal of each contour plot, when the ratio of propagation rates is approximately equal to the ratio of

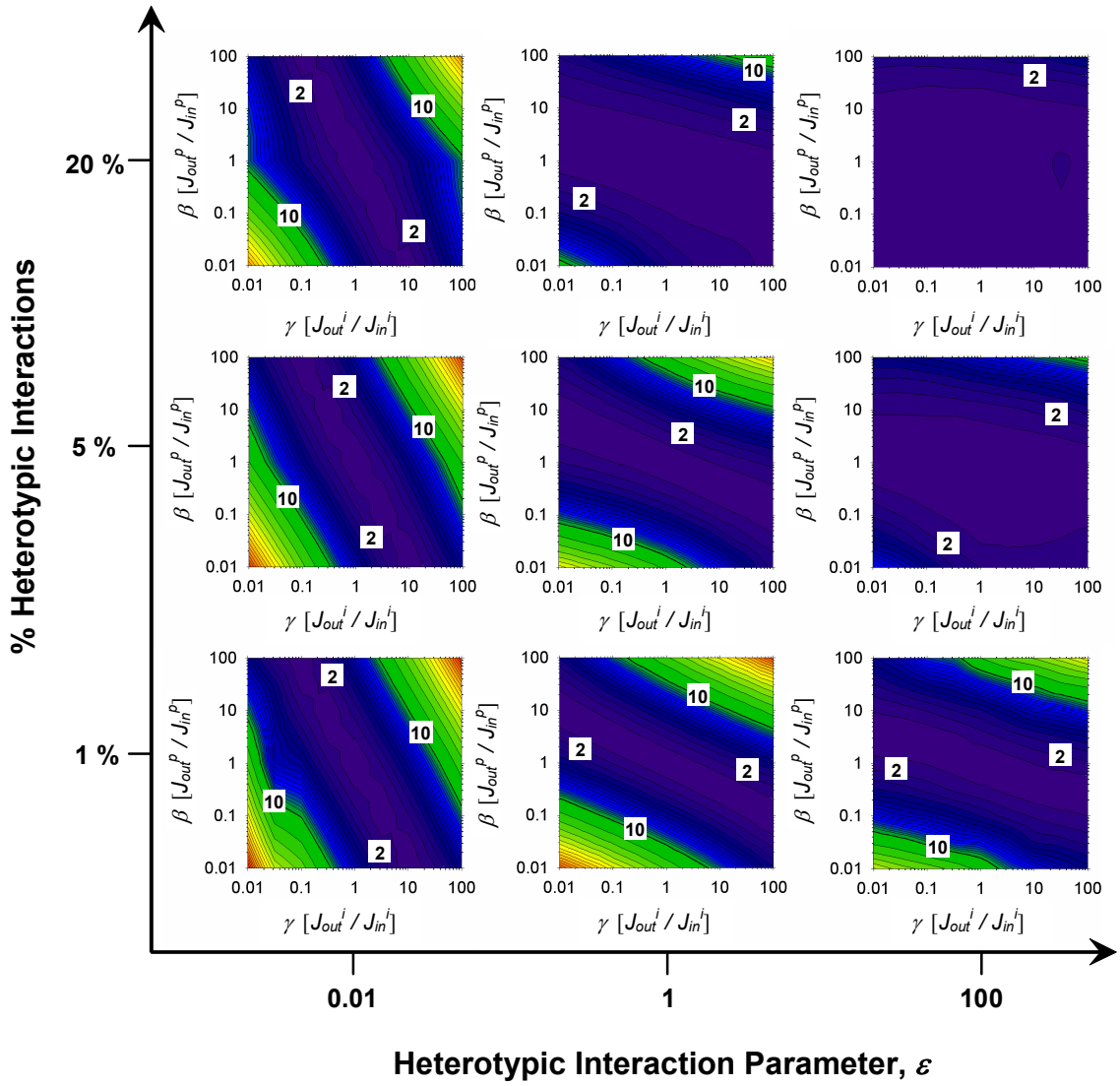

Figure 8.5 Predicted values for the disparity ratio in co-cultured tissue constructs. Monte Carlo simulations were used to predict the kinetics of IIF in co-cultured tissues for different tissue geometries (1%, 5%, and 20% heterotypic interactions) and degree of interaction at heterotypic cell-cell interfaces (ε = 0.01, 1, 100), while holding the average nondimensional rate of propagation constant (α = 100). For all tissue configurations, the ratio of nondimensional propagation rates ($\beta = J_{out}^{p} / J_{in}^{p}$), and the ratio of nondimensional spontaneous nucleation rates ($\gamma = J_{out}^{i} / J_{in}^{i}$) were varied. The optimal region for cryopreservation is indicated by the 'valley of compatibility', or region of the contour plots where the disparity ratio was minimized (purple region, disparity ratio < 1.5).

spontaneous nucleation rates (*i.e.*, $\beta \approx \gamma$). In addition, the disparity ratio reaches its maximum value when $\gamma >> 1$, and $\beta >> 1$. In other words, when both the spontaneous nucleation rate and ice propagation rate for the cells surrounding the islands is significantly greater than the rates for the cells inside the islands, maximum differences in freezing kinetics will be seen for all tissue geometries and ε values.

Next, we investigated the effect of tissue geometry on the disparity ratio, by focusing on the region of the disparity plots where the disparity ratio was maximized (*i.e.*, $\gamma = \beta = 100$). For all tissue configurations, Figure 8.6 presents the disparity ratio calculated from our model predictions for all values of ε, or the degree of interaction at heterotypic cell-cell interfaces. It can be seen that for all values of ε, as the degree of heterotypic interactions increases, the disparity ratio decreases, with a maximum reduction occurring at $\varepsilon = 1$. Therefore one promising strategy to minimize disparity in freezing kinetics is to maximize the degree of heterotypic interactions when designing co-cultured tissue geometry. If changing tissue geometry is not a feasible option, our results indicate that further reductions in the disparity ratio can be gained simply by increasing the degree of interaction at heterotypic interfaces (ε).

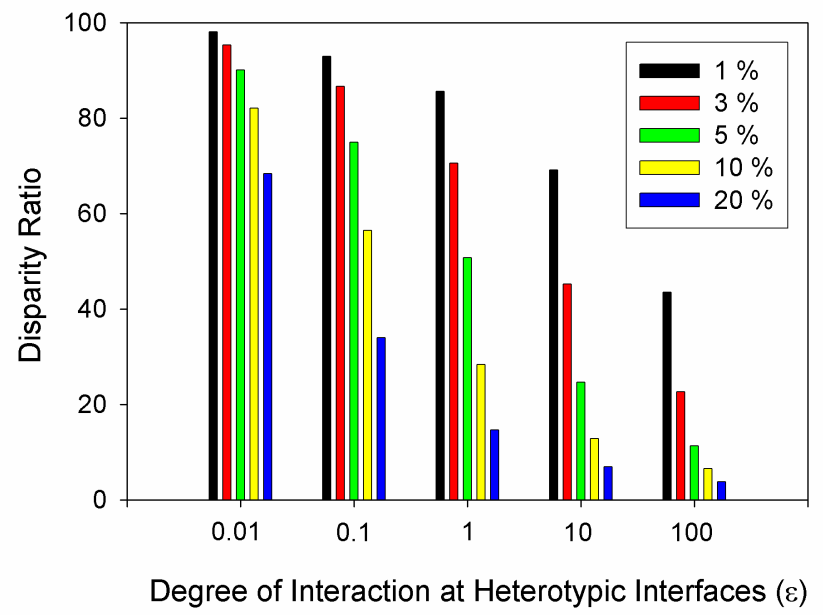

Figure 8.6 Effect of micropattern geometry on the disparity ratio with varying epsilon. Our Monte Carlo simulations were used to predict the disparity ratio as the geometry of the co-cultured tissue, and degree of interaction at heterotypic cell-cell interfaces (ε) were varied. Data are presented for tissue geometries with: 1% (black bars, corresponding to Figure 1E), 3% (red bars, corresponding to Figure 1D), 5% (green bars, corresponding to Figure 1C), 10% (yellow bars, corresponding to Figure 1B), and 20% (blue bars, corresponding to Figure 1A) heterotypic interactions. For all simulations, $\alpha = \gamma = \beta = 100$.

Until this point, all data has been presented for a constant average rate of ice propagation for the tissues (α = 100). Therefore, to investigate the effect of α on the disparity ratio, we again focused on the region of maximum disparity, or $\gamma = \beta$ = 100, now with ε = 1. The disparity ratio was calculated for all tissue geometries while the average rate of ice propagation for the tissue (α) was varied (Figure 8.7). Model predictions suggested that for all tissue geometries, the disparity ratio decreased as the average propagation rate was increased. Further reductions in the disparity ratio were gained by increasing the degree of heterotypic interactions. The best case scenario (for the worst case condition of $\gamma = \beta$ = 100), occurred when heterotypic interactions were maximized at 20% and the average rate of propagation was increased (α = 100).

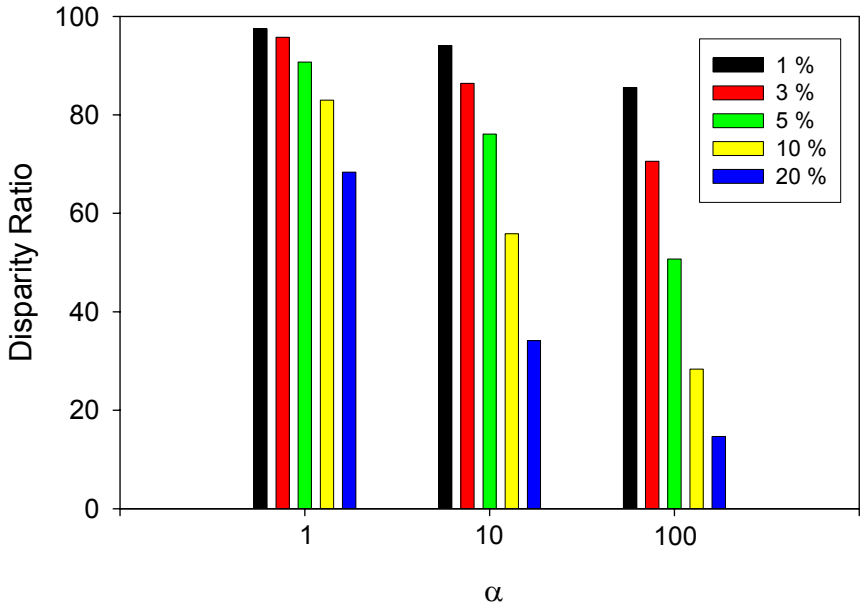

Figure 8.7 Effect of micropattern geometry on the disparity ratio with varying α. Predictions of disparity ratio from our Monte Carlo simulations for all tissue geometries (legend represents percentage of heterotypic interactions) while varying the average ice propagation rate for the tissues. For all simulations ($\varepsilon = 1$, and $\gamma = \beta = 100$), the disparity ratio decreased as the ratio of heterotypic interactions increased. Further reductions were seen as the average ice propagation rate, α, increased.

Earlier in this chapter, we identified a valley of compatibility, or region in which the combination of interaction parameters resulted in low disparity ratios. Now, we released the constraint on the average rate of propagation in the tissue (previously in Figure 8.5, α = 100), and investigated how the valley of compatibility changed in response to variations in α. Since we are primarily interested in the valley of compatibility (purple zone in Figure 8.5), we isolated the regions of the resulting contour plots in which the disparity ratio was ≤ 1.5. In Figure 8.8, the results for two tissue geometries: 80x80 cell islands, and 5x5 cell islands (the minimum and maximum ratios of heterotypic interactions, respectively) are presented. For each tissue geometry, as the average rate of ice propagation in the tissue, α, increased, the orientation of the valley of compatibility changed. For low rates of propagation (α = 1), the valley of compatibility was more sensitive to changes in the ratio of spontaneous nucleation rates. As the rate of propagation increased, the valley of compatibility became less sensitive to changes in the spontaneous nucleation rates and more sensitive to changes in the ratio of propagation rates. In addition, for the tissue geometry with maximum heterotypic interactions (Figure 8.8B, 5x5 cell islands) as the average rate of ice propagation increases, the valley of compatibility increases in size. In contrast, in Figure 8.8A where heterotypic interactions are minimized, the valley of compatibility was approximately the same size for all values of α.

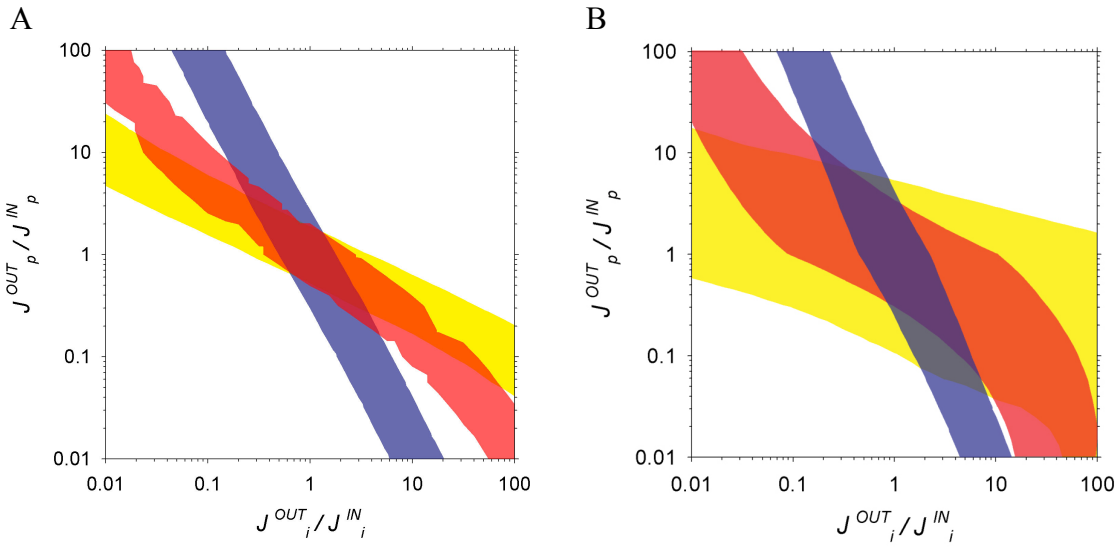

Figure 8.8 Prediction of the valley of compatibility as the average rate of ice propagation is varied. Monte Carlo simulations were used to predict the disparity ratio in co-cultured tissues of two different geometries: (A) 80x80 cell islands, or 1% heterotypic interactions (represented by Figure 1E), and (B) 5x5 cell islands, or 20% heterotypic interactions (represented by Figure 1A). The resulting valleys of compatibility, or zones where the disparity ratio was ≤ 1.5, are shown as they vary with the average rate of ice propagation in the tissue: $\alpha = 1$ (blue), $\alpha = 10$ (red), and $\alpha = 100$ (yellow). For all simulations, $\varepsilon = 1$.

We expected to see symmetry in our model predictions as the ratios of propagation and spontaneous nucleation rates varied. However, as evident from our results, this was not the case. The asymmetry of the model predictions was more noticeable in the 'extreme' regions of the disparity ratio plots (Figure 8.5). Specifically, for large variations in the rate of ice propagation between the two cell types (β), our results were sensitive to the physical placement of each cell type. In other words, it mattered which cell type was placed inside the islands, and which cell type surrounded the islands. To investigate the effect of cell placement, we defined a new metric, Percent Reduction, which quantifies the amount the disparity ratio could be reduced with changing or swapping cell location:

$$\%\text{Reduction} = \left(\frac{\left. \frac{\tau_{50}^{slow}}{\tau_{50}^{fast}} \right|_{swapped}}{\left. \frac{\tau_{50}^{slow}}{\tau_{50}^{fast}} \right|_{original}} - 1 \right) \cdot 100 \tag{8.8}$$

where 'swapped' was defined as the condition in which the biophysical properties for the cells in the discontinuous islands were swapped with the biophysical properties for the surrounding cells. Figure 8.9 graphically illustrates the two conditions.

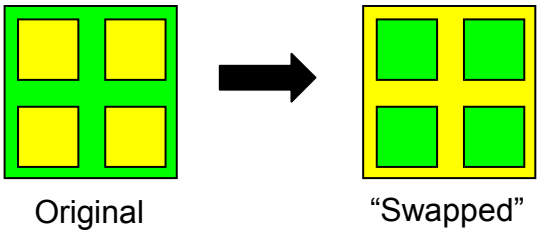

Figure 8.9 Illustration of change in cell placement in co-cultured tissues. To investigate the effects of cell placement on the disparity ratio, the cells in the micropatterned islands were ‘swapped’ with the cells that originally surrounded the islands. The percent reduction metric quantifies the change in the disparity metric from changes in cell placement (all else the same).

A parametric analysis was completed for the 5x5 island tissue geometry (20% heterotypic interactions), this time evaluating the percent reduction in the disparity ratio as a consequence changing the position of each cell type. The effect of variations in the degree of interaction at the heterotypic interface, ε, was investigated, with the results presented in Figure 8.10. From Figures 8.10A and 8.10B, it can be seen that as ε increases, the benefit gained from switching cell position increases significantly. Interestingly, for high ε values, the percent reduction is almost completely insensitive to changes in the ratio of spontaneous nucleation rate.

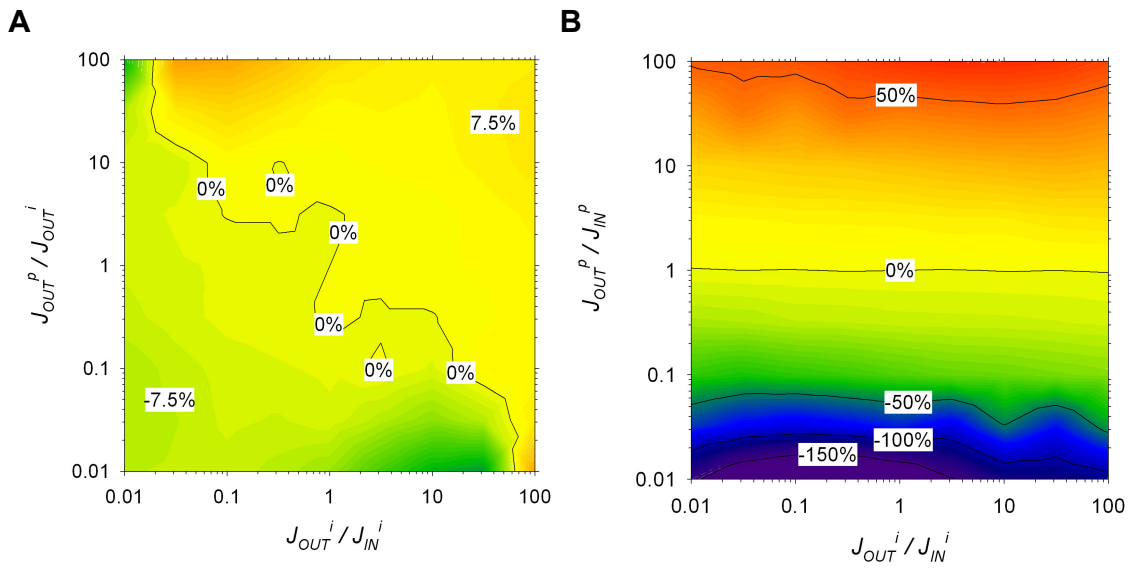

Figure 8.10 Prediction of the percent reduction of the disparity metric as a result of swapping positions of the two cell types, with variations in ε. Axes indicate the ratio of cell properties in the original position. Shown are the results for (A) 5x5 islands, $\varepsilon = 0.1$, $\alpha = 100$, and (B) 5x5 islands, $\varepsilon = 10$, $\alpha = 100$.

Next, we investigated the effect of the average rate of ice propagation, α, on the percent reduction metric (holding ε constant). Analyzing the 5x5 island tissue geometry, a parametric analysis was conducted with the results presented in Figure 8.11. As α was increased, our model indicated that significant gains in the disparity metric could be achieved by proper positioning of cell types. Translating these results into a more physical interpretation: placement of cells with a high intercellular ice propagation rate (and/or high degree of heterotypic cell-cell interaction) in the discontinuous cell islands has a protective effect against IIF. Intuitively, this strategy makes sense. Once a spontaneous nucleation event occurs in a cell of this type, the ice rapidly propagates freezing the entire island but then stops due to the discontiguous nature of the island

patterns. Conversely, if this rapidly propagating cell type is placed in the continuous outer tissue location, once IIF is initiated, the entire population of the cells will rapidly freeze through propagation.

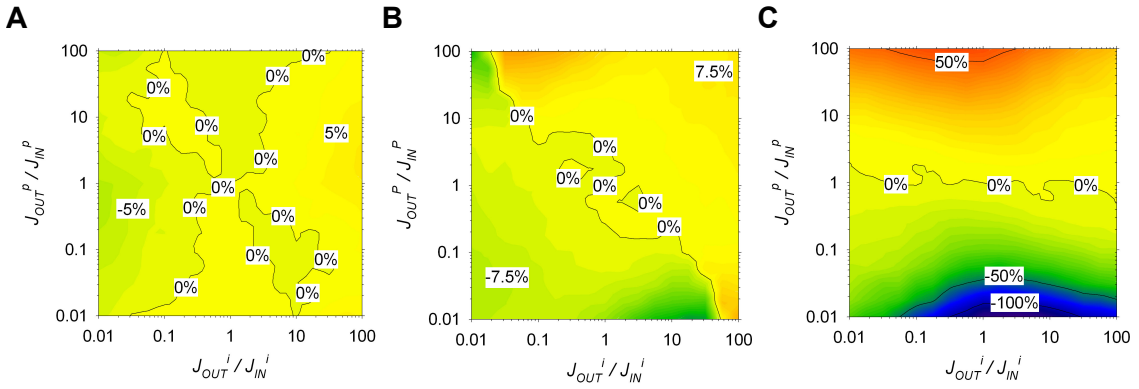

Figure 8.11 Prediction of the percent reduction of the disparity metric as a result of swapping positions of the two cell types, with variations in α. Shown are the results for tissue geometry shown in Figure 1A (5x5 islands) with (A) $\alpha = 1$, (B) $\alpha = 10$, and (C) $\alpha = 100$. For all simulations, $\varepsilon = 1$. See text for details.

Lastly, we investigated for any bias that may have resulted from the tissue size evaluated in this study (112 x 112 cells). The tissue lattice size was doubled (224 x 224 cell); increasing the number of cells in each experiment by a factor of four. To ensure a rigorous test, the tissue geometries that represented the minimum and maximum percentage of heterotypic interactions were selected for this analysis (1% and 20%, respectively), at conditions that were known to produce the largest variations in the disparity metric (*i.e.*, $\alpha = 100$, $\varepsilon = 1$). As with the rest of our simulations, 35 experiments were simulated for each condition, with the disparity ratio results presented in Table 8.1.

The results indicate that all results differed by less than 2%, and as such, we are confident that our tissue size was sufficiently large.

Table 8.1 Influence of tissue size on predictions of the disparity ratio. For all simulations, $\alpha = 100$, $\varepsilon = 1$.

γ	β	Island Dimensions	Disparity Ratio	
			112x112 Domain	224x224 Domain
0.01	0.01	5x5 (20% Heterotypic)	11.81	11.79
0.1	0.1	5x5 (20% Heterotypic)	2.16	2.19
10	10	5x5 (20% Heterotypic)	2.38	2.37
100	100	5x5 (20% Heterotypic)	14.66	14.62
0.01	0.01	80x80 (1% Heterotypic)	82.60	83.34
0.1	0.1	80x80 (1% Heterotypic)	8.64	8.66
10	10	80x80 (1% Heterotypic)	8.72	8.72
100	100	80x80 (1% Heterotypic)	85.58	85.38

8.4 Conclusion

Cryopreservation of co-cultured tissues is a challenging problem. Not only must one consider the biophysical phenomena introduced by cell-substrate and cell-cell interactions, the differences in freezing kinetics for each cell type in the heterogeneous tissue must also be accounted for. For problems such as this, mathematical models of IIF provide great utility in the rational design of cryopreservation protocols. By conducting a parametric analysis of all potential tissue and freezing conditions, an optimal zone of high viability can be identified without the need of costly trial and error experiments. In this chapter, the first model of intracellular ice formation in a micropatterned co-cultured

tissue was presented. Model predictions were used to identify strategies that would minimize the disparity in freezing kinetics between the two cell types. Specifically, a 'valley of compatibility' was defined for all cell parameters that will assist the user in identifying cell types with compatible properties that will results in uniform freezing properties. However, since it is rarely feasible to select a cell type based on its 'freezability', alternative strategies were also identified to minimize differences in freezing kinetics. First, increasing the percentage of heterotypic interactions was shown to minimize the disparity between cell populations. Second, specific cell properties could be targeted to reduce additional damage through ice propagation. One such example would be the addition of a peptide gap junction blocker that would temporarily shut down cell-cell interactions during freezing. The results of our model would allow the user to perform a cost/benefit analysis for the reduction in ice propagation rate. Lastly, our model predictions suggest that large improvements in the uniformity of freezing kinetics can be achieved by the changing the spatial locations of the cells. Using micropatterning techniques, it would be possible to design a co-cultured tissue construct such that the cell type with the faster rate of intercellular ice propagation was located in discontinuous cell islands. Such a simple change in design would improve the success rate of the cryopreservation protocol, while maintaining all of the same tissue properties that were originally desired. The utility of this model extends beyond these brief examples related to the cryopreservation of co-cultured tissues. With a few modifications, this model can be further extended to predict tissue destruction, rather than preservation, ideal for cryosurgical planning. As such, models that can predict the mechanisms of intracellular

ice formation and ice propagation in homogeneous and heterogeneous tissue can be of great benefit to both the fields of cryopreservation and cryosurgery.

CHAPTER 9

PARAMETRIC ANALYSIS OF INTERCELLULAR ICE PROPAGATION DURING CRYOSURGERY, SIMULATED USING MONTE CARLO TECHNIQUES*

9.1 Introduction

In the last decade cryosurgery has experienced a growth in popularity as an effective treatment for cancerous tissues in the prostate, liver, breast, kidney, bone and soft tissue sarcomas[9-14]. To maximize tumor destruction, the ice ball diameter is typically extended 1 cm beyond the tumor edge, mimicking the surgical margins used in conventional tumor resection[10,14,176]. This practice causes damage to the healthy tissue surrounding tumor, with undesirable sequelae. For example, in the treatment of prostatic cancer, extension of the ice ball beyond the tumor can cause surgical complications including impotence and rectal fistulas[177,178]. The ability to decrease collateral damage to the normal tissue surrounding the targeted tumor may increase the utility of cryosurgery by allowing cryosurgical procedures to be used for ablation of malignancies in close proximity to sensitive tissue or organs. Adjuvant therapies using mechanical, thermal or biochemical approaches have previously been attempted in order to increase the specificity of damage during cryosurgery, achieving varying degrees of success.

---

* Stott, S.L., Irimia, D., and Karlsson, J.O.M. *Technology in Cancer Research and Treatment*, **3** (2) 113-124, 2004. http://www.tcrt.org, reprinted with permission.

Increased sensitivity of the tumor to freezing injury has been achieved by the injection of antifreeze proteins (AFPs)[179,180], pre-treatment with chemotherapeutic drugs[181] or a combination of hyperthermia and exposure to acidic conditions[182]. Attempts to reduce damage in healthy tissue have been limited to thermal approaches, such as the use of urethral warmers and or cryoheaters[183,184]. Mathematical models of the process of cryosurgery can be useful in the identification of novel strategies for improving the specificity of tissue damage during cryosurgery. However, while many models have previously been developed for simulating the biophysical response of tumors during cryosurgery[52,53,109,185-190], these studies have not taken into consideration the effects of the freezing procedure on the healthy tissue at the periphery of the tumor. The present work addresses this limitation by investigating the biophysical response to freezing of a heterogeneous tissue comprising both the tumor and the surrounding normal cells.

Cell destruction by cryosurgery is thought to result from a combination of deleterious mechanisms[15]. These include immediate, direct cell injury due to intracellular ice formation (IIF) or excessive cell dehydration[2], as well as delayed, indirect damage due to apopotosis[191,192] or ischemic tissue injury resulting from vascular stasis[15,193]. However, only IIF will be considered in the present paper. The probability of IIF is known to increase in the presence of cell-cell contact[60,64], an effect thought to be due to intercellular propagation of deleterious ice crystals via gap junctions[56,58]. We have previously developed a mathematical model able to predict the effect of cell-cell communication on the kinetics of IIF in tissue[58,61]. In our model, the rate of IIF in each cell was expressed as a sum of contributions from two distinct mechanisms: the

propagation of ice from a frozen neighbor across the corresponding cell-cell interface; and the spontaneous formation of intracellular ice through interaction-independent, non-propagative processes. These interaction-independent mechanisms of IIF may include surface and volume catalyzed nucleation[23], osmotic rupture[40], or mechanical rupture[41]. Whereas the effect of cell-cell communication on the kinetics of IIF has only recently been understood, previous models of cryosurgery have neglected the effects of intercellular ice propagation[52,53,109,185-189]. One exception is a recent study by Zhang *et al.*, in which an attempt to adapt our model of intercellular ice propagation to predict the kinetics of IIF in a four-cell system representing cancerous breast tissue is presented[190]; unfortunately, this paper was later shown to contain serious errors[97]. In the present study, we will simulate the effects of cell-cell communication in multicellular tissue (comprising $\sim 10^4$ cells), and also account for the different properties of normal and neoplastic cells.

Tumor cells are known to exhibit down-regulated gap junctional intercellular communication[194]. Due to the reduced gap junction activity in tumor cells, we have hypothesized that the rate of intercellular ice propagation in the tumor will be lower than in the surrounding normal tissue. This hypothesis is consistent with *in vivo* observations that malignant cells are more resistant than normal cells to freezing injury[195]. In the present study, we will consider a heterogeneous tissue that contains two different cell types, each characterized by a different set of values for the rates of interaction-independent IIF and intercellular ice propagation. By varying the relative magnitude of these rates for the two tissue types, our model can capture the inherent differences in the

biophysical properties of normal and cancerous cells, as well as the effect of any clinical interventions which affect the cells' response to cryosurgery.

The goal of this study is to develop computational tools which will help to gain insight into the IIF-interactions between the tumor and healthy tissue during cryoablation. In particular, we have simulated the effects of the recently recognized phenomenon of intercellular ice propagation, and present a parametric analysis towards the goal of developing novel strategies for improving specificity of tissue damage during cryosurgery. The parameters investigated include the levels of gap junction intercellular communication in healthy and tumor tissue, the relative magnitudes of the rates of interaction-independent IIF in healthy and tumor tissue, and thermal gradients associated with cryoprobe placement.

9.2 Theoretical Background

9.2.1 Modeling Assumptions

We have previously developed a mathematical model to predict the effect of cell-cell communication on the kinetics of IIF in tissue[58]. In our model, each cell in the tissue can freeze via one of two classes of mechanisms: (i) intercellular ice propagation, comprising all possible processes of IIF which depend on the state (frozen vs. unfrozen) of the cell's nearest neighbors; (ii) interaction-independent IIF, comprising any mechanisms which are independent of the state of the neighboring cells. By writing the governing equations in a non-dimensional form, the model becomes invariant to the rate

of interaction-independent IIF, i.e., model predictions can be obtained without making any *a priori* assumptions about the mechanisms or kinetics of this process.

To investigate the distribution of injury between normal and malignant cells during cryosurgery, we have adapted our previous model to account for spatially varying biophysical properties. As illustrated in Figure 9.1, we have represented a section of tissue as a lattice of 99×99 cells, each interior cell being in communication with four neighbors. The control volume was divided into two regions, corresponding to tissue targeted for cryoablation (within which destruction must be maximized), and non-targeted tissue (within which collateral damage must be minimized). Whereas in practice, both such regions may comprise multiple cell types, we have made the simplifying assumption that the targeted and non-targeted tissue regions are both homogeneous, the former containing only identical tumor cells (T) and the latter only identical healthy cells (H). The tumor was centrally located and occupied 50% of the control volume. The cryoprobe was assumed to be located in the center of the tumor. The average rate of interaction-independent IIF was assumed to be different in healthy and tumor cells, as a result of differences in cell properties, differences in water content, or differences induced by selective manipulation of the tumor before or during cryosurgery. Thus, we defined characteristic rates J^i_H and J^i_T, representing the average number of interaction-independent IIF events per unit time per cell in healthy and tumor tissue, respectively. Similarly, the different levels of gap junction expression in normal and cancerous cells were represented by defining different characteristic rates of intercellular ice propagation in the healthy tissue and in the tumor (J^p_H and J^p_T, respectively).

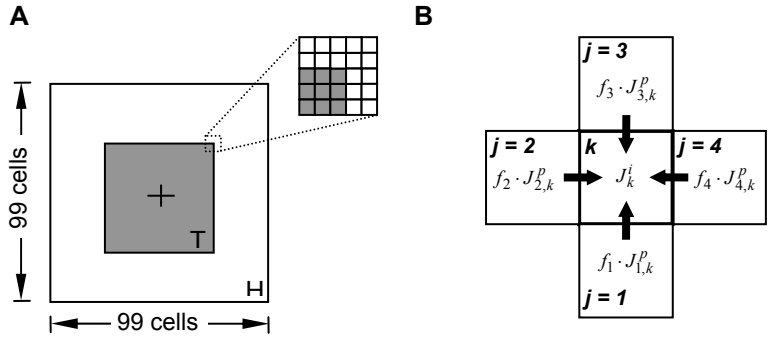

Figure 9.1 (A) Schematic of the tissue geometry, with a tumor (T) consisting of 70×70 cells centered on a 99×99 lattice, surrounded by healthy cells (H). The cross-hairs represent the coordinate system origin, and the location of the cryosurgical probe. (B) Schematic illustrating possible mechanisms of IIF in a cell at lattice point k, which interacts with four neighboring cells (j = 1,…,4). The rate of intercellular ice propagation from cell j to cell k is $f_j \cdot J^{p}_{j,k}$ and the rate of interaction-independent IIF in cell k is J^{i}_{k}. See text for definition of symbols.

Following our previous approach (30), a nondimensional time scale (τ) is defined such that the dimensionless rate of interaction-independent IIF in the healthy tissue becomes constant with unit magnitude:

$$\tau = \int_0^t J^i_H(t) \cdot dt \tag{9.1}$$

By formulating the governing equations in nondimensional form using Equation 9.1, the model predictions will be invariant to assumptions about the mechanism of interaction-independent IIF in the healthy cells, and in particular, will not be affected by any reduction in J^i_H due to cell dehydration during the freezing process.

With the above transformation, a dimensionless rate of interaction-independent IIF in the tumor cells can be defined as follows:

$$\gamma \equiv \frac{J_T^i}{J_H^i} \tag{9.2}$$

The nondimensional system equations also contain dimensionless rates of intercellular ice propagation, defined

$$\alpha_H \equiv \frac{J_H^p}{J_H^i} \tag{9.3a}$$

$$\alpha_T \equiv \frac{J_T^p}{J_H^i} \tag{9.3b}$$

for healthy and tumor tissue, respectively. We have previously shown that to a reasonable approximation, the rate of intercellular ice propagation is proportional to the rate of interaction-independent IIF within a given tissue type[58]. In the present study, we will also make the simplifying assumption that the characteristic rates of interaction-independent IIF in the healthy and tumor cells differ only by a constant multiplicative factor. Thus, the nondimensional parameters γ, α_H, and α_T are all assumed to be approximately constant. In the governing equations for our system, the kinetics of IIF depend only on the magnitudes of these three parameters (as well as on the assumed tissue geometry). For convenience, a dimensionless parameter β was also defined, to describe the relative magnitudes of the propagation rates in healthy and tumor tissue:

$$\beta \equiv \frac{J_T^p}{J_H^p} = \frac{\alpha_T}{\alpha_H} \tag{9.4}$$

Figure 9.1B illustrates the possible mechanisms of IIF in an unfrozen cell k which is flanked by four neighbors (j = 1,...,4). Cell k can freeze by interaction-independent IIF (at an average rate J^i_k), or by propagation of ice from a frozen neighbor j into cell k (at an average rate $J^p_{j,k}$). Thus, the overall rate of IIF for cell k at time t is

$$J_k^{IIF}(t) = J_k^i(t) + \sum_{j=1}^{4} f_j \cdot J_{j,k}^p(t) \tag{9.5}$$

where f_j represents the state of the neighboring cell:

$$f_j = \begin{cases} 1 & \text{if cell } j \text{ is frozen} \\ 0 & \text{if cell } j \text{ is unfrozen} \end{cases}$$

The definition of the rates J^i_k and $J^p_{j,k}$ depends on cell type, and may also be affected by spatial temperature gradients in the vicinity of the cryoprobe, as described below.

9.2.2 Monte Carlo Simulation

We have previously developed Monte Carlo techniques to simulate the kinetics of intercellular ice propagation in tissues too large to be analyzed using the state space approach[59,61]. In the present study, we have used a more efficient Monte Carlo algorithm, based on methods initially developed by Gillespie[94] for simulation of the stochastic time evolution of coupled chemical reactions. Using the computed values of the rates of interaction-independent IIF (J^i_k) and intercellular ice propagation ($J^p_{j,k}$) for each cell in the tissue, Gillespie's algorithm is able to predict the site, mechanism, and timing of each random IIF event.

We initially considered the case where the rates of nucleation and propagation in each cell were not affected by the cell's proximity to the cryoprobe. Thus, $J^i_k = J^i_H$ or $J^i_k = J^i_T$ for normal and tumor cells, respectively. Likewise, for homotypic interactions (cells j and k of the same tissue type), $J^p_{j,k} = J^p_H$ or $J^p_{j,k} = J^p_T$ for healthy and cancerous tissue, respectively. For heterotypic interactions (cells j and k of different types), we have assumed that the slower propagation mechanisms would be rate limiting, such that $J^p_{j,k} = \min(J^p_H, J^p_T)$.

Whereas thermal gradients in the vicinity of the cryoprobe are expected to result in spatial variations of the rate of IIF in the tissue, we analyzed the potential effects of this phenomenon on the ability to selectively destroy the tumor tissue. To describe spatially nonuniform parameters, we defined a Cartesian coordinate system such that the origin was coincident with the cryoprobe location, and the coordinates of a cell k were (x_k,y_k). Thus, we could express the distance between cell k and the cryprobe in nondimensional form, as shown below:

$$r_k \equiv \frac{\sqrt{x_k^2 + y_k^2}}{R} \tag{9.6}$$

where R is the effective tumor radius, i.e., the average distance of the tumor edge from the origin.

In order to keep the model as simple as possible, we represented the effects of the spatially non-uniform temperature field by modifying the local nucleation and propagation rates (J^i_k and $J^p_{j,k}$) such that their magnitudes decreased exponentially with

distance from the cryoprobe. Thus, the rates of interaction-independent IIF in healthy and tumor tissue were assumed to be of the form

$$J_k^i = J_H^i \cdot e^{-r_k/\lambda} \tag{9.7}$$

and

$$J_k^i = J_T^i \cdot e^{-r_k/\lambda} \tag{9.8}$$

respectively. The characteristic dimensionless length scale λ defines the location at which the rate has decreased to 37% (e^{-1}) of the magnitude at the cryoprobe. This dimension is intended to roughly represent the radius of the ice ball, normalized to the effective tumor radius. Thus, the nucleation rates will be negligible outside the tumor if $\lambda \ll 1$, while nucleation rates will be significant in the tissue surrounding the tumor if $\lambda \gg 1$. In the limit $\lambda \to \infty$, we recover the case of spatially uniform rates of IIF, considered above.

The rates of intercellular ice propagation are similarly assumed to be of the form

$$J_{j,k}^p = J_H^p \cdot e^{-r_k/\lambda} \tag{9.9}$$

$$J_{j,k}^p = J_T^p \cdot e^{-r_k/\lambda} \tag{9.10}$$

for homotypic interactions in healthy and tumor tissue, respectively; and

$$J_{j,k}^p = \min(J_H^p, J_T^p) \cdot e^{-r_k/\lambda} \tag{9.11}$$

for heterotypic interactions.

9.2.3 Parametric Analysis

To analyze the specificity of cryoinjury in a control volume containing both tumor and healthy cells, we computed a metric $P^{IIF}{}_H$, defined as the probability of IIF in the healthy tissue at the time point when 50% of the tumor cells contained intracellular ice. Thus, if $P^{IIF}{}_H < 0.5$, cryoinjury due to IIF is occurring at a faster rate in the tumor cells than in the healthy cells, i.e., a desirable specificity of damage has been achieved. The specificity metric $P^{IIF}{}_H$ was computed for a range of values of the parameters γ, β, λ and α_H; a set of critical values of these parameters (γ^*, β^*, λ^* and α^*_H, respectively) were defined as the values at which $P^{IIF}{}_H = 0.5$.

To determine how sensitive the specificity of damage was to variations in the value of a given tissue property x (where $x = \beta$, λ or α_H), we used the standard definition of relative sensitivity:

$$S_{P_H^{IIF}:x} \equiv \left| \frac{x}{P_H^{IIF}} \left(\frac{\partial P_H^{IIF}}{\partial x} \right) \right| \tag{9.12}$$

where $S_{P_H^{IIF}:x}$ indicates the relative sensitivity of the specificity metric to variations in parameter x; Equation 9.12 was evaluated at the critical value of x. If the relative sensitivity is large for a given parameter x, then a small relative change in the value of x can produce a large relative change in the specificity metric; indicating that manipulation of the corresponding tissue property may be an effective strategy for controlling specificity of cryoinjury during cryosurgery.

9.3 Results and Discussion

9.3.1 Spatially Uniform Rates

Using our adaptation of the Monte Carlo algorithm proposed by Gillespie[94], we investigated the effects of various tissue properties, including the ratio of rates of interaction-independent IIF (γ) and the propagation rate ratio (β), on the kinetics of IIF in a heterogeneous tissue comprising both healthy and tumor cells. In order to account for statistical fluctuations due to the stochastic nature of the IIF process, results from an ensemble of 35 simulations were pooled for each set of tissue parameters investigated (convergence of results was confirmed by comparison with ensembles comprising up to 100 simulations; data not shown). In our initial investigations, we assumed that the cell biophysical properties (i.e., the rates of interaction-independent IIF and intercellular ice propagation) were spatially uniform within a given tissue type. This is a reasonable assumption if gradients in temperature and water concentration are negligible on the length scale of the tissue control volume.

Representative results from our simulations of IIF in the absence of thermal gradients, in a tissue consisting of 99×99 cells, are shown in Figure 9.2. In Figure 9.2A-D, the sequence of IIF events during freezing of a homogeneous tissue, i.e. with identical properties for the healthy and tumor cells ($\gamma = 1$; $\beta = 1$), is illustrated. It is seen that IIF is initiated randomly throughout the tissue volume via interaction-independent ice formation events (e.g., nucleation), followed by the growth of independent domains of frozen cells via intercellular ice propagation; these domains eventually impinge on one another, until the entire control volume is transformed. Whereas the tissue properties have been assumed to be homogeneous, the distribution of sites of interaction-

independent IIF (and hence, the distribution of frozen domains) is fairly uniform throughout the tissue.

A sequence of images from a representative simulation of IIF in a heterogeneous tissue is shown in Figure 9.2E-F. In this simulation, the intercellular ice propagation rate was assumed to be an order of magnitude lower in the tumor tissue than in the healthy tissue (i.e., $\beta = 0.1$), representing the downregulation of gap junction in cancer cells[194]. As a result, the probability of IIF is reduced within the tumor, and the peripheral healthy tissue is destroyed by IIF before significant damage has been sustained by the tumor cells (Figure 9.2G). This effect may be counteracted by an increase in the rate of interaction-independent IIF (e.g., intracellular nucleation) in the tumor tissue, such as may result from increased water content in cancerous cells[196-201] or the reduced rates of water transport within a tumor mass[190,202]. One goal of the parametric analysis in the present study is to establish the required relationship between the interaction-independent IIF rate ratio (γ) and the intercellular propagation rate ratio (β) in the two tissue types in order to minimize damage to healthy cells during cryoablation of tumor tissue.

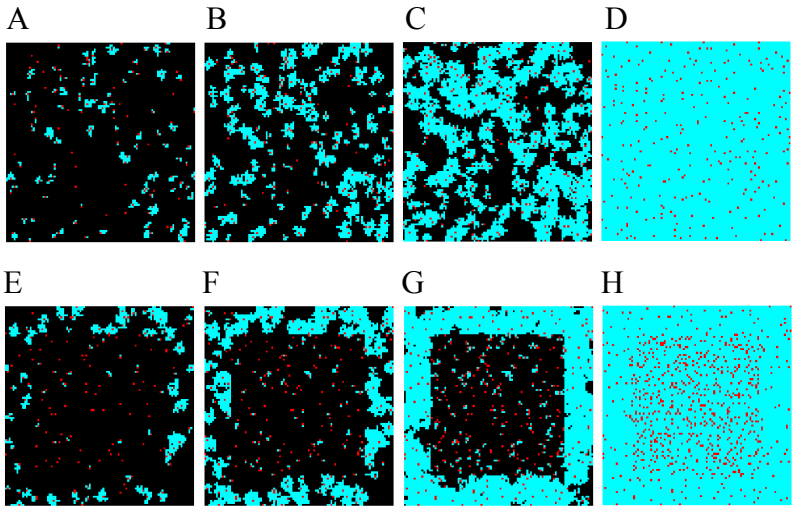

Figure 9.2 Progression of IIF during representative simulations of freezing of homogeneous tissue (A-D), or heterogeneous tissue comprising a tumor with $\beta = 0.1$ (E-H), representing down regulation of gap junctions in cancerous cells. The tissues are shown at 10% (A, E), 25% (B, F), 50% (C, G), and 100% (D, H) probability of IIF; black regions represent unfrozen tissue, whereas red sites indicate cells frozen by interaction-independent IIF, and blue sites indicate cells frozen via intercellular ice propagation. In both simulations, rates were assumed to be spatially uniform within each tissue type, and the dimensionless propagation rate was $\alpha_H = 100$; in the heterogeneous tissue, interaction-independent IIF was assumed to occur at the same rate in tumor and healthy cells ($\gamma = 1$).

In Figure 9.3, destruction of healthy tissue by IIF is tracked as a function of the cumulative incidence of IIF in the tumor. Thus, if the tumor cells are assumed to have biophysical properties identical to those of healthy cells ($\gamma = 1$; $\beta = 1$), the probability of IIF in both tissue types are approximately the same throughout the freezing process. Paradoxically, the probability of IIF in the healthy tissue is in fact slightly lower than in the tumor for this case, even though both tissue types have been assumed to have the same biophysical properties. We have previously demonstrated that the spatial distribution of the average probability of IIF can be non-uniform in homogeneous tissue, as a result of edge effects due to finite tissue size[59,61]. Thus, whereas the tumor is located in the center of the control volume, the probability of IIF in this region of the tissue will be larger than in the healthy cells at the edge of the control volume, even in the absence of differences in tissue properties. As expected, when the intercellular ice propagation rate is reduced by an order of magnitude in the tumor tissue ($\beta = 0.1$) while keeping the rates of interaction-independent IIF equivalent in the two tissue types ($\gamma = 1$), the average rate of IIF in the healthy tissue is significantly larger than in the tumor. As shown in Figure 9.3, the probability of IIF in the tumor cells for this case is less than 0.1% when 50% of the healthy cells have frozen; conversely, 100% cell destruction by IIF is predicted in the healthy tissue at the time point when the probability of IIF in the tumor is 50%. Also illustrated in Figure 9.3 is the effect of assuming a rate of interaction-independent IIF that is one order of magnitude higher in the cancerous cells than in the normal cells ($\gamma = 10$), while keeping the rates of intercellular ice propagation equivalent in the two tissue types ($\beta = 1$). As expected, the overall probability of IIF is higher in the

tumor than in the peripheral healthy tissue for these conditions; thus, there is only 9% IIF in the normal cells when the 50% of the tumor is intracellularly frozen.

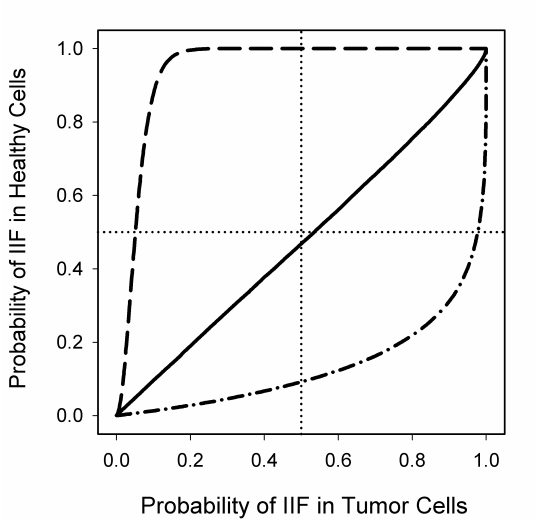

Figure 9.3 Probability of IIF in healthy tissue as a function of the cumulative incidence of IIF in the tumor, for tissues with $\alpha_H = 100$ and spatially uniform rates within each tissue type. Shown are predictions for a homogeneous tissue with $\gamma = 1$ and $\beta = 1$ (solid line), and for heterogeneous tissue with $\gamma = 1$ and $\beta = 0.1$ (dashed line) or $\gamma = 10$ and $\beta = 1$ (dash-dotted line). Also shown are two reference lines (dotted lines). The vertical reference line indicates the time point at which 50% of the tumor is intracellularly frozen; the probability of IIF in the healthy tissue at this time point (P_{IIFH}) was defined as a metric to assess specificity of tissue injury. If the corresponding point on the plot falls below the horizontal reference line (i.e., $P_{IIFH} < 0.5$), then IIF-related damage occurs selectively in the tumor, sparing the normal tissue.

For further analysis of the specificity of cryoinjury, we computed a metric P^{IIF}_H, defined as the probability of IIF in the healthy tissue at the timepoint when 50% of the tumor cells contained intracellular ice (corresponding to the vertical reference line in Figure 9.3). Thus, if there is preferential destruction of the tumor by IIF, then $P^{IIF}_H < 0.5$; conversely, if $P^{IIF}_H > 0.5$, then intracellular ice forms preferentially in the healthy tissue, an undesirable situation for cryosurgery. Contour plots of the specificity metric as a

function of the ratios of the intercellular propagation rate and the interaction-independent IIF rate are shown in Figure 9.4. Whereas the IIF kinetics also depend on the absolute propagation rates, results for two values of the nondimensional propagation rate in the healthy tissue are shown ($\alpha_H = 10$ and $\alpha_H = 1000$). Consistent with our observations above, specificity of cryoinjury worsens (i.e., P^{IIF}_H increases) with a decreasing propagation rate ratio β, and specificity improves (P^{IIF}_H decreases) with increasing rates of interaction-independent IIF in the tumor relative to the healthy tissue (i.e., increasing γ). Interestingly, the specificity of damage appears to be relatively insensitive to the magnitude of β, as long as $\beta \leq 0.1$. Thus, for $\alpha_H = 10$ (Figure 9.4A), cryoinjury by IIF will occur preferentially in the tumor cells if and only if the ratio of interaction-independent IIF rates is greater than a critical value $\gamma^* \approx 5$, for any value of $\beta \leq 0.1$. As shown in Figure 9.4B, the trends are similar for $\alpha_H = 1000$, but the critical value for the ratio of interaction-independent IIF rates (i.e. the value of γ at which $P^{IIF}_H = 0.5$) is now $\gamma^* \approx 100$. Whereas results were insensitive to β for $\beta \leq 0.1$, the calculated specificity as a function of γ and α_H is shown in Figure 9.4C, for $\beta = 0.1$. It can be seen that the critical ratio of interaction-independent IIF rates increases with the nondimensional propagation rate in the healthy tissue; in particular, the approximately linear relationship between the logarithms of γ^* and α_H observed for $\alpha_H > 1$ in Figure 9.4C represents a power law dependence $\gamma^* \sim \sqrt{\alpha_H}$. A potentially important result predicted from our simulations is that if the rate of interaction-independent IIF is less than this critical value, but at least on the same order of magnitude as the corresponding rate in the healthy tissue (i.e., $1 < \gamma < \gamma^*$), then a significant improvement in specificity of cryoinjury can be achieved by increasing the propagation rate ratio to a magnitude approaching unity. For example,

as shown in Figure 9.4B, if $\alpha_H = 1000$ and $\gamma = 10$, increasing the propagation rate ratio from $\beta = 0.1$ to $\beta = 1$ will result in a ~90% reduction in P^{IIF}_H.

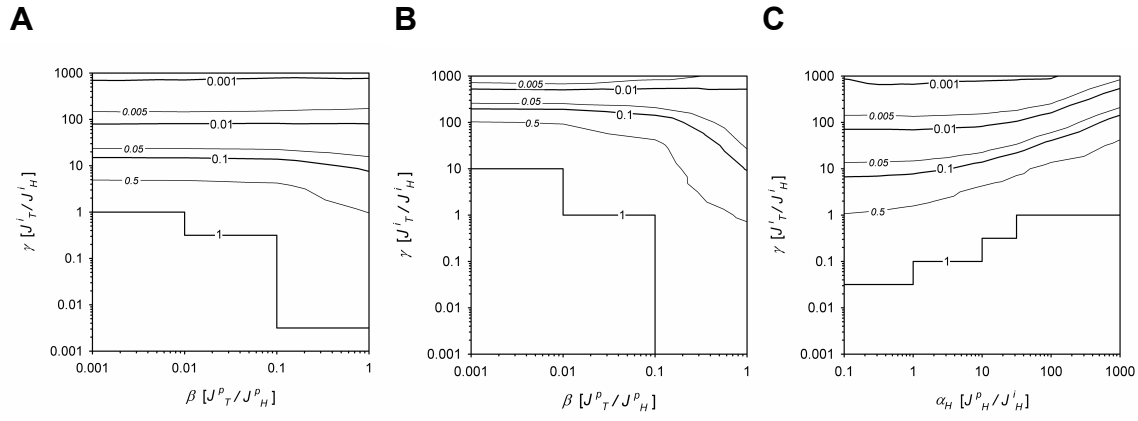

Figure 9.4 Predicted values of the specificity metric (P_{IIFH}) as a function of γ and β, for the case of spatially uniform rates, with $\alpha_H = 10$ (A) or $\alpha_H = 1000$ (B). Also shown is the specificity metric calculated as a function of γ and α_H (C), for $\beta = 0.1$.

To date, the only quantitative measurement of an intercellular propagation rate in the literature is our measurement of an effective nondimensional propagation rate $\alpha = 10.4$ in human hepatoma cells[59,61]. This value is more likely to be representative of ice propagation in tumor tissue than in healthy tissue; thus, we expect realistic values of the nondimensional propagation rate in non-cancerous cells to be in the range $\alpha_H \gg 1$, and physiological ranges for the propagation rate ratio to be on the order $\beta \ll 1$. Whereas the rate of intracellular ice nucleation has a highly nonlinear dependence on water content[203], it is difficult to predict likely ranges for γ in a real tumor. If the differential in water content between cancerous and normal cells is not sufficient to increase γ beyond its critical value γ^*, then additional measures must be taken to improve specificity of

damage during cryosurgery. Two distinct approaches for achieving this goal are suggested by the results of the present study. In particular, we propose a novel strategy for minimizing collateral damage to healthy tissue, by increasing the propagation rate ratio β. In principle, this can be achieved either by treating the healthy tissue with a gap junction inhibitor, or by attempting to upregulate gap junctional communication in the tumor prior to cryosurgery. An alternative strategy for improving specificity of damage is to selectively increase the rate of interaction-independent IIF in the tumor. One example of this approach is the injection of AFPs into the tumor[179,180], which has the effect of modifying the extracellular ice morphology in such a way that the rate of interaction-independent IIF increases, as a result of deleterious mechanical interactions between the cells and the extracellular ice crystals[41]. Another factor which may cause a selective increase in the rate of interaction-independent IIF in the tumor is the temperature differential in the two tissue types due to placement of the cryosurgical probe. The effect of such thermal gradients is investigated below.

9.3.2 Spatially Non-Uniform Rates

To represent the effect of thermal gradients in the vicinity of the cryosurgical probe, we assumed that the rate of IIF would decrease with distance from the probe, and used Equations 9.6 - 9.11 to estimate the magnitude of the rates of interaction-independent IIF and intercellular ice propagation as a function of location in the tissue. A dimensionless distance (λ) was used to define the characteristic length scale of the thermal gradient relative to the size of the tumor. For simplicity, the effect of differences in the tissue-specific rates of interaction-independent IIF was neglected (i.e., $\gamma = 1$), and the specificity metric P^{IIF}_{H} was computed from Monte Carlo simulations for various

combinations of the parameters λ, β, and α_H. The specificity of cryoablation will improve if $\gamma > 1$ (as demonstrated in Figure 9.4); thus, the results obtained below (assuming $\gamma = 1$) represent conservative predictions.

For a given combination of values β and α_H, we determined the critical value λ^*, representing the upper bound for λ in order to selectively induce IIF in the tumor cells. The critical value λ^* is shown as a function of β and α_H in Figure 9.5A. It is clear that for physiological conditions ($\alpha_H \gg 1$ and $\beta \ll 1$), the upper bound on λ is less than unity. This result suggests that in the absence of adjuvant therapies that may reduce the intercellular ice propagation rate in healthy tissue (thus decreasing α_H and increasing β), the size of the ice-ball must be kept small, such that the rate of intracellular ice nucleation is negligible at the tumor edge. On the other hand, if it is possible to manipulate the tissue properties such that the propagation rate ratio will approach unity, then specificity of damage may be achieved even with an ice-ball larger than the tumor ($\lambda > 1$). It may be hypothesized that urethral warmers[183] and or cryoheaters[184] confer a benefit by decreasing λ and by reducing the rates of nucleation and propagation in the healthy tissue, thus decreasing α_H and increasing β.

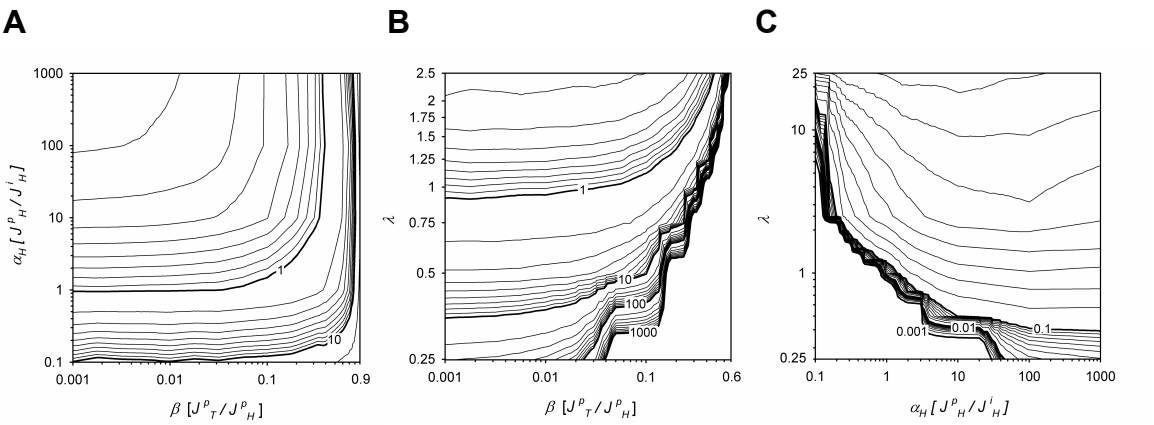

Figure 9.5 Predicted critical parameter values: (A) λ*; (B) α_H*; (C) β*. For all cases, rates of propagation and interaction-independent IIF were spatially nonuniform, and the tumor and healthy tissue properties differed only with respect to the rates of intercellular ice propagation (i.e., $\gamma = 1$). See text for details.

In Figure 9.5B, the critical value α_H* is shown as a function of the parameters λ and β. In order to achieve specificity of damage during cryosurgery, the healthy tissue must have $\alpha_H < \alpha_H$*. Thus, it can be seen that physiological ranges for the healthy tissue propagation rate (i.e., $\alpha_H \gg 1$) are admissible only if the propagation rate ratio (β) approaches unity magnitude, or if the thermal gradient length scale is smaller than the tumor radius ($\lambda < 1$). The critical value β*, i.e. the lower bound on the propagation rate ratio required to achieve selective destruction of the tumor, is shown as a function of the parameters λ and α_H in Figure 9.5C. For $\alpha_H \gg 1$ (hypothesized physiological range), the required lower bound on the propagation rate ratio decreases with decreasing λ (i.e., as the thermal gradients become more steep). Whereas the permissible regime for the values of λ and α_H is demarcated by the contour $\beta^* = \beta$ for a given propagation rate ratio β, Figure 9.5C shows that the constraints on λ and α_H are relatively insensitive to β for $\beta < 0.1$, consistent with our results for the case of spatially uniform rates. In a standard

cryosurgical procedure, the ice-ball extends somewhat beyond the tumor edge, and thus a realistic magnitude for the dimensionless gradient length scale is likely $\lambda \sim 1$. Thus, the predictions in Figure 9.5 reiterate the importance of attempting to increase β or reduce α_H as strategies for minimizing damage to the healthy tissue.

In order to determine which of the experimental parameters (λ, α_H, β) would be most effective for improving the specificity of cryoinjury, we computed the relative sensitivity of $P^{IIF}{}_H$ to variations in each of these variables, using Equation 9.12. The relative sensitivity to changes in given parameter was evaluated for variations about the corresponding critical value, and the magnitude of the partial derivative in Equation 9.12 was estimated using finite differences. Thus, Figure 9.6A shows the relative sensitivity of $P^{IIF}{}_H$ to variations in λ about λ^*, as a function of β and α_H. Similarly, Figure 9.6B shows the relative sensitivity of $P^{IIF}{}_H$ to variations in α_H about α_H^*, as a function of β and λ; and Figure 9.6C shows the relative sensitivity of $P^{IIF}{}_H$ to variations in β about β^*, as a function of α_H and λ. Comparison of the three graphs in Figure 9.6 reveals that the specificity metric is most sensitive to variations in λ, followed by β and then α_H. As seen in Figure 9.6A, in the putative physiological regime ($\alpha_H \gg 1$ and $\beta \ll 1$), the relative sensitivity of $P^{IIF}{}_H$ to variations in λ is larger than unity, indicating that a small relative change in the parameter λ will yield a larger relative change in the magnitude of the specificity metric, making this parameter the best candidate for strategies to minimize damage in the healthy tissue. In contrast, as shown in Figure 9.6C, the relative sensitivity of $P^{IIF}{}_H$ to variations in α_H is uniformly less than unity for all values tested, indicating that large relative changes in α_H would yield smaller relative changes in $P^{IIF}{}_H$, and making this the least effective strategy for improving specificity of damage. Whereas the

magnitude of the dimensionless thermal gradient length scale is likely on the order $\lambda \sim 1$ during typical cryosurgical procedures, Figure 9.6B reveals that the relative sensitivity of $P^{IIF}{}_H$ to variations in β is close to unity for large values of the nondimensional propagation rate α_H; thus, under physiological conditions, a relative change in the propagation rate ratio β will result in a relative change of comparable magnitude in the specificity metric.

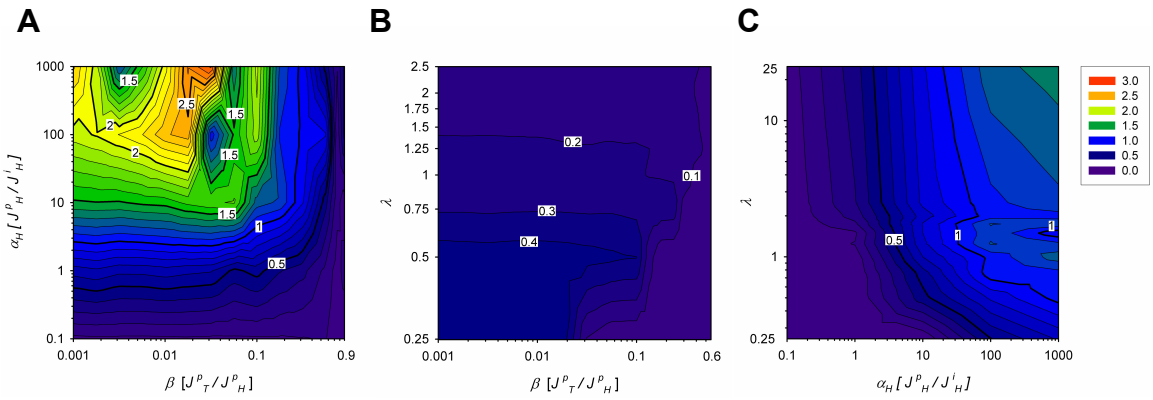

Figure 9.6 Estimated relative sensitivity of $P^{IIF}{}_H$ to changes in various experimental parameters, for $\gamma = 1$ and spatially nonuniform rates: (A) relative sensitivity of $P^{IIF}{}_H$ to variations in λ about λ^*; (B) relative sensitivity of $P^{IIF}{}_H$ to variations in α_H about α_H^*; (C) relative sensitivity of $P^{IIF}{}_H$ to variations in β about β^*. See text for details.

9.4 Model Limitations and Future Directions

Cell dehydration during the freezing process is known to reduce the incidence of IIF[15]; due in part to the reduction of ice nucleation rates with decreasing intracellular water content[23,203]. It should be noted that even though the present IIF model does not explicitly incorporate water transport equations, our predictions would not be affected by a reduction of the nucleation rate due to cell dehydration: any changes in the magnitude

of J^i_H would only affect the conversion from nondimensional to dimensional time (Equation 9.1). Thus, only the absolute timing of IIF events, not their relative sequence, would be altered.

The effect of cell dehydration on the rate of intercellular ice propagation is not known. Nonetheless, it is not unreasonable to expect that the ice propagation rate and nucleation rate have a similar dependence on the degree of intracellular supercooling, with water transport affecting both mechanisms of IIF in a similar way. Thus, our present assumption that the rates of nucleation and propagation differ only by a constant multiplicative factor should be adequate for purposes of initial analysis. The validity of this assumption has been verified, but only under conditions of rapid freezing, for which little or no water transport is expected[58,59,61]; it is possible that this aspect of the model will have to be refined when data on the concentration-dependence of the rate of intercellular ice propagation becomes available.

Another important issue is the scale-up of predictions to tumors of physiologically relevant dimensions. Whereas the scale of our present IIF calculations is unprecedented in the literature, the results presented here are nonetheless limited to simulations for tissue control volumes comprising only 99×99 cells (*ca.* 1 mm^2). We observed no significant changes in the predicted results when calculations were repeated for tissues up to four times this size (data not shown). However, theoretical analysis of intercellular ice propagation in one-dimensional tissue constructs have demonstrated that tissue size can in fact affect the kinetics, distribution, and dominant mechanism of IIF, depending on the magnitude of the intercellular ice propagation rate[59,61]. Unfortunately, due to prohibitive computational cost, simulation of IIF in tissues containing more than ~10^5 cells is not

practical using the present techniques. Alternative methods for analysis of IIF kinetics in macroscale tissue volumes are currently under development[204].

Additional topics of future research include the incorporation of non-IIF cell injury mechanisms. For example, it may be possible to use existing models of freezing-induced tissue dehydration[52,109,190] to estimate the extent of "solution effects" injury[2]. Such studies would complement the present analysis, which provides predictions of the distribution of IIF-related damage in healthy and tumor tissue under a broad range of conditions relevant to cryosurgery.

9.5 Conclusion

The present study represents the first model of intercellular ice propagation during freezing of a heterogeneous tissue volume comprising over 10^3 tumor cells, and the first investigation of the potential effects of thermal gradients on the dynamics of intercellular ice propagation. Whereas a number of simplifying assumptions were made in the model development, the present quantitative predictions should be interpreted as first-order approximations. Nonetheless, we believe that the qualitative trends revealed by parametric analysis are reasonably robust, and that the general conclusions of our present work will not be affected by quantitative refinements of the model. Our analysis has provided some insight into the benefits conferred by some proposed adjuvant therapies such as the use of AFPs or cryoheaters, and has suggested a novel strategy for improving specificity of ablation during cryosurgery, by manipulating gap junction activity in the tumor and/or its peripheral normal tissue. Our mathematical model of intercellular ice propagation also represents an important complement to ongoing efforts to develop

computer-aided treatment planning tools for cryosurgery, which hitherto have neglected the effects of cell-cell communication.

CHAPTER 10

CONCLUSION AND RECOMMENDATIONS FOR FUTURE WORK

10.1 Conclusion

Cryopreservation is a core technology necessary for the production, banking and distribution of tissue engineered products. However, significant loss of tissue function can result from cell damage caused by intracellular ice formation (IIF) during cooling to cryogenic storage temperatures. For adherent cells and tissues, the probability of IIF is known to be greater than the probability for single suspended cells, resulting in an increased susceptibility to deleterious IIF events. The goal of the studies presented in this dissertation was to elucidate the dominant mechanisms of IIF in adherent cells and tissues. Specifically, the effects of cell-substrate and cell-cell interactions were investigated.

To this end, a novel high speed digital video cryomicroscopy system was developed, allowing for imaging at sub-millisecond and sub-micron resolutions. Using this system, we observed and quantified the initiation and growth of intracellular ice during freezing of single micropatterned endothelial cells. The process of IIF manifested as a single advancing front, radiating outwards from an initiation site. Shortly after initiation of the IIF event, a gradual darkening of the cell occurred. These results were surprising, in that for the past 50 years cell darkening has been used as the primary indicator of IIF during cryomicroscopy. In addition, the appearance of a single, growing ice front was unexpected, as it had never been previously witnessed. Thus, to further

investigate the kinetics of ice formation, we both characterized the kinetics of the ice front growth and cell darkening, while systematically investigating parameters thought to influence IIF.

10.1.1 Cell-Substrate Interactions

With our high speed video cryomicroscopy system, the time, temperature, and initiation point of IIF could be directly measured. As such, for single micropatterned endothelial cells, we investigated the effects of cell attachment area, time in culture and fibronectin coating density on the initiation of IIF. During our investigations of IIF kinetics, a new phenomenon was discovered, where microscale ice dendrites penetrated the paracellular space between the basal membrane of the cell and the substrate. We tested our hypothesis that these ice dendrites were penetrating small gaps between the attached cell and the substrate by applying pore theory to our experimental data, and found that this hypothesis was plausible. In addition, a correlation was shown between the temperature of paracellular ice penetration and the temperature of the subsequent IIF events. These paracellular ice dendrites were also shown to spatially co-localize with IIF initiation, leading us to hypothesize that these dendrites were a pre-cursor to IIF. Our investigations showed that the frequency of paracellular ice penetration increased as cell diameter and culture time were increased. In addition, a decrease in fibronectin coating density was shown to increase the frequency of paracellular ice penetration as well as the rate of IIF co-localized with paracellular ice dendrites. For each of these conditions, quantitative immunofluorescent studies revealed that the increase in frequency of paracellular ice penetration correlated with an increase in number of gaps between focal adhesion proteins along the cell periphery.

For all single cell cryomicroscopy studies, the majority of IIF events initiated at the cell periphery. This was another surprising result that suggested the most commonly accepted theory of IIF in suspended cells, surface-catalyzed nucleation, may not be directly applicable to attached cells. To investigate this finding, cryomicroscopy experiments were conducted by systematically increasing cell attachment area while maintaining a constant cell shape. Analysis of the results indicated that the kinetics of IIF events initiating at the cell periphery scaled with cell perimeter, not with cell attachment area, thus supporting our hypothesis of an alternative primary mechanism of IIF for attached cells. In addition, the rate of peripheral initiation of IIF was also shown to correlate with the number of gaps between focal adhesion proteins at the cell periphery.

Our single cell studies suggest that two dominant mechanisms are responsible for initiating IIF in attached cells. The dominant mechanism of IIF in single attached cells appears to be associated with initiation sites at the cell perimeter. A second mechanism of IIF correlates with the initial formation of paracellular ice dendrites, followed by IIF initiation co-localized with these dendrites. Interestingly, the rate of each mechanism has been shown to scale with the average number of gaps between focal adhesion proteins along the cell periphery. It is too early to speculate as to the exact cause of each mechanism.

From our results, novel strategies to reduce the probability of IIF in attached cells can be identified. Considering the strong correlation between focal adhesion gap number and increased susceptibility to IIF, one can postulate that increasing the density of focal adhesions at the cell periphery may provide a protective effect against IIF. Our

fluorescent staining indicates that this can be done through reduction in cell attachment area, increasing fibronectin coating density or reducing culture time.

10.1.2 Cell-Cell Interactions

The results of the studies presented in this dissertation provided the first temporally resolved measurement of intercellular ice propagation. Micropatterned pairs of primary endothelial cells were analyzed and gap junction intercellular communication was verified for all experimental conditions. During freezing of bovine endothelial cells in rectangular two-cell pairs, IIF initiation was shown to be preferentially located at the cell-cell interface for cells in direct contact with a previously frozen cell. This result supports the hypothesis that intercellular ice propagates through cell-cell contacts. It was interesting to discover that in comparison to single cell controls, the addition of cell-cell contact did not increase the overall probability of IIF for bovine endothelial cells. Our data indicate that the rate of IIF initiation due to the presence of ice in the neighboring cell was dramatically increased ($\alpha = 42$), whereas the spontaneous initiation rate of IIF was shown to decrease as a consequence of cell-cell contact. The combination of these two rate changes resulted in a null effect. However, if the experimental system were increased to include more than two cells, the rapid propagation rate would be expected to have a dominating effect.

The influence of cell-cell contact on the probability of IIF was also investigated using human endothelial cells in bow tie shaped patterns. Our hypothesis was that as the degree of cell-cell contact increased, the rate of propagation would scale accordingly. However, the results of our human endothelial cells were unexpected. Despite the presence of cell-cell communication, human cells in bow tie patterns demonstrated low

rates of intercellular ice propagation. In addition, in direct contrast to the results in our previous study, none of IIF events in the second cell of the pair to freeze initiated at the cell-cell interface. Thus, it was not surprising that increasing the level of cell-cell contact in the human bow tie patterns did not influence the rate of intercellular ice propagation.

Despite the differences in experimental outcomes between the two propagation studies, interesting observations can be made based on the results. First, the data from the bovine cells confirm that intercellular ice propagation does indeed occur, and for primary endothelial cells, it can occur at a very rapid rate. This is significant in that a high rate of ice propagation will potentially make endothelial cells far more susceptible to freezing damage. Thus, considering the outcomes of our bovine study, the results of our human study are all the more intriguing. Elucidating the mechanism behind this response would be of great interest to the field of cryobiology, and the potential control of ice propagation via altering culture conditions would be a unique strategy for improving cell survival during cryopreservation. Moreover, in the field of cryosurgery, understanding how one can promote intercellular ice propagation in select biological tissues would be of great value.

10.1.3 Mathematical Models of IIF in Heterogeneous Tissue

Two mathematical models were presented in this dissertation to demonstrate their utility in predicting freezing kinetics in heterogeneous tissue. Conducting a parametric analysis of all culture conditions through model simulations to identify optimal regimes for cryopreservation is far more cost effective than the trial and error experiments typically performed. For example, from our parametric analysis of a micropatterned co-cultured tissue construct, data revealed that simple geometric placement of cells with a

fast intercellular ice propagation rate (i.e., our endothelial cells) in discontinuous islands can dramatically improve the disparity in freezing kinetics. In addition, novel strategies can be identified for cryosurgery treatment planning as a result of model predictions. From our cryosurgery model, our parametric analysis indicated that the selective changes in cell-cell communication may be an effective strategy for reducing collateral damage to healthy tissue surrounding the targeted tumor.

10.2 Recommendations for Future Work

Many interesting questions were raised from our results. Several specific recommendations for future work will be briefly outlined with respect to the different mechanisms of IIF examined in these studies.

In regards to cell-substrate interactions, anecdotal evidence was seen in our data suggesting that extracellular ice played a role in initiating IIF. A small number of researchers have presented qualitative data that also supports the hypothesis that extracellular ice mechanically interacts with cells during freezing[41,105]. One interesting trend in these previous reports is that both the extent of cell deformation and supposed consequential injury disappears when cryoprotectant additives (CPAs) (*e.g.,* DMSO, or glycerol) are included in the system[41,105]. Adding DMSO to suspended cells has been shown to modulate the cell membrane structure and stability[205], as well as change membrane transport properties[206]. In addition, recent experiments using laser tweezers have shown an increase in cell membrane stiffness with the addition of DMSO[207]. Thus, cryoprotective additives may change the mechanical properties of the cell membrane, reducing its susceptibility to deformation injury. Thus, it would be interesting to study

the effects of CPAs on both IIF initiation and the mechanical properties of the cell. Correlating the two changes would help to further elucidate the mechanisms of damage in attached cells.

Rapid changes to cell membrane properties and cell-substrate interactions can be achieved through the addition of biochemical modifiers. Within minutes, pharmacological agents could alter cytoskeleton tension, bound integrin adhesion strength and membrane tension in our micropatterned cells. Potential additives include: (*i*) NHS-ester sulfo-BSOCOES, which cross-links integrins bound to fibronectin (increasing bound integrin adhesion strength)[143]; (*ii*) cholesterol and methyl-β-cyclodextrin (increasing and decreasing membrane tension, respectively)[124]; (*iii*) 2,3-butanedione 2-monoxime (BDM), a myosin isoform inhibitor that induces actin bundle loss without loss of actin meshwork (decreasing cytoskeleton tension)[151,208]. The use of such biochemical modifiers would allow for near identical long-term culture conditions, while acutely altering the mechanical properties of the cells immediately prior to freezing.

Localized changes in cell adhesion properties in a single attached cell have been achieved through micropatterning of arrays of small adhesion islands[101,144]. These micron-sized islands serve as discontinuous attachment points for a single spread cell, resulting in localized areas of attachment with portions of the cell membrane not anchored to the substrate. Freezing cells with known areas of cell substrate attachment (and separation between attachment points) would provide additional information regarding the mechanisms of both peripheral initiated IIF events and paracellular ice penetration.

For two-cell experiments, work has already commenced to develop an assay to directly quantify cell-cell communication during freezing. Gap junctions are sensitive intercellular channels that have been shown to rapidly decouple[156]. Thus, the ability to verify gap junction communication immediately prior to freezing would be necessary to confirm or refute the role of gap junctions in the propagation of ice. Inspired by a new technique developed by Dakin *et al.*[209], we are attempting to use caged fluorescent molecules to quantify cell-cell communication. Prior to freezing, cells would be loaded with the caged fluorescent molecule and cultured on micropatterned substrates. After loading the sample on the cryostage, immediately prior to the temperature plunge, the fluorescent molecule (permeable only through gap junctions) would be uncaged through UV light. Verification of cell-cell communication would be immediate and the cryomicroscopy experiment could continue as planned.

The use of short-interfering RNA (siRNA) technology provides a wealth of opportunities for future experiments in cell adhesion properties as well as cell-cell interactions[152]. However, most of the current gene databases for siRNA are for human or murine cells. As such, human endothelial cells were selected for our two-cell experiments with the intention of incorporating siRNA techniques in future experiments. Specifically, silencing connexin gene expression through siRNA techniques would greatly contribute to the results presented in this dissertation[153]. The subsequent knock down of gap junction proteins would provide an interesting experimental system for the study of intercellular ice propagation. In addition, many cell adhesion molecules, such as vinculin, can also be silenced through siRNA[99], which would contribute to the knowledge gained from our cell-substrate studies.

Finally, experimental results from this work highlight improvements that can be made in our mathematical models. The use of a single rate of propagation may not be an accurate model of intercellular ice propagation in primary cells. In addition, a more nuanced relationship between the rate of spontaneous initiation of IIF, J_i, and the rate of ice propagation, J_p, should be reflected in the model. As such, more complex models of spontaneous IIF initiation and propagation rates would be important improvements to our Monte Carlo simulations.

In summary, the long term goal of the studies presented in this dissertation was to develop mathematical models that accurately predict the response of homogeneous and heterogeneous tissues to freezing. The studies performed for this dissertation provided insights into the mechanisms of intracellular ice formation in biological tissue. Quantification of the effect of cell-substrate and cell-cell interactions on the kinetics of IIF enabled the creation of mathematical models that accurately predict the freezing kinetics for both single attached cells and heterogeneous tissues. Moreover, understanding the mechanisms of intracellular ice formation and intercellular ice propagation, as well as the identification of new phenomena associated with IIF, significantly contributed to our understanding of IIF in tissue. As such, the combined experimental and theoretical work presented in this dissertation significantly contribute to this long term goal, bringing closer the rational design and optimization of cryopreservation protocols and cryosurgical treatment planning.

APPENDIX A

QUANTIFICATION OF CELL DARKENING DURING FREEZING

A.1 High Speed Digital Video Analysis

A program was created in LabView 8.0 with IMAQ 8.0 (National Instruments) to quantify the darkening of the cell after IIF initiation. The program performed a frame-by-frame analysis of the 8bit grayscale images, dynamically tracking the cell as it drifted during the experiment. For success operation of the program the user must input the following values:

- First frame of IIF
- Last frame of video (if file save was truncated)
- Position of the control background box (i.e., top, bottom, left, or right, of the cell position).

The graphical user interface of the program is shown in Figure A.1.

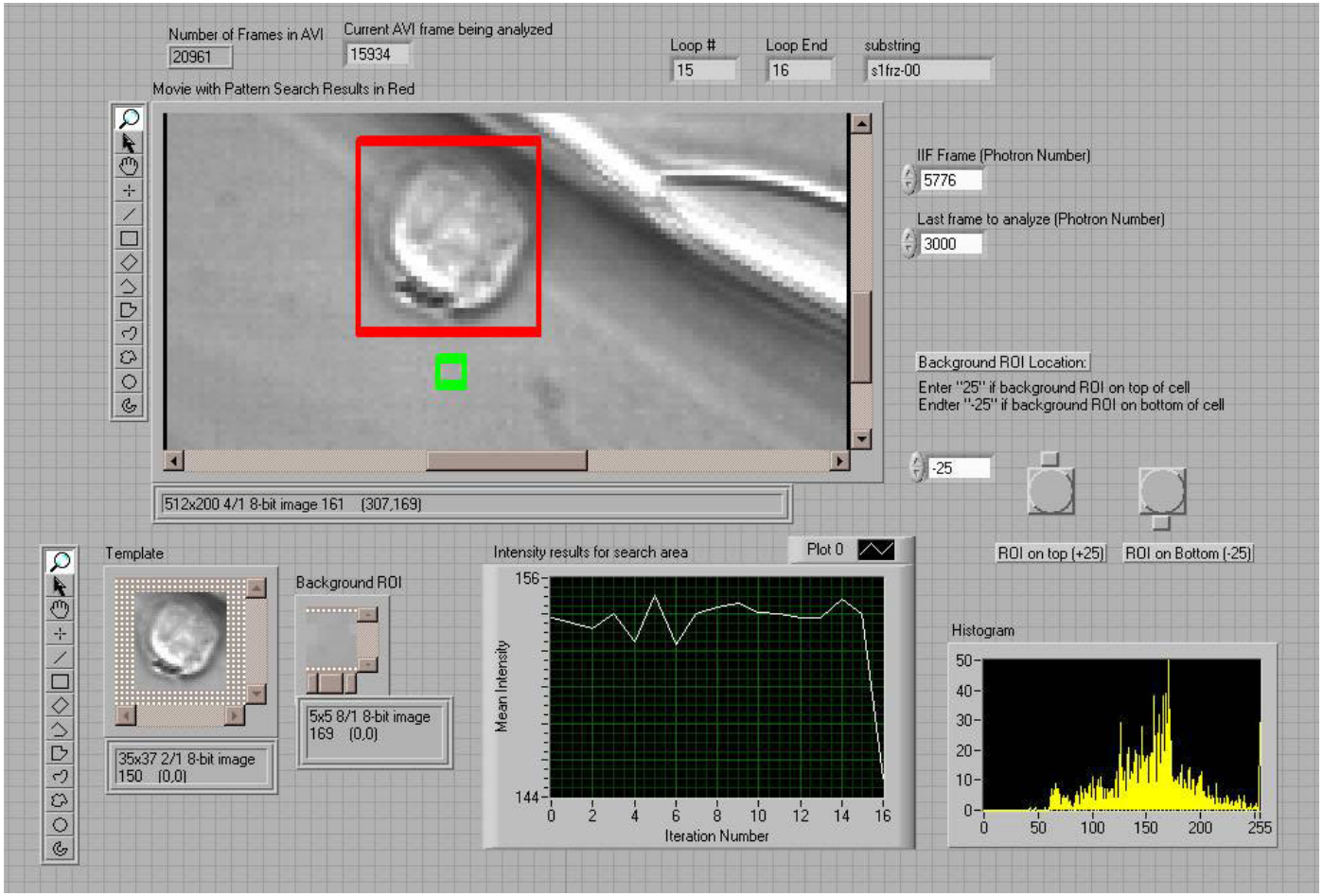

Figure A.1 Front panel user interface for cell darkening high speed video analysis. Red rectangle represents region of cell analyzed for gray scale intensity changes (dynamically shifting with cell movement). The green rectangle represents the control background area.

Analysis began with the image identified as the first frame of IIF. In the program, the image identified as the first frame of IIF is uploaded into a graphic user interface (Figure A.1), prompting the user to select a region for analysis of the entire span of the movie. The user should select a region that will encompass the position of the cell for the full duration of the movie (accounting for cell drift), while decreasing the size of each image that needs to be processed (increasing processing time). Using this image, the user defined a bounding box that tightly surrounds the 20 μm diameter micropatterned cell. This initial template was then used to start the particle-tracking algorithm that captures the motion of the cell as it moves throughout the video. An additional 9x9 pixel box was automatically created along the periphery of the cell bounding box. This box served as a control, and recorded intensity changes in the background of the video. After the initial IIF frame was analyzed, the program proceeded to analyze every subsequent tenth frame, recording the full histogram as well as average grayscale intensity for the cell and the background box. Screen captures of the program code is presented in Figures A.2-4.

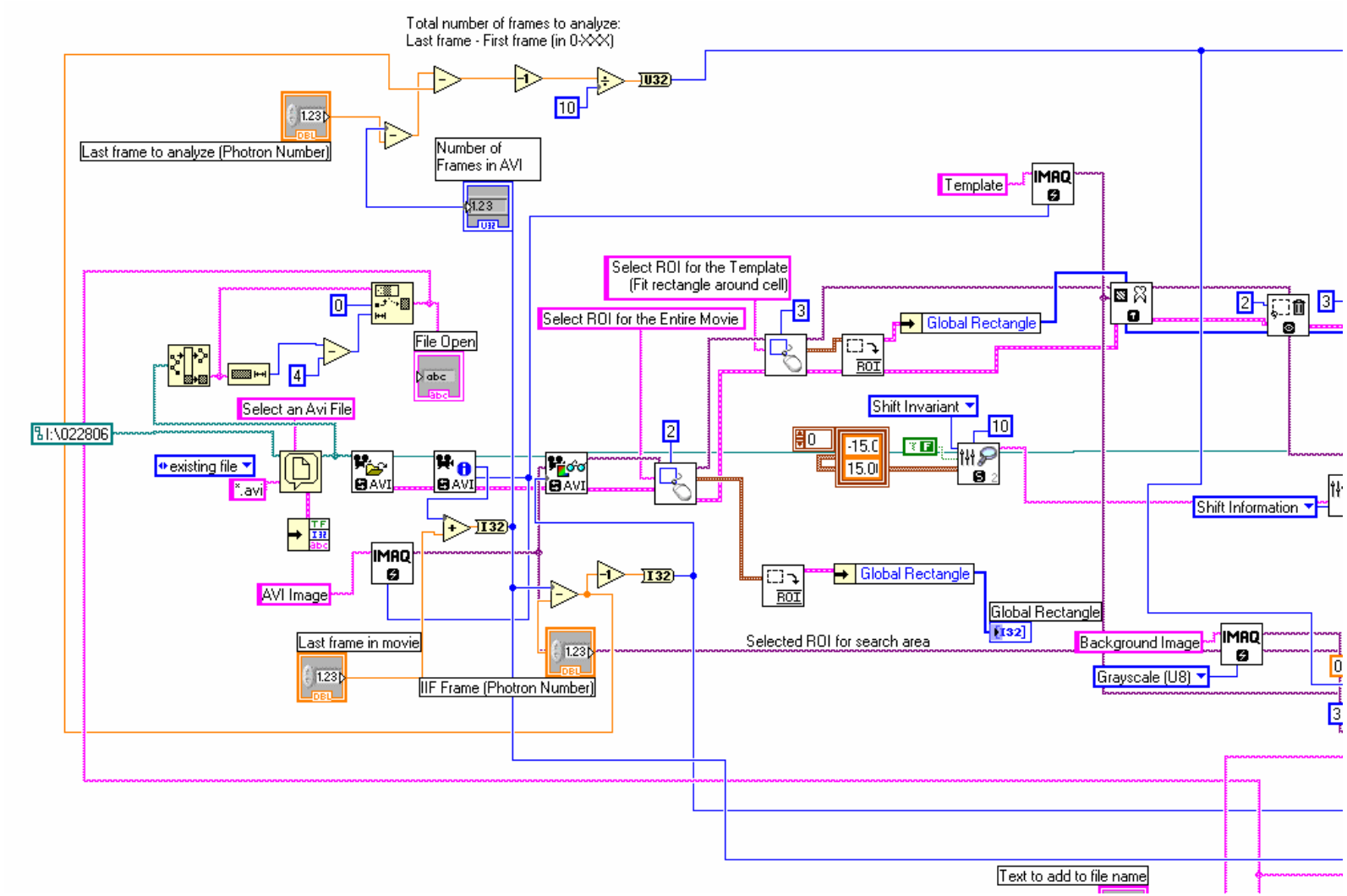

Figure A.2 Graphic representation of LabView code used to analyze high speed videos of cell darkening.

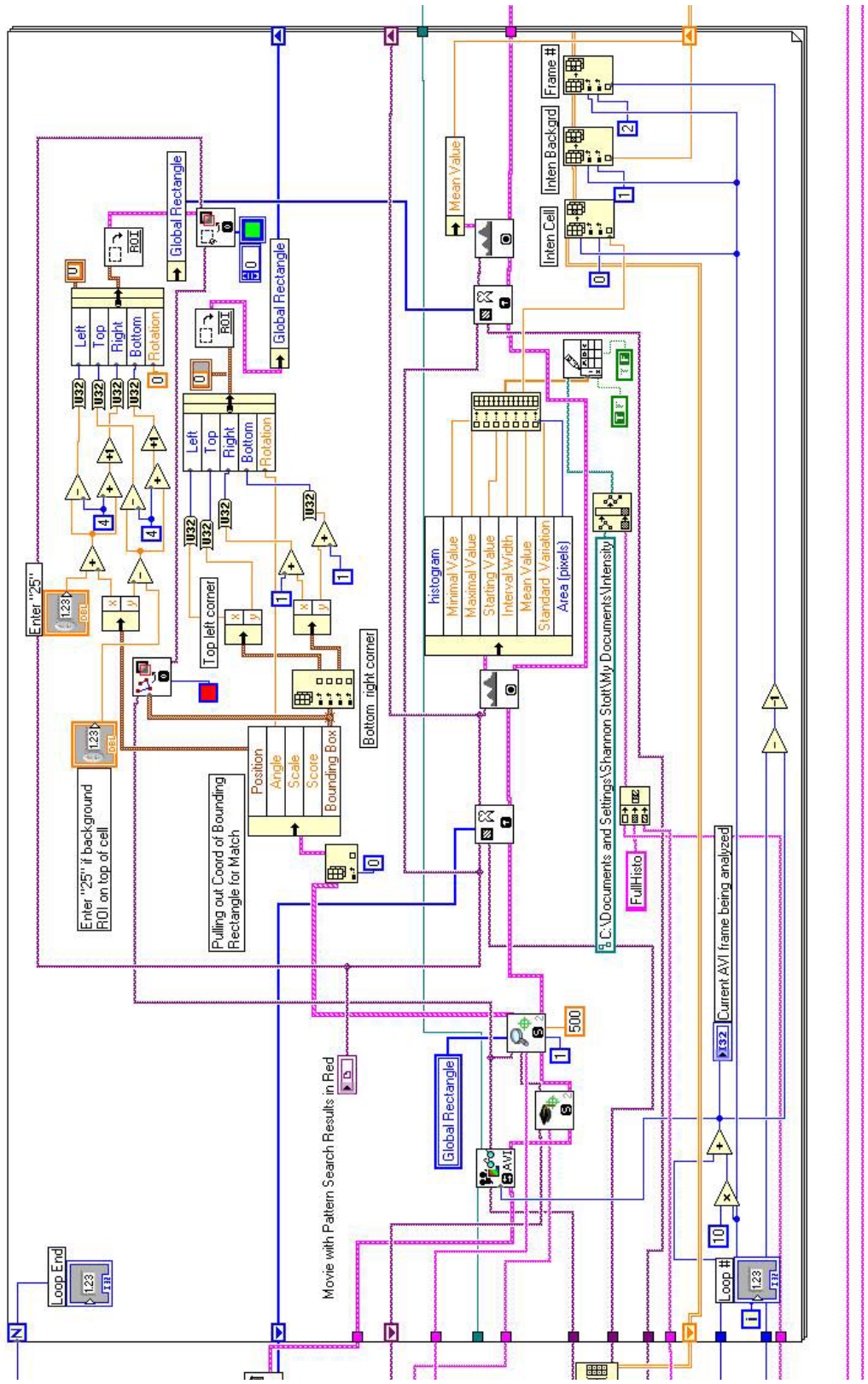

Figure A.3 Graphic representation of LabView code used to analyze high speed videos of cell darkening.

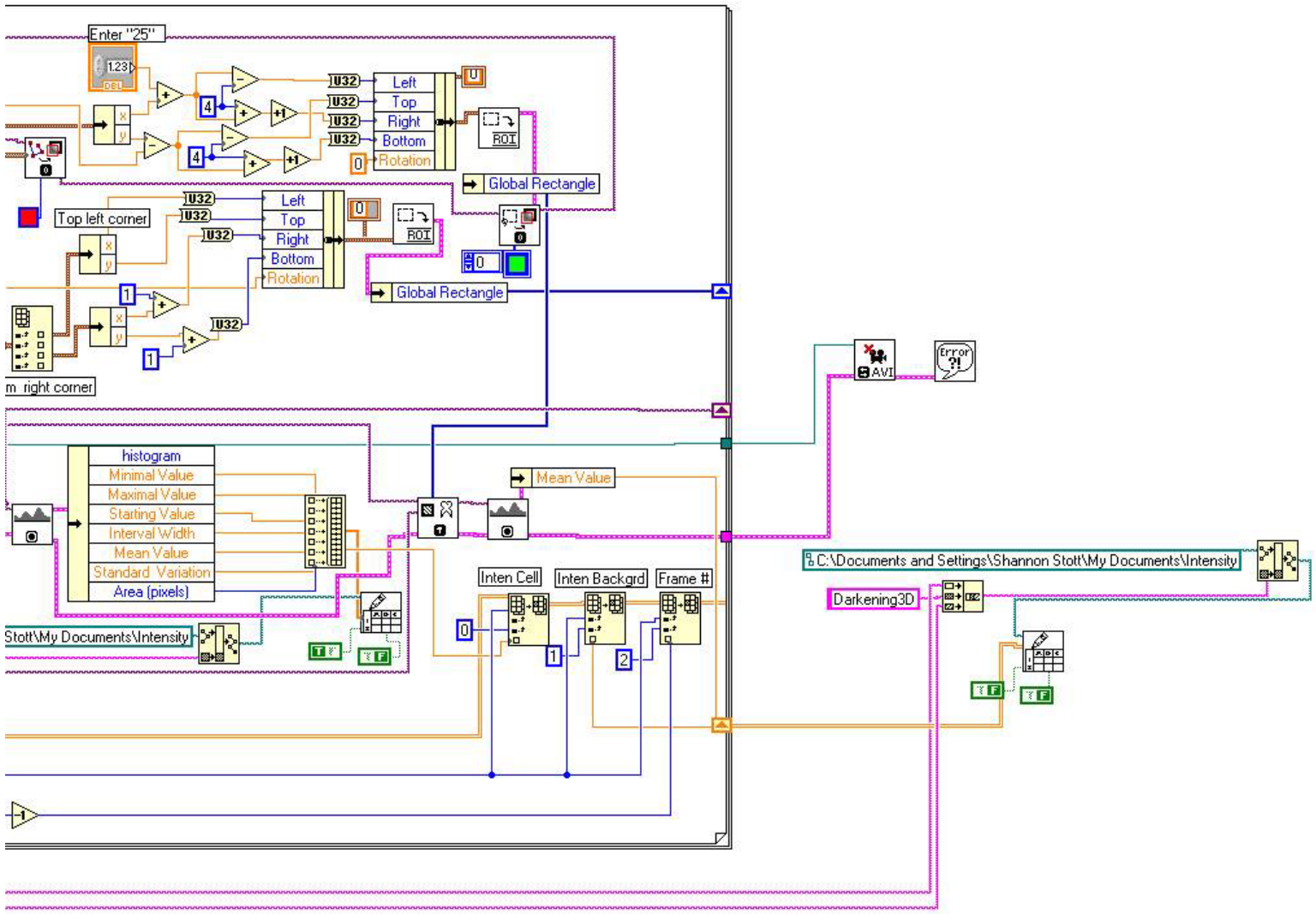

Figure A.4 Graphic representation of LabView code used to analyze high speed videos of cell darkening.

A.2 Conventional Digital Video Analysis

Due to different digital image formats, a separate program was created to analyze the convention (30Hz) cryomicroscopy data (Figure A.5). To prevent loss of any image information, the conventional 12-bit gray scale images were converted to 8-bit gray scale images using 4 shift registers as shown in pseudo-code presented in Figures A.6-8.

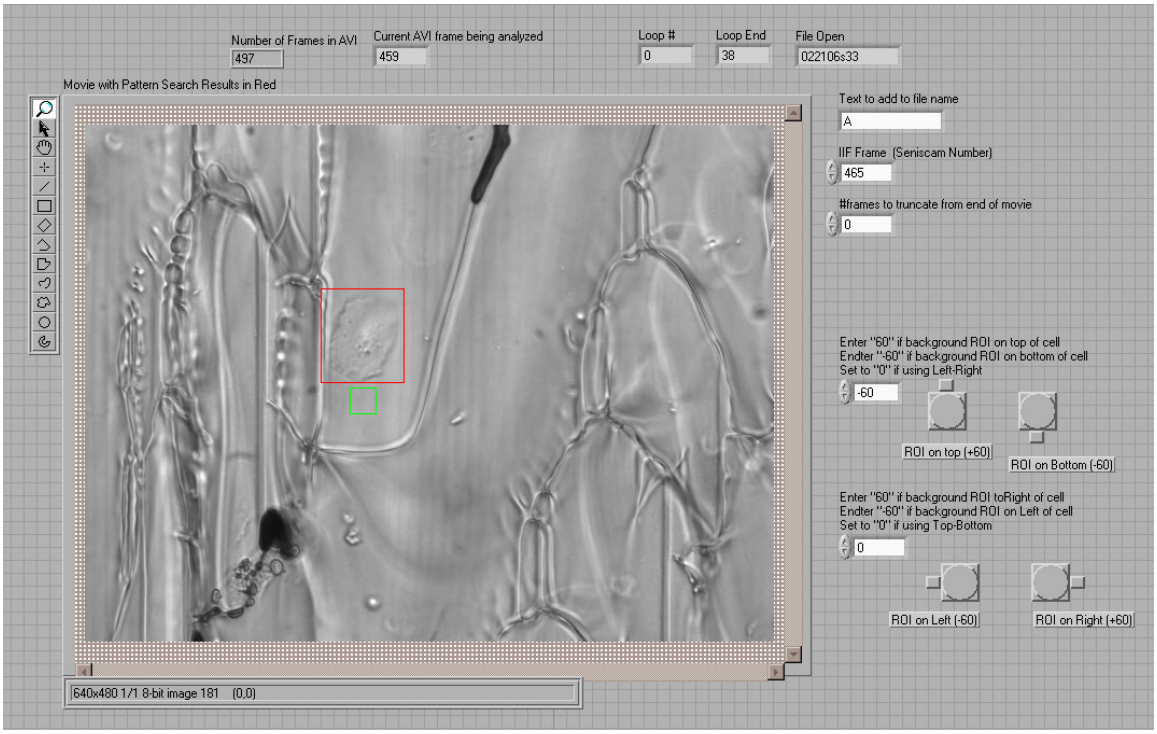

Figure A.5 Front panel user interface for cell darkening convention (12-bit grayscale) video analysis. Red rectangle represent region of cell analyzed for gray scale intensity changes. The green rectangle represents the control background area. Both red and green bounding boxes dynamically shift with the movement of the cell. Cell under analysis is a BPAEC cultured in a 30x40μm rectangular pattern.

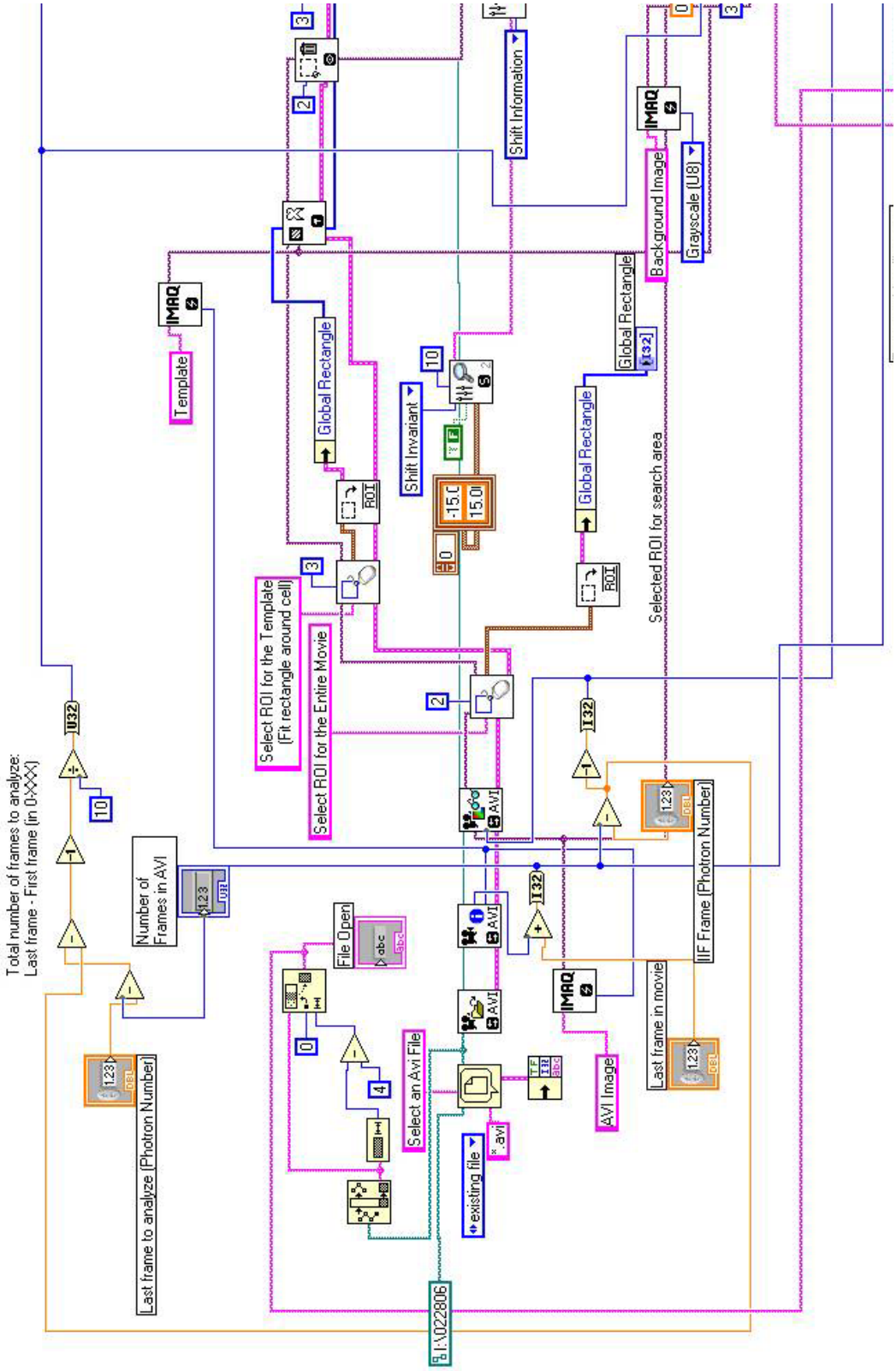

Figure A.6 Graphic representation of LabView code used to analyze 12-bit videos of cell darkening.

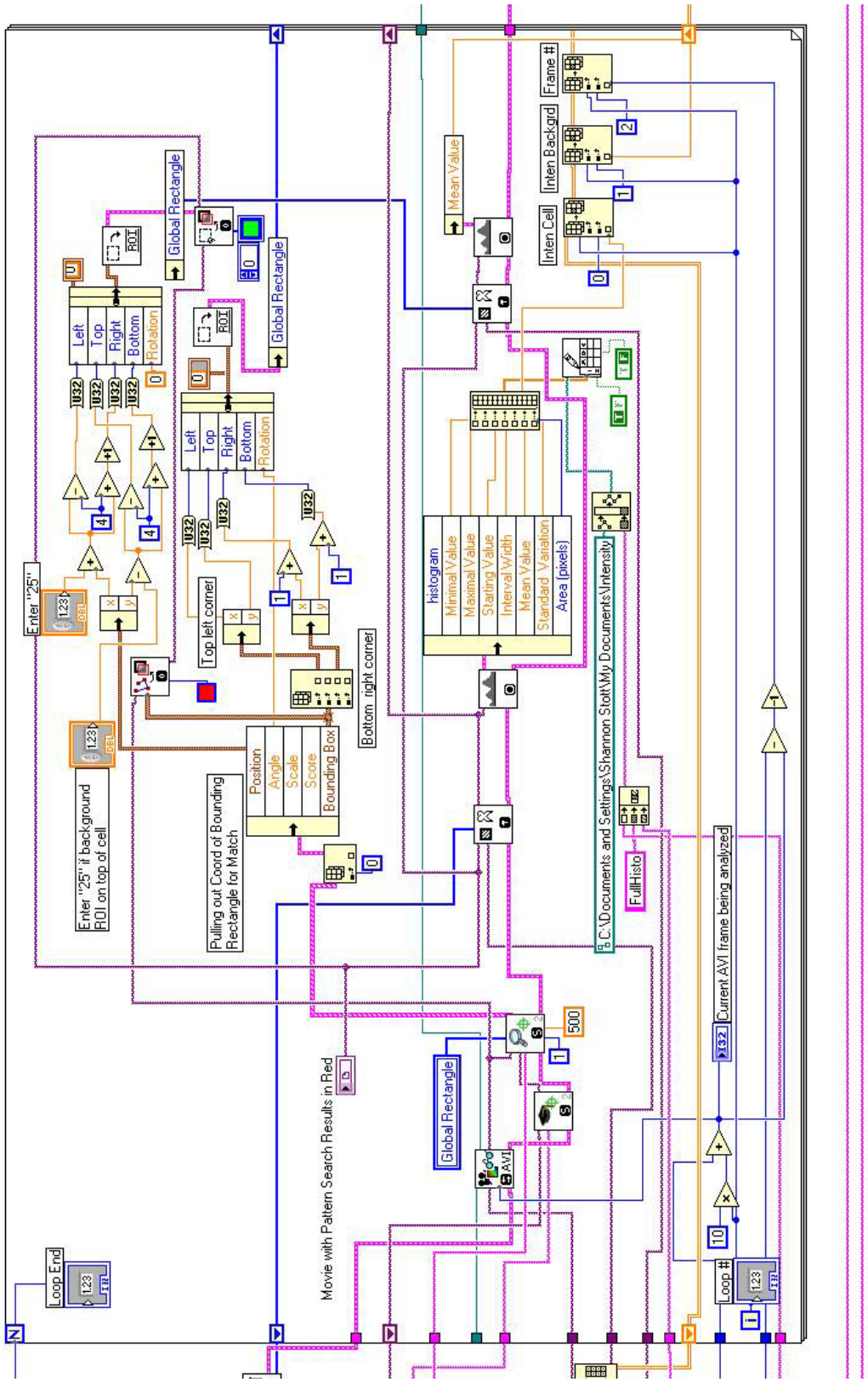

Figure A.7 Graphic representation of LabView code used to analyze 12-bit videos of cell darkening.

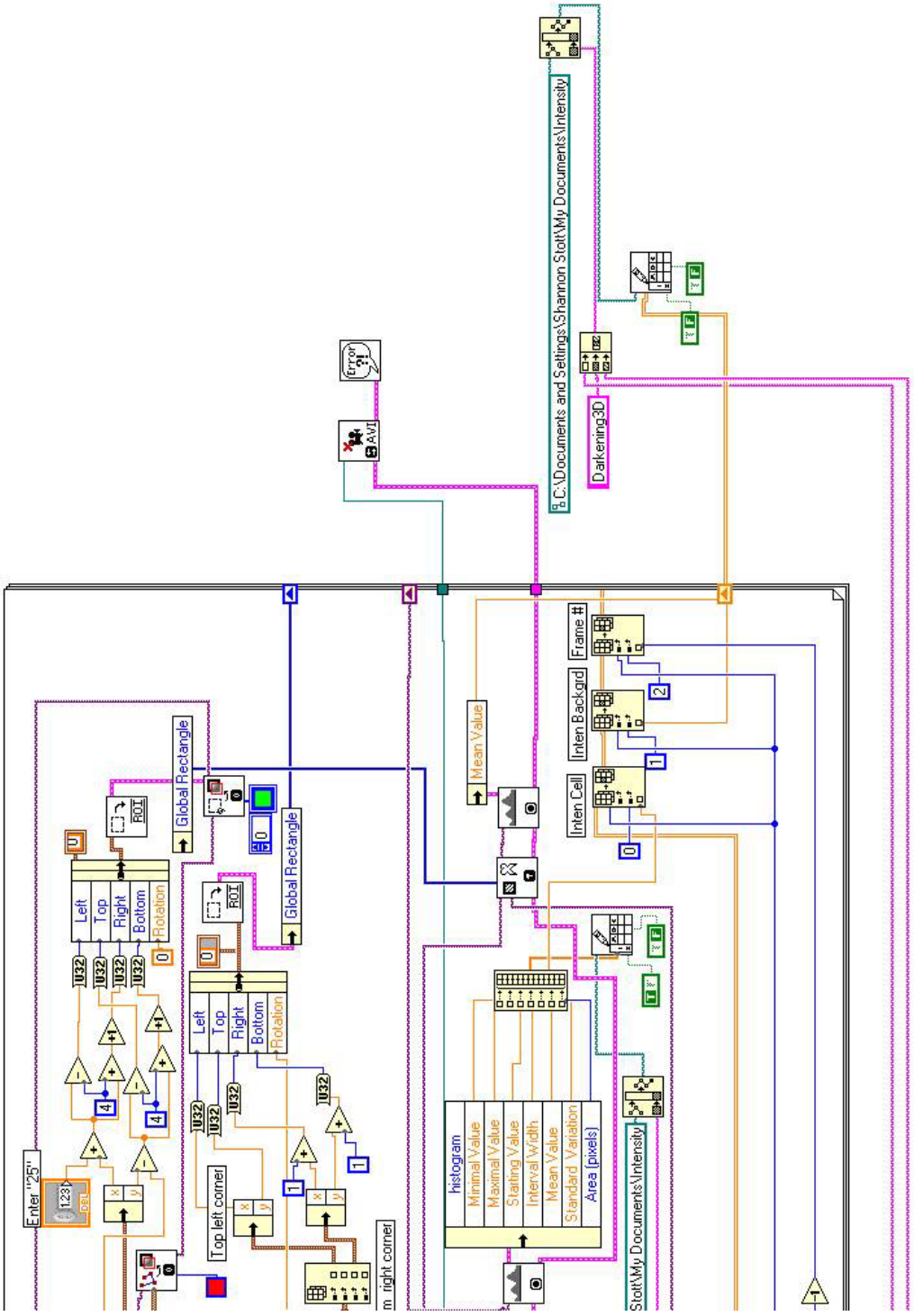

Figure A.8 Graphic representation of LabView code used to analyze 12-bit videos of cell darkening.

APPENDIX B

QUANTIFICATION OF VINCULIN STAINING AT CELL PERIPHERY

B.1 LabView Image Processing Code

A program was created in LabView 8.0 with IMAQ 8.0 (National Instruments) to quantify the dimensions of focal adhesion proteins at the peripheral regions of our micropatterned cells. The user inputs the name of a single 12-bit grayscale image and the rest of the analysis is automatic (regardless of cell size). For success operation of the program the user must input the following:

- File name of micrograph

Multiple output spreadsheets are created with the measured values for each segment detected. The graphical user interface of the program is shown in Figure B.1.

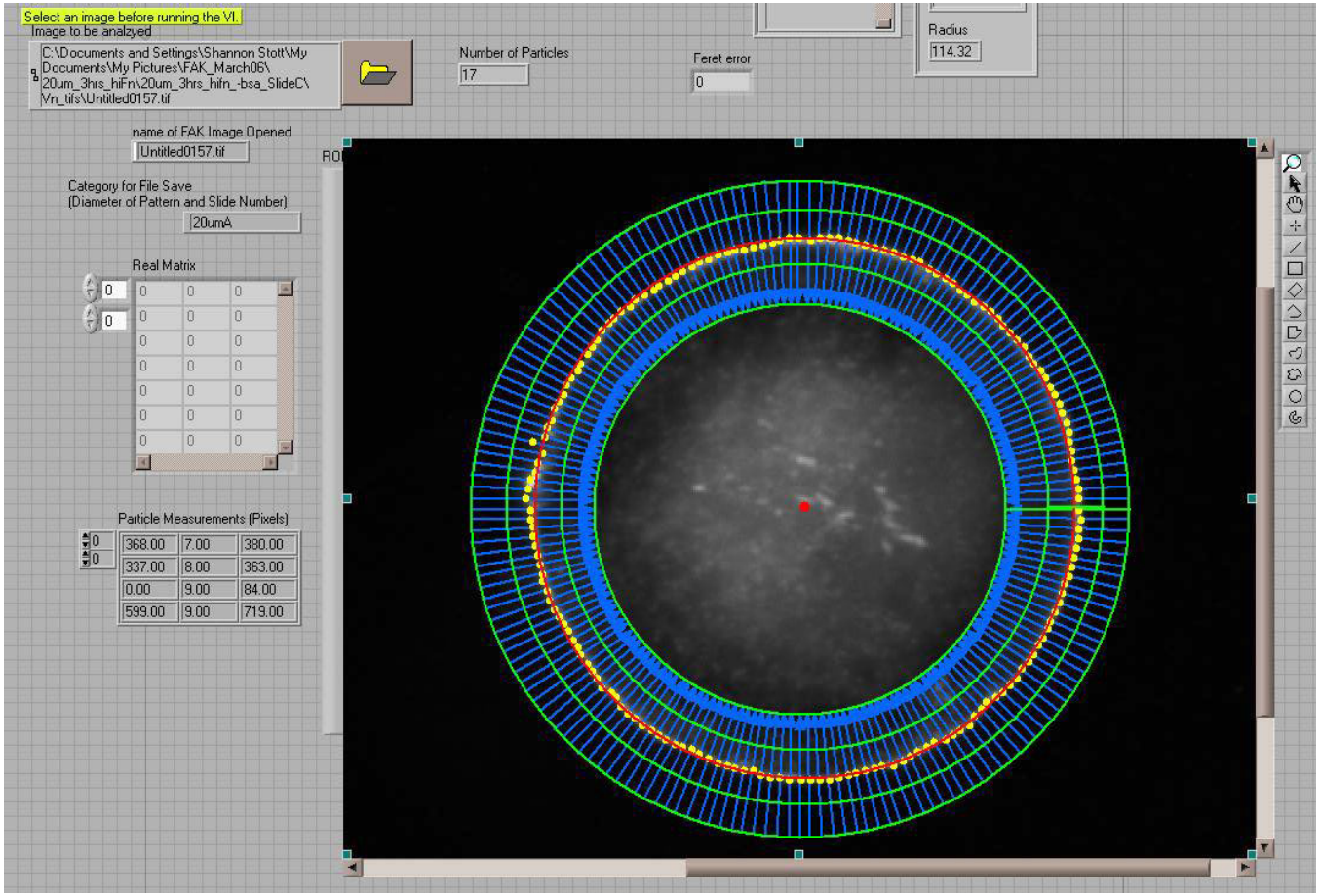

Figure B.1 Front panel user interface for focal adhesion analysis. After the user inputs the name of the image to be analyzed, the code locates the cell in the image, and detects the center of the cell (red dot). The outer periphery of the cell is then detected (yellow dots) based on intensity profiles. Following this, a peripheral region of the cell is isolated (± 10% of cell radius), with the radius determined for each cell by the cell detection algorithm. This peripheral region is then isolated, 'unwrapped' and segmented.

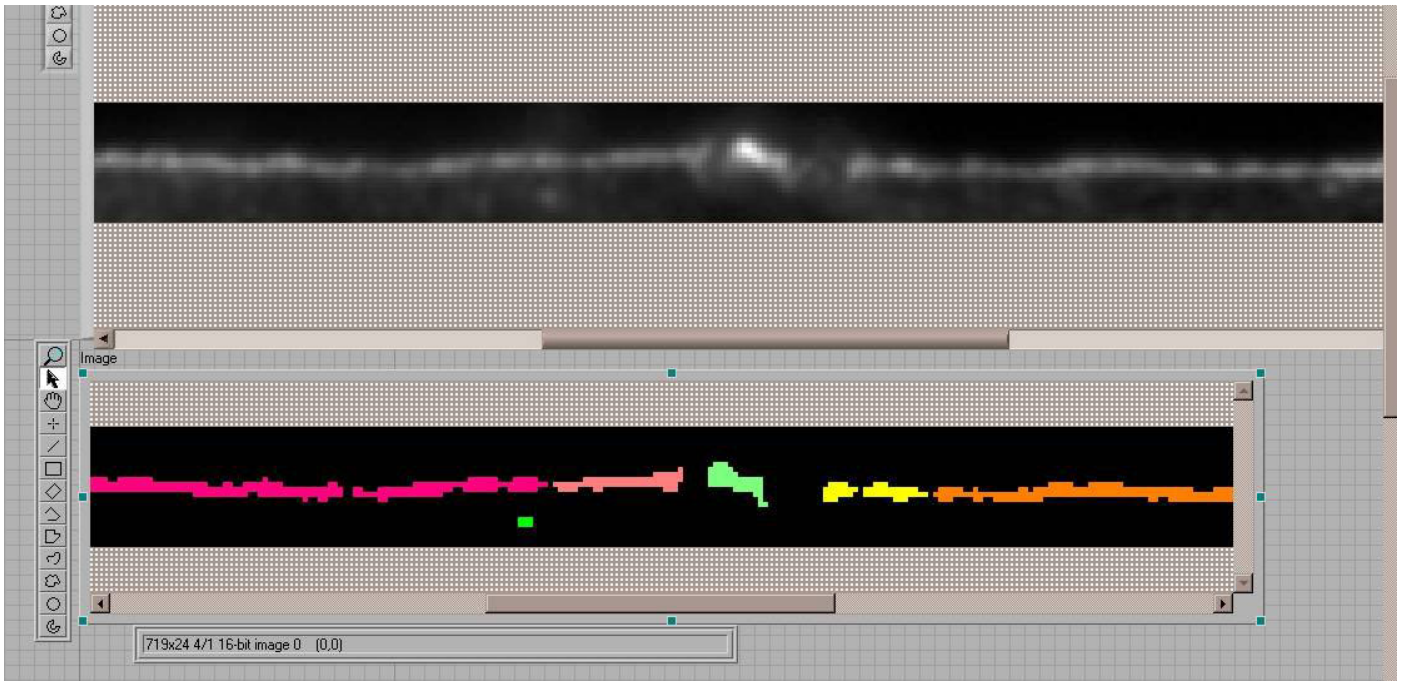

Figure B.2 Front panel user interface for focal adhesion analysis. For each image analyzed, the user is shown the unprocessed, unwrapped portion of the cell (grayscale image at top of figure). In addition, the user is also shown the resulting segmented image that was used for vinculin measurements. See Chapters 4 and 5 for further details.

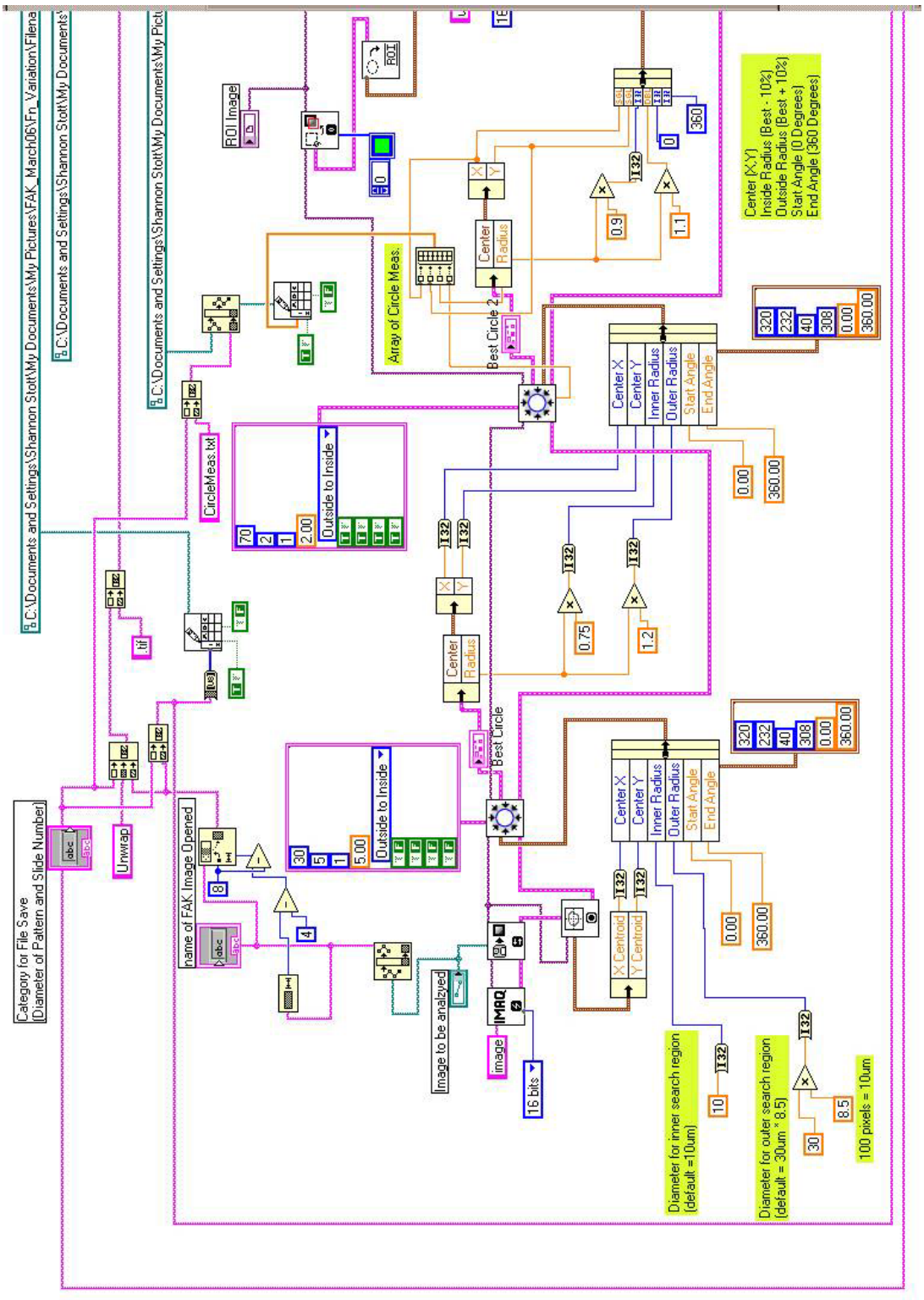

Figure B.3 Graphic representation of LabView code used to analyze focal adhesion spacing along the cell periphery.

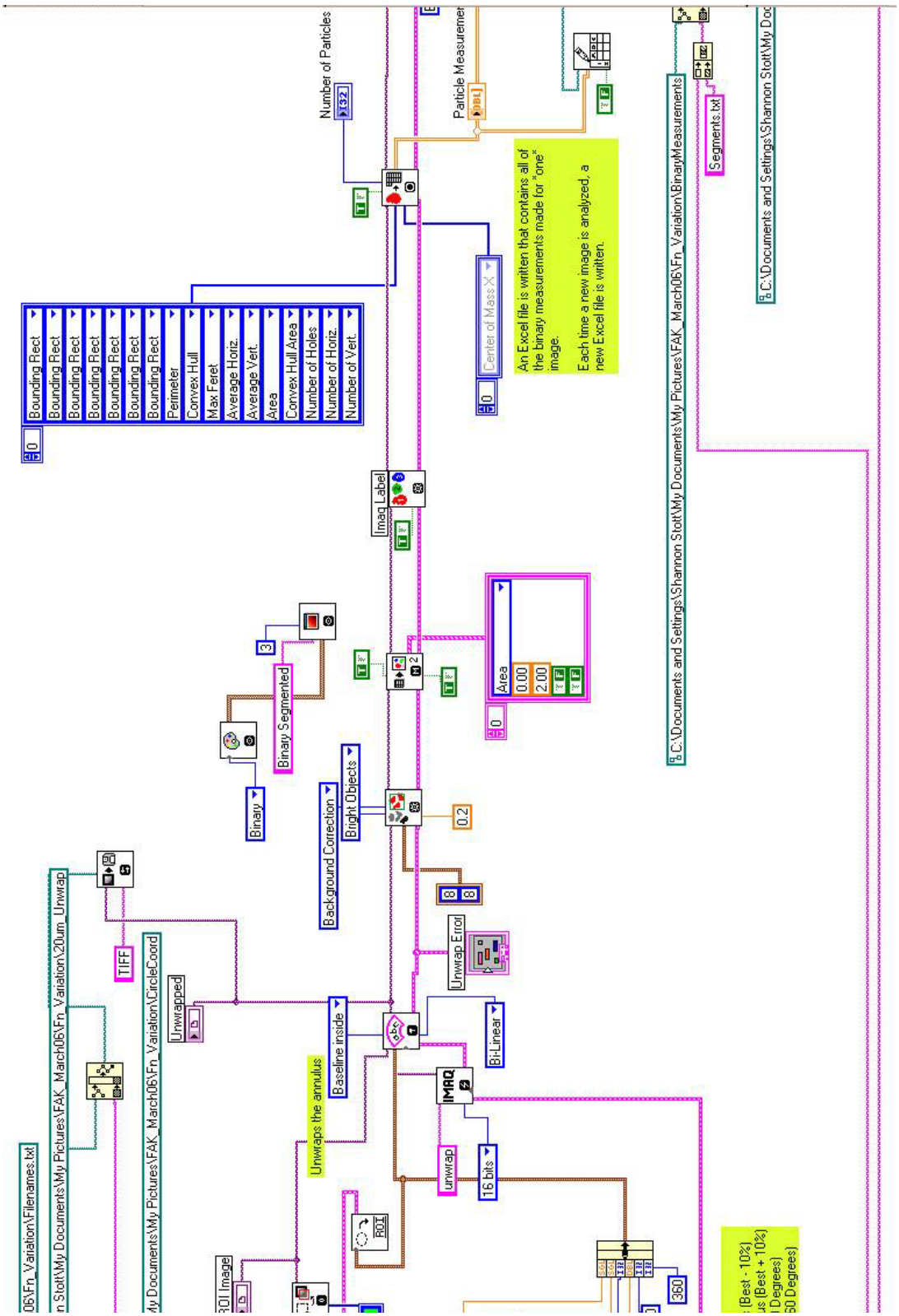

Figure B.4 Graphic representation of LabView code used to analyze focal adhesion spacing along the cell periphery.

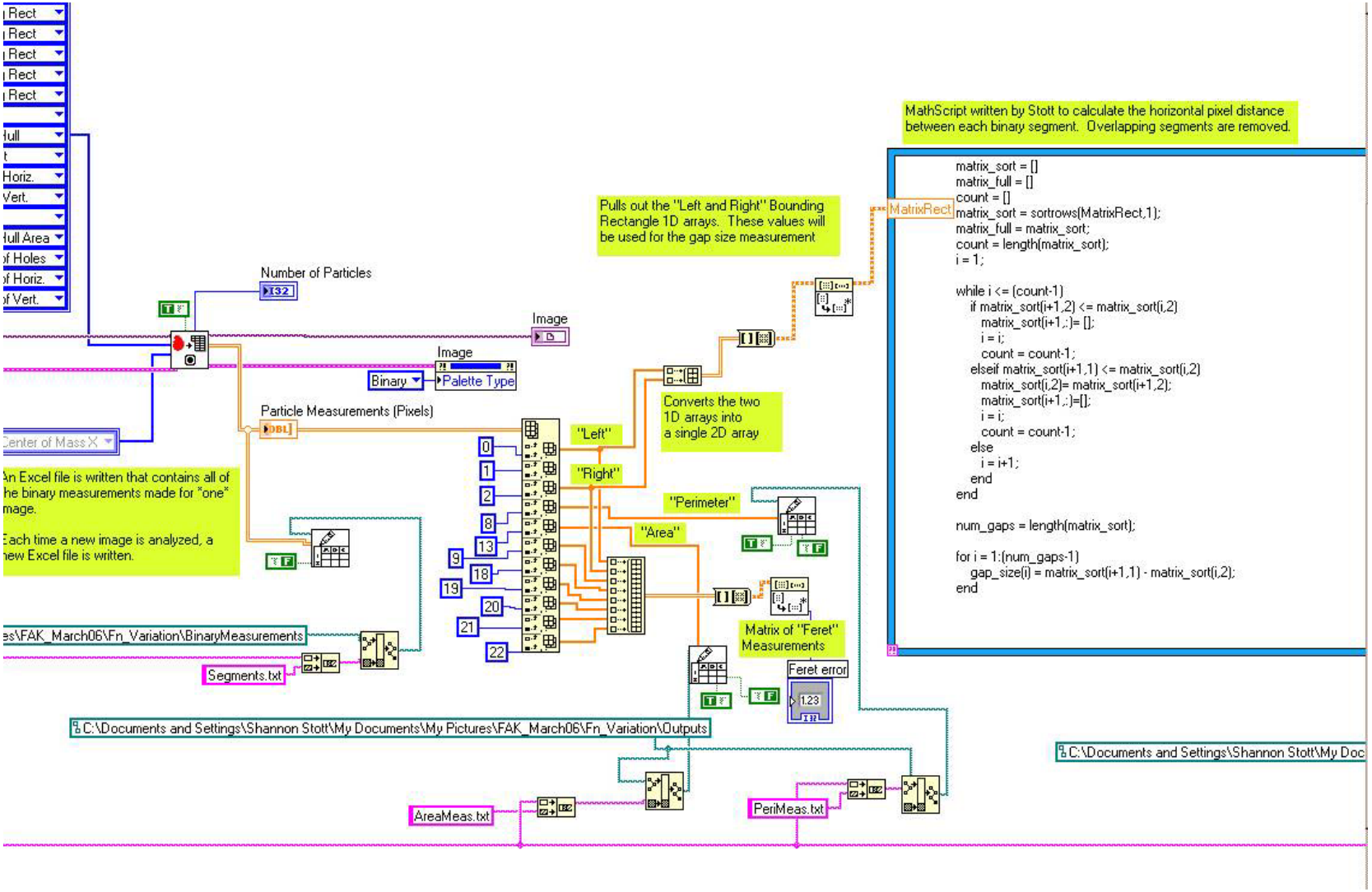

Figure B.5 Graphic representation of LabView code used to analyze focal adhesion spacing along the cell periphery.

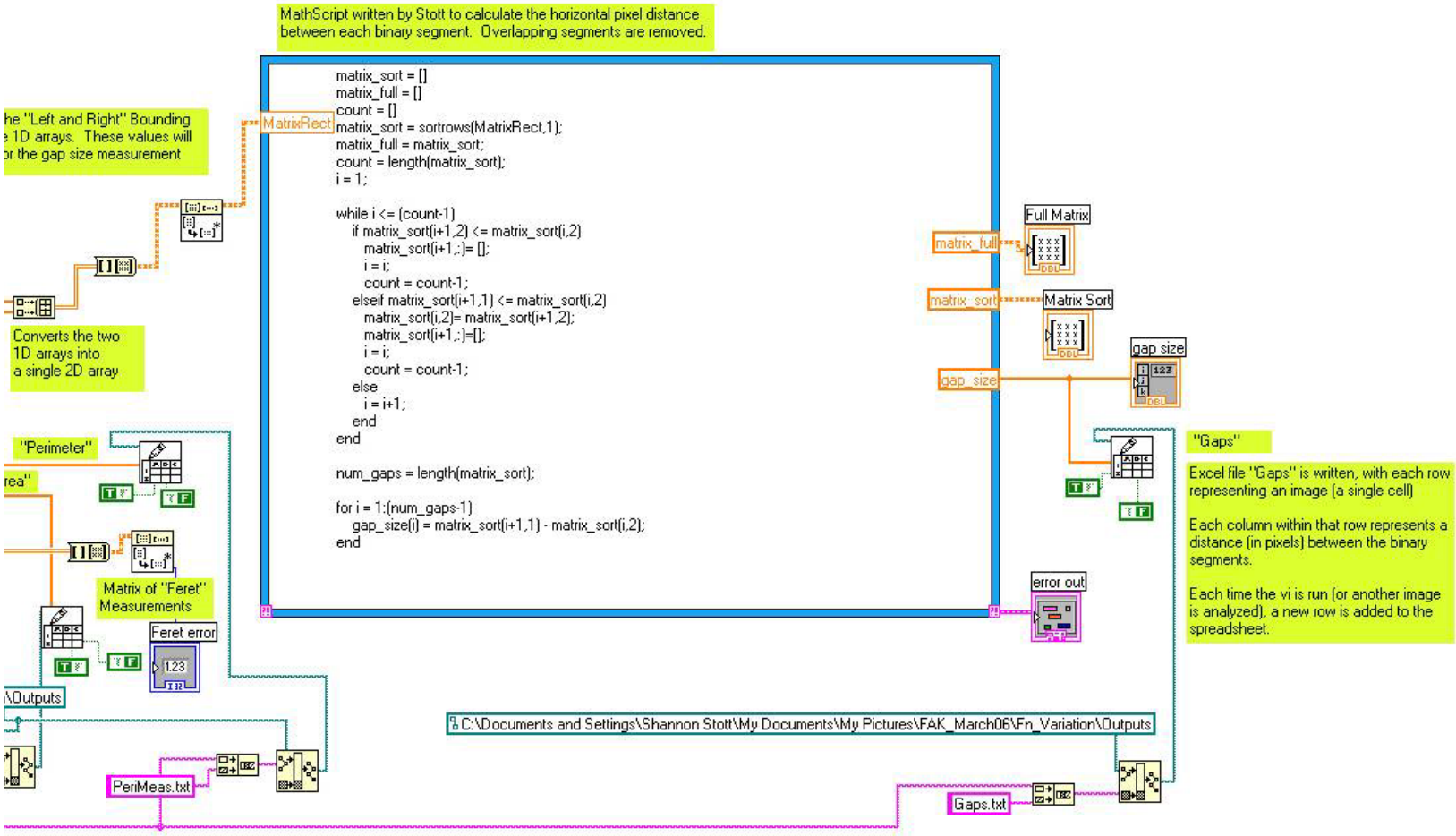

Figure B.6 Graphic representation of LabView code used to analyze focal adhesion spacing along the cell periphery.

APPENDIX C

QUANTIFICATION OF ACTIN AND VINCULIN STAINING FOR THE WHOLE MICROPATTERNED CELL AREA

C.1 LabView Image Processing Code

A program was created in LabView 8.0 with IMAQ 8.0 (National Instruments) to quantify the dimensions of actin filaments and focal adhesion proteins (via fluorescent image markers) in our micropatterned cells. The user inputs the name of a single 12-bit grayscale image and the rest of the analysis is automatic (regardless of cell size). For success operation of the program the user must input the following:

- File name of micrograph

Multiple output spreadsheets are created with the measured values for each segment detected. The graphical user interface of the program is shown in Figure C.1, with the program code presented in Figures C.2-5.

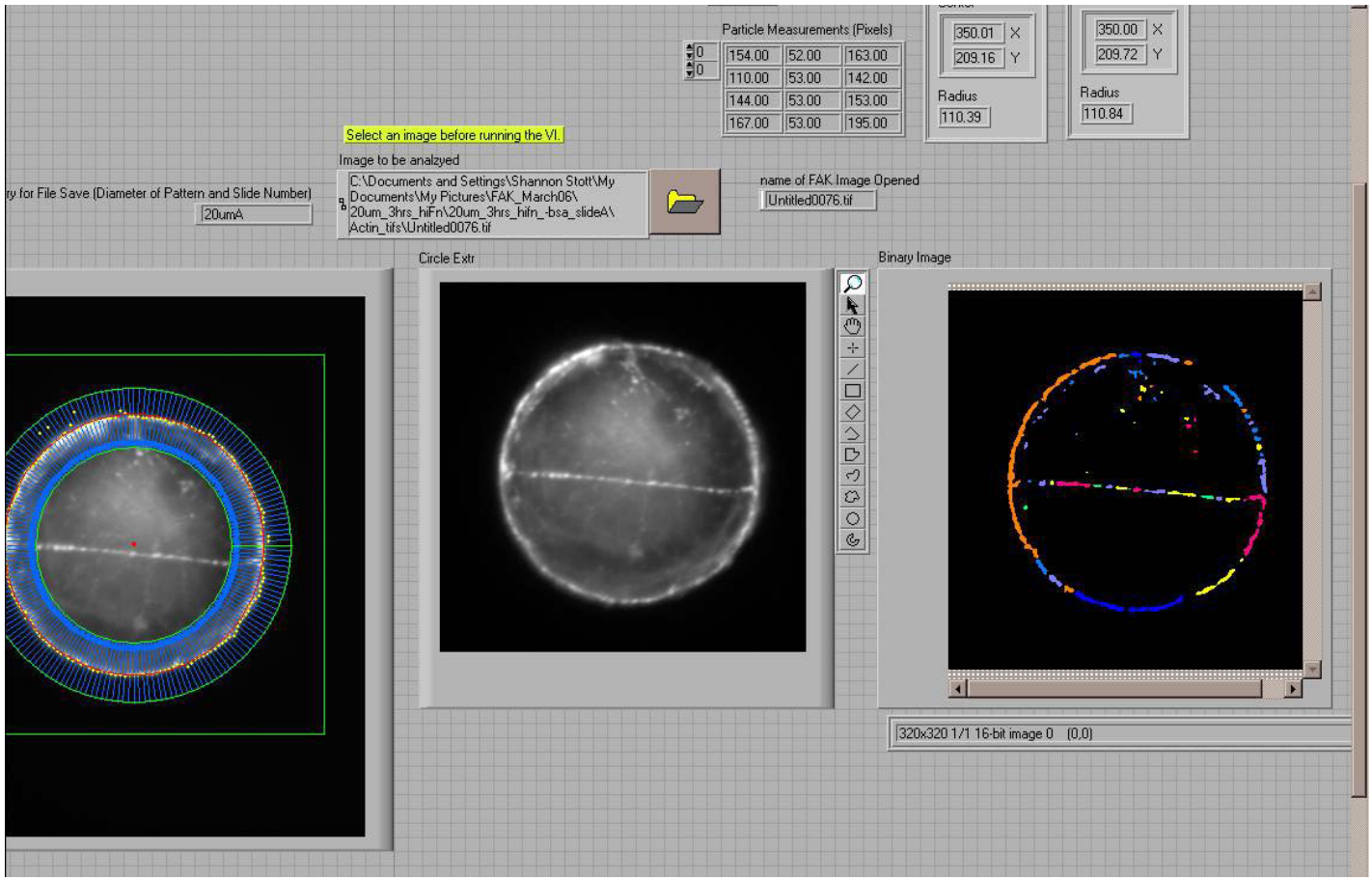

Figure C.1 Front panel user interface for image analysis of F-actin and vinculin. After the user inputs the name of the image to be analyzed, the code locates the cell in the image, and detects the center of the cell (red dot). In contrast to the previous program presented in Appendix B, this code evaluates the entire cell area, determining the average intensity of the image, and dimensions of the segments for the image (F-actin or vinculin, depending on the image being analyzed. The original image is shown at the center of the front panel, with the resulting segmented image shown to the right.

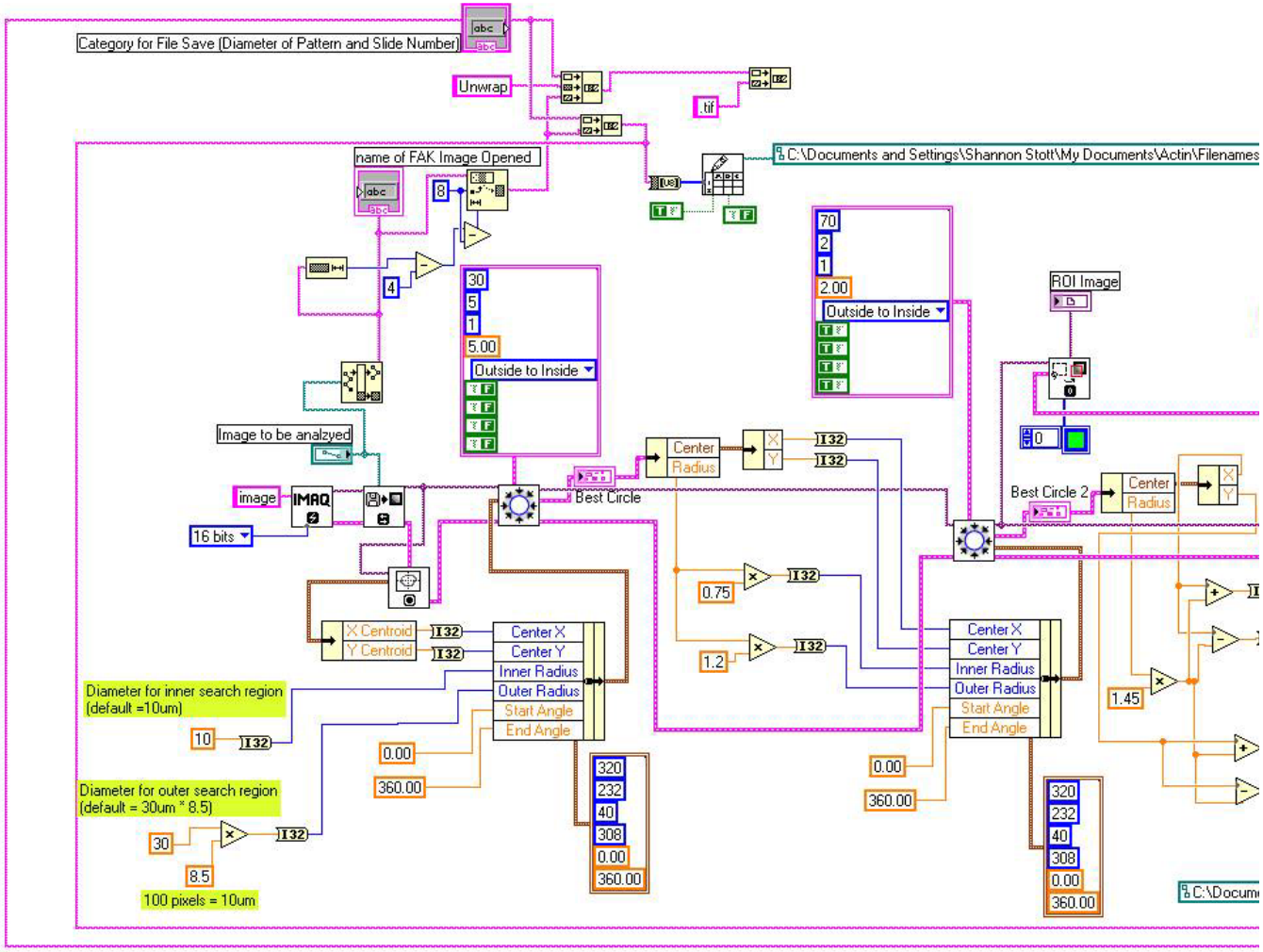

Figure C.2 Graphic representation of LabView code used to analyze F-actin and vinculin staining over the entire cell area. See Chapter 5 for more details.

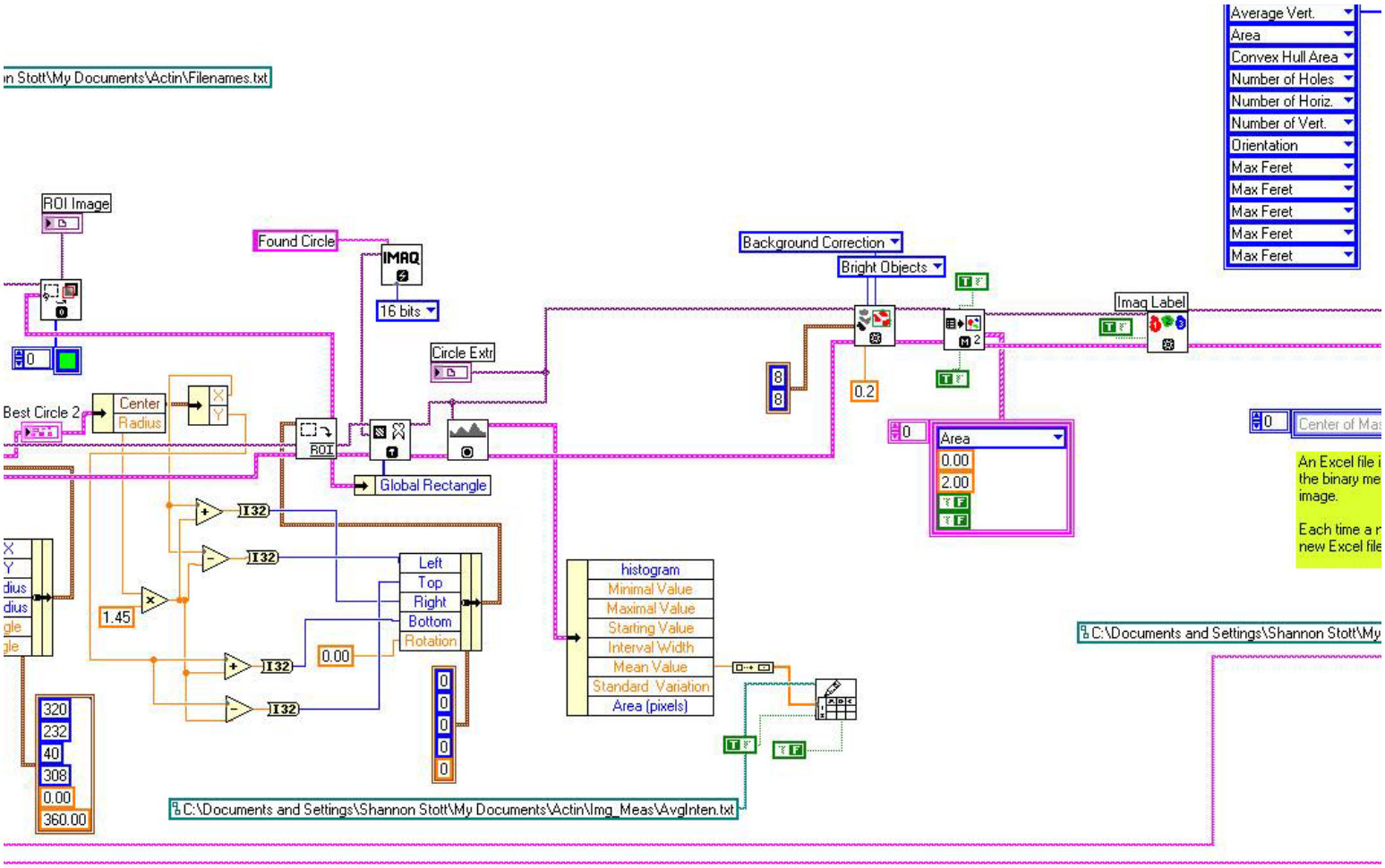

Figure C.3 Graphic representation of code used to analyze F-actin and vinculin staining over the entire cell area.

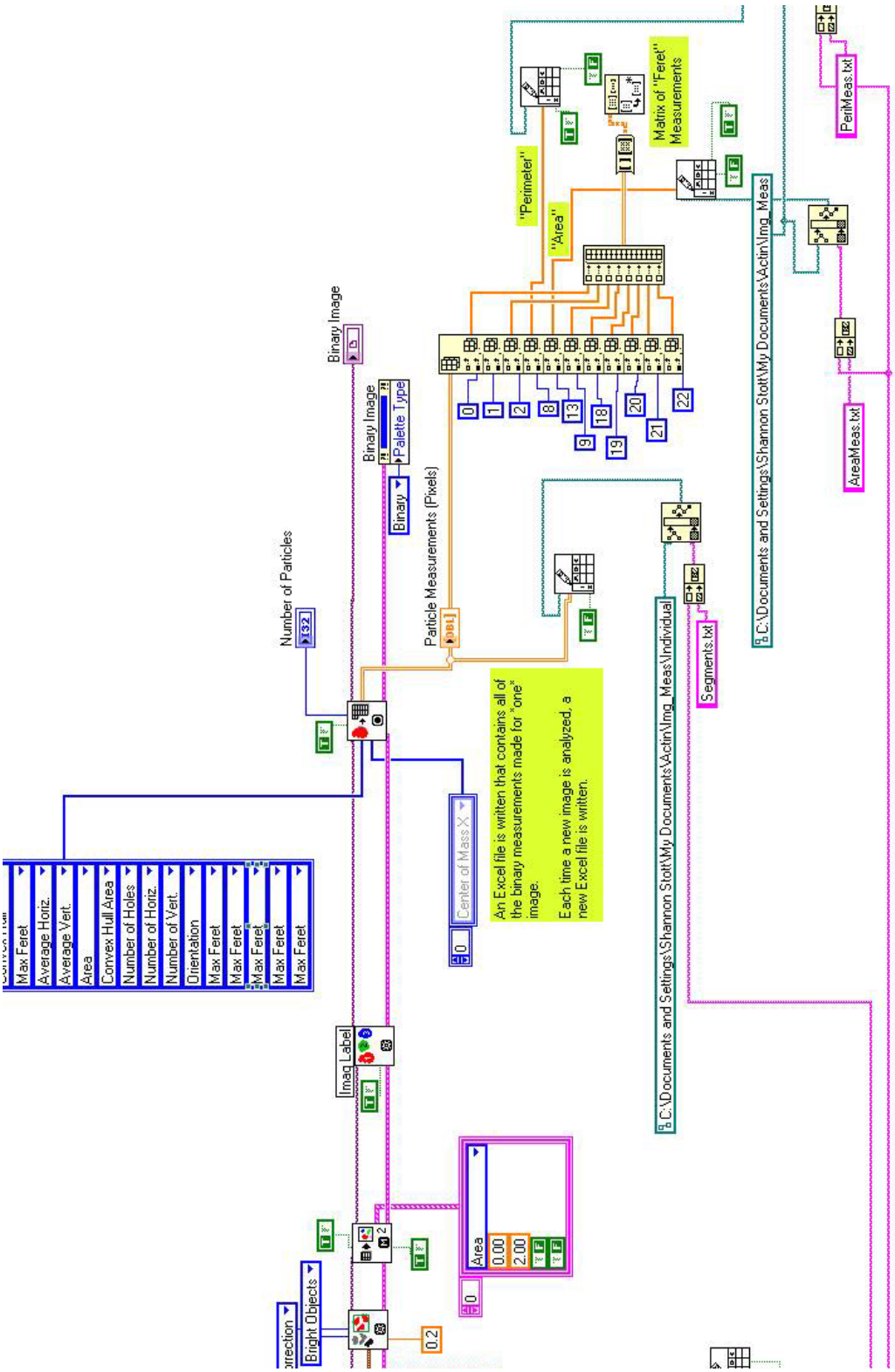

Figure C.4 Graphic representation of code used to analyze F-actin and vinculin staining over the entire cell area.

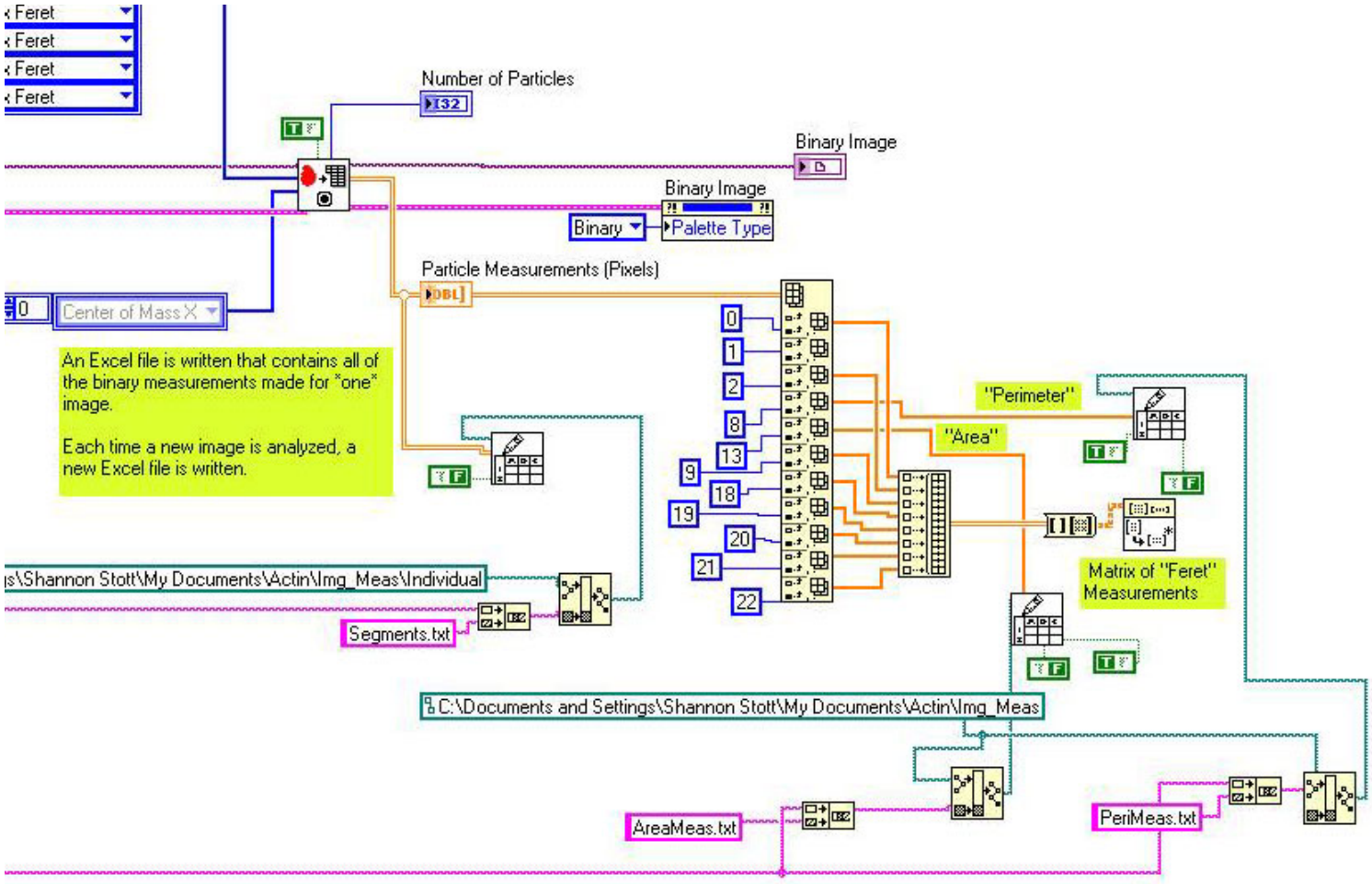

Figure C.5 Graphic representation of code used to analyze F-actin and vinculin staining over the entire cell area.

REFERENCES

1. Karlsson, J.O. & Toner, M. Long-term storage of tissues by cryopreservation: critical issues. *Biomaterials* **17**, 243-256 (1996).

2. Mazur, P. Freezing of living cells: mechanisms and implications. *Am J Physiol* **247**, C125-142 (1984).

3. Song, Y.C., Khirabadi, B.S., Lightfoot, F., Brockbank, K.G. & Taylor, M.J. Vitreous cryopreservation maintains the function of vascular grafts. *Nat Biotechnol* **18**, 296-299 (2000).

4. Bourne, W.M., Nelson, L.R. & Hodge, D.O. Comparison of three methods for human corneal cryopreservation that utilize dimethyl sulfoxide. *Cryobiology* **39**, 47-57 (1999).

5. Rich, S.J. & Armitage, W.J. Corneal tolerance of vitrifiable concentrations of propane-1,2-diol. *Cryobiology* **28**, 159-170 (1991).

6. Armitage, W.J. & Juss, B.K. The influence of cooling rate on survival of frozen cells differs in monolayers and suspensions. *Cryo Letters* **17**, 213-218 (1996).

7. Karlsson, J.O.M. & Toner, M. Cryopreservation. In: Principles of Tissue Engineering, 2nd Edition, 293-307 (Academic Press, 2000).

8. Rubinsky, B. Cryosurgery. *Annu Rev Biomed Eng* **2**, 157-187 (2000).

9. Shinohara, K. Prostate cancer: cryotherapy. *Urol Clin North Am* **30**, 725-736, viii (2003).

10. Seifert, J.K., Achenbach, T., Heintz, A., Bottger, T.C. & Junginger, T. Cryotherapy for liver metastases. *Int J Colorectal Dis* **15**, 161-166 (2000).

11. Simmons, R.M. Ablative techniques in the treatment of benign and malignant breast disease. *J Am Coll Surg* **197**, 334-338 (2003).

12. Shingleton, W.B. & Sewell, P.E., Jr. Cryoablation of renal tumours in patients with solitary kidneys. *BJU Int* **92**, 237-239 (2003).

13. Kollender, Y. et al. Role of adjuvant cryosurgery in intralesional treatment of sacral tumors. *Cancer* **97**, 2830-2838 (2003).

14. Menendez, L.R., Tan, M.S., Kiyabu, M.T. & Chawla, S.P. Cryosurgical ablation of soft tissue sarcomas: a phase I trial of feasibility and safety. *Cancer* **86**, 50-57 (1999).

15. Gage, A.A. & Baust, J. Mechanisms of tissue injury in cryosurgery. *Cryobiology* **37**, 171-186 (1998).

16. Debenedetti, P.G. & Stanley, H.E. Supercooled and glassy water. *Physics Today* **56**, 40-46 (2003).

17. Khvorostyanov, V.I. & Curry, J.A. Thermodynamic theory of freezing and melting of water and aqueous solutions. *Journal of Physical Chemistry A*. **108**, 11073-11085 (2004).

18. Bartell, L.S. & Chushak, Y.G. in Water in Confining Geometries. (eds. V. Buch & J.P. Devlin) (Springer, Berlin; 2003).

19. Sastry, S. Water - Ins and outs of ice nucleation. *Nature* **438**, 746-747 (2005).

20. Turnbull, D. & Fisher, J.C. Rate of Nucleation in Condensed Systems. *Journal of Chemical Physics* **17**, 71-73 (1949).

21. Heneghan, A.F., Wilson, P.W. & Haymet, A.D.J. Heterogeneous nucleation of supercooled water, and the effect of an added catalyst. *Proceedings of the National Academy of Sciences of the United States of America* **99**, 9631-9634 (2002).

22. Shaw, R.A., Durant, A.J. & Mi, Y. Heterogeneous surface crystallization observed in undercooled water. *Journal of Physical Chemistry B* **109**, 9865-9868 (2005).

23. Toner, M., Cravalho, E.G. & Karel, M. Thermodynamics and kinetics of intracellular ice formation during freezing of biological cells. **67**, 1582-1593 (1990) *Erratum: J. Appl. Phys. 10, 4653 (1991)*.

24. Ohsaka, K. & Trinh, E.H. Apparatus for measuring the growth velocity of dendritic ice in undercooled water. *Journal of Crystal Growth* **194**, 138-142 (1998).

25. Ayel, V., Lottin, O., Faucheux, M., Sallier, D. & Peerhossaini, H. Crystallisation of undercooled aqueous solutions: Experimental study of free dendritic growth in cylindrical geometry. *International Journal of Heat and Mass Transfer* **49**, 1876-1884 (2006).

26. Teraoka, Y., Saito, A. & Okawa, S. Ice crystal growth in supercooled solution. *International Journal of Refrigeration-Revue Internationale Du Froid* **25**, 218-225 (2002).

27. Hindmarsh, J.P., Sederman, A.J., Gladden, L.F., Wilson, D.I. & Johns, M.L. Rapid measurement of dispersion and velocity in freezing drops using magnetic resonance methods. *Experiments in Fluids* **38**, 750-758 (2005).

28. Wilson, P.W., Lester, D. & Haymet, A.D.J. Heterogeneous nucleation of clathrates from supercooled tetrahydrofuran (THF)/water mixtures, and the effect of an added catalyst. *Chemical Engineering Science* **60**, 2937-2941 (2005).

29. Holzmann, E.G. Excess Velocity Potential of Platelet Crystal in a Supercooled Melt. *Journal of Applied Physics* **41**, 4769-& (1970).

30. Qin, F.G.F., Chen, X.D. & Farid, M.M. Growth kinetics of ice films spreading on a subcooled solid surface. *Separation and Purification Technology* **39**, 109-121 (2004).

31. Shibkov, A.A., Zheltov, M.A., Korolev, A.A., Kazakov, A.A. & Leonov, A.A. Crossover from diffusion-limited to kinetics-limited growth of ice crystals. *Journal of Crystal Growth* **285**, 215-227 (2005).

32. Mazur, P., Leibo, S.P. & Chu, E.H.Y. 2-Factor Hypothesis of Freezing Injury - Evidence from Chinese-Hamster Tissue-Culture Cells. *Experimental Cell Research* **71**, 345-& (1972).

33. Diller, K.R. Bioheat and mass transfer as viewed through a microscope. *J Biomech Eng* **127**, 67-84 (2005).

34. Diller, K.R. Quantitative Low-Temperature Optical Microscopy of Biological-Systems. *Journal of Microscopy-Oxford* **126**, 9-28 (1982).

35. Scheiwe, M.W. & Korber, C. Quantitative cryomicroscopic analysis of intracellular freezing of granulocytes without cryoadditive. *Cryobiology* **24**, 473-483 (1987).

36. Berrada, M.S. & Bischof, J.C. Evaluation of freezing effects on human microvascular-endothelial cells (HMEC). *Cryo Letters* **22**, 353-366 (2001).

37. Asahina, E. Frost Injury In Living Cells. *Nature* **196**, 445-& (1962).

38. Steponkus, P.L. Role of the plasma membrane in freezing injury and cold acclimation. *Ann Rev Plant Physiol* **35**, 543-584 (1984).

39. Steponkus, P.L., Dowgert, M.F. & Gordon-Kamm, W.J. Destabilization of the plasma membrane of isolated plant protoplasts during a freeze-thaw cycle: the influence of cold acclimation. *Cryobiology* **20**, 448-465 (1983).

40. Muldrew, K. & McGann, L.E. The osmotic rupture hypothesis of intracellular freezing injury. *Biophys J* **66**, 532-541 (1994).

41. Ishiguro, H. & Rubinsky, B. Mechanical interactions between ice crystals and red blood cells during directional solidification. *Cryobiology* **31**, 483-500 (1994).

42. Takamatsu, H. & Rubinsky, B. Viability of deformed cells. *Cryobiology* **39**, 243-251 (1999).

43. Mazur, P. Causes of Injury in Frozen and Thawed Cells. *Federation Proceedings* **24**, S175-& (1965).

44. Mazur, P. Role of Cell Membranes in Freezing of Yeast and Other Single Cells. *Annals of the New York Academy of Sciences* **125**, 658-& (1965).

45. Mazur, P. Physical Factors Implicated in the Death of Micro-Organisms at Subzero Temperatures. *Annals of the New York Academy of Sciences* **85**, 610-629 (1960).

46. Karlsson, J.O., Cravalho E.G., Borel Rinkes, I.H., Tompkins, R.G., Yarmush, M.L. & Toner, M. Nucleation and growth of ice crystals inside cultured hepatocytes during freezing in the presence of dimethyl sulfoxide. *Biophys J* **65**, 2524-2536 (1993).

47. Toner, M., Cravalho, E.G. & Karel, M. Cellular response of mouse oocytes to freezing stress: prediction of intracellular ice formation. *J Biomech Eng* **115**, 169-174 (1993).

48. Karlsson, J.O., Eroglu, A., Toth, T.L., Cravalho, E.G. & Toner, M. Fertilization and development of mouse oocytes cryopreserved using a theoretically optimized protocol. *Hum Reprod* **11**, 1296-1305 (1996).

49. Korber, C. Phenomena at the advancing ice-liquid interface: solutes, particles and biological cells. *Q Rev Biophys* **21**, 229-298 (1988).

50. Bischof, J.C. Quantitative measurement and prediction of biophysical response during freezing in tissues. *Annu Rev Biomed Eng* **2**, 257-288 (2000).

51. Cui, Z.F., Dykhuizen, R.C., Nerem, R.M. & Sambanis, A. Modeling of cryopreservation of engineered tissues with one-dimensional geometry. *Biotechnol Prog* **18**, 354-361 (2002).

52. Diller, K.R. & Raymond, J.F. Water Transport through a Multicellular Tissue During Freezing - a Network Thermodynamic Modeling Analysis. *Cryo-Letters* **11**, 151-162 (1990).

53. Rubinsky, B. & Pegg, D.E. A mathematical model for the freezing process in biological tissue. *Proc R Soc Lond B Biol Sci* **234**, 343-358 (1988).

54. Viskanta, R., Bianchi, M.V.A., Critser, J.K. & Gao, D. Solidification Processes of Solutions. *Cryobiology* **34**, 348-362 (1997).

55. Xu, X. & Cui, Z.F. Modeling of the co-transport of cryoprotective agents in a porous medium as a model tissue. *Biotechnol Prog* **19**, 972-981 (2003).

56. Berger, W.K. & Uhrik, B. Freeze-induced shrinkage of individual cells and cell-to-cell propagation of intracellular ice in cell chains from salivary glands. *Experientia* **52**, 843-850 (1996).

57. Acker, J.P., Elliott, J.A. & McGann, L.E. Intercellular ice propagation: experimental evidence for ice growth through membrane pores. *Biophys J* **81**, 1389-1397 (2001).

58. Irimia, D. & Karlsson, J.O. Kinetics and mechanism of intercellular ice propagation in a micropatterned tissue construct. *Biophys J* **82**, 1858-1868 (2002).

59. Irimia, D. & Karlsson, J.O. Kinetics of intracellular ice formation in one-dimensional arrays of interacting biological cells. *Biophys J* **88**, 647-660 (2005).

60. Acker, J.P., Larese, A., Yang, H., Petrenko, A. & McGann, L.E. Intracellular ice formation is affected by cell interactions. *Cryobiology* **38**, 363-371 (1999).

61. Irimia, D., Effects of cell-cell and cell-substrate interactions on ice formation in micropatterned tissue constructs. Ph.D. Thesis, University of Illinois, Chicago (2002).

62. McGrath, J.J., Cravalho, E.G. & Huggins, C. An experimental comparison of intracellular ice formation and freeze-thaw survival of HeLa S-3 cells. *Cryobiology* **12**, 540-550 (1975).

63. Porsche, A., Korber, C. & Rau, G. Freeze-thaw behavior of cultured (bovine corneal) endothelial cells: suspension vs monolayer. *Cryobiology* **32**, 545 (1991).

64. Yarmush, M.L. et al. Hepatic tissue engineering. Development of critical technologies. *Ann N Y Acad Sci* **665**, 238-252 (1992).

65. Stuckey, I.H. & Curtis, O.F. Ice formation and the death of plant cells by freezing. *Plant Physiol.* **13**, 815-833 (1938).

66. Brown, M.S. Freezing of nonwoody plant tissues. IV. Nucleation sites for freezing and refreezing of onion bulb epidermal cells. *Cryobiology* **17**, 184-186 (1980).

67. Tsuruta, T., Ishimoto, Y. & Masuoka, T. Effects of glycerol on intracellular ice formation and dehydration of onion epidermis. *Ann. N.Y. Acad. Sci.* **858**, 217-226 (1998).

68. Yang, H., Jia, X.M., Ebertz, S. & McGann, L.E. Cell junctions are targets for freezing injury. *Cryobiology* **33**, 672-673 (1996).

69. Bogner, P. et al. Stabilization of intercellular contacts in MDCK cells during Ca2+ deprivation. Selective effects of monocarboxylic acids on desmosomes. *J Cell Sci* **103 (Pt 2)**, 463-473 (1992).

70. Lagunes, R., Ruiz, L. & Frixione, E. Contraction of epithelial (MDCK) cells in response to low extracellular calcium is dependent on extracellular sodium. *J Muscle Res Cell Motil* **20**, 761-770 (1999).

71. Frixione, E., Lagunes, R., Ruiz, L., Urban, M. & Porter, R.M. Mechanical responses of single non-confluent epithelial cells to low extracellular calcium. *J Muscle Res Cell Motil* **24**, 477-485 (2003).

72. Berger, W.K. Ice can penetrate invertebrate tissues via paracellular pathways. *Cryo Letters* **25**, 139-146 (2004).

73. Yano, T., Hernandez-Blazquez, F.J., Omori, Y. & Yamasaki, H. Reduction of malignant phenotype of HEPG2 cell is associated with the expression of connexin 26 but not connexin 32. *Carcinogenesis* **22**, 1593-1600 (2001).

74. Yang, J., Ichikawa, A. & Tsuchiya, T. A novel function of connexin 32: marked enhancement of liver function in a hepatoma cell line. *Biochem Biophys Res Commun* **307**, 80-85 (2003).

75. Carruba, G. et al. Intercellular communication and human hepatocellular carcinoma. *Ann N Y Acad Sci* **1028**, 202-212 (2004).

76. Yin, C. et al. Adhesion contact dynamics of HepG2 cells on galactose-immobilized substrates. *Biomaterials* **24**, 837-850 (2003).

77. Vara, D.S. et al. Cardiovascular tissue engineering: state of the art. *Pathol Biol (Paris)* **53**, 599-612 (2005).

78. Heyligers, J.M., Arts, C.H., Verhagen, H.J., de Groot, P.G. & Moll, F.L. Improving small-diameter vascular grafts: from the application of an endothelial cell lining to the construction of a tissue-engineered blood vessel. *Ann Vasc Surg* **19**, 448-456 (2005).

79. Butcher, J.T. & Nerem, R.M. Valvular endothelial cells regulate the phenotype of interstitial cells in co-culture: effects of steady shear stress. *Tissue Eng* **12**, 905-915 (2006).

80. Skanes, A.C., Klein, G., Krahn, A. & Yee, R. Cryoablation: potentials and pitfalls. *J Cardiovasc Electrophysiol* **15**, S28-34 (2004).

81. Nelson, C.M. & Chen, C.S. Cell-cell signaling by direct contact increases cell proliferation via a PI3K-dependent signal. *FEBS Lett* **514**, 238-242 (2002).

82. Reinhart-King, C.A., Dembo, M. & Hammer, D.A. The dynamics and mechanics of endothelial cell spreading. *Biophys J* **89**, 676-689 (2005).

83. Kawakami, K., Tatsumi, H. & Sokabe, M. Dynamics of integrin clustering at focal contacts of endothelial cells studied by multimode imaging microscopy. *J Cell Sci* **114**, 3125-3135 (2001).

84. Nelson, C.M. & Chen, C.S. VE-cadherin simultaneously stimulates and inhibits cell proliferation by altering cytoskeletal structure and tension. *J Cell Sci* **116**, 3571-3581 (2003).

85. Luscinskas, F.W. & Lawler, J. Integrins as dynamic regulators of vascular function. *Faseb J* **8**, 929-938 (1994).

86. Zhang, Z., Vuori, K., Reed, J.C. & Ruoslahti, E. The alpha 5 beta 1 integrin supports survival of cells on fibronectin and up-regulates Bcl-2 expression. *Proc Natl Acad Sci U S A* **92**, 6161-6165 (1995).

87. de Wit, C., Hoepfl, B. & Wolfle, S.E. Endothelial mediators and communication through vascular gap junctions. *Biol Chem* **387**, 3-9 (2006).

88. Yeh, H.I., Rothery, S., Dupont, E., Coppen, S.R. & Severs, N.J. Individual gap junction plaques contain multiple connexins in arterial endothelium. *Circ Res* **83**, 1248-1263 (1998).

89. Dora, K.A. Cell-cell communication in the vessel wall. *Vasc Med* **6**, 43-50 (2001).

90. Ebertz, S.L. & McGann, L.E. Cryoinjury in endothelial cell monolayers. *Cryobiology* **49**, 37-44 (2004).

91. Pegg, D.E. Cryopreservation of vascular endothelial cells as isolated cells and as monolayers. *Cryobiology* **44**, 46-53 (2002).

92. Canals, M. et al. Optimization of a method for the cryopreservation of rabbit corneas: attempted application to human corneas. *Cell Tissue Bank* **1**, 271-278 (2000).

93. Fong, L.P., Hunt, C.J., Taylor, M.J. & Pegg, D.E. Cryopreservation of rabbit corneas: assessment by microscopy and transplantation. *Br J Ophthalmol* **70**, 751-760 (1986).

94. Gillespie, D.T. A general method for numerically simulating stochastic time evolution of coupled chemical reactions. *J Comp Phys* **22**, 403-434 (1976).

95. Shimada, K. & Asahina, E. Visualization of Intracellular Ice Crystals Formed in Very Rapidly Frozen Cells at -27 Degreesc. *Cryobiology* **12**, 209-218 (1975).

96. Acker, J.P., Elliott, J.A. & McGann, L.E. Ice growth through pores: experimental evidence for the propagation of intracellular ice. *Cryobiology* **41**, 354-355 (2000).

97. Karlsson, J.O. Theoretical analysis of unidirectional intercellular ice propagation in stratified cell clusters. *Cryobiology* **48**, 357-361 (2004).

98. Carte, A.E. Probability of Freezing. *Proceedings of the Physical Society of London* **73**, 324-324 (1959).

99. Gallant, N.D., Michael, K.E. & Garcia, A.J. Cell adhesion strengthening: contributions of adhesive area, integrin binding, and focal adhesion assembly. *Mol Biol Cell* **16**, 4329-4340 (2005).

100. Alexiades, V. & Solomon, A.D. in Mathematical modeling of melting and freezing processes 119-120 (Hemisphere Publishing Group, Washington, DC; 1993).

101. Chen, C.S., Alonso, J.L., Ostuni, E., Whitesides, G.M. & Ingber, D.E. Cell shape provides global control of focal adhesion assembly. *Biochem Biophys Res Commun* **307**, 355-361 (2003).

102. Burmeister, J.S., Truskey, G.A. & Reichert, W.M. Quantitative analysis of variable-angle total internal reflection fluorescence microscopy (VA-TIRFM) of cell/substrate contacts. *J Microsc* **173 (Pt 1)**, 39-51 (1994).

103. Burmeister, J.S., Vrany, J.D., Reichert, W.M. & Truskey, G.A. Effect of fibronectin amount and conformation on the strength of endothelial cell adhesion to HEMA/EMA copolymers. *J Biomed Mater Res* **30**, 13-22 (1996).

104. Davies, P.F., Robotewskyj, A. & Griem, M.L. Endothelial cell adhesion in real time. Measurements in vitro by tandem scanning confocal image analysis. *J Clin Invest* **91**, 2640-2652 (1993).

105. Mazur, P., Seki, S., Pinn, I.L., Kleinhans, F.W. & Edashige, K. Extra- and intracellular ice formation in mouse oocytes. *Cryobiology* **51**, 29-53 (2005).

106. Tsuruta, T., Kawamizu, T., Nonaka, I. & Masuoka, T. in. (eds. M. Giot, F. Mayinger & G.P. Celata) 1999-20051997).

107. Myers, S.P., Pitt, R.E., Lynch, D.V. & Steponkus, P.L. Characterization of intracellular ice formation in Drosophila melanogaster embryos. *Cryobiology* **26**, 472-484 (1989).

108. Korber, C., Englich, S. & Rau, G. Intracellular ice formation: cryomicroscopical observation and calorimetric measurement. *J Microsc* **161 (Pt 2)**, 313-325 (1991).

109. Devireddy, R.V., Raha, D. & Bischof, J.C. Measurement of water transport during freezing in cell suspensions using a differential scanning calorimeter. *Cryobiology* **36**, 124-155 (1998).

110. Rastogi, R.P. & Bassi, P.S. Mechanism of eutectic crystallization. *Journal of Physical Chemistry* **68**, 2398-& (1964).

111. Santarius, K.A. Freezing. The effect of eutectic crystallization on biological membranes. *Biochim Biophys Acta* **291**, 38-50 (1973).

112. Kristiansen, J. Leakage of a trapped fluorescent marker from liposomes: effects of eutectic crystallization of NaCl and internal freezing. *Cryobiology* **29**, 575-584 (1992).

113. Han, B. & Bischof, J.C. Direct cell injury associated with eutectic crystallization during freezing. *Cryobiology* **48**, 8-21 (2004).

114. Chen, N.J., Morikawa, J. & Hashimoto, T. Effect of amino acids on the eutectic behavior of NaCl solutions studied by DSC. *Cryobiology* **50**, 264-272 (2005).

115. Kristiansen, J. & Westh, P. Freezing behavior of multilamellar vesicles in 0.9-percent sodium-chloride. *Cryo-Letters* **12**, 167-176 (1991).

116. Morris, G.J. & McGrath, J.J. Intracellular ice nucleation and gas bubble formation in spirogyra. *Cryo Letters* **2**, 341 (1981).

117. Bryant, G., Heschel, I. & Rau, G. The influence of gas-bubbles on intracellular ice formation. *Cryo-Letters* **15**, 113-118 (1994).

118. Lipp, G., Korber, C., Englich, S., Hartmann, U. & Rau, G. Investigation of the Behavior of Dissolved-Gases during Freezing. *Cryobiology* **24**, 489-503 (1987).

119. Kutala, V.K., Parinandi, N.L., Pandian, R.P. & Kuppusamy, P. Simultaneous measurement of oxygenation in intracellular and extracellular compartments of lung microvascular endothelial cells. *Antioxid Redox Signal* **6**, 597-603 (2004).

120. Wang, N. & Ingber, D.E. Control of cytoskeletal mechanics by extracellular matrix, cell shape, and mechanical tension. *Biophys J* **66**, 2181-2189 (1994).

121. Thoumine, O., Cardoso, O. & Meister, J.J. Changes in the mechanical properties of fibroblasts during spreading: a micromanipulation study. *Eur Biophys J* **28**, 222-234 (1999).

122. Raucher, D. & Sheetz, M.P. Cell spreading and lamellipodial extension rate is regulated by membrane tension. *J Cell Biol* **148**, 127-136 (2000).

123. Sheetz, M.P. & Dai, J. Modulation of membrane dynamics and cell motility by membrane tension. *Trends Cell Biol* **6**, 85-89 (1996).

124. Goldstein, A.S. & DiMilla, P.A. Examination of membrane rupture as a mechanism for mammalian cell detachment from fibronectin-coated biomaterials. *J Biomed Mater Res A* **67**, 658-666 (2003).

125. Delanoe-Ayari, H., Al Kurdi, R., Vallade, M., Gulino-Debrac, D. & Riveline, D. Membrane and acto-myosin tension promote clustering of adhesion proteins. *Proc Natl Acad Sci U S A* **101**, 2229-2234 (2004).

126. Hynes, R.O. et al. The diverse roles of integrins and their ligands in angiogenesis. *Cold Spring Harb Symp Quant Biol* **67**, 143-153 (2002).

127. Faull, R.J., Kovach, N.L., Harlan, J.M. & Ginsberg, M.H. Affinity modulation of integrin alpha 5 beta 1: regulation of the functional response by soluble fibronectin. *J Cell Biol* **121**, 155-162 (1993).

128. Geiger, B., Bershadsky, A., Pankov, R. & Yamada, K.M. Transmembrane crosstalk between the extracellular matrix--cytoskeleton crosstalk. *Nat Rev Mol Cell Biol* **2**, 793-805 (2001).

129. Izzard, C.S. & Lochner, L.R. Cell-to-substrate contacts in living fibroblasts: an interference reflexion study with an evaluation of the technique. *J Cell Sci* **21**, 129-159 (1976).

130. Chen, C.S., Mrksich, M., Huang, S., Whitesides, G.M. & Ingber, D.E. Micropatterned surfaces for control of cell shape, position, and function. *Biotechnol Prog* **14**, 356-363 (1998).

131. Ito, Y. Surface micropatterning to regulate cell functions. *Biomaterials* **20**, 2333-2342 (1999).

132. Ingber, D.E. Mechanosensation through integrins: cells act locally but think globally. *Proc Natl Acad Sci U S A* **100**, 1472-1474 (2003).

133. Deng, T., Tien, J., Xu, B. & Whitesides, G.M. Using patterns in microfiche as photomasks in 10-mu m-scale microfabrication. *Langmuir* **15**, 6575-6581 (1999).

134. Deng, T., Wu, H.K., Brittain, S.T. & Whitesides, G.M. Prototyping of masks, masters, and stamps/molds for soft lithography using an office printer and photographic reduction. *Analytical Chemistry* **72**, 3176-3180 (2000).

135. Geiger, B., Tokuyasu, K.T., Dutton, A.H. & Singer, S.J. Vinculin, an intracellular protein localized at specialized sites where microfilament bundles terminate at cell membranes. *Proc Natl Acad Sci U S A* **77**, 4127-4131 (1980).

136. Galbraith, C.G., Yamada, K.M. & Sheetz, M.P. The relationship between force and focal complex development. *J Cell Biol* **159**, 695-705 (2002).

137. Hynes, R.O. Integrins: a family of cell surface receptors. *Cell* **48**, 549-554 (1987).

138. Chen, C.S., Tan, J. & Tien, J. Mechanotransduction at cell-matrix and cell-cell contacts. *Annu Rev Biomed Eng* **6**, 275-302 (2004).

139. Hetzel, F.W., Kruuv, J., McGann, L.E. & Frey, H.E. Exposure of mammalian cells to physical damage: effect of the state of adhesion on colony-forming potential. *Cryobiology* **10**, 206-211 (1973).

140. Hornung, J., Muller, T. & Fuhr, G. Cryopreservation of anchorage-dependent mammalian cells fixed to structured glass and silicon substrates. *Cryobiology* **33**, 260-270 (1996).

141. Reinhart-King, C.A., Dembo, M. & Hammer, D.A. Endothelial cell traction forces on RGD-derivatized polyacrylamide substrata. *Langmuir* **19**, 1573-1579 (2003).

142. Dubin-Thaler, B.J., Giannone, G., Dobereiner, H.G. & Sheetz, M.P. Nanometer analysis of cell spreading on matrix-coated surfaces reveals two distinct cell states and STEPs. *Biophys J* **86**, 1794-1806 (2004).

143. Garcia, A.J., Huber, F. & Boettiger, D. Force required to break alpha5beta1 integrin-fibronectin bonds in intact adherent cells is sensitive to integrin activation state. *J Biol Chem* **273**, 10988-10993 (1998).

144. Chen, C.S., Mrksich, M., Huang, S., Whitesides, G.M. & Ingber, D.E. Geometric control of cell life and death. *Science* **276**, 1425-1428 (1997).

145. Sumpter, M.L. Johnson-Mehl-Avrami kinetics of intracellular ice formation in confluent tissue constructs. MS Thesis, Georgia Institute of Technology (2003).

146. el-Fouly, M.H., Trosko, J.E. & Chang, C.C. Scrape-loading and dye transfer. A rapid and simple technique to study gap junctional intercellular communication. *Exp Cell Res* **168**, 422-430 (1987).

147. Opsahl, H. & Rivedal, E. Quantitative determination of gap junction intercellular communication by scrape loading and image analysis. *Cell Adhes Commun* **7**, 367-375 (2000).

148. el-Sabban, M.E. & Pauli, B.U. Cytoplasmic dye transfer between metastatic tumor cells and vascular endothelium. *J Cell Biol* **115**, 1375-1382 (1991).

149. Czyz, J., Irmer, U., Schulz, G., Mindermann, A. & Hulser, D.F. Gap-junctional coupling measured by flow cytometry. *Exp Cell Res* **255**, 40-46 (2000).

150. Darr, T.B. & Hubel, A. Postthaw viability of precultured hepatocytes. *Cryobiology* **42**, 11-20 (2001).

151. Nelson, C.M., Pirone, D.M., Tan, J.L. & Chen, C.S. Vascular endothelial-cadherin regulates cytoskeletal tension, cell spreading, and focal adhesions by stimulating RhoA. *Mol Biol Cell* **15**, 2943-2953 (2004).

152. Timmons, L. The long and short of siRNAs. *Mol Cell* **10**, 435-437 (2002).

153. Li, X. et al. Leukemogenic AML1-ETO fusion protein upregulates expression of connexin 43: The role in AML1-ETO-induced growth arrest in leukemic cells. *J Cell Physiol* (2006).

154. Simon, A.M., McWhorter, A.R., Chen, H., Jackson, C.L. & Ouellette, Y. Decreased intercellular communication and connexin expression in mouse aortic endothelium during lipopolysaccharide-induced inflammation. *J Vasc Res* **41**, 323-333 (2004).

155. Armitage, W.J. & Juss, B.K. Freezing monolayers of cells without gap junctions. *Cryobiology* **46**, 194-196 (2003).

156. Goldberg, G.S., Valiunas, V. & Brink, P.R. Selective permeability of gap junction channels. *Biochim Biophys Acta* **1662**, 96-101 (2004).

157. Atala, A. Tissue engineering and regenerative medicine: Concepts for clinical application. *Rejuvenation Research* **7**, 15-31 (2004).

158. Bhatia, S.N., Balis, U.J., Yarmush, M.L. & Toner, M. Effect of cell-cell interactions in preservation of cellular phenotype: cocultivation of hepatocytes and nonparenchymal cells. *Faseb J* **13**, 1883-1900 (1999).

159. Lavender, M.D., Pang, Z., Wallace, C.S., Niklason, L.E. & Truskey, G.A. A system for the direct co-culture of endothelium on smooth muscle cells. *Biomaterials* **26**, 4642-4653 (2005).

160. Tan, W. & Desai, T.A. Microscale multilayer cocultures for biomimetic blood vessels. *J Biomed Mater Res A* **72**, 146-160 (2005).

161. Koike, N. et al. Tissue engineering: creation of long-lasting blood vessels. *Nature* **428**, 138-139 (2004).

162. Brown, A.N., Kim, B.S., Alsberg, E. & Mooney, D.J. Combining chondrocytes and smooth muscle cells to engineer hybrid soft tissue constructs. *Tissue Eng* **6**, 297-305 (2000).

163. Risbud, M.V., Karamuk, E., Moser, R. & Mayer, J. Hydrogel-coated textile scaffolds as three-dimensional growth support for human umbilical vein endothelial cells (HUVECs): possibilities as coculture system in liver tissue engineering. *Cell Transplant* **11**, 369-377 (2002).

164. Brown, A.L. et al. Bladder acellular matrix as a substrate for studying in vitro bladder smooth muscle-urothelial cell interactions. *Biomaterials* **26**, 529-543 (2005).

165. Zhang, Y. et al. Coculture of bladder urothelial and smooth muscle cells on small intestinal submucosa: potential applications for tissue engineering technology. *J Urol* **164**, 928-934; discussion 934-925 (2000).

166. Bhatia, S.N., Yarmush, M.L. & Toner, M. Controlling cell interactions by micropatterning in co-cultures: hepatocytes and 3T3 fibroblasts. *J Biomed Mater Res* **34**, 189-199 (1997).

167. Kang, I.K., Kim, G.J., Kwon, O.H. & Ito, Y. Co-culture of hepatocytes and fibroblasts by micropatterned immobilization of beta-galactose derivatives. *Biomaterials* **25**, 4225-4232 (2004).

168. Khademhosseini, A. et al. Layer-by-layer deposition of hyaluronic acid and poly-L-lysine for patterned cell co-cultures. *Biomaterials* **25**, 3583-3592 (2004).

169. Takayama, S. et al. Patterning cells and their environments using multiple laminar fluid flows in capillary networks. *Proc Natl Acad Sci U S A* **96**, 5545-5548 (1999).

170. Yousaf, M.N., Houseman, B.T. & Mrksich, M. Using electroactive substrates to pattern the attachment of two different cell populations. *Proc Natl Acad Sci U S A* **98**, 5992-5996 (2001).

171. Yamato, M., Kwon, O.H., Hirose, M., Kikuchi, A. & Okano, T. Novel patterned cell coculture utilizing thermally responsive grafted polymer surfaces. *J Biomed Mater Res* **55**, 137-140 (2001).

172. Nahmias, Y., Schwartz, R.E., Verfaillie, C.M. & Odde, D.J. Laser-guided direct writing for three-dimensional tissue engineering. *Biotechnol Bioeng* (2005).

173. Pitt, R.E., Chandrasekaran, M. & Parks, J.E. Performance of a kinetic model for intracellular ice formation based on the extent of supercooling. *Cryobiology* **29**, 359-373 (1992).

174. Diller, K.R. & Raymond, J.F. Water transport through a multicellular tisse during freezing: A network thermodynamic modeling analysis. *Cryo Letters* **11**, 151-162 (1990).

175. Stott, S.L., Irimia, D. & Karlsson, J.O. Parametric analysis of intercellular ice propagation during cryosurgery, simulated using Monte Carlo techniques. *Technol Cancer Res Treat* **3**, 113-123 (2004).

176. Dwerryhouse, S.J. et al. Hepatic resection with cryotherapy to involved or inadequate resection margin (edge freeze) for metastases from colorectal cancer. *Br J Surg* **85**, 185-187 (1998).

177. Badalament, R.A. et al. Patient-reported complications after cryoablation therapy for prostate cancer. *Arch Ital Urol Androl* **72**, 305-312 (2000).

178. Aus, G., Pileblad, E. & Hugosson, J. Cryosurgical ablation of the prostate: 5-year follow-up of a prospective study. *Eur Urol* **42**, 133-138 (2002).

179. Pham, L., Dahiya, R. & Rubinsky, B. An in vivo study of antifreeze protein adjuvant cryosurgery. *Cryobiology* **38**, 169-175 (1999).

180. Muldrew, K. et al. Flounder antifreeze peptides increase the efficacy of cryosurgery. *Cryobiology* **42**, 182-189 (2001).

181. Clarke, D.M., Baust, J.M., Van Buskirk, R.G. & Baust, J.G. Chemo-cryo combination therapy: an adjunctive model for the treatment of prostate cancer. *Cryobiology* **42**, 274-285 (2001).

182. Burgher, A.H. et al. Sensitization of thermotolerant SCK cells to hyperthermia and freezing with reduction of intracellular pH: implications for cryosurgery. *J Surg Oncol* **82**, 160-169 (2003).

183. Cohen, J.K., Miller, R.J. & Shuman, B.A. Urethral warming catheter for use during cryoablation of the prostate. *Urology* **45**, 861-864 (1995).

184. Rabin, Y. & Stahovich, T.F. Cryoheater as a means of cryosurgery control. *Phys Med Biol* **48**, 619-632 (2003).

185. Bischof, J.C. et al. Cryosurgery of dunning AT-1 rat prostate tumor: thermal, biophysical, and viability response at the cellular and tissue level. *Cryobiology* **34**, 42-69 (1997).

186. Rabin, Y. & Shitzer, A. Numerical solution of the multidimensional freezing problem during cryosurgery. *J Biomech Eng* **120**, 32-37 (1998).

187. Radai, M.M., Abboud, S. & Rubinsky, B. Evaluation of the impedance technique for cryosurgery in a theoretical model of the head. *Cryobiology* **38**, 51-59 (1999).

188. Baissalov, R., Sandison, G.A., Reynolds, D. & Muldrew, K. Simultaneous optimization of cryoprobe placement and thermal protocol for cryosurgery. *Phys Med Biol* **46**, 1799-1814 (2001).

189. Liu, J. & Zhou, Y.X. Analytical study on the freezing and thawing processes of biological skin with finite thickness. *Heat and Mass Transfer* **38**, 319-326 (2002).

190. Zhang, A., Xu, L.X., Sandison, G.A. & Zhang, J. A microscale model for prediction of breast cancer cell damage during cryosurgery. *Cryobiology* **47**, 143-154 (2003).

191. Hollister, W.R., Mathew, A.J., Baust, J.G. & Van Buskirk, R.G. Effects of freezing on cell viability and mechanisms of cell death in a human prostate cancer cell line. *Molecular Urology* **2**, 13-18 (1998).

192. Hanai, A., Yang, W.L. & Ravikumar, T.S. Induction of apoptosis in human colon carcinoma cells HT29 by sublethal cryo-injury: Mediation by cytochrome C release. *International Journal of Cancer* **93**, 526-533 (2001).

193. Mala, T. et al. Hepatic vascular inflow occlusion enhances tissue destruction during cryoablation of porcine liver. *Journal of Surgical Research* **115**, 265-271 (2003).

194. Loewenstein, W.R. Cell-to-cell communication and the control of growth. *Am Rev Respir Dis* **142**, S48-53 (1990).

195. Neel, H.B., 3rd, Ketcham, A.S. & Hammond, W.G. Requisites for successful cryogenic surgery of cancer. *Arch Surg* **102**, 45-48 (1971).

196. Kiricuta, I.C. & Simplaceanu, V. Tissue Water-Content and Nuclear Magnetic-Resonance in Normal and Tumor Tissues. *Cancer Research* **35**, 1164-1167 (1975).

197. Saryan, L.A., Hollis, D.P., Economou, J.S. & Egglesto.Jc Nuclear Magnetic-Resonance Studies of Cancer .4. Correlation of Water-Content with Tissue Relaxation-Times. *Journal of the National Cancer Institute* **52**, 599-602 (1974).

198. Ross, K.F.A. & Gordon, R.E. Water in Malignant-Tissue, Measured by Cell Refractometry and Nuclear Magnetic-Resonance. *Journal of Microscopy-Oxford* **128**, 7-21 (1982).

199. Cameron, I.L., Ord, V.A. & Fullerton, G.D. Characterization of proton NMR relaxation times in normal and pathological tissues by correlation with other tissue parameters. *Magn Reson Imaging* **2**, 97-106 (1984).

200. Vargas, H.I. et al. Focused microwave phased array thermotherapy for ablation of early-stage breast cancer: Results of thermal dose escalation. *Annals of Surgical Oncology* **11**, 139-146 (2004).

201. Cameron, I.L., Hunter, K.E., Ord, V.A. & Fullerton, G.D. Relationships between Ice Crystal Size, Water-Content and Proton Nmr Relaxation-Times in Cells. *Physiological Chemistry and Physics and Medical Nmr* **17**, 371-386 (1985).

202. Bischof, J., Christov, K. & Rubinsky, B. A morphological-study of cooling rate response in normal and neoplastic human liver-tissue - cryosurgical implications. *Cryobiology* **30**, 482-492 (1993).

203. Karlsson, J.O.M., Cravalho, E.G. & Toner, M. A model of diffusion-limited ice growth inside biological cells during freezing. *Journal of Applied Physics* **75**, 4442-4445 (1994).

204. Sumpter, M.L., Stott, S.L. & Karlsson, J.O.M. Avrami kinetic of intercellular ice propagation during freezing of confluent tissues. *Cryobiology* **47** (2003).

205. Yu, Z.W. & Quinn, P.J. The modulation of membrane structure and stability by dimethyl sulphoxide (review). *Mol Membr Biol* **15**, 59-68 (1998).

206. Neulieb, R.L. & Neulieb, M.K. The diverse actions of dimethyl sulphoxide: an indicator of membrane transport activity. *Cytobios* **63**, 139-165 (1990).

207. Titushkin, I. & Cho, M. Distinct membrane mechanical properties of human mesenchymal stem cells determined using laser optical tweezers. *Biophys J* **90**, 2582-2591 (2006).

208. Zhou, R., Watson, C., Fu, C., Yao, X. & Forte, J.G. Myosin II is present in gastric parietal cells and required for lamellipodial dynamics associated with cell activation. *Am J Physiol Cell Physiol* **285**, C662-673 (2003).

209. Dakin, K., Zhao, Y. & Li, W.H. LAMP, a new imaging assay of gap junctional communication unveils that Ca2+ influx inhibits cell coupling. *Nat Methods* **2**, 55-62 (2005).